Relevant Properties and Governing Mechanisms for Oil Recovery and Geological Carbon Dioxide Storage Applied to Jordanian Shale

Dissertation

zur Erlangung des Doktorgrades

der Ingenieurwissenschaften

vorgelegt von

Hanin Samara, M.Sc.

aus Amman, Jordanien

genehmigt von der

Fakultät für Energie- und Wirtschaftswissenschaften

der Technischen Universität Clausthal,

Tag der mündlichen Prüfung

30.06.2023

Dekan

Prof. Dr. mont. Leonhard Ganzer

Vorsitzender der Promotionskommission

Prof. Dr. mont. Leonhard Ganzer

Betreuer

Prof. Dr. Ing. habil. Philip Jaeger

Gutachterin

Prof. Maria José Cocero Alonso

Gutachter

Prof. Omar Salim Al-Ayed

EIDESSTATTLICHE ERKLÄRUNG - Declaration of Authorship

Hiermit erkläre ich an Eides Statt, dass ich die bei der Fakultät für Energie- und Wirtschaftswissenschaften der Technischen Universität Clausthal eingereichte Dissertation selbständig und ohne unerlaubte Hilfe angefertigt habe. Die benutzten Hilfsmittel sind vollständig angegeben.

Unterschrift:

Datum: 15.3.2023

Abstract

In light of the ever-growing energy demand and the increasing atmospheric concentrations of carbon dioxide, the necessity of finding a panacea to these global challenges is unprecedented. In spite of several attempts to accelerate the energy transition, future outlooks indicate that fossil fuels will remain the foundation that supports the livelihood and economic prosperity of global societies. Owing to the declining rates of conventional oil production and the inevitable depletion of conventional reserves, it is predicted that unconventional resources will play a significant role in reshaping future energy markets, implying that the climate change dilemma associated with fossil fuels will linger on. On the other hand, Carbon Capture and Storage (CCS) has emerged as a pathway to decarbonization, whereas enhanced oil recovery using carbon dioxide (CO_2-EOR) has already demonstrated great success in boosting oil production of existing oil fields since the 1970s. Accordingly, the combination of CCS and CO_2-EOR is proposed as a solution to the energy-climate predicament. This approach is also being currently considered in shales, however, little is still known about its applicability in these formations. Accordingly, the current work aims to investigate a series of phenomena that contribute to oil recovery from shale using supercritical CO_2. Additionally, within the context of geological carbon storage (GCS), several decisive interfacial and phase properties are examined, with the objective of combining the use of CO_2 for oil recovery with its own storage. Jordanian oil shale (Sultani) is used as an example in the current work for the potential economic and environmental interest on the one hand, and for the acquired knowledge that can be generalized and transferred to any oil-bearing unconventional reservoir on the other. The presented work is a comprehensive experimental study on the principal phase, interfacial and transport properties taking place when complex oil and water-bearing shale formations are contacted with compressed CO_2.

As an initial step in this investigation, Sultani shale is subject to supercritical fluid extraction using CO_2 as solvent. The impact of several parameters on the yield, which is related to the solubility of various compounds in the supercritical phase, is examined. Apart from the phase behavior that also includes mixture densities, volumetric expansion and gas solubility in hydrocarbons, interfacial properties are the principal focus of this work. Interfacial tension in binary and multicomponent systems at reservoir conditions, i.e. at elevated pressures, is measured using the pendant drop and the rising bubble methods, respectively. The contact angle, a measure of wettability, is determined using the sessile drop in CO_2-brine-shale systems. The captive bubble method is employed to assess the contact angle in the multicomponent system comprising CO_2, brine, oil and shale. Zeta potential is determined for "shale in water/brine" suspensions to investigate the evolution of the charge at the water/brine-shale interface in pursuit of explaining the wettability alteration in response to changing the aqueous phase composition. With respect to the fluid-solid interface, the CO_2 adsorption capacity of shale is measured at pressures and temperatures relevant to gas storage using a gravimetric method, and its relation to the wetting behavior in presence of brines representative of formation water is elucidated. Complementing the interfacial properties and the phase behavior, CO_2 diffusivity within shale formations is quantified. All in all, it is found that the strong interactions of supercritical CO_2 with all coexisting phases alter the system properties significantly, mainly in an advantageous way regarding oil recovery. In terms of GCS, supercritical CO_2 is found to alter system properties in both favorable and unfavorable ways, depending on the gas storage mechanism in question. The findings of the current work give valuable insight into mechanisms, properties, and critical factors which are necessary for the design and implementation of successful oil recovery and CO_2 storage processes.

Kurzfassung

Mit Blick auf den stetig wachsenden Energiebedarf und der damit im Zusammenhang stehenden dramatischen Zunahme der CO_2-Konzentration in der Atmosphäre steht die Menschheit vor der Aufgabe, Antworten auf bislang beispiellose Herausforderungen zu finden. Trotz verstärkter Bemühungen, die sogenannte Energiewende voranzutreiben, geht der Großteil der Vorhersagen davon aus, dass die Grundlage zur Deckung des globalen Energiebedarfes weiterhin durch fossile Brennstoffe gesichert wird. Gleichzeitig ist eine deutliche Abnahme der Produktion aus konventionellen Ölreserven zu verzeichnen, sodass nicht-konventionelle Ressourcen in Zukunft eine größere Rolle übernehmen werden. Auf der anderen Seite werden die Bemühungen zur Abtrennung und Untertagespeicherung von CO_2 als ein Bestandteil der Dekarbonisierung vorangetrieben. Erfahrungen mit der Injektion von CO_2 existieren bereits seit den 1970er Jahren im Rahmen der sogenannten "CO_2-enhanced oil recovery" (CO_2-EOR) mit gutem Erfolg zur Steigerung der Förderraten aus konventionellen Lagerstätten. Daher erscheint es naheliegend, die beiden Prozesse im Sinne einer zügigen Umsetzung der Energiewende zu kombinieren und in der Folge auch für nicht-konventionelle Lagerstätten in Betracht zu ziehen. Über die mögliche Anwendung innovativer Methoden in diesen oft sehr komplexen Gesteinsformationen ist bislang wenig bekannt geworden. Daher befasst sich die aktuelle Dissertation mit einer Reihe an Phänomenen, die im Zusammenhang mit der Applikation von komprimiertem CO_2 auf Schieferformationen relevant sind. Entscheidende Systemeigenschaften wurden in dieser Arbeit untersucht mit dem Ziel, Möglichkeiten zur Kombination einer CO_2-gestützten Förderung von Kohlenwasserstoffen mit der Einspeicherung von CO_2 in nicht-konventionellen Lagerstätten zu evaluieren. Jordanischer Ölschiefer (Sultani) dient hier als Beispiel mit einem erheblichen Potenzial aus wirtschaftlicher und umwelttechnischer Sicht. Es werden umfangreiche und systematische experimentelle Untersuchungen zum grundlegenden Phasen-, Grenzphasen- und

Stofftransportverhalten in komplexen dichten Wasser- und Kohlenwasserstoffhaltigen Gesteinsformationen in Kontakt mit komprimiertem CO_2 vorgestellt.

In einem ersten Schritt wurde Sultani-Schiefer einer Extraktion mit überkritischem CO_2 unterzogen. Dabei wurde der Einfluss unterschiedlicher Betriebsparameter auf die Ausbeute untersucht, die wiederum in direktem Zusammenhang mit der Löslichkeit unterschiedlicher im Ölschiefer enthaltener Komponenten in der CO_2-Phase steht. Neben der Analyse des Mehrphasenverhaltens, zu dem die Bestimmung von Gemischdichten, die Löslichkeit von CO_2 in Kohlenwasserstoffmischungen und die daraus folgende volumetrische Ausdehnung der Kohlenwasserstoffphase gehört, bestand ein Schwerpunkt der Arbeit in der experimentellen Betrachtung von Grenzphaseneigenschaften unter Lagerstättenbedingungen. Als eine maßgebliche Größe wurde die Grenzflächenspannung in mehrphasigen Multikomponentensystemen mittels der Methode des hängenden, stehenden bzw. liegenden Tropfens bestimmt. Die Benetzung an den inneren Porenwänden wird durch den Dreiphasen-Kontaktwinkel beschrieben, der sowohl im System CO_2-Formationswasser-Schiefer als auch in dem System CO_2-Kohlenwasserstoff-Formationswasser-Schiefer an liegenden Tropfen bestimmt wurde. Zur Erklärung der Abhängigkeit der Benetzung von der Zusammensetzung der wässerigen Phase wurden Messungen des Zeta – Potentials an in wässerigen Salzlösungen suspendierten Schieferpartikeln unternommen. Die Grenzfläche Feststoff-CO_2 war hingegen Gegenstand von Messungen mittels einer gravimetrischen Methode, mittels derer die Adsorptionskapazität des Schiefers bestimmt wurde, die einerseits als eine der möglichen Speichermechanismen für CO_2 gilt und andererseits in direkter Beziehung zum Benetzungsverhalten in Anwesenheit von wässerigen Salzlösungen steht. In Ergänzung zu dem Mehr- und Grenzphasenverhalten wurden Diffusionskoeffizienten von komprimiertem CO_2 im Gestein bestimmt, die letzten Endes über die Zeitskala der im Fokus stehenden

ablaufenden Prozesse entscheidet. Im Ergebnis führen die hohen Wechselwirkungen aller beteiligten Phasen mit überkritischem CO_2 zu bedeutenden Änderungen in den Systemeigenschaften, die die Mobilisierung der Kohlenwasserstoffe generell fördern, während sich diese auch negativ auf eine Geo-Speicherung von CO_2 etwa über die Herabsetzung des kapillaren Eindringdruckes auswirken können. Die Arbeit liefert einen wertvollen Einblick in Mechanismen, Systemeigenschaften sowie kritische Faktoren, die für eine erfolgreiche Umsetzung einer CO_2-gestützten Ölförderung und der CO_2-Speicherung bzw. einer Kombination beider Prozesse in nicht-konventionellen Gesteinsformationen relevant sind.

Dedication

In loving memory of my late parents, Dr. Richhan Al-Timimi and Dr. Ihsan Samara.

Acknowledgement

First and foremost, I am indebted to my supervisor, Prof. Philip Jaeger, whose unwavering support and expertise have been invaluable throughout my research journey. His guidance, insightful feedback, and constant motivation have not only shaped my thesis but also fostered my growth as a researcher. I am truly grateful for his mentorship and the trust he has placed in me.

I would like to express my sincere gratitude to Prof. Omar Al-Ayed for consistently providing me with shale samples, which served as the foundation for my investigations. Additionally, I am grateful to Eurotechnica GmbH and its staff, particularly Ms. Tatjana von Ostrowski and Mr. Thomas Schmelling, for their unwavering technical support throughout this endeavor.

I extend my heartfelt appreciation to my dear colleague and friend, Dr. Bettina Jenei, for her constant support and encouragement. Her presence has been a source of inspiration and strength. Furthermore, I would like to thank Dr. Ke Li for the thorough characterization of Sultani shale, which significantly contributed to explaining my research findings.

I cannot forget to express my deepest thanks to my family and friends for their unwavering love and belief in my abilities. Their patience, understanding, and endless support have provided me with strength during the most challenging times.

Table of Contents

List of Figures

List of Tables

List of Symbols

Symbol	Definition, Unit
A	Area, m^2
k_B	Boltzmann constant, J/K
B_o	Bond number, unitless
F_B	Buoyancy force, N
P_c	Capillary pressure, MPa
μ_i	Chemical potential, J/mol
C	Concentration, mol/m^3
Θ	Contact angle, °
ρ	Density, g/cm^3 or kg/m^3
d	Diameter, m
ε	Dielectric constant, unitless
J_D	Diffusive flux, mol/m^2. s
D	Diffusivity, m^2/s
x	Distance, m
μ	Dynamic viscosity, kg/m.s or Pa.s
D_e	Effective diffusivity, m^2/s
U_e	Electrophoretic mobility, μm·cm / V·s
S	Entropy, J/K
D_{fick}	Fick's diffusivity, m^2/s
f	Fugacity, MPa
φ	Fugacity coefficient, unitless
G	Gibbs free energy, J
g	Gravitational acceleration constant, m/s^2
h	Height, m
γ	Interfacial tension, mN/m
$W\gamma$	Interfacial work, mN.m
U	Internal energy, J
D_k	Knudsen diffusivity, m^2/s
K_n	Knudsen number, unitless
m	Mass, kg
M_t/M_∞	Mass uptake, dimensionless
λ	Mean free path length, m
x_i, y_i	Molar fraction, unitless
M	Molar mass, mol/g
D_m	Molecular diffusivity, m^2/s
n_i	Number of moles
τ	Oscillation period, S
k	Permeability, D or m^2
P	Pressure, MPa
$\emptyset$	Porosity, unitless
r	Radius, m

D_{11}	Self-diffusivity, m^2/s
n	Series running index, unitless
Γ_i	Surface excess concentration of component i, mol/m^2
T	Temperature, °C or K
t	Time, min
τ	Tortuosity, unitless
D_{trans}	Transitional diffusivity, m^2/s
R	Universal gas constant, J/ mol.K
V	Volume, m^3
V_E	Volumetric expansion, unitless
F_w	Weight, N
ζ	Zeta potential, mV

1. Introduction

Despite current developments in renewable energy and energy efficiency technologies, fossil fuels continue to be essential energy carriers in the global energy landscape. For instance, electricity generation is still dominated by fossil fuel powered utilities like coal or gas-fired plants in many regions of the world (D. Liu et al., 2019; York, 2012). Conventional fuels are however non-replenishable, and while the concept of peak oil might be debatable, there exists wide consensus that fossil fuel depletion is inevitable (Mahzari et al., 2018), especially that the discovery of easily accessible reserves has decelerated significantly on a global scale. Consequently, the development of technologies that extend the lifespan of current reserves and the exploration of alternative fossil fuel resources are of utmost necessity.

1.1 Overview of the Jordanian Energy Landscape

The Hashemite Kingdom of Jordan is characterized by the scarcity of natural resources such as water and fossil fuels. Accordingly, the energy requirements of the country are satisfied through importing crude oil, petroleum products and natural gas from its neighbors. These imports constitute more than 90% of the country's demand and cost the country more than 40% its annual budget (IEA, 2023), which obviously severely burdens the national economy. With the ever-increasing energy demand as demonstrated in figure 1.1, and in light of the current political landscape, public opposition towards nuclear power plants, and the fluctuation and volatility of oil and gas prices, achieving energy security is a top priority for the Jordanian government. Consequently, there has been a focus shift towards the diversification of the Jordanian energy mix by incorporating local energy potential to reduce the reliance on energy imports. One objective of the first Jordanian master energy strategy proposed in 2007 is the integration of renewable wind and solar energy resources into the electric grid. Despite a targeted share of 10% in 2020, the share of renewable energy (RE) did not exceed 6% (IEA, 2023). Indeed, the contribution of RE cannot be undermined under any

circumstance, however, RE cannot be entirely relied on so far for an uninterrupted electricity supply to the base load, owing to its stochasticity and weather dependence, especially that energy storage technologies are not entirely mature or economically attractive yet (Leonard et al., 2020). Therefore, fossil fuel-fired power plants are relied on for a more robust energy supply.

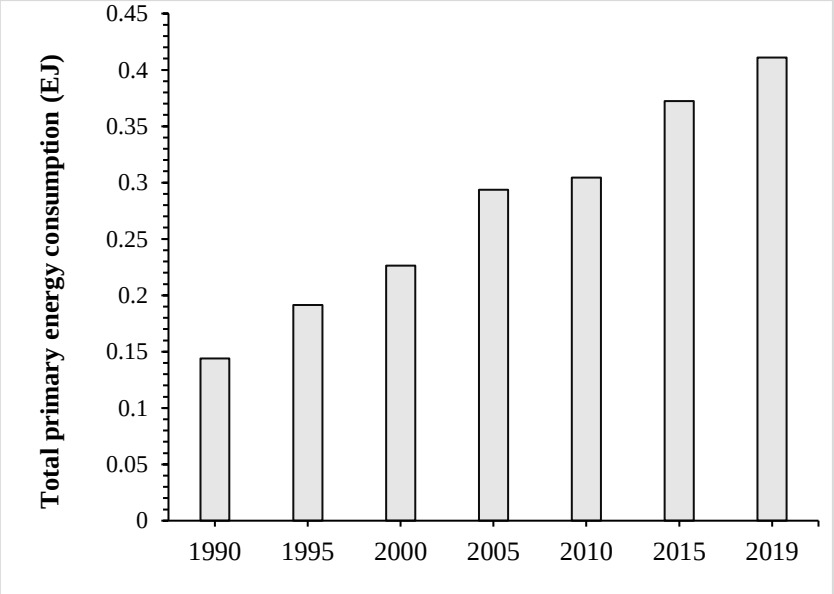

Figure 1.1 - Total Primary Energy Consumption in Jordan (IEA, 2023).

Another objective of the energy strategy is the exploitation of Jordanian shale. Jordan possesses an estimated reserve of 65 $x10^9$ tons of oil shale overlaying 60% of its territory, which renders it a country with the 8^{th} largest global oil shale reserve (Hakimi et al., 2016; Jaber and Probert, 1997). Currently, the exploitation of Jordanian oil shale is restricted to one project manifesting in a shale-fired power plant. The commercial operation thereof was planned to start in 2020. The power plant is operated by the Attarat Power Company (APCO) and utilizes circulating fluidized bed units for the combustion of shale (APCO, 2020). Shale combustion entails two environmental problems. Increased emissions of carbon dioxide (CO_2) and the management of the ash as a byproduct. While the latter maybe used as a self-cementitious material in the construction industry (Salah Alaloul et al., 2021), CO_2 persists as a greenhouse gas (GHG) contributing to climate change and its severe repercussions, imposing further challenges to the country's objective of

decreasing GHG emissions 31% by 2030 (UNDP, 2023). A further endeavor was undertaken by Shell starting 2010, through the use of the In-situ Conversion Process (ICP). The process entails the creation of a closely-spaced array, constituting horizontal electric heaters extending into the shale layer. The heating is conducted at about 325 °C, thereby accelerating the process of kerogen maturation (Meijssen et al., 2014). The ICP project was abandoned since H_2S in the extracted oil was found to be at alarming concentrations according to Jordan Ministry of Energy and Mineral Resources.

It is without a doubt that the escalating energy demand goes hand in hand with elevated atmospheric CO_2 concentrations. Figure 1.2 shows the amount of CO_2 released in Jordan within a 29-year period. The trend follows that of the primary energy consumption shown in figure 1.1, signifying a persisting high reliance on conventional energy resources. The aforementioned constraints necessitate the development of technologies that mitigate or at least stabilize GHGs, while maintaining the supply of a reliable and robust source of energy.

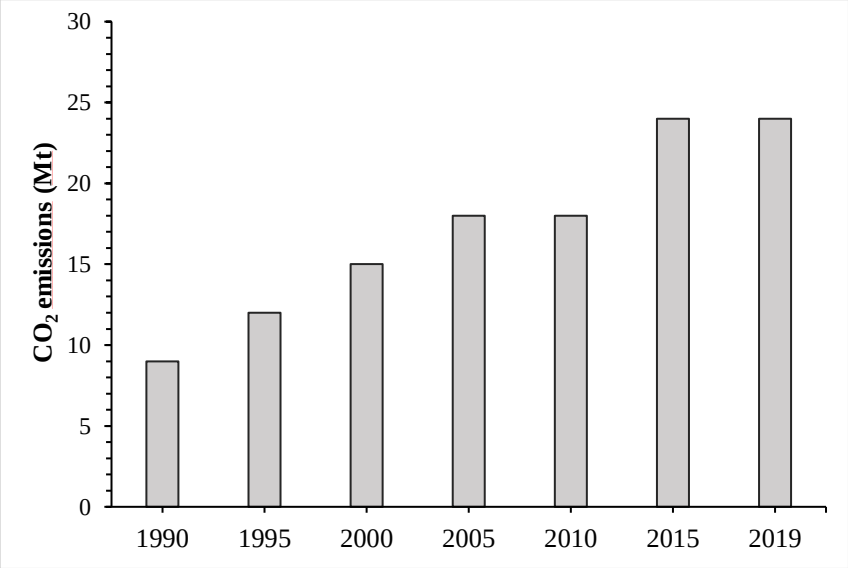

Figure 1.2 - Carbon emissions in Jordan (IEA, 2023).

1.2 Geological Carbon Storage

Carbon capture and storage (CCS) has emerged as a promising option to create a net-zero emission economy. The technology entails the separation of CO_2 from gas streams of industrial emitters and power generations plants -a major contributor to GHG-, followed by its compression, transportation, and finally its long-term storage by injection in geological formations. The last step in the CCS chain is termed Geological Carbon Storage (GCS). Several commercial projects have proven the success of the proposed approach. These include the Norwegian Sleipner project, where CO_2 injection started in 1996. The formation into which CO_2 is injected is a saline aquifer. The project has a daily injection rate of 3000 tons and a planned total storage capacity of 20 Mt CO_2. Another project is the In Salah depleted gas reservoir in Algeria (operational since 2004), with a daily CO_2 injection rate of up to 4000 tons and a total planned capacity of 17 Mt CO_2. Last but not least is the Canadian Weyburn project (operational since 2000), a carbonate reservoir with a daily injection rate of 5000 tons and a planned total storage capacity of 20 Mt (IPCC, 2005). The CO_2 is separated from a gasification plant in North Dakota, liquified and transported through a pipeline to the Weyburn oil field.

Several trapping mechanisms coexist during GCS. Structural trapping refers to the process in which CO_2 -either in a supercritical or gaseous state - is trapped under caprocks with permeabilities ranging between 10^{-18}-10^{-21} m^2 (Fleury et al., 2010), preventing it from escaping to the atmosphere. An oversimplification of the mechanism is that the buoyant gas encounters a seal with a capillary entry pressure that exceeds the buoyancy exerted by CO_2 (Zhang and Song, 2014), thereby preventing the gas from “leaking” into the caprock, however the partial invasion of the caprock by CO_2 may not necessarily imply that the gas is bound to leak to the atmosphere, and this partial invasion may contribute to an accelerated decrease in the overpressure on the one hand, and may significantly increase the storage capacity of the formation (Fleury et al., 2010). Accordingly,

the term leakage should be used with a proper clarification. This trapping mechanism constitutes the most important prerequisite for any storage formation, at least until other storage mechanisms are activated with time. The most prevalent caprocks are shales and evaporites (Grunau, 1987).

Residual or capillary trapping entails the entrapment of CO_2 as a discontinuous phase (isolated blobs) within the pores, where it is surrounded and immobilized by the imbibing formation brine after CO_2 injection is ceased. This trapping mechanism has a significant impact on the saturation and the distribution of CO_2 within the reservoir and will ultimately affect formation storage capacity and other trapping mechanisms. Additionally, the CO_2 storage security by means of capillary trapping is increased by minimizing the buoyant stress acting upwards on the caprock (Krevor et al., 2015). Solubility trapping involves the dissolution of CO_2 into formation fluids by molecular diffusion. The dissolution is further enhanced by convective mixing. The latter is induced by the evolution of density gradients. After CO_2 dissolution, another slow trapping mechanism takes place, which is the so-called mineral trapping. This mechanism constitutes the perpetual entrapment of CO_2 via mineral precipitation induced by chemical reactions with formation fluids and formation rocks. Last but not least, in organic rich formations such as coal seams and shales, sorption trapping constitutes another mechanism that significantly enhances the storage capacity and storage integrity.

1.3 Carbon Dioxide Enhanced Oil Recovery

Carbon dioxide Enhanced Oil Recovery (CO_2-EOR) has proven to be an effective method in increasing oil recovery and therefore project profitability on one hand, and on the other hand it contributes to extending the lifetime of conventional reservoirs, thereby reducing the need for new field development with which financial costs and environmental risks are associated. CO_2-EOR processes fall into three main categories, miscible, near miscible and immiscible displacement. During immiscible or partly miscible injection, be it continuous or cyclic, CO_2 is injected below the minimum miscibility pressure (MMP), while during miscible

flooding, CO_2 is injected above the MMP (Rudyk et al., 2013). The general mechanisms responsible for the enhanced recoverability of the oil during CO_2 injection are namely vaporization of the oil components into the gas phase (Abedini and Torabi, 2014a), reduction of interfacial tension between reservoir fluids (Hemmati-Sarapardeh et al., 2014), the reduction of oil viscosity, volumetric expansion of the oil (H. Li et al., 2013) and wettability alteration (Seyyedi et al., 2015). There exist several schemes of CO_2 injection. These include CO_2 flooding, water alternating gas injection, CO_2 huff and puff and carbonated water injection (Jia et al., 2019).

The success of CO_2-EOR has been proven in conventional reservoirs such as the Weyburn. The special characteristic of this project is that it couples CCS with CO_2-EOR and the overall process is therefore termed CCS-EOR. The injection of CO_2 into the reservoir leaves a substantial amount of the GHG retained underground. The recovered effluents constitute oil, CO_2 and water. The water and CO_2 are recycled and reinjected along with additional supply of fresh CO_2 from the pipeline. Accordingly, the double benefit of GHG mitigation and economic value addition to the CCS process -by retrieving a valuable product, i.e. oil- is achieved. On the other hand, little is still known about the applicability of CO_2-EOR in tight formations. Despite the advancement of horizontal drilling and multistage fracturing which increase the recovery factors of tight shale plays like the Bakken in North America, the recovery rate still lies between 3-10%, leaving substantial quantities of original oil in place behind. Therefore, pilot tests were initiated to investigate the suitability of CO_2-EOR for increasing the recovery factors of the Bakken and the possibility of implementing GCS in the formation (Jia et al., 2019). In similarity to the aforementioned, and despite the differing characteristics (shale oil versus oil shale) (Sheng, 2017), oil recovery using CO_2 in conjunction with GCS in Jordanian oil shales is worth investigating.

1.4 Objectives and Novelty

The current work aims to investigate a series of phenomena that contribute to the recovery of shale oil using supercritical CO_2. Additionally, several properties that are decisive for CO_2 storage in shale formations are examined, with the objective of coupling the use of CO_2 for oil recovery to its own storage. Jordanian oil shale (Sultani) is used as an example in this work for the potential economic and environmental interest on the one hand, and for the gained knowledge that can be generalized and transferred to any oil-bearing unconventional reservoir on the other.

To begin with, the extraction of oil using supercritical CO_2 is performed under varying conditions in order to investigate their impact on the yield of the extraction process. So far and up to the best of my knowledge, no systematic work on the extraction of oil using solely supercritical CO_2 has been performed on Sultani shale. Further on, the extracted oil was subject to compositional analysis which also constitutes part of the novelty of the work at hand. Compositional analysis for Jordanian shale oil has indeed been performed earlier, however, the oil had already undergone thermal decomposition prior to its analysis. The principal mechanisms elucidated in this work are of high relevance not only to the specific system under investigation, but to all non-reactive applications in porous media that show strong interactions at elevated pressures. Such applications are GCS, CO_2-EOR or coupled GCS and CO_2-EOR.

In the context of GCS, Sultani shale can either be viewed as a sealing caprock towards the injected CO_2 or as a carbon sink (reservoir). Interfacial properties will play different roles in the storage integrity and/or the storage potential of CO_2 in Sultani shale depending on how the shale is considered (caprock or storage reservoir). Therefore, the evaluation of the interfacial tension (IFT) in binary CO_2-brine systems is investigated as a function of CO_2 pressure and brine salinity. Further on, wettability alteration is investigated in ternary CO_2-brine-shale systems at conditions corresponding to those of a potential GCS scenario. Both,

the IFT and the wettability determine the capillary pressure (which will either positively or negatively influence the fluid displacement and saturation) and consequently gas trapping mechanisms, storage capacity, and integrity. The storage mechanisms of interest in the current work are structural trapping, residual trapping and solubility trapping as explained in section 1.2. Adsorption is investigated as an additional storage mechanism and its influence on wettability alteration is examined.

Solubility trapping of CO_2 is directly related to a change in formation brine density. The density of CO_2-saturated brines is measured as a function of pressure and salinity. On the one hand, this phase property is required for assessing the interfacial tension in binary CO_2-brine systems and on the other, the density change due to CO_2 dissolution alters the flow behavior of the brine within the reservoir, consequently influencing caprock performance in terms of gas storage integrity and reservoir performance in terms of gas storage capacity. Since the density of CO_2-saturated brine is a consequence of the solubility of the gas in the aqueous phase, solubility is also calculated at corresponding conditions, as it also constitutes an important parameter that reflects the amount of gas stored in formation brine. The calculated solubilities are inputs for a subsequent model proposed in the literature for calculating CO_2-saturated brine densities. Following, a comparison is made between calculated and experimental densities to examine the accuracy of the proposed model under varying saturation pressures and salinity conditions.

Regarding systems containing hydrocarbons, the interfacial behavior of binary CO_2-oil systems in response to pressure is subject to a systematic study under varying oil phase composition, pressure and temperature. The significance of the IFT and the so-called minimum miscibility pressure (MMP) is that they are key parameters for the design of a successful CO_2-EOR process. In the presence of two phases, capillary forces can cause the entrapment of one phase and negatively impact the recovery process. To achieve high oil displacement efficiency, the IFT

must reduce to zero, where the two phases (CO_2 and oil) become completely miscible, forming a single phase regardless of their respective proportions in the mixture. Consequently, capillary forces are eliminated. The measurement of IFT is also performed in binary water/brine-oil and ternary CO_2-water/brine-oil systems to investigate the impact of CO_2 pressure and brine salinity. A systematic investigation is performed in ternary brine-oil-shale and quaternary CO_2-water/brine-oil-shale systems to explore the impact of pressure, formation brine salinity and ion type on the wettability alteration of shale. So far, no study in the literature has addressed shale wettability in quaternary systems. The wettability of calcite at similar conditions is also evaluated and a comparison to shale is made.

Densities of CO_2-saturated oils are measured as a function of pressure. In analogy to the aqueous systems mentioned previously, these densities are necessary for calculating the IFT in binary and ternary systems. Further on, the volumetric expansion of the oil under varying pressures, salinities and ion types is investigated. No earlier studies investigating the impact of aqueous phase salinity on volumetric expansion have been performed so far. Moreover, a new procedure is proposed for correctly quantifying the volumetric expansion. In this procedure, artefacts such as extraction or CO_2 diffusion into dead volumes are prevented. Last but not least, a new approach is proposed to determine the solubility of CO_2 in the oil phase. This approach utilizes the measured density of pure and CO_2-saturated oils and the measured volumetric expansion. To the best of my knowledge, no such method has been previously proposed in the literature. This approach can be readily used by any experimentalist handling equipment for measuring density and IFT at reservoir conditions.

Complementing the phase behavior and interfacial properties described above, CO_2 transport within shale formations is relevant for various different reasons:

- Propagation of CO_2 in the shale matrix during injection and storage.
- Leakage through the shaly caprock.

- Extraction of hydrocarbons from the shale matrix.

So far, the diffusion of CO_2 in shale – as the principal transport mechanism – has not been addressed systematically, therefore this topic has also been a subject of investigation in this work.

1.5 Thesis Outline

The work at hand is divided into 8 chapters. The first constitutes an introduction where a statement on current issues regarding energy supply and climate change has been made and where the motivation behind this study and its objectives are discussed.

The second chapter presents the theoretical background and a literature review on each of the principal phenomena. In chapter 3, the materials constituting shale, hydrocarbons, aqueous phases and CO_2 as utilized in this work are presented. Material characterization and the experimental methods are also laid out.

Chapter 4 presents the results of oil extraction from Sultani shale using supercritical CO_2 followed by a discussion of the findings. Results and discussions on the investigated interfacial and mass transport phenomena are presented in chapter 5, while chapter 6 covers the phase behavior of various different systems under investigation.

Chapter 7 offers thermodynamic analysis of the supercritical CO_2 extraction cycle under different operating conditions, followed by an economic analysis covering the cost of oil extracted using sCO_2. In chapter 8, the findings of the work at hand are concluded and their relevance to the application of interest is discussed. Finally, based on these conclusions, planned future investigations are presented.

2. Theoretical Background

2.1 Extraction using Supercritical Carbon Dioxide

A supercritical fluid is defined as a fluid that is compressed and heated beyond its critical point. The latter is unique to each fluid and positively correlates with the molecular weight, polarity and the intramolecular hydrogen bonding. In the supercritical region fluids exhibit attractive physiochemical characteristics including liquid-like densities with which an appreciable solvation strength is associated, gas like transport properties of diffusivity and viscosity and a vanishing surface tension (McHugh and Krukonis, 1994). With the growing opposition to the use of toxic solvents as well as the costs associated with these solvents, CO_2 has emerged as the most attractive due to its high availability, low cost, nontoxicity, nonflammability, nonreactivity and its convenient critical temperature and pressure of 31.1 °C and 7.38 MPa (Phelps et al., 1996). Supercritical carbon dioxide ($scCO_2$) has had a wide range of applications across various industrial landscapes. To give a few examples, in pharmaceutical applications $scCO_2$ is used in the fabrication of polymeric drug carriers and the extraction of medicinal compounds from plants (Kankala et al., 2017; Qamar et al., 2021), in toxicology it is employed in soil decontamination (Sunarso and Ismadji, 2009). Further use of $scCO_2$ encompasses textile processing and dying (Montero et al., 2000), polymer synthesis, processing and coating (I. Cooper, 2000; Wang et al., 2002), aerogel drying (Mißfeldt et al., 2020), food preservation, drying and the extraction of consumable targeted compounds (W. Wang et al., 2021) or the removal of those undesired, such as the removal of caffeine from coffee (Zabot, 2020). The use of $scCO_2$ has been further extended to EOR technologies (Orr and Taber, 1984; Parker et al., 2009). Generally, when applying a compressed gas to a hydrocarbon reservoir, an uptake of reservoir fluid into the dense gas will take place, a process that is called extraction in the petroleum community. When applying carbon dioxide at conditions beyond its critical

parameters (see figure 2.1), from a process engineering perspective this process is named supercritical fluid extraction (SFE) with CO_2 as solvent.

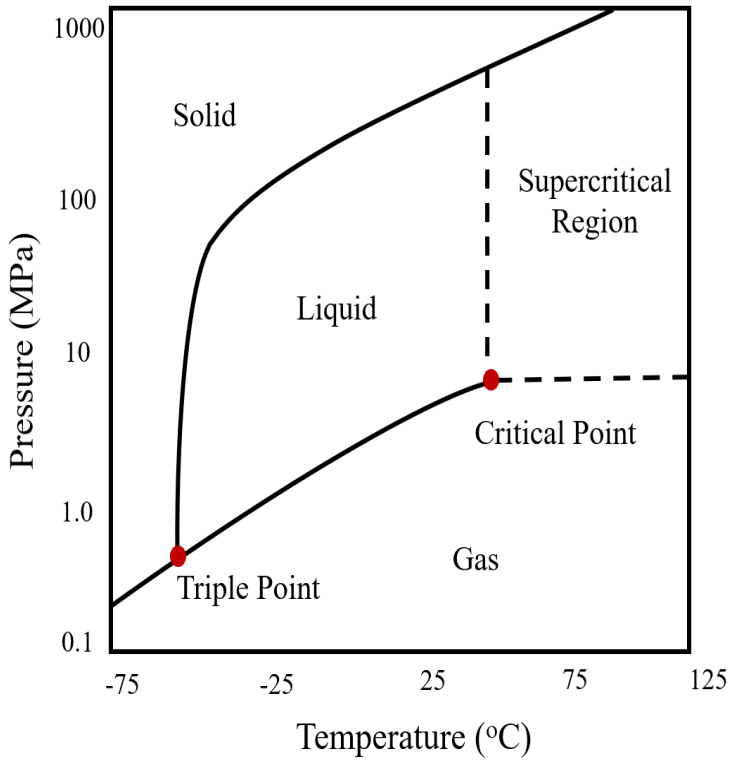

Figure 2.1 - Phase diagram of carbon dioxide.

The yield of this type of process is highly dependent on the solubility of the solute in the solvent, which in this case is the compressed or supercritical CO_2 ($scCO_2$). Normally at higher pressures, higher solubility of the solute in the CO_2 is achieved due to the higher density of the latter (See figure 2.2), i.e. as the density of the CO_2 increases so will its solvation power (Guiliano et al., 2000). In terms of temperature, the solubility of a solute in CO_2 typically exhibits two characteristic behaviors. At low pressures, increasing the temperature will decrease the solubility, and a reduction of CO_2 solvation power -due to the lower density- prevails. Alternatively, at high pressures, increasing the temperature increases the solubility and therefore the extraction yield. This is attributed to two superposing effects: when the temperature increases, on the one hand the density of the solvent decreases as shown in figure 2.2. This decrease in solvent density is opposed by

an increasing vapor pressure of the solute, where it becomes the dominating factor (Brunner, 1994).

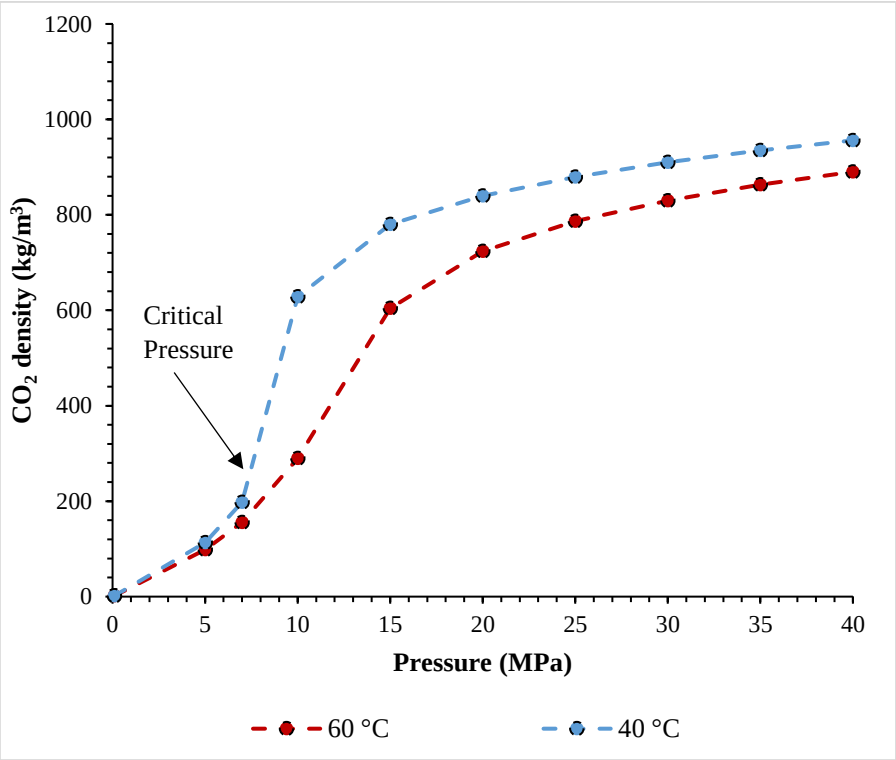

Figure 2.2 - Density of CO_2 as a function of pressure and temperature (Kunz and Wagner, 2012).

(Cao et al., 2017) investigated $scCO_2$ extraction of oil from oil-saturated kieselguhr and found that the yield at 20 and 30 MPa increased when temperature was increased from 50 to 70 °C. Accordingly, the highest yield was reported to be at the highest pressure and temperature applied to the process. (Al-Marzouqi et al., 2007) investigated $scCO_2$ extraction of oil from oil-saturated soil at two pressure and temperature ranges; the first being 8, 10 and 12 MPa at corresponding temperatures of 40, 50 and 60 °C. The second range investigated was at pressures of 20, 25 and 30 MPa at corresponding temperatures of 100, 120 and 140 °C. They found the highest yield to be at 30 MPa and 100 °C and reported a negative correlation between the yield and the temperature in both parametric ranges. This is owing to the fact that the extraction pressures applied are 30 MPa

and below. Above 30 MPa an inversion occurs, i.e. higher oil yields are obtained at higher temperature (Eggers, 2008).

The extraction parameters using $scCO_2$ will not only influence the yield but will also influence the selectivity towards the extracted solute (Viganó et al., 2016). In the scientific community, there is consensus that a higher pressure positively influences the carbon number of the extracted hydrocarbons and that CO_2 preferentially dissolves non-polar substances, as it is considered a non-polar molecule. Therefore, a substantial quantity of the extract will comprise non-polar and low-polarity substances (Sovová, 2012). Mostly, the polarity of a solvent - and in turn its ability to extract polar solutes- is related to its dielectric constant (Raveendran et al., 2005). The dielectric constant is a measure of the polarization of a molecule in the presence of a homogenous electric field (Keyes and Kirkwood, 1930). The CO_2 possesses a low dielectric constant due to the net sum of zero-dipole moment which originates from the symmetrically arranged bond dipoles on both sides of the carbon atom. However, the dielectric constant of CO_2 is found to increase with pressure and decreases with temperature according to (Keyes and Kirkwood, 1930). On the other hand, the large charge separation due a partially negative oxygen atom and a positively charged carbon atom results in a large quadrupole moment (Raveendran et al., 2005), giving rise to strong quadrupole-dipole or quadrupole-induced dipole interactions (Kauffman, 2001; Samara et al., 2022a), which eventually bring about the unique solvation power of CO_2 , especially towards hydrocarbons.

In the work of (Guiliano et al., 2000), at low pressure mainly non-polar linear alkanes along with a few branched and cycloalkanes were extracted. As the pressure was increased, the fraction of heavier alkanes in the extract increased. This was accompanied by a significant increase in branched and cycloalkanes. A further increase up to 30 MPa increased the amount of branched and cycloalkanes to a greater extent and introduced aromatics into the extract. In terms of temperature, (Allawzi et al., 2011) reported that increasing the temperature

increased the fraction of low molecular weight hydrocarbons. A similar finding was reported by (Cao et al., 2017). (Al-Marzouqi et al., 2007) further reported that in the low-pressure range, increasing the temperature increased the amount of extracted light hydrocarbons, while at elevated pressures, the influence of temperature on the composition of the extracted oil diminished. All in all, it can be stated that when the solvation power is increased (by means of increasing the pressure), the selectivity diminishes, while at low pressures the selectivity is high but the yield is low.

Further on, the mass transport in extraction processes heavily depends on the length of the transport path within the substrate. Larger particles mean longer diffusion pathways for the CO_2 to enter the pores and the dissolved solute to migrate to the surface, from where it is transported to the bulk CO_2 (Samara et al., 2019).

The sub-processes constituting the overall supercritical CO_2 extraction cycle as employed in this work are discussed in depth in Chapter 7.

2.2 Capillary Action and Capillary Pressure

As initially observed by Hauksbee in 1706 (Extrand, 2016), capillary action originates from the difference in "affinity" of a capillary tube wall towards the fluids involved. When the affinity of the tube towards one fluid (e.g. water) exceeds that towards the other (e.g. air), a spherically shaped meniscus with a concave curvature forms in the case of a very thin capillary. Across this meniscus, a lower pressure exists at the concave side and the so-called Laplace pressure develops. As a result, the fluid towards which the capillary wall has higher affinity advances upwards until this pressure is balanced by the hydrostatic height of the fluid inside the tube as illustrated in figure 2.3-A. The opposite situation is depicted in figure 2.3-B.

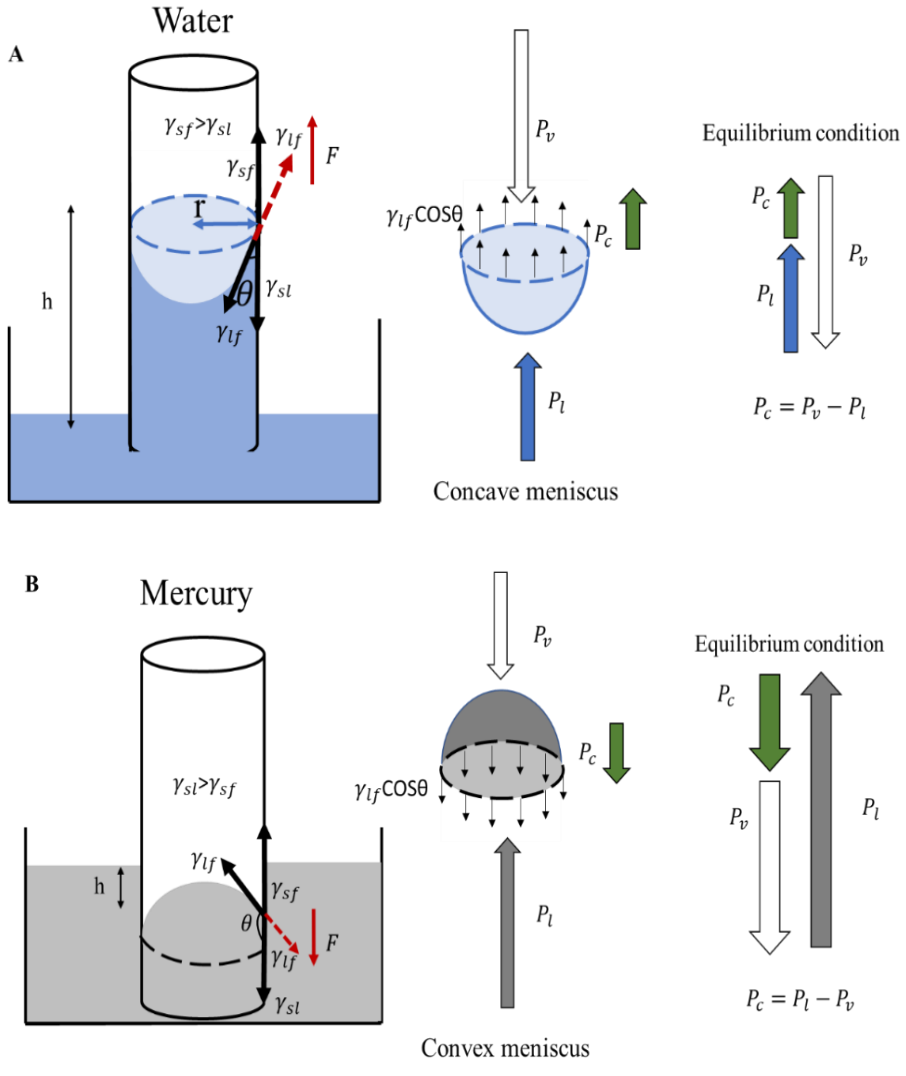

Figure 2.3 - Capillary action in thin tubes.

The force acting on the circumference of the tube is written as:

$$F = 2\pi r(\gamma_{sv} - \gamma_{sl}) = 2\pi r\gamma_{lf}\, cos\theta \quad (2.1)$$

where γ_{lf} is defined as the force per unit length and $cos\theta$ accounts for the vertical component of the force at the point of the three-phase contact, where θ is the contact angle. Pressure is defined as the force per unit area and the pressure across the meniscus can then be given by:

$$P_c = \frac{2\pi r\gamma_{lf}\, cos\theta}{\pi r^2} = \frac{2\gamma_{lf}\, cos\theta}{r} \quad (2.2)$$

Which is the so-called Young-Laplace equation. Another way to derive the pressure across the interface is by calculating the pressures at two points at the curvature; where one point is within the water phase (P_w) and the other is within the air phase (P_A) as illustrated in figure 2.4. The pressure at points A* and B* is given by:

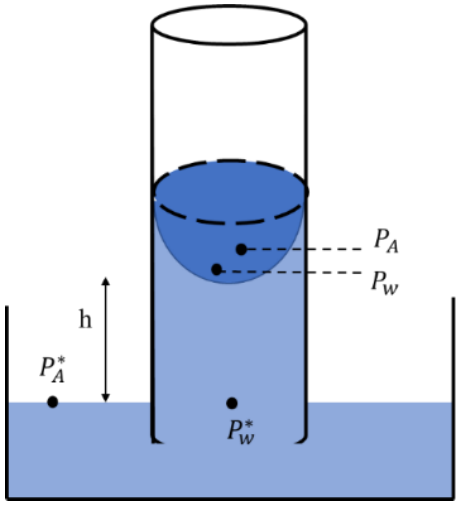

Figure 2.4 - Derivation of pressure difference across an interface.

$$P_A^* = P_A + \rho_{air}gh \quad (2.3)$$

$$P_w^* = P_w + \rho_{water}gh \quad (2.4)$$

$$P_A^* = P_w^* \quad (2.5)$$

Substituting equations 2.3 and 2.4 in equation 2.5 yields the equation of the pressure difference across the curvature.

$$P_A - P_w = P_c = \Delta\rho g h \quad (2.6)$$

Equating equation 2.2 with equation 2.6 yields:

$$h = \frac{2\gamma_{lf}cos\theta}{\Delta\rho g r} \quad (2.7)$$

Which is the equation used in the capillary rise method, where surface/interfacial tension or contact angles are measured. According to the above discussion, it can be seen that the capillary pressure which controls the flow and distribution of fluids inside thin capillaries -representative of porous media- depends on two system properties: the interfacial or surface tension between the participating fluids and the contact angle (see equation 2.2), which drives the motivation of their investigation in the current work.

2.3 Interfacial Tension

An interface is defined as that region of space separating two phases of matter. Several types of interfaces exist and are classified generally as follows: liquid-liquid interfaces, liquid-solid interfaces, liquid-gas interfaces and solid-gases interfaces. Although to the human eye an interface may appear as a sharp boundary dividing two bulk phases, e.g water and oil, the reality is not so. Within the interface, the change in the concentration of each component as we move away from its bulk phase towards that of the other is not abrupt, it rather happens gradually (Martinus Oversteegen et al., 1999). In real systems, the spatial extension of an interface between two phases is illustrated in figure 2.5 where it is indicated that the composition at the interface differs from that of either bulk phases.

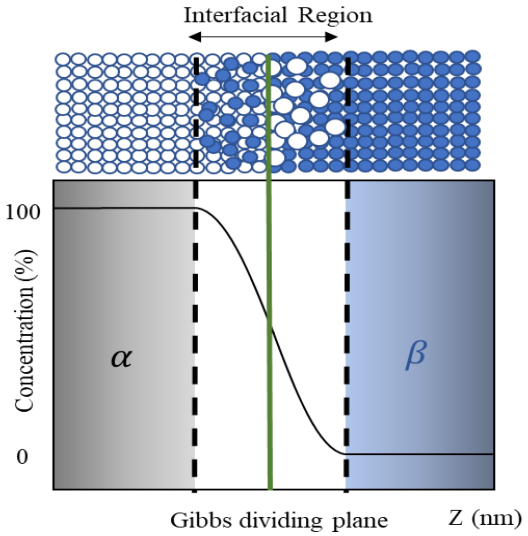

Figure 2.5 - Graphical representation of concentration variation of the α-phase within the interfacial region and bulk phases.

In the bulk phase α, each molecule experiences a uniform force field due to its mutual attraction with neighboring molecules resulting in the so-called cohesion forces. Thus, the forces acting on a molecule in the bulk are balanced. The situation is similar for a molecule existing in the bulk phase β. However, at the interface an α molecule experiences anisotropic interactions with both bulk phases α and β. Consequently, there exists a resultant net force on the α molecule acting tangentially to the interface and inward towards the bulk phase enriched with the same species (α). A simplification of both situations, i.e. inside the bulk phase and at the interface for an α molecule, is presented in figure 2.6.

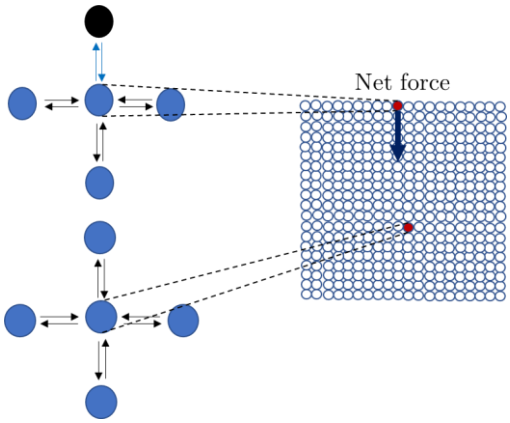

Figure 2.6 - A graphical representation of forces exerted on a molecule within the bulk phase and at the interface.

Similarly, and from a thermodynamic perspective, a molecule in the bulk phase will interact with its neighboring molecules via certain molecular interaction potentials such that the energetic state of the molecule takes a minimum value. Therefore, the molecule in the bulk phase is at a certain "reference" energy state. When an interface is created, interfacial work (W_γ) must be applied to allocate the molecules at the interface. For a unidirectional extension of an interface, the interfacial tension represents the amount of energy required in order to extend an interface by a unit area as given by the below equations:

$$\gamma = \frac{dW_\gamma}{dA} \tag{2.8}$$

It follows that for an open system composed of two homogeneous bulk phases in equilibrium and separated by a flat interface, the fundamental thermodynamic relation relating the microscopic change in internal energy (dU) to the microscopic change of entropy (dS), volume (dV), number of moles (dn_i) and interfacial area (dA) is expressed as (Lyklema, 1991):

$$dU = TdS - PdV + \sum \mu_i \, dn_i + \gamma dA \tag{2.9}$$

where T is the temperature, P is the pressure, μ_i is chemical potential of component i and γ is the surface tension.

Integrating the above equation yields:

$$U = TS - PV + \sum \mu_i \, n_i + \gamma A \tag{2.10}$$

The differentiation of the equation 2.10 mathematically yields:

$$dU = TdS + SdT - PdV - VdP + \sum \mu_i \, dn_i + \sum n_i d\mu_i + \gamma dA + Ad\gamma \tag{2.11}$$

Comparing equations 2.9 with 2.11 yields equation 2.12, known as the Gibbs-Duhem equation:

$$SdT - VdP + \sum n_i d\mu_i + Ad\gamma = 0 \tag{2.12}$$

This equation can also be derived by differentiating the integrals of any of the other thermodynamic functions (Enthalpy H, Gibbs free energy G and Helmholtz free energy F) and equating them to the differential thermodynamic functions (dH, dG and dF).

At a constant pressure and temperature, the Gibbs-Duhem equation relates the change in surface tension to the change of chemical potential (or the partial molar Gibbs free energy of component i) as per below:

$$Ad\gamma = -\sum n_i d\mu_i \tag{2.13}$$

Introducing the concept of surface excess concentration Γ_i yields:

$$\frac{n_i}{A} = -\frac{d\gamma}{d\mu_i}\Big|_{T,P} = \Gamma_i \tag{2.14}$$

For an ideal gas, the chemical potential of component i is given by equation 2.15:

$$\mu_i = \mu_i^o + RTlnx_i \tag{2.15}$$

where μ_i^o is the chemical potential of the component at a reference state, R is the gas constant and T is the absolute temperature and x_i is the mole fraction of component i in the mixture. The microscopic change of the chemical potential of component i is given by equation 2.16:

$$d\mu_i = RTdlnx_i \tag{2.16}$$

Substituting equation 2.16 in equation 2.14 yields the Gibbs adsorption isotherm:

$$\Gamma_i = -\frac{1}{RT}\frac{\partial\gamma}{\partial lnx_i}\Big|_T \tag{2.17}$$

The above equation relates the surface excess concentration (defined as number of molecules per unit area) to a distinct hypothetical planar surface called the Gibbs dividing plane (see figure 2.5).

The Gibbs free energy is given by equation 2.18 below:

$$G = U + PV - TS \tag{2.18}$$

The total differential of the above equation yields:

$$dG = dU + PdV + VdP - TdS - SdT \tag{2.19}$$

Substituting dU by the fundamental thermodynamic relation expressed in equation 2.9 yields:

$$dG = -SdT + VdP + \sum \mu_i \, dn_i + \gamma dA \tag{2.20}$$

At isothermal conditions and a constant number of molecules, the above equation reduces to:

$$\mathrm{d}G|_{T,n_i} = VdP + \gamma dA \tag{2.21}$$

Differentiating equation 2.21 with respect to A first and then with respect to P while keeping other variables constant yields:

$$\frac{\partial}{\mathrm{d}A}\left(\frac{\partial G}{\partial p}\Big|_{A,T,n_i}\right)\Big|_P = \frac{\partial V}{\partial A} \tag{2.22}$$

Differentiating equation 2.21 with respect to P first and then with respect to A while keeping the other variables constant yields:

$$\frac{\partial}{\mathrm{d}P}\left(\frac{\partial G}{\partial A}\Big|_{P,T,n_i}\right)\Big|_A = \frac{\partial \gamma}{\partial P} \tag{2.23}$$

The differentiation with respect to A then to P is mathematically equivalent to the differentiation with respect to P then to A. This yields the Maxwell relation relating the change in interfacial tension to the change in pressure and the change in volume to the change in surface area (Lyklema, 2000a):

$$\frac{\partial \gamma}{\partial P}\Big|_{A,T,n_i} = \frac{\partial V}{\partial A}\Big|_{P,T,n_i} \tag{2.24}$$

In systems where the interfacial tension decreases with pressure as a result of adsorption (positive surface excess concentration Γ_i), the above equation implies that when the area of the interface is extended at a given pressure (See figure 2.7-A and 2.7-B), the molecules accumulate there and the specific volume they require at the interface is less than the volume they occupy in the bulk phase, i.e,

the molar volume per molar area decreases (Lyklema, 2000a). Therefore, in order to maintain a constant pressure within the system, the volume needs to be reduced (see figure 2.5-C).

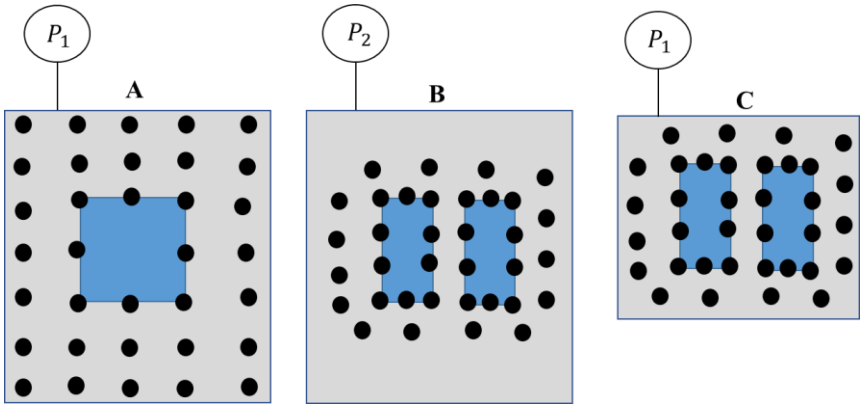

Figure 2.7 - The impact of surface excess concentration on system volume in response to increasing the interfacial area.

The contribution of the change in interfacial volume and the change in bulk volume to the change in the total volume of the system is given by:

$$\Delta A \frac{\Delta\gamma}{\Delta P} = \Delta V = \Delta V_{Interface} - \Delta V_{Bulk} \quad (2.25)$$

Assuming a negligible change in interfacial volume and substituting the change in system volume in equation 2.25 with the ideal gas law in equation 2.26 yields equation 2.27:

$$\Delta V_{bulk} = \frac{\Delta n_i RT}{P} \quad (2.26)$$

$$\frac{\Delta\gamma}{\Delta P} = -\frac{\Delta n_i RT}{\Delta A P} \quad (2.27)$$

Rearranging equation 2.27 yields an equation similar to Gibbs adsorption isotherm as given in equation 2.17:

$$\frac{n_i}{A} = \Gamma_i = -\frac{P}{RT}\frac{\partial\gamma}{\partial P}\Big|_T \quad (2.28)$$

Below a literature review of IFT in different systems is presented along with the experimental conditions.

2.3.1 Binary Systems (CO_2-Brine)

In binary CO_2-brine systems, IFT is a function of pressure, temperature, brine salinity and ion type. As the pressure increases, it is generally agreed that the IFT decreases, following the principal behavior explained earlier in equation 2.17. The response of IFT to temperature is not as straight forward. (Li et al., 2012a, 2012b) report higher IFT for the lower temperatures at pressures up to 6 -10 MPa, and higher IFT at higher temperatures at P>6-10 MPa. A similar observation at the high pressure range (>5 MPa) is reported by (Aggelopoulos et al., 2011, 2010; Bachu and Bennion, 2009; Chalbaud et al., 2009). The salinity positively correlates with the IFT, i.e. higher brine salinities yield higher IFTs (Aggelopoulos et al., 2011; Bachu and Bennion, 2009; Mutailipu et al., 2019b). Further on, the IFT of a CO_2-brine system depends on the cation type. As the ratio of cation charge to its surface area increases, the IFT increases (Aggelopoulos et al., 2011; Chalbaud et al., 2009). A review of previously conducted studies on CO_2-water/brine systems is presented in table 2.1.

Table 2.1 - Summary of previous studies on IFT measurements in CO_2-water/brine systems.

Reference	Salinity (wt%)	Brine composition	Experimental conditions
(Yang et al., 2005a)	0.4	Saskatchewan reservoir brine	0.1-30 MPa 27 and 58 °C
(Chiquet et al., 2007)	0 and 2	NaCl	5-45 MPa 34-110 °C
(Bachu and Bennion, 2009)	0 – 33.4	Mixed brine composed of Na, K, Ca, Mg, Cl, SO_4, HCO_3 ions	2-27 MPa 20-127 °C
(Chalbaud et al., 2009)	0.5-16	NaCl	4.5-25.5 MPa 27,70, 100 °C
(Aggelopoulos et al., 2011)	0.75- 25	NaCl + $CaCl_2$	5-25 MPa 27,71, 100 °C
(Aggelopoulos et al., 2010)	0.5-30	$CaCl_2$	5-25 MPa 27,71, 100 °C
(Li et al., 2012a)	6	NaCl + KCl	2-50 MPa 25-200 °C
(Li et al., 2012b)	4.6-55	$CaCl_2$, $MgCl_2$, Na_2SO_4	2-50 MPa 70-150 °C
(Lun et al., 2012)	1.4 and 2.1	Mixed brine composed of Na, Ca, Mg, Cl, SO_4, HCO_3 ions	0.1-36 MPa 45 and 97.5 °C
(Liu et al., 2017)	0-10.5	NaCl	3-12 MPa 27-80 °C
(Mutailipu et al., 2019b)	6-28	NaCl and KCl	3-15 MPa 25-100 °C
(Y. Liu et al., 2016)	0 and 10	NaCl	0.1-34 MPa 27, 72 and 125 °C
(Bikkina et al., 2011)	0		1.5 – 20.8 MPa 25-60 °C
(Hebach et al., 2002)	0		0.1-20 MPa 5-60 °C

2.3.2 Binary Systems (CO_2-Oil)

In binary CO_2-oil systems, IFT depends on several factors, including pressure, temperature, and oil composition. While IFT is a decreasing function of pressure, the impact of temperature additionally depends on the pressure and phase composition. At low pressures, IFT is found to decrease with increasing temperature. Conversely, at high pressures, the enhanced effect of mutual solubilities may lead to a reduction in IFT at lower temperatures (Hemmati-Sarapardeh et al., 2014). On the other hand, the IFT is positively correlated with the molecular weight and polarity of the oil constituents (Yang et al., 2015). A review of previously conducted studies on CO_2-oil systems is presented in table 2.2.

Table 2.2 - Summary of previous studies on IFT measurements in CO_2-oil/alkane systems.

Reference	Oleic phase	Experimental conditions
(Farahabadi and Lashkarbolooki, 2022)	Iranian Crude oil	4.1-19 MPa 25, 50 and 75 °C
(Ibrahim et al., 2022)	4 crude oils	0.1-10 MPa 50 and 90 °C
(Hemmati-Sarapardeh et al., 2014)	Crude oil	0.7-15 MPa 40-100 °C
(Yang et al., 2015)	2 crude oils	5-45 MPa 25-139 °C
(Mutailipu et al., 2019a)	Alkanes	0.1-15 MPa 25-100 °C
(Lashkarbolooki and Ayatollahi, 2018)	Crude oil	3.4-11.7 MPa 30-80 °C
(Zhang and Gu, 2016)	Dead and live crude oil	3.5-11.8 MPa 53 °C
(Abedini and Torabi, 2014a, 2014b, 2013)	Crude oil	0.1-14.6 MPa 21 and 30 °C
(Georgiadis et al., 2010)	Decane, Dodecane and Hexadecane	0.1-23 MPa 25-170 °C
(Rezk and Foroozesh, 2019)	Crude oil	0.1-24 MPa 50 and 95 °C
(Li et al., 2017)	C10-C20 alkanes	1-17.4 MPa 50 and 70 °C
(Abedini et al., 2014)	Crude oil	0.1-14.6 MPa 21-40 °C

2.3.3 Ternary Systems (CO_2-Oil-Brine)

In ternary CO_2-oil-water/brine systems, the general tendency is similar to that of binary systems, i.e. a decreasing IFT at increasing gas solubility under high pressures (Georgiadis et al., 2011; Honarvar et al., 2017; Yang et al., 2015). In terms of oil composition, the amount of acidic or basic components in the crude oil and the pH are parameters that may also be considered (Lashkarbolooki et al., 2017). Furthermore, interfacial behavior in ternary systems is influenced by brine salinity and ion type (Lashkarbolooki et al., 2019; Nowrouzi et al., 2019). While (Khaksar Manshad et al., 2016) and (Nowrouzi et al., 2019) claim that there exists an optimal salinity where IFT is minimal, (Rahimi et al., 2020) state that the IFT steadily increases with salinity. A review of previous studies on ternary systems is presented in table 2.3.

Table 2.3 - Summary of previous studies on IFT measurements in CO_2-oil-water/brine systems.

Reference	Aqueous phase composition	Oleic phase	Experimental conditions
(Hamouda and Bagalkot, 2019)	0.9 wt% $MgCl_2$ 0.3 wt% Na_2SO_4	n-decane	1-10 MPa 25,35,45 °C
(Khaksar Manshad et al., 2016)	Varying concentrations of different salts	Crude oil	3.5-13.8 MPa 35-75 °C
(Honarvar et al., 2017)	Sea water and formation brine	Crude oil	6.9-17.2 MPa 40 - 100 °C
(Nowrouzi et al., 2019)	Varying concentrations of different salts	Crude oil	13.8 MPa 75 °C
(Lashkarbolooki et al., 2018, 2017)	Deionized water	Crude oils	3.4-27.5 MPa 30-80 °C
(Zaker et al., 2020a, 2021)	1.5 wt% $MgSO_4$ 1.5 wt% Na_2SO_4	Crude oil	3.4-27.5 MPa 30-80°C
(Georgiadis et al., 2011)	Deionized water	n-decane	0.1-48 MPa 25-170 °C
(Yang et al., 2005a)	Reservoir brine	Crude oil	0.1-28 MPa 27 and 58 °C
(Rahimi et al., 2020)	Sea water, formation water and 0.1-8 wt% NaCl and $CaCl_2$	Crude oil	6.9 MPa 80 °C

2.4 Wettability

Wettability is defined as the affinity of the solid surface towards a particular phase relative to another. Wettability is described by Young's equation (Young, 1805) and is derived as follows: the volume and surface area of a drop of a radius *r* deposited on an ideal flat surface are given by equations 2.29 and 2.30 respectively, (Whyman et al., 2008):

$$V = \frac{\pi r^3}{3}(1 - cos\theta)^2(2 + cos\theta) \quad (2.29)$$

$$A = 2\pi r^2(1 - cos\theta) \quad (2.30)$$

The Gibb's free energy of the system is expressed as:

$$G = \pi\gamma_{lf} + \pi(r\, sin\theta)^2(\gamma_{sl} - \gamma_{sf}) \quad (2.31)$$

where γ_{lf} is the interfacial energy between the liquid and the fluid, $\gamma_{sf}$is the interfacial energy of the solid and fluid, γ_{sl} is the interfacial energy between the solid and the liquid and θ is the contact angle as illustrated in figure 2.8. Introducing a constant for the special case of a homogeneous flat surface:

$$a = \gamma_{sf} - \gamma_{sl} \quad (2.32)$$

Equation 2.31 is rewritten as:

$$G = \pi\gamma_{lf} - \pi(r\, sin\theta)^2 a \quad (2.33)$$

At a constant drop volume, substituting equations 2.29 and 2.30 into equation 2.33 yields:

$$G = \left[\frac{9\pi V^2}{(1-cos\theta)(2+cos\theta)^2}\right]^{1/3}(2\gamma_{lf} - a(1 + cos\theta)) \quad (2.34)$$

From the above equation, the Gibbs free energy becomes a function of only one θ. Differentiation of G with respect to θ yields:

$$\frac{dG}{d\theta} = \left[\frac{9\pi V^2}{(1-cos\theta)^4(2+cos\theta)^5}\right]^{1/3} 2(a - \gamma_{lf} cos\theta)sin\theta \quad (2.35)$$

At equilibrium $\frac{dG}{d\theta} = 0$, a condition that can only be satisfied when:

$$a = \gamma_{lf} cos\theta \tag{2.36}$$

Substituting a in equation 2.32 yields Young's equation for equilibrium contact angle on flat homogeneous surfaces:

$$\gamma_{lf} cos\theta = \gamma_{sf} - \gamma_{sl} \tag{2.37}$$

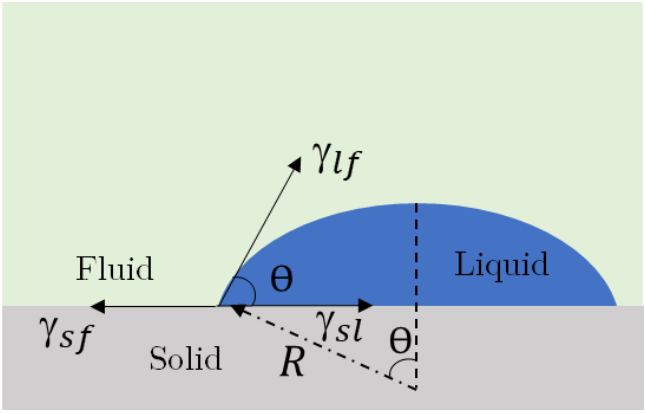

Figure 2.8 - Representation of the contact angle in a three-phase system.

The contact angle in petroleum applications is usually measured in the denser phase (i.e. aqueous phase). According to the classification proposed by (Schön, 2011), when $\theta < 70°$, the solid is considered water wet. When $70° < \theta < 110°$, the solid is intermediate water-wet and when $\theta > 110°$, the solid is non-water wet.

Several parameters impact the wettability of shales. Aside from pressure and temperature, there are also the salinity of the brine, the mineral composition of the shale, amount of TOC and the thermal maturity thereof, as well as the surface structure (roughness). In CO_2-brine-shale systems, it is observed that increasing the CO_2 pressure increases the contact angle, i.e the surface becomes more CO_2 wet. Regarding the impact of temperature, (Arif et al., 2017a), (Pan et al., 2018) and (Yekeen et al., 2021) found higher water wetting at higher temperatures. The amount of TOC is observed to positively correlate with the water contact angle. For instance, (Arif et al., 2017a) found higher CO_2 wetting at high TOC content. A similar observation was made by (Pan et al., 2020) who further reported a decreasing influence of the temperature at high TOC, i.e the change in wettability

in response to temperature decreases as the TOC increases. Additionally, the presence of high fractions of highly water-wet minerals such as quartz and clay minerals in the shale may counteract the impact of TOC on wetting, i.e. these minerals increase water wetting. Further on, as the brine salinity increases, the contact angle also increases, signifying reduced water wetting (Shojai Kaveh et al., 2016; Yekeen et al., 2021).

In oil-brine-shale systems, no influence of pressure on the contact angle is found by (Pan et al., 2020), yet (Roshan et al., 2016) report a slightly higher oil wetting with pressure, while (Yekeen et al., 2021) report a slightly higher water wetting. In terms of temperature, (Mirchi et al., 2015), (Roshan et al., 2016) and (Yekeen et al., 2021) report higher oil wetting at higher temperatures. While (Yekeen et al., 2021) and (Roshan et al., 2016) found a positive correlation between salinity and oil wetting, (Safari et al., 2022) reported an increasing contact angle of the brine with increasing concentration of $MgCl_2$ until a certain concentration is reached, after which the contact angle drops monotonically with increasing salt concentration and the shale becomes increasingly water wet. On the other hand, they reported a steadily increasing brine contact angle (increased oil wetting) upon increasing the concentration of NaCl salt. In terms of ion type, (Roshan et al., 2016) further reported an increasing contact angle in brines with similar molal concentration of salts in the following order $MgCl_2$>$CaCl_2$> NaCl>KCl regardless of the pressure applied to the system.

A review of available data on shale wettability in the literature is presented in table 2.4. No studies in the literature exist on the wettability in CO_2-oil-brine-shale systems.

Table 2.4 - Summary of previous experimental studies on shale wettability in Ternary systems.

Reference	Lithology	System	Salinity (wt%)	Brine Composition	Experimental conditions
(Arif et al., 2017a)	4 different shales	CO_2-brine-shale	5.8	NaCl	0.1-20 MPa 50-70 °C
(Pan et al., 2018)	Shengli shale	CO_2-water/brine-shale	0-5	Formation water	0.1-30 MPa 25-70 °C
(Pan et al., 2020)	Several shales	CO_2-brine-shale C12-brine-shale	5	NaCl	0.1-25 MPa 25 and 50 °C
(Qin et al., 2017)	Non-disclosed	CO_2-water - shale	0	None	6-18 MPa 80 °C
(Safari et al., 2022)	Non-disclosed	Crude oil-water-shale	0.1-1	NaCl and $MgCl_2$	0.1 bar 20 °C
(Mirchi et al., 2015)	2 shales of non-disclosed origin	Crude oil-brine-shale	24% reservoir brine 29% NaCl brine	Reservoir brine NaCl	20 MPa and 80 °C
(Shojai Kaveh et al., 2016)	North Sea shale	CO_2-water/ brine-shale	0 and 5.8	NaCl	1-15 MPa 45 °C
(Yekeen et al., 2020) (Yekeen et al., 2021)	Malaysian shale	CO_2-brine-shale Light crude oil-brine-shale	0-7	NaCl	8-22 MPa 80-180 °C
(Roshan et al., 2016)	New South Wales Shale	Brine-Decane-Shale	0.58-11	NaCl, KCl, $MgCl_2$ and $CaCl_2$	0.1, 1 and 20 MPa 35 and 70 °

2.5 The Electric Double Layer and Zeta Potential

Rocks can act as colloidal surfaces dispersed in an aqueous media (Tetteh et al., 2022) and the electrical state of the charged particle (rock) is determined by the spatial distribution of ions around it (Delgado et al., 2007). When a rock particle (shale) is suspended in an aqueous solution, an electric double layer (EDL) -also known as the electric interfacial layer- forms at the interface between the particle's

surface and electrolyte solution (brine-rock interface). The EDL, as the name implies, is divided into two layers, namely the stern layer and the diffuse layer. In the stern layer, a high concentration of oppositely charged ions (counter ions) are tightly adsorbed to the surface of the solid, however they do not entirely neutralize the surface charge of the solid, accordingly a diffuse layer is formed where both co-ions as well as counter-ions simultaneously exist (Al Mahrouqi et al., 2017). Ions in the diffuse layer have a higher freedom of mobility than those existing in the stern layer. The formation of such EDL at the oil-brine interface has also been claimed by (Buckley et al., 1989; Jackson et al., 2016; Koleini et al., 2019). A measure of the electric potential at the so-called slipping plane of the diffuse layer is the Zeta potential (ζ) which gives insight into the surface charge of the suspended particles. A graphical representation of the EDL and zeta potential is presented in figure 2.9.

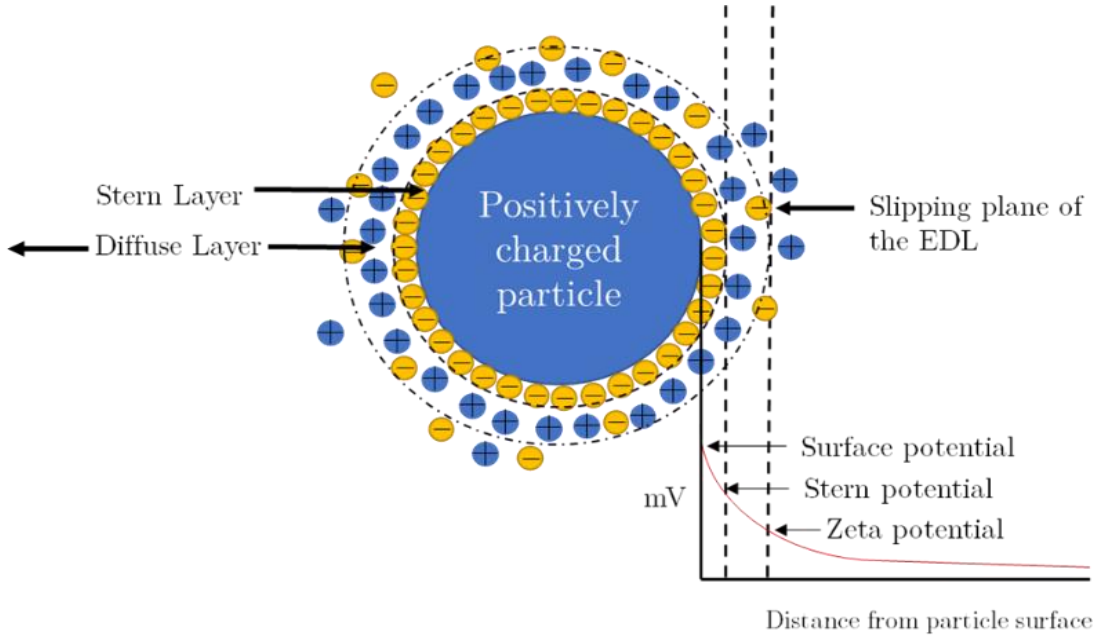

Figure 2.9 - Graphical representation of the electric double layer.

Relationship between EDL, Zeta Potential and Wettability

The wettability relies on the stability of the water film (EDL) between the rock-brine and the brine-oil interfaces (Bonto et al., 2019). The type of electrostatic interaction between these interfaces will dictate the stability of the EDL (Tetteh et al., 2022). Should these interfaces have similar electric charges, repulsion occurs and the EDL expands and stabilizes leading to higher/stronger water wetting (Bonto et al., 2019), while in the case of opposite electric charges, the double layer collapses as attraction forces dominate and oil adsorbs directly on the surface of the rock, rendering it more oil wet (Abdi et al., 2022). The situation is illustrated in figure 2.10.

The stability of this water film is controlled by the brine salinity, ion composition, pH and oil composition (Buckley et al., 1989). A measure of the electric charges of the brine-rock and brine-oil interfaces as described earlier is the zeta potential, which has been widely employed by the scientific community to investigate the role of wettability alteration in increasing oil recovery during low salinity/smart water injection. The wettability is found to be related to the sign and magnitude of the zeta potential at the participating interfaces (Nasralla and Nasr-El-Din, 2012). A summary of the impact of multiple parameters on the zeta potential at both the brine-carbonate interface and the brine-oil interface is presented in table 2.5.

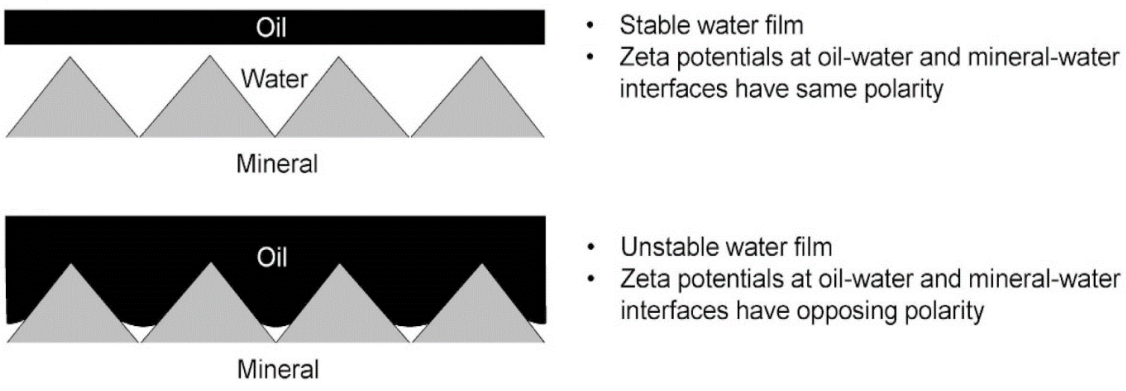

Figure 2.10 - Water film between the oil and the mineral, adapted from and modified after (Jackson et al., 2016).

Table 2.5 - Parameters influencing the zeta potential of interfaces.

Interface	pH	Salt Concentration	Temperature
Brine-Carbonate	Becomes more negative as pH increases (Al Mahrouqi et al., 2017) (Chen et al., 2014) and (Thompson and Pownall, 1989).	Becomes more positive as salt concentration increases, especially for $CaCl_2$ (Chen et al., 2014) (Mahani et al., 2017a).	Decreases (less positive) as temperature increases. (Hamouda and Gomari, 2006). At low ionic strength of NaCl, it becomes more positive with increasing temperature. At high ionic strength no impact is found. (Al Mahrouqi et al., 2016). Both increasing and decreasing trends are observed in the work of (Mahani et al., 2017b).
Oil-brine	Becomes more negative as pH increases (Creux et al., 2009; Marinova et al., 1996).	Becomes more positive as salt concentration increases. (Graciaa et al., 2002; Marinova et al., 1996).	At low ionic strength, zeta potential becomes more positive as temperature increases (Mahani et al., 2017b). This increase is less pronounced at high ionic strength.

2.6 Density of CO_2-saturated Phases

The densities of reservoir fluids are crucial properties that control fluid flow and migration inside the reservoir. For instance, during carbon storage processes, gravity segregation takes place due to differences between the density of the injected gas and formation brine. As the brine layer underlying the free gas phase becomes enriched with CO_2, its density gradually increases at the top layer causing a gravitational instability. When this layer becomes saturated and of a suitable thickness, a plume of CO_2-saturated brine migrates downwards. This downward migration of the CO_2-saturated brine is accompanied by the upward migration of the lighter unsaturated brine resulting in convective currents. These convective currents are triggered by the density gradient at the CO_2-brine interface and contribute to increasing the rate of gas dissolution into the brine (Tang et al., 2019). Therefore, this density increase represents the efficiency of the solubility trapping mechanism on the one hand, and on the other contributes to the reduction of the buoyancy-driven migration of CO_2, which may jeopardize the structural integrity of the caprock (Lu et al., 2009). In analogy, in CO_2-EOR gravity segregation also occurs as follows: initially, the injected CO_2 will tend to segregate and migrate to the top of the oil layer. The diffusion-driven dissolution of CO_2 into the oil creates a region where the density of the mixture is higher than both CO_2 and the original oil, resulting in convective mixing in the miscible region, which ultimately impacts reservoir fluids flow (Elenius and Gasda, 2021). Further on, reservoir performance prediction, the estimation of recoverable oil and/or the CO_2 storage potential of the formation will highly depend on fluid densities (Santos et al., 2021). On the experimental side and in particular regarding the current work, the measurement of IFT in binary and ternary systems requires the knowledge of the densities of the coexisting phases (see equation 3.7). Also, the calculation of CO_2 solubility in the oil using the method proposed in section 3.2.10 requires the measurement of pure oil and CO_2-saturated oil densities.

An alternative to experimental data is the calculation of mixture densities using thermodynamic models. Each model produces a different density curve, and uncertainties persist due to the scarcity of experimental data that are required for tuning these models to be valid at pressures and temperatures relevant to reservoir conditions. For example, the Peng-Robinson equation of state is strictly applicable for non-polar fluids and does not account for any polar interactions. Mixing rules are introduced to account for the quadrupole CO_2 which further complicate the equations and reduce their accuracy (Marra et al., 1987). Another equation of state characterized by its high predictability of thermodynamic properties is the PC-SAFT (Chi et al., 2020), which in its turn requires experimental data for modelling the interaction parameters (Kleiner and Sadowski, 2007). Therefore, experimental density data are always desirable (Zhang and Sun, 2021). Despite their significance, experimental data on the density of CO_2-saturated brines are limited. An up-to-date review is presented in tables 2.6 summarizing the studies available in the literature so far. On the other hand, there exists a body of literature regarding the densities of CO_2-alkane mixtures, where alkanes are often used as model hydrocarbons representative of real systems. However, the studied hydrocarbons and conditions in the current work have not been investigated so far. Table 2.7 lists some of the available data concerning CO_2-hydrocarbon systems.

While the density of a pure alkane is a function of pressure (positive), temperature (negative) and its chain length (positive) (Seyer et al., 1944), the density of gas-alkane mixtures is a function of two additional parameters which are: the nature of the gas and its concentration in the solution. (Note that in this work, the use of "mixture" as an expression only reflects the alkane-rich phase). To exhibit the impact of the nature of the gas on gas-alkane mixtures, different behaviors are observed for CO_2 and CH_4. For example, at 40 MPa and 50 °C, the density of n-decane containing 0.6 mol of CH_4 is 0.62 g/cm^3, while the density of the pure n-decane at a similar condition is 0.74 g/cm^3 (Regueira et al., 2016). Alternatively, the density of n-decane containing 0.6 mol of CO_2 at 40 MPa and 50 °C is 0.79

g/cm^3 (T. Yang et al., 2021). This implies that the density highly depends on the specific intermolecular interactions between the gas and alkane molecules. The density of CO_2-alkane mixtures increases with increasing pressure at a given CO_2 molal concentration and temperature. On the other hand, the density dependence on temperature exhibits an inverse relation, i.e. lower density of the mixture at higher temperatures while holding the pressure and concentration constant (Chacon Valero et al., 2020; Song et al., 2012). At a given pressure and temperature, the density of the mixture increases with increasing CO_2 concentration in the alkane-rich phase. Further on, the density increase due to CO_2 dissolution is negatively correlated with the hydrocarbon chain length (Y. Wang et al., 2021). The aforementioned also applies to brine-CO_2 mixtures. In analogy to hydrocarbon chain length, as the salt concentration in the brine (salinity) increases, the brine density increases. Alternatively, as the salinity increases, the density increase due to CO_2 decreases (see section 2.8).

Table 2.6 - Summary of previous experimental studies on the density of CO_2-saturated aqueous phases.

Reference	Salinity Range (wt%)	Brine Composition	Experimental conditions
(Hebach et al., 2004)	0	None	1-30 MPa 10-60 °C
(Li et al., 2004)	0 and 9.2	Pure water and Weyburn brine	0.5-29 MPa 59 °C
(Yan et al., 2011)	0-29%	NaCl	5-40 MPa 50-140 °C
(Yang and Gu, 2006)	0.43	Instow brine	0.2-9 MPa 27 and 58 °C
(Y. Zhang et al., 2011)	N/A	Tianjin brine	10-18 MPa 40-80 60 °C
(Tegetmeier et al., 2000)	0	None	0.1-30 MPa 21-101 °C
(Song et al., 2013)	5.8-23.4	NaCl	10-18 MPa 60-140 °C

*N/A denotes the unavailability of data in the published work.

Table 2.7 - Summary of previous experimental studies on the density of CO_2-saturated oleic phases.

Reference	Oleic phase	Experimental conditions
(Nourozieh et al., 2013a)	C10, C18, and their binary mixtures	1-6 MPa 50 °C
(Nourozieh et al., 2013b)	C10, C13 and their binary mixtures	1-6 MPa 100°C
(Ren and Scurto, 2007)	C10	1.7-10.1 MPa 71 °C
(Shaver et al., 2001)	C10	0.9-13 MPa 71 °C
(Yu et al., 2006)	C8	1-15 MPa 40-120 °C
(Tanaka et al., 1993)	C15, C16 and their binary mixtures	1-6 MPa 40 °C

2.7 Volumetric Expansion of Hydrocarbons

As one of the relevant mechanisms in CO_2-EOR, the volumetric expansion due to CO_2 dissolution causes isolated oil ganglia to swell and coalesce with other disconnected oil ganglia, forming a continuous phase with improved mobility (Rezk and Foroozesh, 2019), leading to higher relative permeability of oil (Mosavat, 2014).

The volumetric expansion -or the so-called oil swelling- is found to increase with increasing pressure (Lashkarbolooki et al., 2020, 2019), and is higher in lighter oils (Lashkarbolooki et al., 2020). While (Lashkarbolooki et al., 2019) and (Zaker et al., 2020b) studied the impact of ion type on oil swelling, so far the impact of salinity has not been covered in the literature. Moreover, up to date investigations of volumetric expansion in CO_2-oil systems either employ the pendant drop method or PVT cells supplemented with a viewing glass (Abedini et al., 2014; Abedini and Torabi, 2014a; Lashkarbolooki and Ayatollahi, 2018; Mosavat et al., 2014; Rezk and Foroozesh, 2019). However, difficulty arises in quantifying volumetric expansion due to the extraction effect experienced by the oil at elevated pressures. Alternatively, the standing drop (rising bubble) method is employed in ternary CO_2-water/brine-oil systems, where the oil is confined by an aqueous phase (Bagalkot and Hamouda, 2018; Lashkarbolooki et al., 2020, 2019; Zaker et al., 2020b). Nevertheless, CO_2 diffusion into dead volumes (capillaries/needles) contributes to the expansion of an oil drop attached to a needle, resulting in overestimating the volumetric expansion. A summary of available literature studies on binary and ternary systems is presented in tables 2.8 and 2.9, respectively.

Table 2.8 - Summary of previous experimental studies on volumetric expansion in CO_2-oil systems.

Reference	Oleic phase	Experimental conditions
(Lashkarbolooki and Ayatollahi, 2018)	Crude oil	3.4-11.7 MPa 30-80 °C
(Abedini and Torabi, 2014a, 2014b, 2013)	Crude oil	0.1-14.6 MPa 21 and 30 °C
(Rezk and Foroozesh, 2019)	Crude oil	0.1-24 MPa 50 and 95 °C
(Abedini et al., 2014)	Crude oil	0.1-14.6 MPa 21-40 °C

Table 2.9 - Summary of previous experimental studies on volumetric expansion in CO_2-brine-oil systems.

Reference	Aqueous phase composition	Oleic phase	Experimental conditions
(Bagalkot and Hamouda, 2018)	Pure water	n-decane and n-hexane	1-10 MPa 25,35,45 °C
(Lashkarbolooki et al., 2020)	Deionized water	Crude oils	3.4-27.5 MPa 30-80°C
(Lashkarbolooki et al., 2019)	1.5 wt% of different salts	Crude oil	3.4-27.5 MPa 30-80°C
(Zaker et al., 2020b)	1.5 wt% $MgSO_4$ 1.5 wt% Na_2SO_4	Crude oil	3.4-27.5 MPa 30-80°C

2.8 Solubility of Carbon Dioxide

Within the context of geological carbon storage, solubility trapping is considered one of the safest CO_2 storage mechanisms. For instance, in a saline aquifer, the injected CO_2 starts accumulating between the impermeable caprock and the reservoir brine by means of gravity segregation. This is followed by the dissolution of CO_2 in the brine, a process accelerated by convective mixing (W. Zhang et al., 2011). In CO_2-EOR, the solubility of CO_2 in a hydrocarbon phase will dictate the reduction in IFT and oil viscosity as well as the volumetric expansion of the isolated oil ganglia, which are the main displacement mechanisms in CO_2-EOR processes (Kumar et al., 2022). Further on, CO_2 solubility will alter the densities of oil and brine which in their turn dictate the fluid flow inside the reservoir. For these reasons, CO_2 solubility is an important parameter to consider for the proper design and simulation of GCS and CO_2-EOR processes and for ensuring their success.

At equilibrium, the solubility of CO_2 in an aqueous phase is governed by temperature, pressure and composition of the aqueous phase (ion type and salinity). Experimental measurements show that CO_2 solubility is positively correlated with pressure (Wiebe and Gaddy, 1940), and inversely related to temperature and salinity (Yan et al., 2011). In CO_2-oil systems, the solubility is positively correlated with saturation pressure and inversely correlated with temperature and the molecular weight of the crude oil (Mosavat et al., 2014). Table 2.10 lists some of the literature studies that have dealt with CO_2 solubility in aqueous phases. In table 2.11, a literature review on CO_2 solubility in different alkanes and conditions is presented along with the respective test conditions.

Table 2.10 - Summary of previous experimental studies on CO_2 solubility in aqueous solutions.

Reference	Salts	Concentration (wt%)	Temperature range (°C)	Pressure range (MPa)
(Bando et al., 2003)	NaCl	1 and 3	30-60	10-20
(Koschel et al., 2006)	NaCl	6 and 18	50 and 100	5-20
(Liu et al., 2011)	NaCl, KCl, $CaCl_2$	10	35-55	2-20
(Yan et al., 2011)	NaCl	0-29	50-140	5-40
(Gilbert et al., 2016)	NaCl, $CaCl_2$, Na_2SO_4, $NaHCO_3$	0-48 (0-3.4 mol/kg)	35-140	1-35
(Tong et al., 2013)	$CaCl_2$ and $MgCl_2$	9.5-55 (1,3 and 5 mol/kg)	36-151	1.2-28

Table 2.11 - Summary of previous experimental studies on CO_2 solubility in alkanes.

Reference	Oil phase composition	Temperature range (°C)	Pressure range (MPa)
(Nieuwoudt and du Rand, 2002)	C12-C36	40-70	8.2-29.2
(Sato et al., 1998)	C20-C28	50-100	5.9-40
(Charoensombut-amon et al., 1986)	C16	35-70	0.68-26
(He et al., 2021)	C16-C20	40-100	0.8-23
(Mosavat et al., 2014)	Light crude oil	25 and 40	1-8
(Mulliken and Sandler, 1980)	Crude oil	43-93	2-16
(Kordikowski and Schneider, 1993)	C16, C19, C20 and C24	30-120	10-25
(Tanaka et al., 1993)	C15, C16	40	1-6
(Rezk and Foroozesh, 2019)	Light crude oil	50 and 95.5	0.1-10
(Gasem and Robinson, 1985)	C20-C44	50-150	0.5-9.6
(Huang et al., 1988)	C20	50-300	0.9-5
(Huie et al., 1973)	C20 and a binary mixture of C10 and C20	37-100	0.5-7.5
(Al Ghafri et al., 2014)	Synthetic crude oil	25-150	0.1-36

2.9 Gas Adsorption on Shale

Adsorption is defined in this work as the accumulation of gas molecules on the surface of a solid by means of non-reactive intermolecular interactions, resulting in the formation of a layer that possesses a higher density than that of the bulk gas phase surrounding the solid (Rani et al., 2019b). Accordingly, adsorption on the one hand increases the storage capacity of geological formations towards CO_2 and on the other, reduces the possibility of CO_2 leakage through overpressure (Wang et al., 2022). Shales have proven to be appropriate caprocks for oil and natural gas containment. Therefore, their ability to act as seals towards CO_2 is worthy of investigation. Further on, due to their nanoporous structure and the presence of organic matter, shales in particular can store significant amount of CO_2 through adsorption (Jia et al., 2022).

The adsorption capacity of shale is affected by several parameters. These include the injection pressure and reservoir temperature, shale mineral composition, structural properties of the pores (surface area, pore size and pore volume), amount of total organic carbon and the moisture content. A comprehensive review is presented in table 2.12, listing all the available studies in the open literature concerning CO_2 adsorption on shales. The maximum excess adsorption capacities are also extracted from each study and reported along with the respective experimental conditions.

Table 2.12 - Summary of previous experimental studies on CO_2 adsorption on shales.

Reference	Method	Lithology	Experimental conditions	Maximum Adsorption capacity (Excess)
(Rani et al., 2019a)	Volumetric	Indian Shale	0.6- 5.3 MPa (Subcritical) 40 °C	0.36 mmol/g at 5.3 MPa
(Heller and Zoback, 2014)	Volumetric	Barnett, Eagle Ford, Marcellus, Montney Shales	0.8-3.2 MPa (Subcritical) 40 °C	Barnett shale – 0.1 mmol/g at 3.2 MPa
(Fakher and Imqam, 2020)	Volumetric	Oklahoma Shale	3.5-13.8 MPa 25, 40 and 60 °C	0.5 mmol/g at 10.3 MPa and 25 °C
(Merey and Sinayuc, 2016)	Volumetric	Dadas Shale-Turkey	1.4-13.8 MPa 25, 50 and 75 °C	0.22 mmol/g at 6.2 MPa and 25 °C
(Lafortune et al., 2014)	Gravimetric	Upper and lower Toarcian shale	0.1-9 MPa 25, 40, 45 and 55 °C	Upper shale 0.43 mmol/g at 8 MPa and 40 °C
(Busch et al., 2008)	Volumetric	Muderong Shale	0.1-16 MPa 50 °C	1 mmol/g at 12 MPa
(Bakshi et al., 2020)	Volumetric	Indian Shales	0.1-9 MPa 40 °C	1.4 mmol/g at 6 MPa
(Mahmoud et al., 2020)	Gravimetric	Shale (formation is undisclosed)	0.1-4.5 MPa 50, 100 and 150 °C (Subcritical)	13.26 mmol/g at 4.5 MPa and 100 °C (584 mg/g)
(Hui et al., 2019)	Gravimetric	Longmaxi, Yanchang and Wufeng Shales	0.1-18 MPa 45 °C	0.85 mmol/g at 10 MPa, Yanchang shale
(Yang et al., 2018)	Volumetric	Qaidam Shale	0.1-5 MPa 50 °C (Subcritical)	0.27 mmol/g at 5 MPa
(Weniger et al., 2010)	Volumetric	Brazilian Shale	0.1-25 MPa 45 °C	0.54 mmol/g at 10 MPa
(Lu et al., 2016)	Volumetric	Longmaxi Shale	0.1-16 MPa 35-75 °C	0.06 mmol/g at 9 MPa and 35 °C
(Wu et al., 2019)	Gravimetric	Argentinian Shale and isolated kerogen	0.1-15 MPa 60, 90 and 120 °C	0.11 mmol/g for shale and 1.3 mmol/g for kerogen at 9 MPa and 60 °C
(Qin et al., 2021)	Volumetric	Yanchang Shale	0.1-5 MPa 40 °C (Subcritical)	0.25 mmol/g at 5 MPa

Table 2.12 - Continued				
(Duan et al., 2016)	Gravimetric	Sichuan Shale	0.1-2 MPa 5,25 and 45 °C (Subcritical)	0.38 mmol/g at 2 MPa and 5 °C
(Gu et al., 2017)	Gravimetric	Longmaxi Shale	0.1-2 MPa 5,25 and 45 °C (Subcritical)	0.4 mmol/g at 2 MPa and 5 °C
(Zhou et al., 2018)	Volumetric	Longmaxi and Wufeng Shales	0.1-11 MPa 35 °C	Wufeng 0.15 mmol/g at 11 MPa
(J. Liu et al., 2019)	Gravimetric	Longmaxi Shale	0.1-7 MPa 30 °C (Subcritical)	0.26 mol/g at 7 MPa
(C. Wang et al., 2020)	Gravimetric	Longmaxi Shale	0.1-10 MPa 75 and 115 °C	0.06 mmol/g at 10 MPa and 75°C
(Du et al., 2019)	Volumetric	Yanchang and Wufeng Shales	3-8 MPa 45, 65 and 85 °C	Wufeng 0.16 mmol/g at 8 MPa and 45 °C
(K. Yang et al., 2021)	Volumetric	Longmaxi and Wufeng Shales	0.1-6 MPa 25,45 and 65 °C (Subcritical)	Longmaxi 0.25 mml/g at 4 MPa and 25 °C
(Chareonsuppanimit et al., 2012)	Volumetric	New Albay shale	0.1-12.4 MPa 55 °C	0.12 mmol/g at 9.75 MPa
(Zhao et al., 2017)	Gravimetric	Neuquen Shale Isolated Kerogen	0.1-3 MPa 25, 50 and 65 °C (Subcritical)	Shale 0.75 mmol/g at 3 MPa and 25 °C Isolated Kerogen 0.6 mmol/g at 3 MPa and 25 °C
(Fujii et al., 2010)	Gravimetric	Shale (formation is undisclosed)	0.1-20 MPa 50 and 100 °C	0.4 mmol/g at 12.5 MPa and 50 °C
(Charoensuppanimit et al., 2016)	Volumetric	Woodford Shale	0.1-12.4 MPa 55 °C	0.16 mmol/g at 9.7 MPa
(Lutyński et al., 2017)	Volumetric	Pomeranian Shale	0.1-15 MPa 50 and 80 °C	0.51 mmol/g at 5.8 MPa and 50 °C
(Jia et al., 2022)	Gravimetric	Bakken Shale	0.1-38 MPa 110 °C	0.25 mmol/g at 12 MPa

Details on the applied measurement technique (volumetric or gravimetric) can be found in the respective reference. The principle of the gravimetric method is mostly similar to the one used in this work. The grand part of the results varies within the range of 0.1 to 1.4 mmol/g and no direct correlation can be inferred between the adsorption capacity and the investigated storage conditions when

different shales are compared. This reveals the importance of individual factors of influence that will be discussed in detail in section 5.2.

2.10 Gas Diffusion

The gas transport mechanism in porous media highly depends on pressure, temperature, surface concentration, the gas specie and the structural properties of the pore network (Choi et al., 2001). While in high permeability porous media the dominating mass transport mechanism is the convective flow, in low permeability formations such as shale, fluid velocities are low, consequently diffusion becomes a significant mass transport mechanism (Jia et al., 2019).

Since the pore structure of shale is heterogeneous and complex, several mass transport mechanisms may coexist. The mass transport regime may be characterized through a widely recognized dimensionless number, which is the Knudsen number (k_n) as demonstrated in figure 2.11. The Knudsen number is defined in equation 2.38 as the ratio of the free mean path length of a molecule (λ) to the characteristic pore diameter (d) (Dongari et al., 2009):

$$k_n = \frac{\lambda}{d} \tag{2.38}$$

The mean free path length is defined as the average distance travelled by a molecule before it collides with other molecules (McWhorter, 2021) and is given by the equation below (Vincenti and Kruger, 1965):

$$\lambda = \frac{\mu}{P}\sqrt{\frac{\pi k_B T}{2m}} \tag{2.39}$$

where k_B is the Boltzmann constant, μ and P are the dynamic viscosity and pressure respectively, T is the absolute temperature and m is the mass of the molecule. The mean free path length is inversely proportional to gas pressure; however, it is directly related with temperature. As seen in equation 2.39, the sensitivity of the free mean path length towards pressure is higher than temperature. The importance of the response of λ to pressure and temperature lies

in the fact that the change in this characteristic length can change the mass transport regime within the porous media independently of the characteristic pore diameter (P.d. et al., 2015). According to (McWhorter, 2021) the characteristic pore dimension (*d*) may be estimated using equation 2.40:

$$d = k^{0.5} \tag{2.40}$$

where *k* is the intrinsic permeability of the porous media.

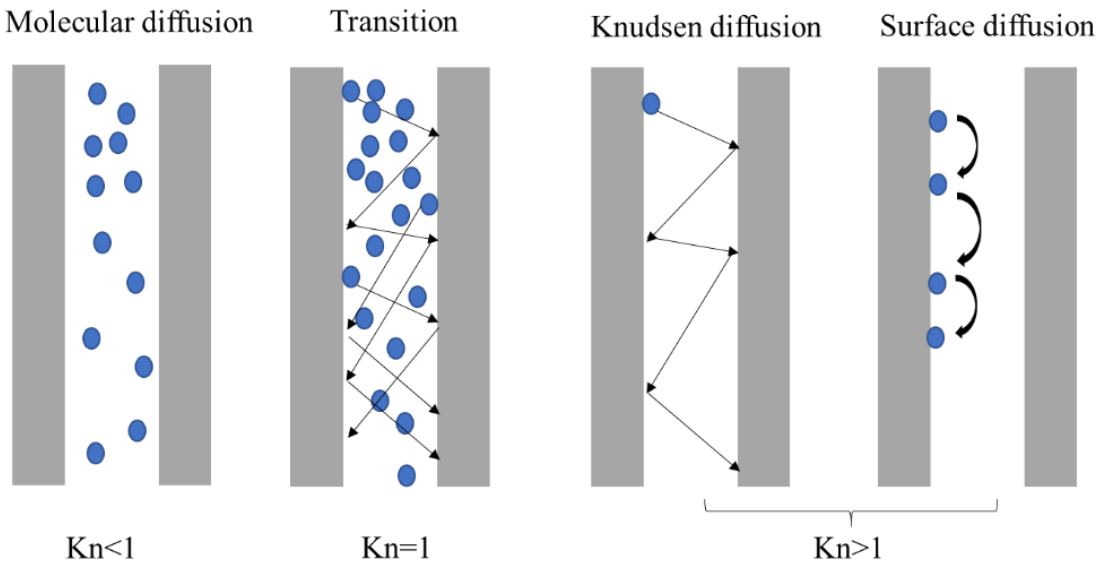

Figure 2.11 - Different diffusion regimes in porous media.

Diffusion is a concentration-driven mass transport phenomenon, whereby mass transport takes place from areas of high concentration to areas of low concentration (Dongari et al., 2009). The Knudsen number characterizing molecular diffusion is <1, owing to the fact that the diffusion space is dominated by molecule-molecule collisions and the pore size is large enough that the impact of molecule-pore wall collisions on the flow is negligible (Jian et al., 2012). Molecular diffusion usually occurs in formations with an intrinsic permeability in the order of millidarcy (McWhorter, 2021) and is described by Fick's first and second laws for steady and non-steady state, respectively (Crank, 1975) below:

$$J_D = -D_{fick} \frac{\partial C}{\partial x} \tag{2.41a}$$

$$\frac{\partial C}{\partial t} = -D_{fick}\frac{\partial^2 C}{\partial x^2} \quad (2.41b)$$

where J_D is the diffusive flux, D_{fick} is the proportionality constant or the so-called diffusion coefficient, $\frac{\partial C}{\partial x}$ is a unidimensional spatial concentration gradient, and $\frac{\partial C}{\partial t}$ is the change in concentration with time. The molecular diffusion coefficient *D* of gases in liquids can be estimated by equation 2.42 (Kim et al., 2015):

$$D = \frac{k_B T}{6\pi\mu r_{molecule}} \quad (2.42)$$

where μ is the viscosity of the liquid and $r_{molecule}$ is the radius of the gas molecule. The so-called Knudsen diffusion prevails when the pore size is less than the mean free path length of the molecules, indicated by k_n>1. Accordingly, the influence of the wall pore on the mass transport becomes very significant. Knudsen diffusion coefficient D_K is estimated by equation 2.43 (Javadpour et al., 2007):

$$D_K = \frac{2r_{pore}}{3}\sqrt{\frac{8RT}{\pi M}} \quad (2.43)$$

where r_{pore} is the pore radius, *R* is the universal gas constant and *M* is the molar mass.

In a transition flow regime, K_n is close to 1, as both intermolecular collisions and molecule-pore wall collisions are significant (Choi et al., 2001). The diffusion coefficient in the transition diffusion regime is estimated by equation 2.44 (Kim et al., 2015):

$$D_{Trans} = (\mathrm{D}_m^{-1} + D_K^{-1})^{-1} \quad (2.44)$$

According to (S. Li et al., 2019) and (S. Li et al., 2018a), Knudsen diffusion is the governing CO_2 mass transport mechanism in oil-saturated pores with a radius below 0.01 μm, while for pore radii larger than 1 μm, the governing mechanism is molecular diffusion. Both mechanisms superpose in pores of radii ranging between 0.01-1 μm.

Another mass transport phenomenon emanates due to adsorption. On the one hand, the adsorbed layer imposes resistance to the common concentration-driven mass transport, owing to high attractive intermolecular interactions between the molecules and pore walls and the consequent accumulation of gas molecules thereon. As a consequence, the cross-sectional area of the pore available to molecular or Knudsen diffusion is reduced by means of pore volume occupation (Liu and Emami-Meybodi, 2022; Strangfeld, 2021). For example, (Long et al., 2021) found lower CO_2 diffusivities than CH_4 and N_2 due to the higher CO_2 adsorption capacity of coal. On the other hand, a concentration gradient exists between the adsorbed layer and the bulk phase (Do and Wang, 1998) and between sites highly occupied by molecular clusters and those with less occupancy (adsorption patches) (Do et al., 2001; Spanakos and Rigby, 2020). These concentration gradients give rise to surface diffusion which is defined as the migration of molecules in the adsorbed state within the potential field of adsorption (Medveď and Černý, 2011). Surface diffusion significantly contributes to mass transport in nanopores and can account for more than 50% of the total mass flux (Liu and Emami-Meybodi, 2022). Being a complex activated process, it entails random hopping of the molecules between adsorption sites and is dependent on the interaction between the adsorbed molecule and the solid surface as well as the lateral interaction with other atoms. When monolayer adsorption capacity is still not reached, a molecule weakly adsorbed to the surface will oscillate due to the non-adiabatic coupling between the molecule and the surface (Ala-Nissila et al., 2002). Once it acquires enough energy, it hops to another free adsorption site and vibrates again. This process is repeated until the molecule acquires enough energy to overcome the energy barrier (adsorption energy) and desorbs, thereby returning to the gaseous phase (Cunningham and Williams, 1980). As the adsorption capacity increases, the surface diffusivity also increases, arriving at a maximum when the monolayer adsorption capacity is reached. When the capacity further increases passing on to multilayer adsorption, the diffusivity

exhibits a decrease and then increases again (Choi et al., 2001), i.e. surface diffusivity is a function of the surface coverage (loading) and exhibits a non-linear relationship as depicted in figure 2.12. Other factors of influence on surface diffusivity include pressure, temperature, properties of the gas, structural properties of the solid and the interaction between the solid and the gas (Wu et al., 2015).

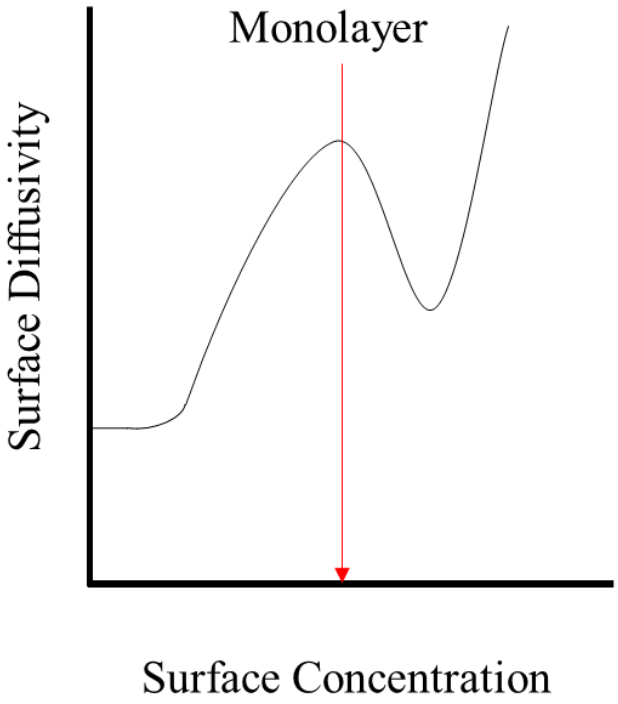

Figure 2.12 - Surface diffusivity as a function of surface concentration.

Even in the molecular diffusion regime, molecular diffusivities tabulated in literature must be corrected to account for the presence of a porous media, i.e. reduction in the cross-sectional area available for gases to diffuse and the increase in diffusion path length due to pore tortuosity. The aforementioned will result in an "effective" diffusivity that is less than the diffusivity of a gas in a non-confined space. For instance, (Wang and Hou, 2021) and (Lou et al., 2021) reported effective CO_2 diffusivities in oil-saturated porous media that are one or even two orders of magnitude lower than those of CO_2 diffusivity in a bulk oil phase, owing to the hindrance effect induced by the rock matrix. (Lou et al., 2021) reported a reduction of one order of magnitude in the effective diffusion coefficient when

the porosity of the investigated samples decreased from 18 to 8%. Additionally, the tortuosity – defined as the ratio of the actual length of the flow path to the length of the straight distance between the beginning and end of the flow path- is found to strongly impact diffusion. In porous media, a fluid flows through a tortuous path rather than a straight one, which means that the effective path of fluid flow is much longer than the apparent length (Gao et al., 2019). Therefore, samples with a higher tortuosity exhibit lower diffusivities (Du and Nojabaei, 2020). A relation between the diffusivity D and effective diffusivity D_e is proposed as below (Lou et al., 2021):

$$D_e = \frac{D\emptyset}{\tau} \tag{2.45}$$

where $\emptyset$ is the effective porosity and τ is the tortuosity of the sample.

A further factor taking influence on gas diffusivity in porous media is the presence of other components inside the pores. Especially in shales, compressed gases may dissolve in kerogen, leading to its swelling which ultimately narrows the flow channels and possibly causes the blockage of micropores, imposing further resistance to the mass transport (Rani et al., 2018; Zhao et al., 2016). Moisture content is found to negatively impact the CO_2 diffusivity as water hinders the gas transport either by reducing the diffusion volume available for the gas or by inducing swelling in rocks with a high clay content (Wang and Hou, 2021; Yuan et al., 2014). In the presence of oil in the pores, counter current diffusion of the oil occurs which will ultimately lower the diffusivity of the gas (Zhao et al., 2021). Alternatively, when both oil and water coexist in the pores, higher CO_2 diffusivities have been reported upon increasing oil saturation and simultaneously reducing water saturation (Li et al., 2016). This is attributed to the higher solubility of CO_2 in oil compared to brine. It has also been reported that the direction of core bedding also influences the mass transport (Chen et al., 2022; Samara et al., 2022b). Further, mechanical pressure (overburden pressure) on the formation rock influences the pore network and shall therefore be taken into

account when performing gas flooding tests in order to mimic actual reservoir conditions (Chen et al., 2022). Based on the aforementioned, a comprehensive literature review is presented in table 2.13 below on work conducted so far for measuring CO_2 diffusivities in tight lithologies.

Table 2.13 - Summary of previous experimental studies on CO_2 diffusion in tight formations.

Reference	Method	Experimental Conditions/Materials	Porosity	Perm.	Effective Diffusivity
(Zhu et al., 2018)	Pressure decay method	6.2-12.6 MPa 60 °C C12-saturated shale	4.7-5%	25-42 μD	2.4-12.5 $x10^{-10}$ m^2/s
(Li et al., 2016)	Pressure decay method	6.5-30 MPa 70-150 °C Low permeability rocks from Shengli Oil field The cores are saturated with crude oil from the same oil field	13.59-20.23%	8.39-985.06 mD	0.25-28.3 $x10^{-10}$ m^2/s
(Rani et al., 2018)	Volumetric adsorption-diffusion method	2-6 MPa 40 °C Indian shale.	N/A	N/A	1-2.7$x10^{-12}$ m^2/s
(Lv et al., 2019)	Pressure decay method	10-27 MPa 60-100 °C decane-saturated Berea Sandstone	16 and 22.5%	50 and 100 mD	0.6-13.2 $x10^{-10}$ m^2/s
(Du et al., 2019)	Volumetric adsorption-diffusion method	3-8 MPa 45-85 °C Wufeng and Yanchang shales	2.4 and 4.7%	N/A	1.2-2.9 $x10^{-11}$ m^2/s
(Gao et al., 2019)	Pressure decay method	15-30 MPa 20-80 °C Oil-saturated artificial cores	10-38%	20-2272 mD	2-54.5 $x10^{-10}$ m^2/s

Table 2.13 - Continued					
(S. Li et al., 2019)	Pressure decay method	15 MPa and 70 °C Core plugs saturated with Changji oil	3.3-4.5%	3.7-21.6 μD	23.8-64.9 $x10^{-10}$ m^2/s
(S. Li et al., 2018a)	Pressure decay method	15 MPa and 70 °C Core plugs saturated with Changji oil	4.3-15.4%	0.104-301.5 mD	88.3–161.1 $x10^{-10}$ m^2/s
(S. Li et al., 2018b)	Pressure decay method	5-23.4 MPa 25-85 °C Core plugs saturated with Changji oil	3.9-5.8%	5.8-191 μD	26.3–164.4$x10^{-10}$ m^2/s
(Li and Dong, 2009)	Pressure decay method	2.3-6.3 MPa 40 °C Hexadecane saturated-Berea cores	18%	160-263 mD	5.6-7.6 $x10^{-10}$ m^2/s
(Wang and Hou, 2021)	Pressure decay method	50 MPa and 120 °C Oil-saturated Breccia, sandstone and siltstone	8.2-19%	8-1292 mD	6.9-25.5 $x10^{-10}$ m^2/s
(Peng and Sheng, 2023)	Pressure decay method	9−10 MPa, 90 °C Jismar Shale core saturated with Jismar oil	10%	0.4-19 μD	1.4-5.5$x10^{-11}$ m^2/s

*N/A denotes the unavailability of data in the published work.

In the pressure decay method, a core sample is placed inside a diffusion cell and vacuum is applied. The diffusion cell is then pressurized with CO_2 to a certain pressure using a syringe pump. After reaching the desired pressure, the inlet valve connecting the gas pump to the diffusion cell is closed and the diffusion cell is isolated from the gas source. Afterwards, the pressure inside the diffusion cell drops due to gas diffusion into the core. This pressure drop is monitored with time and recorded. The experimental pressure decay curve is then fitted using a diffusion model in order to determine the effective diffusion coefficient (Li et al., 2006).

3. Materials and Methods

3.1 Materials and Material Characterization

3.1.1 Sultani Shale

Shale samples originating from the Sultani deposit located 100 km southeast of the capital city of Amman, Jordan are the focus of the current work. The samples were collected from the open pit site excavated by the Natural Resources Authority (NRA) of Jordan. Figure 3.1 shows the geographical location of the Sultani deposit. The Sultani deposit extends over an area of 31.2 km^2, where the oil shale layer has an average thickness of 31.6 m and a geological reserve of around 1130 million tons (Alali et al., 2014).

Figure 3.1 - Geographical location of Al-Sultani deposit in Jordan.

Sultani shale was deposited in a shallow marine environment consisting of synclinal basins that were part of the southern epicontinental shelf of the Neo-Tethys Ocean (Jaber et al., 2011). This deposition took place during the period extending between the Maastrichtian and the early Paleocene (Jaber, 2000; Jaber and Probert, 1997). Along the epicontinental shelf, an upswelling regime of the circumglobal current took place, and primarily deep, cold and nutrient-rich waters were carried towards the surface of the sea (Abed et al., 2010) leading to increased bio productivity of Phytoplanktons, which ultimately resulted in high sedimentation rates of organic matter (Abed, 2013). The preservation of the

organic matter was reinforced by the anoxic conditions prevailing in the lower part of the water column (Hakimi et al., 2016). This regime proceeded until the merging of the African Arabian and Eurasian plates during the Eocene, which resulted in the regression of the Neo-Tethys ocean (Khrewesh et al., 2014). Planktons, zooplanktons, and small traces of terrestrial debris, such as pollen, spores, and cuticles of higher plants constitute the main source of organic matter in Sultani shale (Abed et al., 2005; Hakimi et al., 2018). The Sultani shale belongs to the Muwaqqar Chalk Marl (MCM) which consists of layers of organic-rich bituminous marls interbedded with marly limestone and chalk layers. The MCM formation overlays Al-Hisa Phosphorite formation, and both formations belong to the Balqa Group as depicted in figure 3.2.

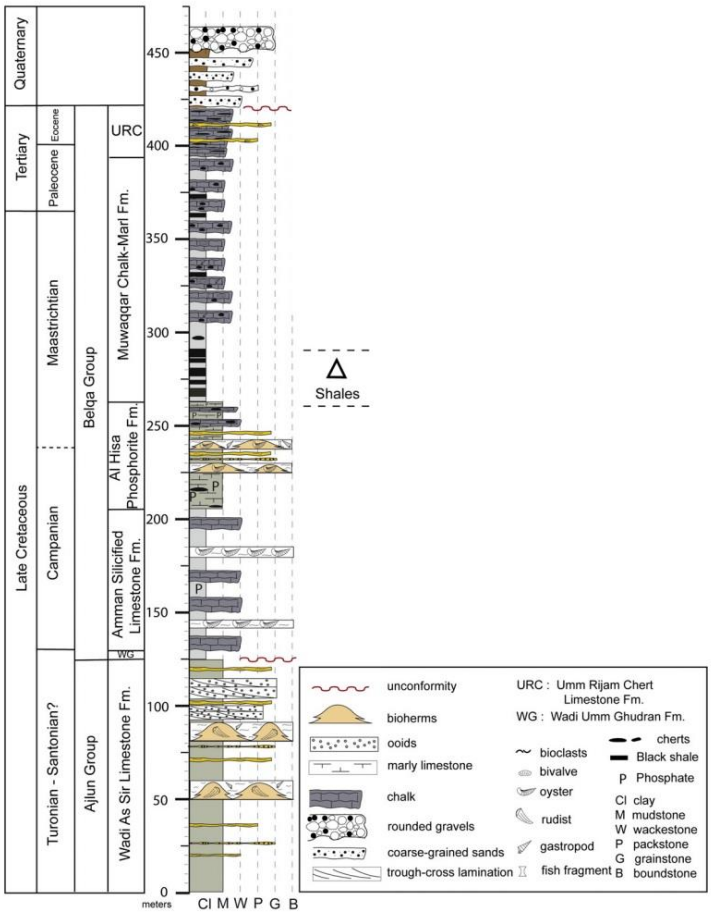

Figure 3.2 - Chrono-lithostratigraphic column of Central Jordan, adapted from (Fleurance et al., 2013), reused with permission.

3.1.1.1 Mineral Composition

Several X-ray diffraction (XRD) tests have been performed on samples originating from the same reservoir to determine the mineral phases. X-ray diffraction results as reported in (Samara et al., 2021) are shown in figure 3.3. The X-ray diffraction was performed on powdered Sultani shale samples that were loaded into the diffractometer (Empyrean – Malvern Panalytical, UK) with Cu Kα radiation and a nickel filter in a 2θ range of ≈ 10°- 90°. The results indicate that the mineral composition is dominated by Calcite, followed by Quartz, Dolomite and Pyrite.

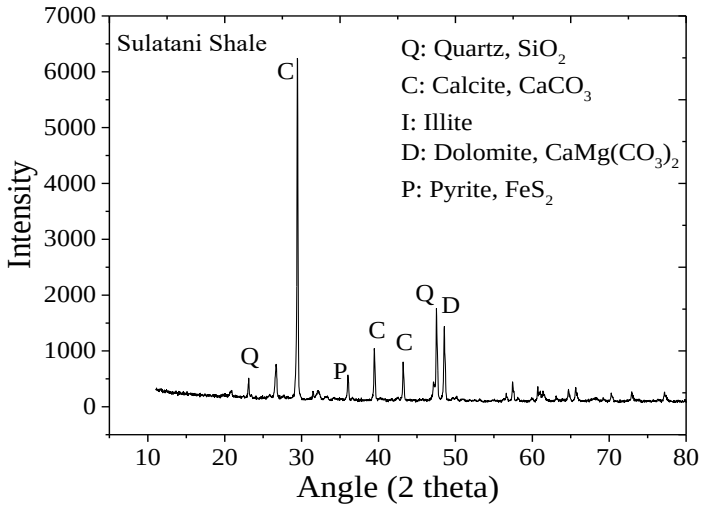

Figure 3.3 - X-ray diffraction of Sultani shale, adapted from (Samara et al., 2021).

The mineral composition of the Sultani shale in the work of (K. Li et al., 2019) is shown in figure 3.4 and shows that calcite has a share of 67.25%, followed by Quartz (18.25%), Apatite (6.5%) and traces of Pyrite (4.25%) and dolomite (3.62%). In the work of (Sauerer et al., 2021) the mineral composition of Sultani shale is summarized in table 3.1.

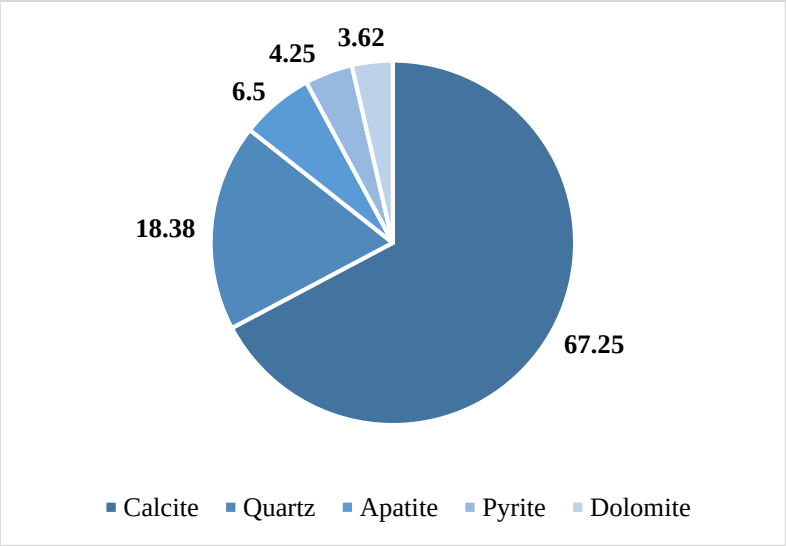

Figure 3.4 - Mineral composition of Sultani shale.

Table 3.1 - Mineral composition of Sultani as reported by (Sauerer et al., 2021).

Sample	Calcite (%)	Quartz (%)	Illite (%)	Montmorillonite (%)	Pyrite (%)
1	69.8	12.3	12.1	4.7	1.2
2	62.4	27.8	6.4	1.7	1.7
3	61.5	27.6	7.2	1.6	2.1

Even with the slight inconsistencies in the mineral composition as reported in the mentioned studies, which are mainly due to the anisotropy of shale, it is evident that the dominant mineral in the composition is Calcite. Sultani shale classification extends between a carbonate-dominated lithotype and mixed carbonate mudstone. Figure 3.5 demonstrates a backscattered electron scanning electrons microscopy (BSE-SEM) of polished Sultani samples where the different minerals constituting the Jordanian shale are demonstrated. The apparent density of Sultani shale is measured to be 1.79 g/cm^3.

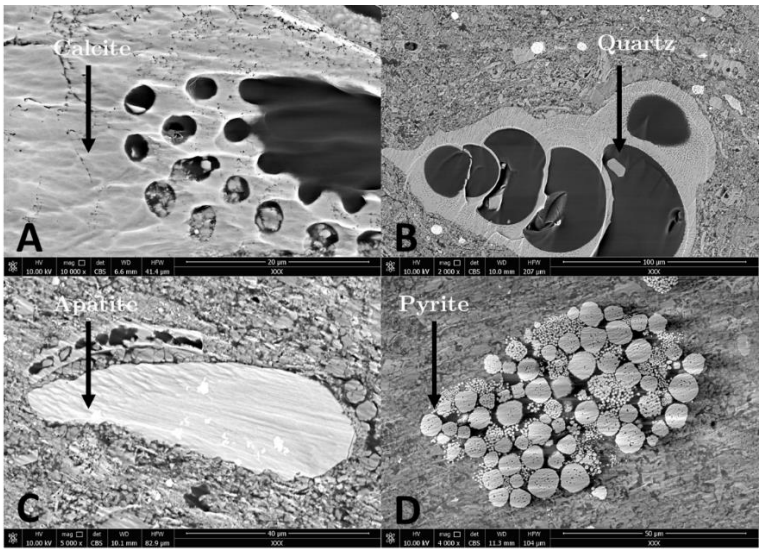

Figure 3.5 - Minerals constituting Sultani shale; (A) Calcite. (B) Quartz. (C) Apatite. (D) Pyrite aggregate, adapted from (Li, 2022), reused with permission.

3.1.1.2 Organic Matter Characterization

Despite the low thermal maturity of Sultani shale indicated by a vitrinite reflectance of 0.4-0.5%, it has strong potential to be an oil generating source rock due to the high Total Organic Carbon (TOC) content of around 16.5% (Sauerer et al., 2021). The TOC of Sultani is divided into free hydrocarbons of around 4.3% and the so-called residual hydrocarbons (those with hydrocarbon generation potential such as bitumen and kerogen) of around 95.7%. Figure 3.6 shows an image of kerogen extracted from Sultani shale using the kerogen isolation methods described by (Li, 2022).

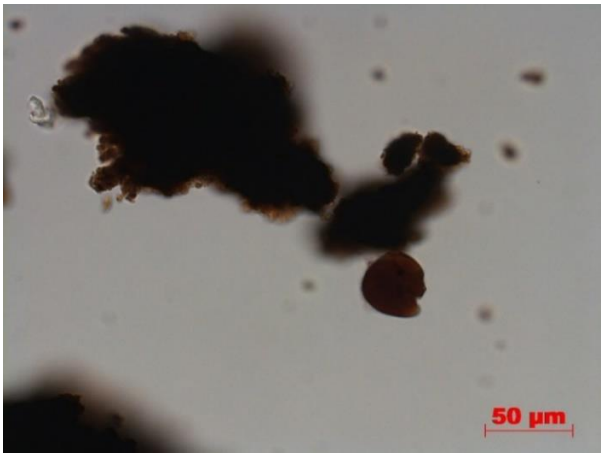

Figure 3.6 - Kerogen extracted from Sultani shale, adapted from (Li, 2022), reused with permission.

Although the definition of kerogen is constantly evolving across the scientific community, there exists consensus that kerogen is the solid fraction of organic matter in sedimentary rock, possessing a high-molecular weight and a complex chemical structure (Weck et al., 2017). Kerogen is insoluble in aqueous, alkaline or organic solvents (Hutton et al., 1994). Bitumen, on the other hand, is defined as an intermediate product that evolves during the transformation of kerogen into hydrocarbons (Craddock et al., 2015).

3.1.1.3 Pore Space Characteristics

Figure 3.7 shows a thin section image of Sultani shale. The foraminifera fossil pores are the main spaces accommodating the organic matter. These fossil pores are 50-500 μm in size, independent and are poorly connected, rendering Sultani shale a typical tight reservoir with an average porosity of 7.6% and low permeability of 4.1 nD or $40x10^{-22}$ m^2 according to (Li, 2022) who measured the permeability using the Gas Research Institute method (GRI).

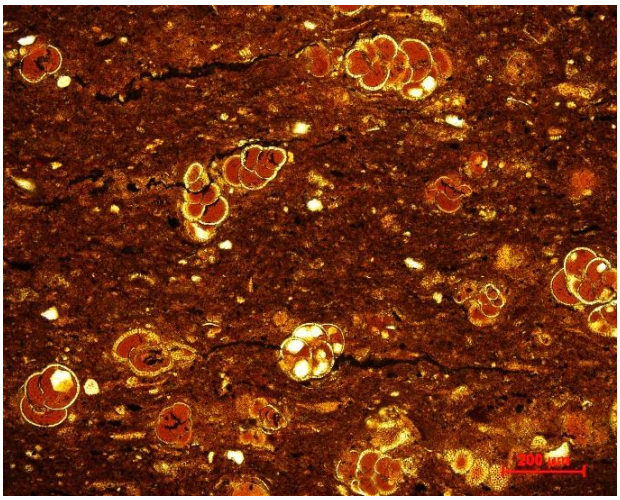

Figure 3.7 - Thin section image of Sultani shale, adapted from (Samara et al., 2019).

For the characterization of surface area, pore volume and pore diameter, Brunauer-Emitt-Teller (BET) and Barrett, Joyner and Halenda (BJH) analyses were performed using a BET analyzer (Tristar II 3020, United States). The characterized sample weighed 0.3 g and had undergone supercritical CO_2 extraction (40 MPa, 60 °C), i.e. the extractable oil fraction is mainly removed.

The sorption isotherms were conducted using the non-reactive nitrogen (N_2) at -195.8 °C and a relative pressure (P/P_o) ranging between 0.014-0.996 for adsorption and 0.996-0.083 for desorption, where P_o is the vapor saturation pressure of N_2, which happens to be -195.8 °C at 0.1 MPa. The results of the BET and the BJH are shown in figures 3.8 and 3.9.

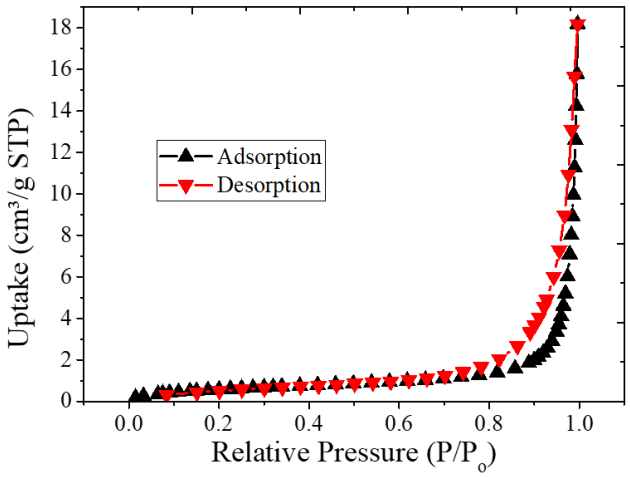

Figure 3.8 - N_2-BET sorption for surface area characterization of Sultani shale.

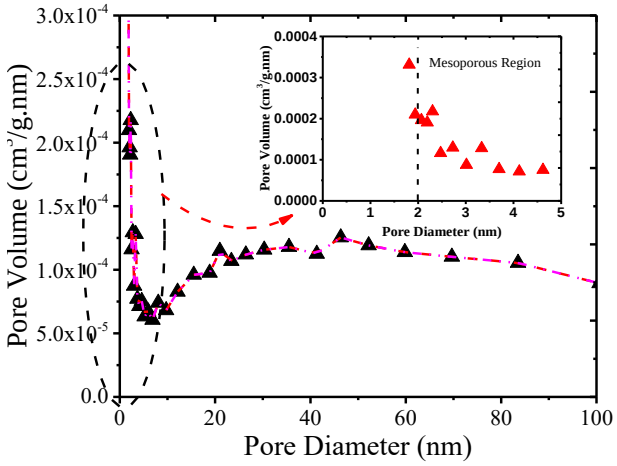

Figure 3.9 - Pore volume with respect to pore size of Sultani shale.

As shown in figure 3.9, the smallest pores in the Sultani shale are of a size of around 2 nm. The International Union of Pure and Applied Chemistry (IUPAC) classifies pore sizes falling between 2-50 nm as mesopores (Mays, 2007). The mesoporosity of the shale is further indicated by the shape of the sorption isotherm shown in figure 3.8, reflecting a combination of type II isotherm, typically found in macroporous material and type IV isotherm typically found in mesoporous

materials (Horikawa et al., 2011), where the presence of a hysteresis loop between the adsorption and desorption curves is associated with capillary condensation which is unique to mesopores (Lowell et al., 2004). The low N_2 adsorption capacity at low relative pressures indicates the absence of micropores (less than 2 nm) as seen in figure 3.9 and the narrow hysteresis loop indicates that the sample is dominated by fine macropores or large mesopores (Kuila and Prasad, 2013), which is further confirmed by average pore size of approximately 43 nm as calculated using the BJH method. The average surface area, pore volume and pore diameter are summarized in table 3.2. According to hysteresis loop classification of IUPAC, the shape of the pores can be inferred from the sorption isotherm, however, with the heterogeneous pore system of the shale, drawing conclusions regarding pore shape is not a straight forward task. As seen in figure 3.8, the steep desorption branch accompanied by a narrow vertical hysteresis loop indicates an H1 loop normally associated with cylindrical pores (both ends open), nevertheless, with H1 loops a limit in adsorption is found at high relative pressures, where a plateau in adsorption is reached (see figure 3.10), which is absent in the analysis presented here. On the other hand, the loop presented in figure 3.8 shares similarities with the H3 hysteresis loop in figure 3.10. This hysteresis loop is normally associated with the presence of non-rigid aggregates of plate-like particles such as certain clays, the presence of slit-like pores, and the presence of macropores that are not completely filled with the adsorbate (Liu et al., 2021; Thommes et al., 2015). Therefore, it can be inferred that the shale consists of a complex pore system where cylindrical, slit-like mesopores and macropores are present. It should be noted that this conclusion is strictly valid for N_2 adsorption, and will not yield similar results when CO_2 is applied as the adsorbing phase in the BET analysis (Hui et al., 2019).

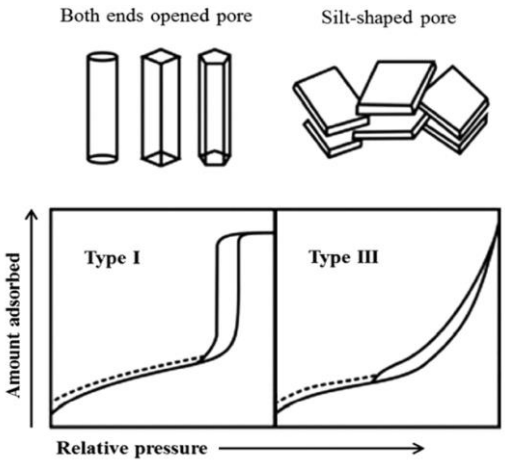

Figure 3.10 - H1 and H3 loops and corresponding pore shapes, adapted from and modified after (Liu et al., 2021), reused with permission.

Table 3.2 - Average surface area, pore volume and pore diameter of Sultani shale.

Average surface area m^2/g	**Average pore volume cm^3/g**	**Average pore size nm**
2.2597	0.0220	42.8904

3.1.2 Calcite

As a model mineral, a Calcite crystal (Iceland Spar) was purchased from Ward's science – USA. The Calcite crystal was also subject to XRD analysis and the results thereof are reported in figure 3.11. The Calcite crystal is composed entirely of calcium carbonate ($CaCO_3$).

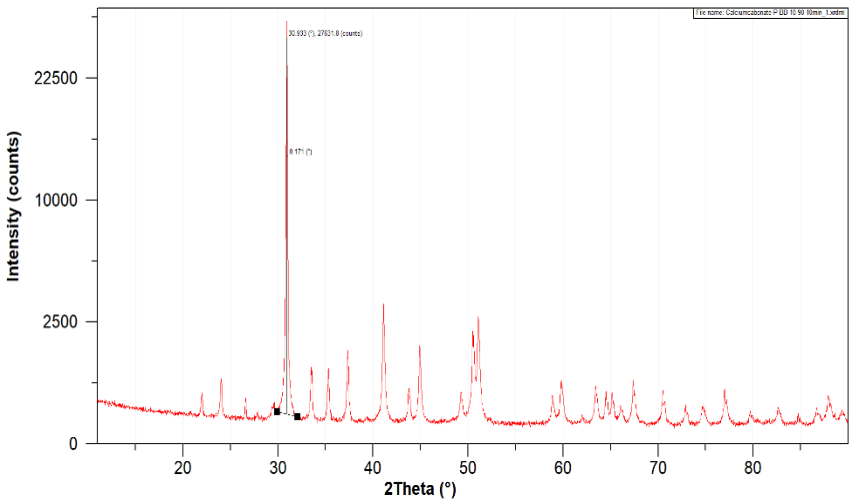

Figure 3.11 - X-ray Diffraction of Iceland Spar (Calcite).

3.1.3 Fluids

3.1.3.1 Oleic Phases

The oleic phases investigated in this work include the below:

- An oil mixture consisting of oils subject to different extraction conditions, i.e. 15, 30 and 40 MPa at 40 and 60 °C (See Chapter 4). This mixture will be referred to as SFEM. Figure 3.12 shows the collected oil at extraction conditions of 30 MPa and 60 °C.

Figure 3.12 - Oil extracted by supercritical CO_2 at 30 MPa and 60 °C.

- Oil extracted from Sultani shale at extraction conditions of 40 MPa and 60 °C. This oil will be referred to as SFE40. The density of the oil at ambient conditions was measured to be 0.9307 g/cm^3. The oil was subject to Gas Chromatography (GC) analysis. The results thereof are shown below in figures 3.13 and 3.14.

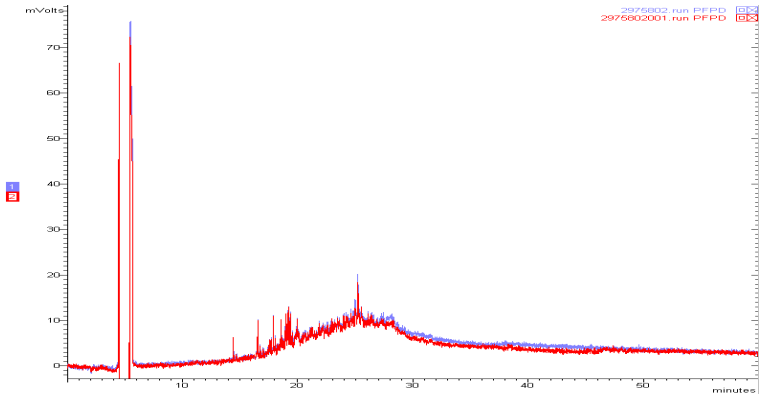

Figure 3.13 - Chromatogram of SFE40.

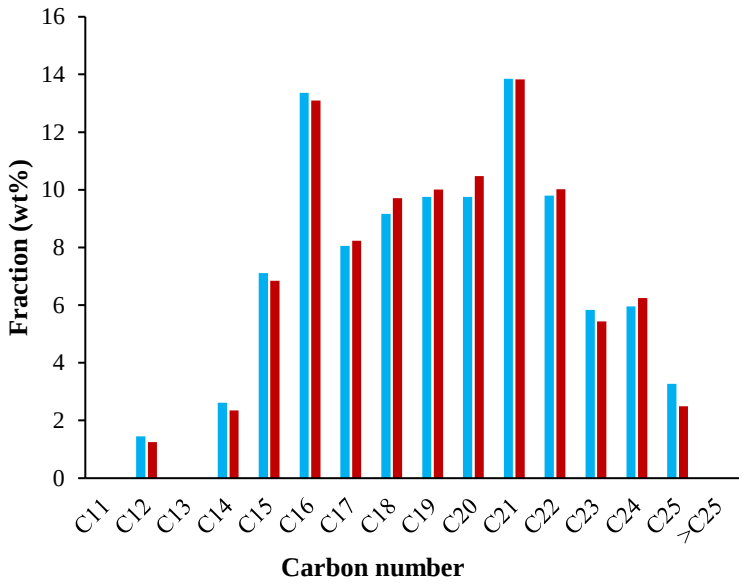

Figure 3.14 - Composition of SFE40.

Due to the high viscosity of the extracted oil, it was diluted with hexane purchased from Merck KGaA, Germany and fortified with bicyclohexyl 92-51-3 purchased from Sigma-Aldrich, Germany. The GC (Varian GC CP-3800, United States) was equipped with an autosampler (CTC analytics Combipal, 10 μL syringe, liquid injection, 1.0 μL injected), a spit/spitless injector (CP-1177) used in a spitless mode, a capillary column (Petrocol DH, 30 m long with an internal diameter of 0.25 mm and a film thickness of 0.5 μm) and a Pulsed Flame Photometric Detector (PFPD, 200 °C, 570V Photomultiplier Voltage, 0,5 msec gate delay set for carbon detection, 8,0 msec gate width, 180 mV trigger level, Air flow 1: 17,0 ml/min, H_2 flow: 13,0 ml/min; Air flow 2: 10,0 ml/min, detector bunch rate 4 points (10 Hz). Initially the oven was held at a temperature of 40 °C for 2 minutes. Temperature was then increased to 300 °C at a rate of 10°/min and was maintained at this temperature for 32 minutes. The chromatograms of the GC analysis for two Sultani oil samples (red and blue) and the respective compositional analysis, indicated by carbon number, are shown in figure 3.13 and 3.14, respectively. The peaking in the signal at 4.5-5.5 min is due to solvent hexane eluting.

- Model oil.

Based on the GC results, a model oil consisting of 45 wt% n-Hexadecane ($C_{16}H_{34}$), 45 wt% Eicosane ($C_{20}H_{42}$) and 10 wt% Tetracosane ($C_{24}H_{50}$) was synthesized in the lab, reducing the multicomponent mixture shown in figure 3.14 to 3 representative carbon numbers.

- Hexadecane.
- Dodecane.
- Hexane (Soxhlet Extraction).

All alkanes were purchased from Fischer Scientific GmbH, Germany at analytical grade (purity of 99%) and were used without undergoing any further purification. Molecular weights and phase change data of the alkanes are reported in table 3.3 below.

Table 3.3 - Physical properties of alkanes.

Property/ Alkane	Hexane	Dodecane	Hexadecane	Eicosane	Tetracosane
Molecular weight (g/mol)	86.2	170.3	226.4	282.5	338.7
Melting point (°C)	-96	-9.6	18.2	36.9	50.8
Boiling point (°C)	69	216.2	286.9	309.7	324.1
Critical temperature (°C)	344.3	385.1	449.0	494.3	526.8
Critical pressure (MPa)	3.0	1.8	1.4	1.07	0.9
Triple point temperature (°C)	-95.1	-9.5	17.8	35.8	50.5

3.1.3.2 Aqueous Phases

Aqueous phases utilized in the current work comprise deionized water (DW), NaCl brines as well as $CaCl_2$ brines. In the process of brine preparation, salts purchased from Merck KGaA, Germany were dissolved in deionized water at

various concentrations. Deionized water was weighed by means of an electronic precision balance (Kern EW 220-3NM, Kern & Sohn, GmbH, Germany) with an accuracy of ±1 mg and the amount of salt needed for obtaining the desired salt concentration was also weighed, and dissolved thereafter in the DW. The solutions were stirred by means of a magnetic stirrer (IKAMAG RET, IKA, Germany) at 500 RPM until no salt crystals were observable. Each brine solution was prepared directly before use in the respective experiment and was preserved in an air-tight container to prevent evaporation. In addition to deionized water, the salts prepared and utilized in this work are as follows: 1% NaCl brine, 3% NaCl brine, 10% NaCl brine and 3% $CaCl_2$ brine.

3.1.3.3 Gaseous Phase

Carbon dioxide at a purity of 99.99 mol% was purchased from Westfalen AG, Germany.

3.2 Methods

3.2.1 Supercritical Fluid Extraction

A supercritical extraction rig (HPE lab-700r, Eurotechnica GmbH, Germany) was used to extract the oil from Sultani shale. The extraction rig comprises: an electrically driven diaphragm gas compressor (Nova Swiss, Switzerland) with an on/off operation mode, an extractor, a back-pressure regulator (BPR) (TESCOM 26-1700, Emerson, United States) and a separator. The maximum allowable operating conditions are summarized in table 3.4 below. The actual rig is presented in figure 3.15 and the schematic diagram thereof is presented in figure 3.16.

Table 3.4 - Maximum allowable operation conditions.

Component	Maximum Temp (°C)	Maximum Pressure (MPa)	Volume (l)	Mass/Volume flow
Compressor		100		2-3 kg/h
Extractor	100	100	4.0	
BPR	80	69		2-3 kg/h
Separator	100	50	0.5	
Heating bath	150	0.1	4.5	15 Nl/min

Figure 3.15 - Supercritical extraction rig (HPE Lab-700r)

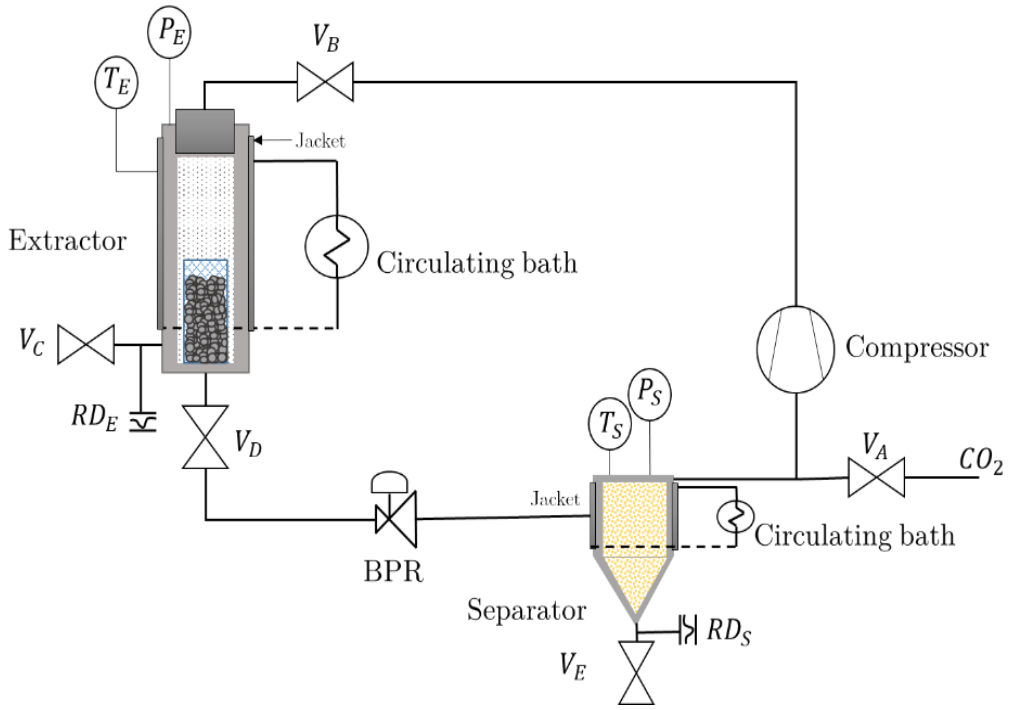

Figure 3.16 - Schematic diagram of the supercritical extraction rig.

Rupture disks (RD_E) and (RD_S) are connected to the system as a safety measure in case of pressure buildup within the extraction cycle during operation. Once that occurs, the rupture disks burst, allowing the system to simultaneously vent the gas and consequently decompress.

Prior to the extraction, large chunks of shale were ground by means of a hammer. Particles of approximately the same size were selected. The crushed shale was loaded into filter bags that were sown shut and were placed in a product basket with a sintered steel bottom. The product basket was then placed into the extraction vessel. The filter bags and the product basket serve to facilitate the handling of the source material and prevent the migration of fine particles into the high-pressure lines, which would result in clogging. Afterwards, the extractor's lid is closed and tightened. The connection between the compressor and the extraction vessel is established using high pressure lines through valve B (V_B). At this point all the valves are kept closed. Valve A (V_A), valve B (V_B), and valve D (V_D) are then opened and CO_2 gas is passed from the dip tube cylinder into the compressor and from there onward to the extractor and then the separator at

cylinder pressure (around 5.5 MPa = saturation pressure at ambient temperature). The compressor is then switched on to increase the pressure in the extraction cycle until the desired pressure is reached. A compression cycle comprises three stages, suction, compression and discharge. During suction, the suction valve opens and the downward stroke of the compressor charges the gas chamber with CO_2 until the piston reaches the bottom dead point. When starting the compression stroke, the suction check valve is forced into the "closed" position. During compression, both valves (suction and discharge) are closed until the pressure reaches the actual discharge value. Subsequently, the discharge valve opens while the suction valve remains closed and the high-pressure gas is released into the extraction cycle lines. Valve A (V_A) remains open in order to compensate CO_2 losses due to removal of CO_2-loaded extract from the separator. The pressure at the separator is controlled by means of the BPR and is maintained at 5.5-6 MPa. The temperatures of the extractor and the separator are controlled by means of thermostatic circulating baths (CD-BC4, Julabo GmbH, Germany) connected to the jackets of both extraction and separation vessels. The temperature at the separator is maintained at 40 ^oC during all extraction runs while the temperature in the extractor is varied. The pressure and temperature at the extractor and the separator are measured with calibrated pressure gauges with an accuracy of ±0.5 MPa and calibrated k-type thermocouples of an accuracy of ±0.5 ^oC, respectively. Valve E (V_E) at the separator is opened on an hourly basis to collect the extract. In cases where the substrate underwent soaking (resembling the Huff and Puff process), valves B, C and D were closed, the compressor was turned off and the temperature in the extractor was lowered to 50 ^oC. Valve C (V_C) is only opened at the end of an extraction run to decompress the entire system in preparation for the next round of extraction using a fresh batch of shale. Four batches underwent supercritical extraction performed at the conditions summarized in table 3.5:

Table 3.5 - Supercritical extraction conditions.

Parameter	Batch 1	Batch 2	Batch 3	Batch 4
Extraction temperature (ºC)	60	60	40	60
Extraction pressure (MPa)	40	30	15	15
Separation temperature (°C)	40	40	40	40
Separation pressure (MPa)	6	6	6	6
Soaking period (hours)		91		

3.2.2 Soxhlet Extraction

Soxhlet extraction using n-Hexane was performed on crushed Sultani shale with particle sizes ranging between 125-160 μm. The extraction was performed using the setup illustrated in figure 3.17. A thimble was filled with 3 grams of crushed shale of particle size ranging between 125-160 μm. The shale particles were thoroughly mixed with 2 grams of Kieselguhr to increase the surface area of shale exposed to the solvent. The distillation flask was filled with 200 ml of Hexane. The Soxhlet extractor was then heated using a heating plate (MOEV lab heater-Gerhard, Germany). The condenser was cooled with water at 4 °C using a cooling circulation bath (FC600, Julabo GmbH, Germany). The extraction time was 4 hours to ensure that the soluble materials are completely extracted. The investigated temperatures were 80, 100 and 120 °C.

During extraction, Hexane vapor flows up from the distillation flask and into the condenser, where it condenses and drips down into the shale-filled thimble inside the extractor, thereby dissolving hydrocarbons contained in the shale. Once the extractor is full, the solution (solvent and solute) is transferred back into the distillation flask through the siphon. The process is resumed again such that the solvent vaporizes and flows upwards, while the solute remains behind in the distillation flask. During each extraction cycle, more of the hydrocarbons is dissolved, leaving the insoluble constituents of the shale behind in the thimble. The extracted hydrocarbons were recovered from Hexane by evaporating the

mixture at 40 °C and 100 mbar in a rotary vacuum evaporator connected to a vacuum pump (Rotilabo, Germany). Afterwards the concentrated extract was left to cool and was weighed.

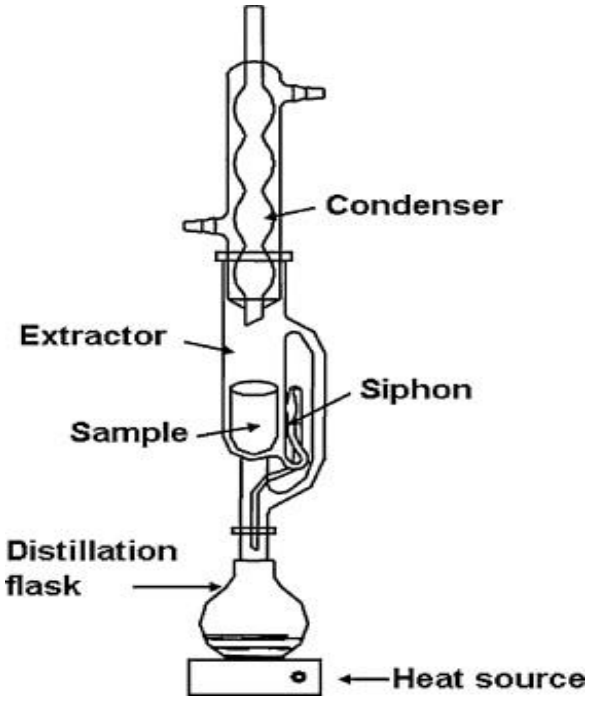

Figure 3.17 - Soxhlet extraction apparatus.

3.2.3 Particle Size Distribution

Particle size distribution analysis is performed to determine the mass median particle diameter (D50) of each batch extracted with $scCO_2$. The D50 denotes the particle size above which 50wt% of the particles in the batch have a larger size and below which 50wt% of the particles in the batch have a smaller size. The analysis is carried out using a vibrating sieve shaker (Kroll, Retsch – Germany) with sieves of pore sizes ranging between 0.2 – 14 mm. Prior to sieving, the mass of the entire batch is measured using an electronic scale of an accuracy of 0.1 g. Each sieve corresponding to a particle size is weighed empty and the values are recorded. The shale is loaded into the top sieve with the largest pore size and sieving is performed for 15 minutes at an operating frequency of 50 kHz. After sieving, each sieve containing the shale particles is weighed again and the values are recorded. The mass of shale in each sieve is calculated by subtracting the mass

of the empty sieve from the total mass of the shale-containing sieves (non-cumulative). The mass retained by each sieve is added to the mass retained by the next sieve owning a larger size and recorded as a cumulative mass. The cumulative value is then divided by the total mass of the batch to infer the percentage of particles retained (% retained) in each sieve. To calculate the percentage of particles passing each sieve (% passing), the % retained is subtracted from 100%. The D50 is calculated using the % passing. The upper and lower limit of the 50% mass fraction (for example 40 and 60%), corresponding to the upper and lower limit of particle sizes (for example sieves of pore diameters of 2 and 4mm), are determined from the previous calculations and the D50 (50%) is calculated by interpolation between these two values using equation 3.1 below:

$$S = 2^{log_2(S^-)+(50-P^-)\frac{(Log_2 S^+ - Log_2 S^-)}{(P^+ - P^-)}} \quad (3.1)$$

where S is the particle size corresponding to D50, P^+ is the percentage of particles on mass basis smaller than S^+, which corresponds to larger sieve pore size (for example 60% and 4 mm, respectively), P^- is the percentage of particles smaller than S^- which corresponds to the smaller sieve pore size (for example 40% and 2 mm, repectively).

3.2.4 Interfacial Tension

Surface and interfacial tension of binary (CO_2-oil or CO_2-brine) and ternary systems (CO_2-oil-water/brine) were measured using a high-pressure, high-temperature drop shape analysis (HP/HT DSA) system with a resolution of 0.01 mN/m. The system comprises a drop shape analysis unit (DSA100, Krüss GmbH - Germany) coupled with a high-pressure system (PDE-1700 MD-H, Eurotechnica GmbH- Germany). The drop shape analysis unit is composed of a light source, a high resolution (1920-1200 pixel) charge-coupled device (CCD) camera connected to a drop shape analysis software (ADVANCE, Krüss GmbH – Germany). The software implements the Axisymmetric Drop Shape Analysis (ADSA) technique, where a theoretical drop profile is determined and fitted to the

actual drop profile to calculate the IFT. This technique is based on the balance between the Young-Laplace pressure across curved interfaces ΔP and the hydrostatic pressure along the height of the drop $\Delta\rho g z$ as shown in equation 3.2:

$$\gamma\left(\frac{1}{r_1}+\frac{1}{r_2}\right) = \Delta P \equiv \Delta P_o - \Delta\rho g z \qquad (3.2)$$

where r_1 and r_2 are the two principal radii of curvature, $\Delta\rho$ is the density difference between the participating phases, g is the gravitational acceleration and z is the height of the drop. ΔP_o is a reference pressure at z=0. By means of axisymmetry, equation 3.2 can be expressed using the differential equations 3.3-3.5. These equations describe the drop profile by relating the cylindrical coordinates (r, z), to the arc length s, measured at the apex of the drop as illustrated in figure 3.18.

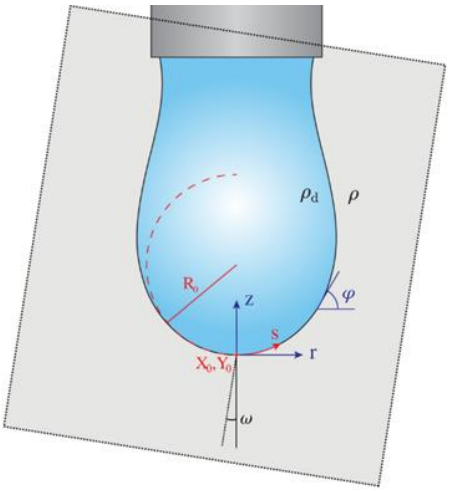

Figure 3.18 - Pendant drop profile, adapted from (Berry et al., 2015), reused with permission.

$$\frac{d\varphi}{d\bar{s}} = 2 - B_o\bar{z} - \frac{sin\varphi}{\bar{r}} \qquad (3.3)$$

$$\frac{d\bar{r}}{d\bar{s}} = cos\varphi \qquad (3.4)$$

$$\frac{d\bar{z}}{d\bar{s}} = sin\varphi \qquad (3.5)$$

The dashed parameters indicate dimensionless quantities scaled with respect to R_o, which is the radius of curvature at the drop apex and B_o is the bond number. The boundary conditions at the drop apex are defined as:

$$\bar{r} = \bar{z} = \bar{s} = \varphi = 0 \qquad (3.6)$$

The resulting set of differential equations are numerically solved by a profile optimization algorithm, and a relation between the radius of curvature, the bond number and the IFT is obtained through equation 3.7:

$$\gamma \equiv \frac{\Delta \rho g R_o^2}{B_o} \qquad (3.7)$$

The complete description of the ADSA can be found in (Song and Springer, 1996a, 1996b). The software allows the recording of the drop images in a sequential manner with time intervals set by the user. On the other hand, the high-pressure system comprises: a view cell (P_{max} = 69 MPa, T_{max} = 200 °C, V=25 ml) supplied with a heating jacket connected to a PID temperature controller (HT43 Hillesheim, Germany), a mini-drop injection unit (V=2 ml) and a brine reservoir. A moveable capillary with an outer diameter of 1.59 mm extends into the view cell and connects the mini drop injection unit to it. Depending on the measurement, this capillary extends into the view cell either from the top for a pendant drop configuration or from the bottom for a standing drop (rising bubble) configuration. The configuration chosen depends on the densities of the participating phases. When the density of the drop phase is higher than the density of the surrounding phase, the pendant drop configuration is adopted. Alternatively, when the density of the drop phase is lower than the density of the surrounding phase, the standing drop configuration is used. Both configurations are illustrated in figures 3.19-A and 3.19-B. A k-type thermocouple with an accuracy of ±0.5 °C is located 10 mm away from the capillary to measure the local temperature of the system. A pressure transducer with an accuracy of ±0.01 MPa is connected to the view cell to measure the pressure within the view cell. Two high-pressure resistant sapphire windows are located at both sides of the view cell, where one window faces the CCD camera of the DSA and the other window faces the light source of the DSA to facilitate the optical visualization of the formed drops.

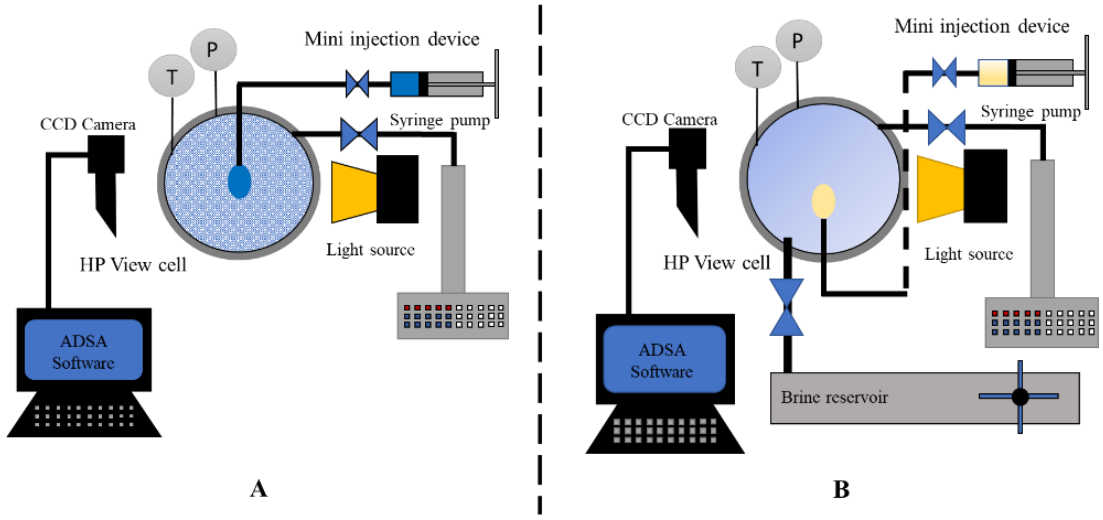

Figure 3.19 - Schematic diagram of HP/HT DSA system. (A) Pendant drop configuration. (B) Standing drop configuration.

The high-pressure system is also connected to a syringe pump with a maximum pressure of 69 MPa (D100, Teledyne ISCO, United States), which is used to supply the system with CO_2 at the required pressures. The syringe pump is connected to a dip tube CO_2 cylinder where CO_2 exists in a liquid state with a vapor pressure at ambient temperature of around 5.5 MPa. Aside from CO_2 compression, the syringe pump also serves to monitor the volumetric flow rate of CO_2 into the system.

Before each test, the system is verified to be contaminant free (see section 3.2.11.2). Once this is achieved, the mini injection device is emptied, dismantled, dried then reassembled for the introduction of the liquid of interest. The heating jacket of the view cell is activated via the temperature controller where the desired temperature is set.

In measurements where the pendent drop configuration is employed, CO_2 is introduced into the view cell by means of the syringe pump, which is pre-pressurized to reduce the time required for reaching the designated pressure. The system temperature is left to equilibrate after the introduction of CO_2 into the view cell. Once the temperature is stable, a drop of liquid of a convenient volume is formed at the tip of the capillary and the IFT is measured. The measurements are

recorded until a constant IFT value is reached. In ternary and quaternary systems where the standing bubble of oil in an aqueous phase is employed, water/brine is pumped from the reservoir into the view cell. The view cell is filled up to ¾ of its volume to leave room for a CO_2 gas cap to form. The gas cap facilitates CO_2 dissolution into the water/brine. A waiting time of 15-30 minutes ensures that the water reaches the desired temperature. A drop of oil is formed at the tip of the capillary. After drop formation, the valve connecting the syringe pump to the view cell is opened and CO_2 is introduced into the system and IFT measurement is initiated. The measurements are conducted until the change in the IFT value is less than 0.1 mN/m per minute. The valve connecting the syringe pump to the view cell is kept open to enable the continuous dissolution of CO_2 into the system, and to maintain a constant pressure inside the cell. A pendant drop and a standing bubble are shown in figures 3.20-A and 3.20-B, respectively. IFT measurement requires the knowledge of the densities of the participating phases, as they are incorporated into the Young-Laplace equation (3.2) through the hydrostatic pressure (Song and Springer, 1996a). The densities of the CO_2 saturated model oils and densities of CO_2 saturated brines are measured using the experimental setup presented in section 3.2.9. For the CO_2-rich fluid phase, the pure CO_2 density is assumed as obtained from the REFPROP software, which employs the GERG-2008 equation of state (Kunz and Wagner, 2012). The error in IFT resulting from using erroneous density data is discussed in section 3.2.11.2. Once measured, mixture density data are available and a density correction can always be applied to the IFT. The correction is performed using the equation below:

$$\gamma_{corr} = \gamma \frac{\Delta\rho_{corr}}{\Delta\rho} \tag{3.8}$$

where γ is the IFT as measured by the software, $\Delta\rho$ is the density difference that has been initially set in the software, and $\Delta\rho_{corr}$ is the corrected density difference according to experimentally measured densities. It is important to note that within the context of IFT evaluation, the density of CO_2-saturated SFEM and

SFE40 were not experimentally measured at elevated pressures. This is due to the limited amount of extract. Instead, an approximation method is employed. The method is elaborated in section 3.2.9.

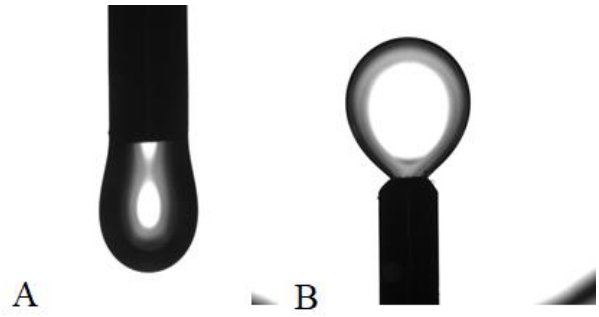

Figure 3.20 - (A) Model oil pendant drop in a CO_2 atmosphere. (B) Model oil standing drop in carbonated 3% NaCl brine, both at 8 MPa and 60 °C.

3.2.5 Wettability and Volumetric Expansion

Wettability and volumetric expansion measurements were performed using the same experimental setup described in the previous section with a drop volume resolution of 10^{-3} µl and contact angle resolution of 0.01°. For ternary systems comprising CO_2-brine-shale, the sessile drop method is employed while for quaternary systems (CO_2-brine-oil-shale), the captive bubble method is employed. The schematic diagrams of both, the sessile drop and the captive bubble methods are presented in figure 3.21 A and B.

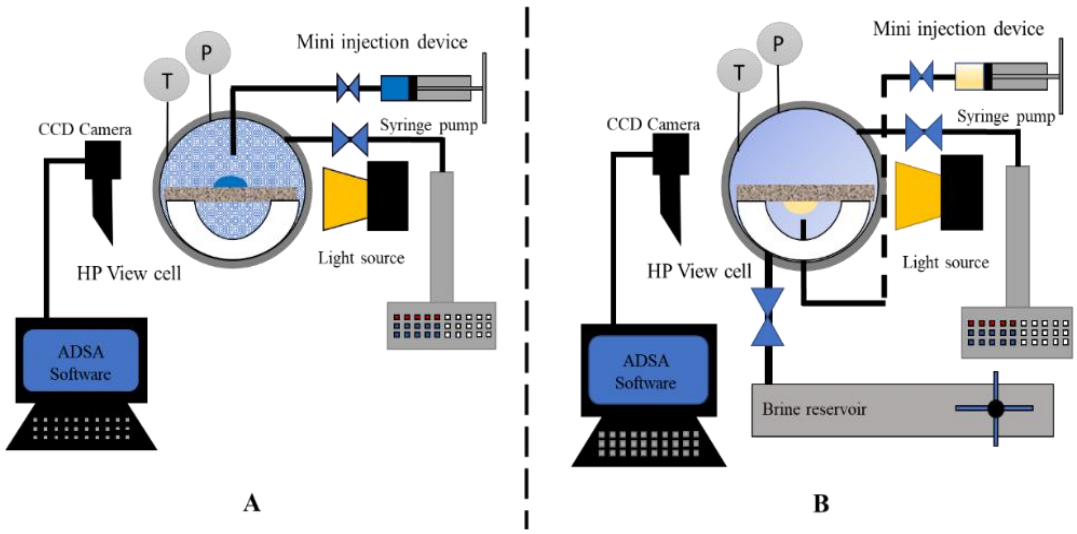

Figure 3.21 - Schematic diagram of (A) Sessile drop method. (B) Captive bubble method, adapted from (Samara and Jaeger, 2022).

The shale samples are used “as is” after breaking them from the large outcrop rock pieces without any further surface treatment in order to preserve the native characteristics of the natural rock. In sessile drop experiments, a shale sample is introduced into the view cell and supported by a PTFE sample holder. The drop forming liquid (brine) is charged into the mini injection device. The heating of the view cell is accomplished by starting the PID temperature controller and setting the desired temperature. The syringe pump is pre-pressurized with CO_2 to the desired pressure. The valve connecting the syringe pump to the view cell is opened and CO_2 is introduced into the view cell. A waiting time of 15-30 minutes ensures temperature and pressure equilibration of the system. Once equilibration is achieved, a drop of brine is introduced from the mini injection device through the tip of the moveable capillary and a liquid drop is deposited on the surface of the shale. The ADSA software creates a theoretical baseline parallel to the rock surface and offers the user the option of adjusting this baseline. The software also detects the drop profile and the three-phase contact point, where the intersection between the baseline and drop profile occurs, and it further records the contact angle. For the captive bubble method, a similar procedure as that of the standing bubble-as described in the previous section- is conducted. The difference lies in placing a shale sample inside the view cell, on which a drop of oil is deposited as the lighter phase inside a surrounding aqueous phase. Each measurement is conducted on a new untreated shale sample. The contact angles are measured in the denser phase, i.e. the aqueous phase, for both configurations and each measurement is conducted until a stable value within ±1° is reached. After each measurement, the entire system is decompressed and cleaned in preparation for the next experimental test.

Volumetric expansion of oil was measured using the captive bubble configuration and following the exact experimental procedure thereof. Quantification of the expansion was performed using the following equation:

$$V_E = \frac{V_f - V_i}{V_i} * 100 \quad (3.9)$$

where V_i and V_f are the initial and final volumes of the oil drop, respectively, in µl. Volumetric expansion was measured on a surface of a calcite crystal. The employment of the captive bubble method on the calcite crystal for quantifying the volumetric expansion serves several purposes. First and foremost, the oil drop is constrained by the presence of the aqueous phase that eliminates the possibility of light oil components to be extracted. Secondly, it aims to isolate the drop from the capillary where CO_2 diffuses and further contributes to the expansion of the oil drop attached to the needle, which would result in overestimating the volume expansion. Furthermore, measurements conducted on the surface of an oil free calcite crystal serve to isolate any interference of oil that may surface in the organic rich shale, as this oil may combine with the oil drop and disturb the measurement. In all measurements, the initial volume of the drop was kept around 25 µL in order to maintain a constant oil to water ratio and to unify the ratio of gravitational forces to interfacial forces, as described by the B_o. Additionally, experiments were conducted until equilibrium was reached, i.e. no change in drop volume was observed. Images of a sessile drop and a captive bubble are presented in figures 3.22-A and 3.22-B.

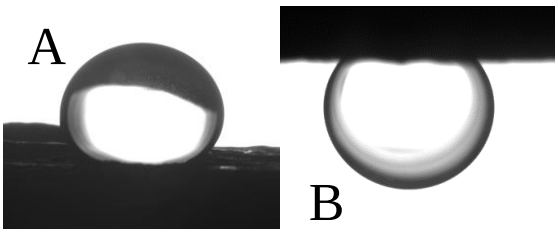

Figure 3.22 - (A) Sessile drop of 3% NaCl brine on Shale at 30 MPa and 60 °C. (B) Captive bubble of model oil on shale in carbonated deionized water at 10 MPa and 60 °C.

3.2.6 Zeta Potential

A Malvern Zetasizer (Nano-ZS – Malvern Panalytical Ltd. -United Kingdom) was used to measure the zeta potential (ζ) of shale - brine suspensions at ambient pressure and temperature. During the measurement, an electrical field is applied

across the sample due to which the charged species in the suspension move towards the oppositely charged electrode. Viscous forces tend to oppose such movement, however, once equilibrium between the two opposite forces is reached, the charged species move with a constant velocity (Charcosset, 2016). The magnitude of the velocity is dictated by the strength of the electric field. This velocity is termed the electrophoretic mobility (U_e). Henry's equation relates the electrophoretic mobility to the zeta potential by the following equation:

$$U_e = \frac{2\varepsilon\zeta f(ka)}{3\mu} \tag{3.10}$$

where ε is the dielectric constant of the medium, μ is dynamic the viscosity of the medium and *f(ka)* is the Henry function.

The suspensions were prepared following the procedure proposed by (Zhang, 2005) as follows; a steel mortar and pestle manufactured at TU Clausthal were used to powder the shale. The desired shale particles were separated by means of a vibrating sieve shaker (Retsch GmbH, Germany). The size of the particles used in the preparation of the solid-brine suspension falls below 50 μm. Shale powder was suspended in the brine at a ratio of 1:100. The suspensions were mixed using a magnetic stirrer (IKAMAG RET, IKA, Germany), were preserved in sealed containers and left to equilibrate for a few days. Prior to the measurement, a sonic probe (Sonoplus HD 60, Bandelin GmbH, Germany), operated at the highest setting, was used to mix the suspensions for 1 minute. The suspensions were left for 20 to 30 minutes to settle and then the measurements were conducted. Furthermore, the pH was measured directly before each measurement and the respective values were recorded. Each measurement was conducted 3 times and the average zeta potential value was calculated. The preparation of the suspensions and the consequent measurements were conducted at ambient conditions in an open system where the dissolution of CO_2 from the ambient air - partial pressure of CO_2 (pCO_2)- was not controlled.

3.2.7 Adsorption

A spherical shale sample of a diameter of 8.3 mm was subject to the adsorption measurements. The sample had already undergone extraction with supercritical CO_2 in order to minimize the impact of the moisture content, which may occupy the adsorption sites, as well as the impact of free hydrocarbons, that may be extracted by the CO_2 during adsorption measurements or in which CO_2 may dissolve (Klewiah et al., 2020). The adsorption on the shale sample was measured using a magnetic suspension balance (MSB) (Rubotherm GmbH, Germany). The MSB has a maximum allowable operating pressure of 45 MPa, a maximum temperature of 150 °C and a resolution of 10 μg. The MSB comprises an analytical balance connected to an electromagnet, both located outside of the measurement cell and are subject to atmospheric conditions. The measurement cell (i.e. adsorption chamber), where the measurement takes place at the designated pressure and temperature conditions, comprises a permanent magnet with a lifting rod, a sensor core, a sensor coil and a load coupling system that connects the sample crucible to the permanent magnet. The electromagnet which hangs from the hook of the analytical balance serves to maintain the permanent magnet in a state of suspension during operation. The position of the permanent magnet is controlled by means of the sensor coil (position transducer) which sends feedback signals to the PID controller on the position of the permanent magnet. Accordingly, the PID controller indicates a change in the current supplied to the electromagnet in order to restore the position of the permanent magnet. The force transmitted to the balance through the electromagnetic coupling is measured and is recorded as mass. More information about the method can be found in (Weireld et al., 1999). The schematic diagram of the MSB is presented in figure 3.23 below.

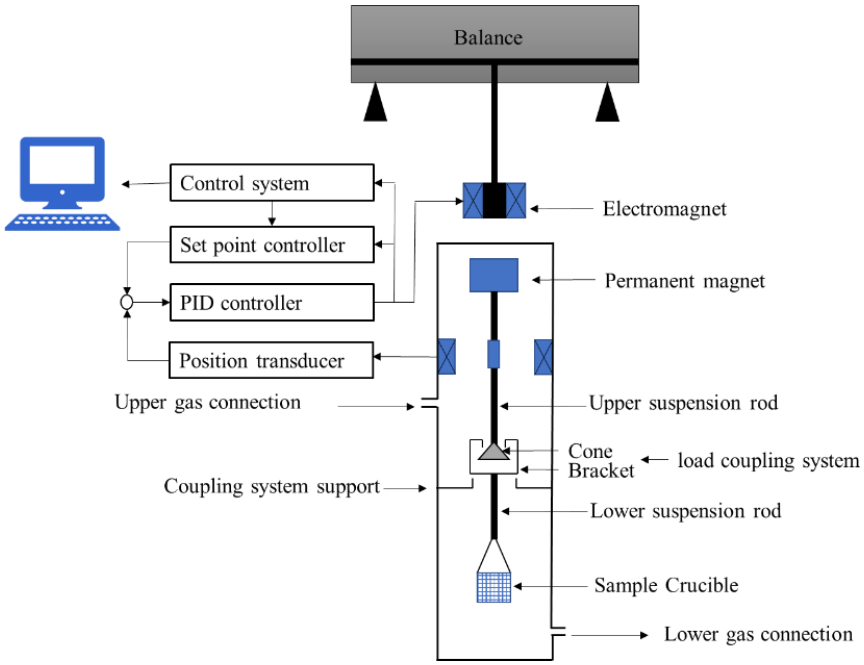

Figure 3.23 - Schematic diagram of the magnetic suspension balance.

There are 3 different measurement positions of the permanent magnet and the load coupling system; off, zero-point and measuring-point positions. When the off position is selected, the coupling system (cone and bracket) rest on the coupling system support and therefore no mass measurement takes place (See figure 3.24-A). In the zero-point position, the permanent magnet is in a suspended state such that the cone neither rests on the bracket (and the support) nor is it in contact with the upper part of the bracket, it rather levitates between both the top and bottom parts of the bracket (See figure 3.24-B). This position reads the mass of the permanent magnet and is usually tared. In the measuring point position, the permanent magnet is further lifted and by means of the coupling system (cone and bracket) the sample crucible is also lifted through the lower rod connected to the bracket (See figure 3.24-C). The mass recorded at the measuring point position yields the mass of the crucible, the lower rod and the mass of the bracket.

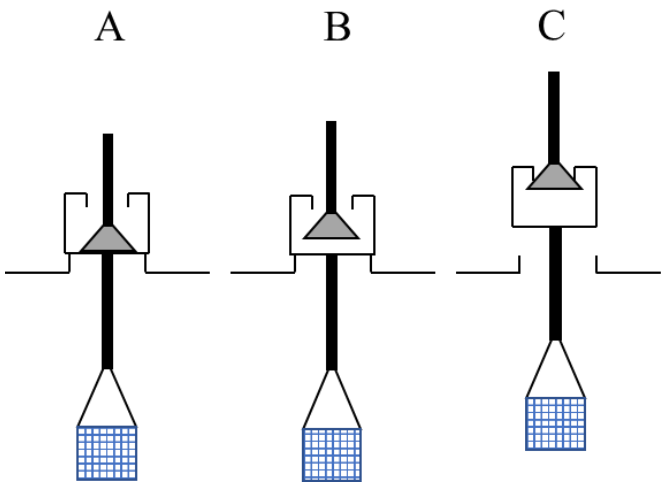

Figure 3.24 - The different positions of the coupling system. (A) Off. (B) Zero point. (C) Measuring point.

Initially, the sample is loaded into the crucible and hung on the lower lifting rod in the off position. The zero-point position is selected where the permanent magnet, and therefore the cone, is lifted. The MSB is tared (set to zero). Afterwards, the measuring point position is selected. This is done at atmospheric conditions and before closing the measurement cell to ensure the proper placement and alignment of the system components. The off position is chosen again and the measurement cell is then closed tightly. After closure, the zero point is selected and the MSB is tared and afterwards it is set to the measurement point.

Valve C (V_C) in figure 3.25 connects the measurement cell to a vacuum pump. The intention behind the application of vacuum is to remove any preabsorbed gas and/or moisture on the shale. At this point, valve B (V_B) and valve D (V_D) are closed. Vacuum is applied until a constant mass reading from the software is attained. Once this is accomplished valve C is closed.

A pneumatic membrane gas compressor (Nova swiss, Switzerland) with a maximum operating pressure of 100 MPa is used to charge CO_2 into a titanium accumulator (Prolight-Proserv, Norway). The accumulator has a volume of 629 cm^3 and maximum pressure and temperature of 69 MPa and 177 °C, respectively. Charging of the accumulator is accomplished through valve A (V_A) - valve B (V_B)

is closed. The accumulator is heated by means of a circulating heating bath (MC4, Julabo GmbH, Germany). The use of the accumulator serves to heat the CO_2 to the designated temperature before it is introduced into the measuring cell. The accumulator is pressurized to a higher pressure than the pressure at which the adsorption is intended to be measured. This is to compensate for the pressure loss due to gas expansion into dead volumes in the high-pressure lines and into the measurement cell. The measurement cell is also heated to the designated experimental temperature by means of a circulating heating bath (MC4, Julabo GmbH, Germany). The temperatures inside both the measurement cell and the accumulator are measured with a type k thermocouple of an accuracy of ±0.5 °C and the pressures are measured by means of pressure transducers with an accuracy of ±0.02 MPa. Valve V_B is opened and CO_2 flows from the accumulator into the measurement cell. After the designated pressure is reached in the measurement cell, V_B is closed. The software records the increase in sample weight as a function of time (adsorption kinetics) and records the measurement pressure and temperature.

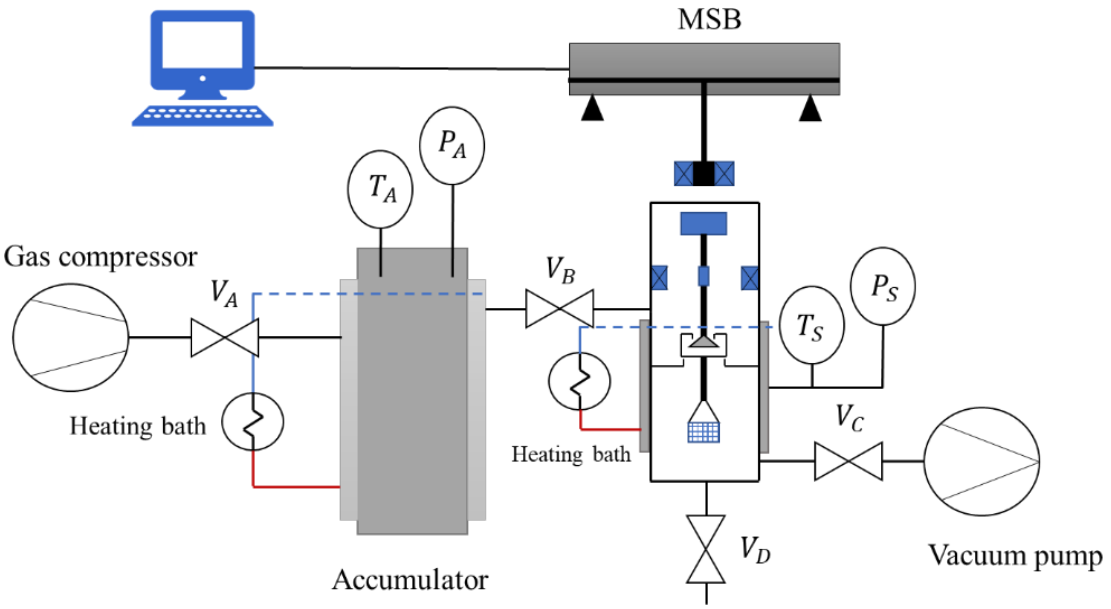

Figure 3.25 - Experimental setup of gas adsorption measurements, adapted from (Samara et al., 2022b).

In the gravimetric sorption measurement method, the net increase in mass uptake is a superposition of two forces; the adsorption of gas molecules on the adsorbent (positive), and the buoyancy force that acts against the latter (negative) (Gasparik et al., 2014). The forces are given in the below equations (Wu et al., 2019):

$$F_w = (m_{sys} + m_s + m_{ads}).g \quad (3.11)$$

where F_w is the gravitational force acting on the system, m_{sys} is the mass of MSB system components, m_s is the mass of the sample and m_{ads} is the mass of the adsorbed layer (also referred to as absolute adsorption).

$$F_B = \left(V_{sys} + V_s + V_{ads}\right)\rho_{bulk}.g \quad (3.12)$$

where F_B is the buoyancy force acting on the system, V_{sys} is the volume of MSB system components and V_s is the volume of the original sample, V_{ads} is the volume of the adsorbed layer and ρ_{bulk} is the density of the bulk phase.

$$m_{MSB} = \frac{F_W - F_B}{g} = m_{sys} + m_s + m_{ads} - \left(V_{sys} + V_s + V_{ads}\right)\rho_{bulk} \quad (3.13)$$

where m_{MSB} is the measured mass as indicated by the MSB.

$$m_{ads} = m_{MSB} - m_{sys} - m_s + \left(V_{sys} + V_s + V_{ads}\right)\rho_{bulk} \quad (3.14)$$

Excess adsorption (m_{ex}) is defined as:

$$m_{ex} = m_{MSB} - m_{sys} - m_s + \left(V_{sys} + V_s\right)\rho_{bulk} \quad (3.15)$$

From equations 3.14 and 3.15, the relation between absolute and excess adsorption is given by:

$$m_{ads} = m_{ex} + V_{ads}\rho_{bulk} \quad (3.16)$$

Since the volume of the adsorbed layer is calculated by:

$$V_{ads} = \frac{m_{ads}}{\rho_{ads}} \quad (3.17)$$

Equation 3.16 can be rewritten as:

$$m_{ads} = \frac{m_{ex}}{1-\frac{\rho_{bulk}}{\rho_{ads}}} \quad (3.18)$$

The term $(1 - \frac{\rho_{bulk}}{\rho_{ads}})$ is often termed the conversion coefficient (Qi et al., 2019; Wu et al., 2021) and directly relates the absolute adsorption to the excess adsorption. In the approach employed in this work, the terms m_{sys}, m_s and the buoyancy effect on the sample and any of the system components are assumed to be constant over the entire test duration. In this way, the excess amount of CO_2 (m_{ex}) can be deduced by subtracting the initial MSB reading from subsequent MSB readings, all under test conditions. Physically it is not possible to establish the test conditions instantaneously at the start of the test. Therefore, a linear extrapolation is performed over a short time of 2-3 minutes that results in a slight underestimation of the sorption values. the mass of adsorbed CO_2 is given by equation 3.19:

$$\Delta m_{MSB} = m_{\mathrm{ex}} \quad (3.19)$$

The adsorption capacity is defined as the ratio of the mass of adsorbed CO_2 -or amount in mmol - to the initial mass of the sample (Wang et al., 2022). To illustrate how the adsorption capacity is calculated, adsorption at experimental conditions of 10.7 MPa and 60 °C is chosen. The adsorption kinetics is exemplarily depicted in figure 3.26. At equilibrium, the mass of adsorbed CO_2 is measured to be 0.017 g. The initial mass of the rock sample is 0.62965 g. The adsorption capacity is calculated to be 2.7% (i.e. g CO_2/ 100 g shale), which corresponds to 0.61 mmol CO_2/g shale.

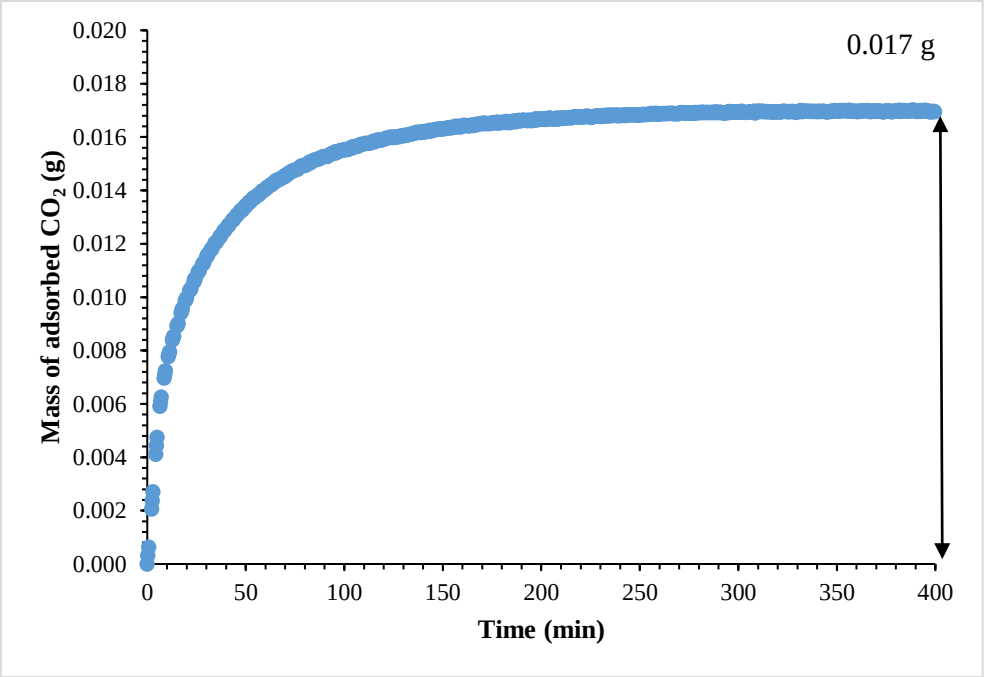

Figure 3.26 - CO_2 adsorption kinetics on Sultani shale at 10.7 MPa and 60 °C.

3.2.8 Diffusion

The measurement of CO_2 diffusion relies on the adsorption kinetics as recorded by the MSB. Based on Fick's law of diffusion, an analytical approach proposed by (Crank, 1975) describing the non-stationary diffusion of a gas into a solid sphere is applied. This is done under the assumption that the shale is a homogeneous poreless but a gas permeable solid. The analytical approach is presented in equation 3.20 below:

$$\frac{M_t}{M_\infty} = 1 - \frac{6}{\pi^2}\sum_{n=1}^{\infty}\frac{1}{n^2}\exp(-Dn^2\pi^2\, t/r^2) \qquad (3.20)$$

M_t/M_∞ is the mass uptake of CO_2 as a function of time t related to the equilibrium value, r is the radius of the solid sphere, D is the diffusivity and n the running index of the series. The curve fitting approach is used as follows: a theoretical adsorption kinetics curve is created using equation 3.6 and the diffusivity is adjusted until the theoretical curve agrees with the experimental data curve as shown in figure 3.27 below.

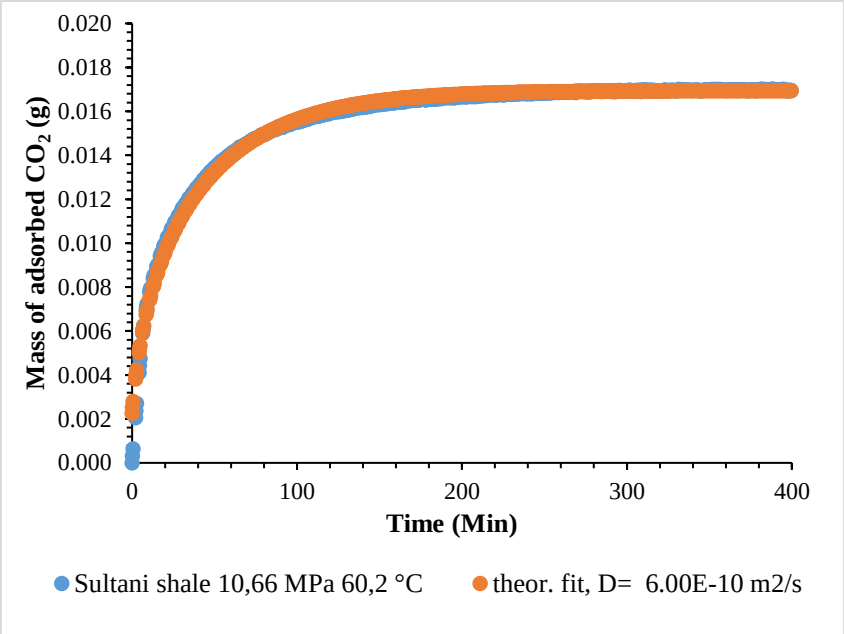

Figure 3.27 - Calculation of the apparent diffusion coefficient by adjusting the parameter D in equation 3.6.

3.2.9 Density

Density measurements are carried out using an oscillating tube densitometer (DMA-HPM, Anton Paar-Austria) with a maximum operating pressure and temperature of 140 MPa and 200 °C, respectively. The densitometer has a resolution of $\pm 1 \times 10^{-5}$ g/cm^3. The U-shaped Hastelloy tube of the equipment is subject to excitation and vibrates at a certain frequency which depends on the density of the sample, and the specific characteristics of the oscillating tube. Within the densitometer, a mathematical conversion is established to relate the oscillation frequency, or time period of oscillation, to the sample density at the designated temperature and pressure. A wide range calibration of the densitometer at several temperatures and pressures is performed using two fluids of known densities, namely water and nitrogen, to set the calibration constants of the equipment. For instance, at atmospheric pressure, these constants and the time period of oscillation are related to the density through equation 3.21.

$$\rho = A\tau^2 + B \qquad (3.21)$$

where ρ is the density of the sample in g/cm^3, τ is the oscillation period in μs and A and B are calibration constants. Many more calibration constants are needed for calibrating the equipment at elevated pressures. Further information about the oscillating tube method can be found in (Rechberger et al., 2019). The densitometer is coupled with a high-pressure injection unit for handling gas saturated liquids (HP-dens-700-HC, Eurotechnica GmbH, Germany). The unit has a maximum operating pressure and temperature of 70 MPa and 150 °C, respectively. The pressure is measured by means of a pressure transducer with an accuracy of ±0.01 MPa. Temperature is measured using a type K thermocouple with an accuracy of ±0.5 °C. Heating of the densitometer is accomplished using a thermostatic bath (CC-K6, Huber AG, Germany) with an accuracy of ± 0.02 °C. The system is placed inside a temperature-controlled oven to ensure temperature homogeneity among all system components, including the solution saturation vessel. Temperature variation within the oven is maintained within ±1 °C of the desired value. An automatic syringe pump (D100, Teledyne ISCO, United States) is used to pressurize CO_2 and transfer it into the saturation vessel. The schematic diagram of the experimental setup is presented in figure 3.28.

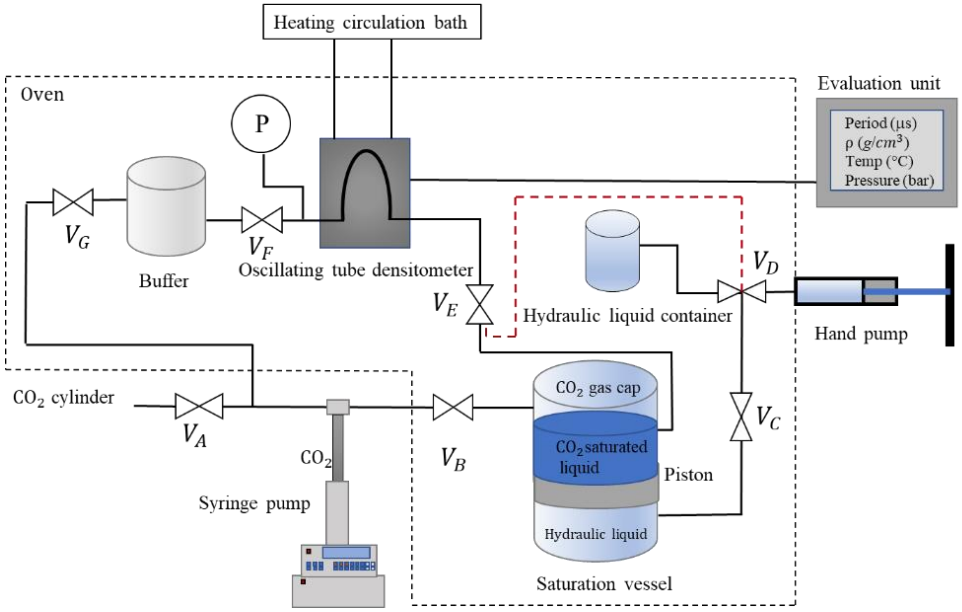

Figure 3.28 - Schematic diagram of density measurement setup, adapted from (Samara et al., 2022a).

Measurements of pure phase densities are performed by directly charging the hand pump with the liquid of interest. The hand pump is then used to transfer the liquid into the densitometer and to pressurize it inside the measurement cell. This configuration is indicated by the red dashed line in figure 3.28. For measuring the densities of CO_2-saturated liquids, the setup is modified as indicated in figure 3.28. The saturation vessel is charged with the liquid of interest, then tightly closed. The syringe pump is pre-pressurized to the designated pressure and valve B is opened for CO_2 to flow into the saturation vessel (valve C and E, closed). Valve B is kept open to ensure the continuous flow of CO_2 until the liquid is completely saturated. The saturation period lasts up to 48 hours and the saturation vessel is rocked regularly to ensure mixture homogeneity. For conducting the measurement, valve B is closed and the hand pump is used to push a hydraulic liquid (water) “through valve C” into the bottom of the saturation vessel where a piston is placed. The piston movement transfers the CO_2-saturated liquid into the measurement cell through valve E. The buffer vessel serves to maintain the pressure constant during the fluid displacement process such that no pressure loss occurs, and therefore a consequent phase separation is avoided. The density is displayed by the evaluation unit and recorded along with the corresponding pressures and temperatures.

Since experimentally measured CO_2-saturated phase densities (model oil and Hexadecane) exhibit linearity, a regression model was created to infer the densities of CO_2-saturated SFEM, SFE40 and dodecane. The densities of the SFEM and SFE40 were measured at atmospheric conditions. Then the slope of the regression model created earlier was used to calculate the CO_2-saturated binary mixture densities. This was also performed for dodecane, however the density thereof at atmospheric pressure and 60 °C was obtained from NIST (Lemmon and Huber, 2004).

3.2.10Solubility

3.2.10.1 Solubility of Carbon Dioxide in the Aqueous Phase

The solubility of CO_2 in brines containing NaCl is calculated using the model proposed by (Duan et al., 2006). Duan's model can be applied for NaCl brines and more complex brines containing various cations such as Ca^{2+}, Mg^{2+}, K^+ and anions such as Cl^- and SO_4^{2-}. The modelling equation is presented below:

$$ln\, m_{CO2} = \ln y_{CO2}\, \varphi_{CO2} P - \frac{\mu_{CO2}^{1(0)}}{RT} - 2\lambda_{CO2-Na}\left(m_{Na} + m_K + 2m_{Ca} + 2m_{Mg}\right) - \xi_{CO2-Na-Cl}\, m_{Cl}\left(m_{Na} + m_K + m_{Mg} + m_{Ca}\right) + 0.07 m_{SO4} \quad (3.22)$$

where y_{CO2} is the mole fraction of CO_2 in the vapor phase and is calculated using equation 3.23 under the assumption that the vapor pressure of water in the vapor mixture is the same as the saturation pressure of pure water:

$$y_{CO2} = \frac{[P - P_{H2O}]}{P} \quad (3.23)$$

P is the pressure of interest in bar. The water vapor pressure can be calculated with the equation below using the critical pressure and temperature of water; 221 bar and 647.14 K, respectively.

$$P_{H2O} = \left[\frac{P_{c,H2O} T}{T_{c,H2O}}\right][1 - 38.640844(-t)^{1.9} + 5.8948420t + 59.876516t^2 + 26.654627t^3 + 10.637097t^4] \quad (3.24)$$

where $t = \frac{T - T_{c,H2O}}{T_{c,H2O}}$ (3.25)

The fugacity coefficient of carbon dioxide in the liquid phase (φ_{CO2}) is calculated using equation 3.26 using parameters $b_1 - b_{15}$:

$$\varphi_{CO2} = b_1 + \left[b_2 + b_2 T + b_3 T + b_4/T + \frac{b_5}{(T-150)}\right] P + [b_6 + b_7 T + b_8/T] P^2 + [b_9 + b_{10} T + b_{11}/T] \ln P + \frac{[b_{12} + b_{13} T]}{P} + \frac{b_{14}}{T} + b_{15} T^2 \quad (3.26)$$

The calculation of the fugacity coefficient depends on parameters $b_1 - b_{15}$ which are region specific, i.e. the parameters utilized to calculate the CO_2 fugacity coefficient vary for each region in the CO_2 phase diagram as shown in figure 3.29.

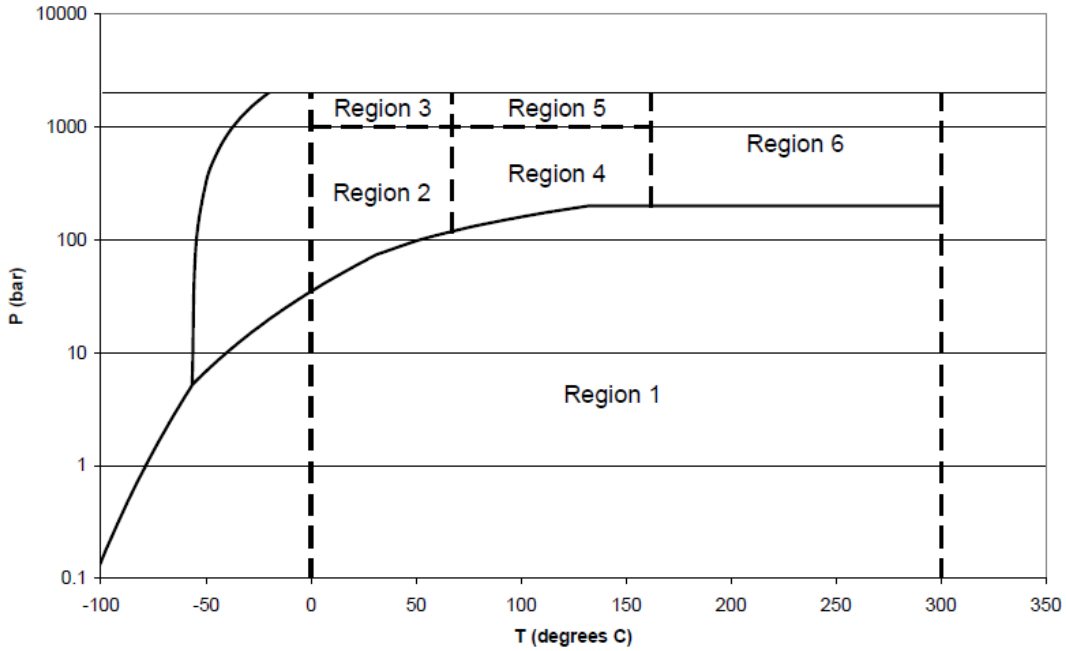

Figure 3.29 - Regions of CO_2 fugacity coefficient calculation in CO_2 phase diagram, adapted from (Hangx, 2005).

Since the experimental brine density measurements were conducted at pressures and temperatures that satisfy the constraints of only two out of the six regions, only the parameters concerning these regions are reported in this work as tabulated in Appendix A - Table A.1.

Constraints of region 1: 305 K < T < 405 K, P_1=75+(T-305) x 1.25, this region is used for the calculation of fugacity coefficients up to 110 bars at 60 °C.

Constraints of region 2: 273 K < T <340 K, P_1<P<1000 bar. This region is used for the calculation of the fugacity coefficient at pressures equal to or higher than 110 bars at 60 °C.

In equation 3.22, λ_{CO2-Na} is the interaction parameter between CO_2 and Na^+, $\xi_{CO2-Na-Cl}$ is the interaction parameter between CO_2, Na^+ and Cl^- and $\mu_{CO2}^{1(0)}$ is the standard chemical potential of CO_2 in the liquid phase (Duan et al., 2006). These

parameters are determined using equation 3.27 (Duan and Sun, 2003). The constants thereof are listed in Appendix A-Table A.2.

$$Parameter(T,P) = C_1 + C_2T + \frac{C_3}{T} + C_4T^2 + \frac{C_5}{630-T} + C_6P + C_7PlnT + \frac{C_8P}{T} + \frac{C_9P}{630-T} + \frac{C_{10}P^2}{(630-T)^2} + C_{11}TlnP \quad (3.27)$$

3.2.10.2 Solubility of Carbon Dioxide in the Oleic Phase

The solubility of CO_2 in the oil phase is inferred from both density and volumetric expansion measurements using the following approach. The density of the CO_2 saturated oil (ρ_{o+CO_2}) is expressed in equation 3.28 below in terms of the initial mass of the oil drop (m_o), the mass of dissolved CO_2 in the oil drop (m_{CO_2}), the initial volume of the oil drop (V_o) and the volume increase due to CO_2 dissolution (V_{CO_2}):

$$\rho_{o+CO_2} = \frac{m_o + m_{CO_2}}{V_o + V_{CO_2}} \quad (3.28)$$

The ratio of the final drop volume ($V_o + V_{CO_2}$) to the initial drop volume drop (V_o) is given by:

$$\nu = \frac{V_o + V_{CO_2}}{V_o} \quad (3.29)$$

where ν is related to the volumetric expansion V_E as defined in equation 3.9 in section 3.2.5 by:

$$\nu = 1 + V_E \quad (3.30)$$

where V_E is expressed in (%). Substituting equation 3.29 into equation 3.28 yields:

$$\rho_{o+CO_2} = \frac{m_o + m_{CO_2}}{V_o * \nu} = \frac{m_o}{V_o * \nu} + \frac{m_{CO_2}}{V_o * \nu} \quad (3.31)$$

Since $\rho_o = \frac{m_o}{V_o}$, being the density of the pure oil at the relevant pressure without CO_2, equation 3.28 can be expressed as:

$$\rho_{o+CO_2} = \frac{\rho_o}{\nu} + \frac{m_{CO_2}}{V_o * \nu} \quad (3.32)$$

Rearranging equation 3.32 and substituting for $V_o = \frac{m_o}{\rho_o}$ yields the following:

$$\frac{m_{CO_2}}{m_o} = \frac{\rho_{o+CO_2}}{\rho_o} * \nu - 1 \quad (3.33)$$

where $\frac{m_{CO_2}}{m_o}$ is the solubility of CO_2 in the oil phase in g CO_2/g oil. Throughout this work, the solubility is expressed in g CO_2/100 g oil, which is obtained by multiplying the numerator and the denominator of the left-hand side in equation 3.33 by 100.

3.2.11Error Analysis

In this section, an extensive analysis is performed on possible error sources and their impact on the presented experimental work in order to be able to evaluate factors of influence and judge the relevance of the results. General statements shall only be made when artefacts can be excluded.

3.2.11.1 Supercritical Extraction

A key result of the supercritical fluid extraction is the yield, i.e. mass of oil extracted ($m_{oil\text{-}ext}$). This mass would ideally be equal to the difference between the mass of the shale before and after extraction (Δm_{shale}). However, there exists differences between these two values which can be justified as follows: Firstly, the amount of extracted oil retained in the high-pressure tubing during the extraction. Secondly, the light fractions of the oil that are indeed extracted yet are lost due to evaporation or are flushed out with CO_2 upon opening the separator valve to collect the extracted oil. The maximum relative error is found in extraction experiments where the yield is very low, summing up to about ±34% and a minimum relative value of ±13% at higher yields. Further sources of error are the accuracy in measuring the temperature and pressure which is negligible in comparison.

3.2.11.2 Interfacial Tension

The factors of influence associated with errors in determining the IFT at elevated pressures can be categorized as follows:

- Errors associated with operating conditions.

The temperature was measured with an accuracy of ± 0.5 °C, the accuracy of the pressure transducer is ±0.01 MPa.

- Errors associated with the density difference of participating phases.

The measurement of IFT relies on the proper measurement of the densities of the coexisting phases. Uncertainty in IFT values may stem from the fact that the pure or unsaturated phase densities are used in calculating the density difference instead of CO_2-saturated phase densities. Such uncertainty amounts to a maximum of ±1% at low pressures and increases to ±4% at 20 MPa due to a decreasing density difference ($\Delta\rho$) as the pressure increases. The impact of the density difference on IFT based on pure and saturated phase densities is demonstrated in figure 3.30. Therefore, it can be stated that for a valid estimate of IFT, in several cases, e.g. process design, pure phase densities may be used.

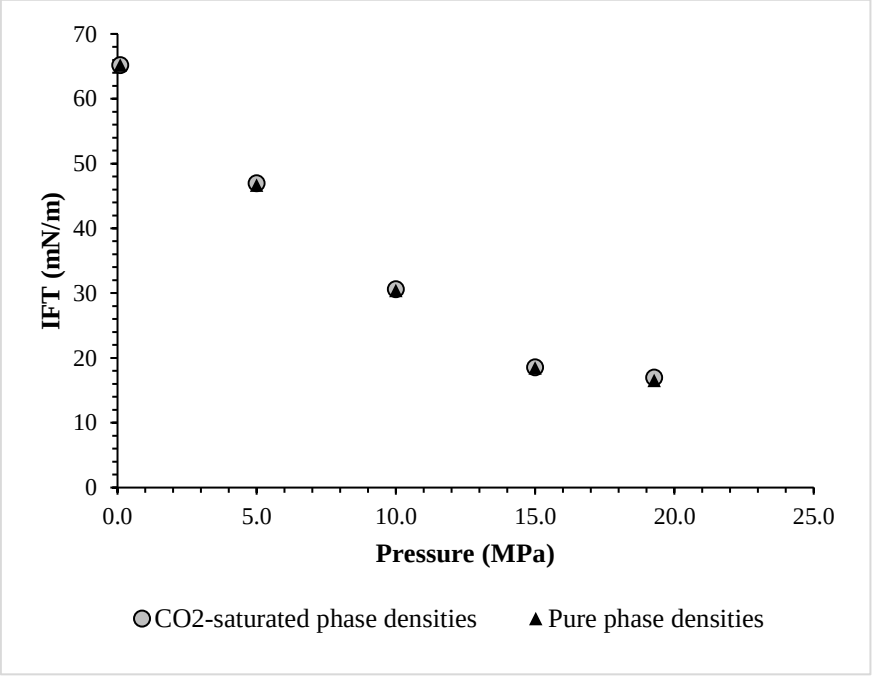

Figure 3.30 - The difference in IFT values measured using pure phase densities and CO_2-saturated phase densities for 3% NaCl brine at 60 °C.

- Errors associated with the uncertainty in the numerical analysis involving the drop shape.

According to (Song and Springer, 1996a, 1996b) the highest accuracy of the method is achieved when the shape factor, indicating the "sphericity of the drop" falls between 0.6 and 0.7. Shape factors lower than 0.5 are the result of drop profiles being too spherical, while shape factors higher than 0.7 are due to drop profiles being too short or slim as represented in figure 3.31. Higher or lower shape factor values could considerably increase the error. For IFT values higher than 10 mN/m, the shape factor can be maintained within the given range with a maximum uncertainty in IFT of ±1%. However, as the pressure increases and lower absolute IFT values (<10 mN/m) are retrieved, the shape factor falls out of its desirable range and the uncertainty of the measurement increases to around ±5% (Guo and Schechter, 1997).

Figure 3.31 - Oil droplet in a CO_2 atmosphere (A) Shape factor =0.68 at moderate pressure. (B) Shape factor = 0.80 at elevated pressure.

- The presence of contaminants in the system.

Measurements of IFT are highly susceptible to contaminations particularly when an aqueous phase is present in the system. Therefore, prior to measurements the system is thoroughly cleaned and is verified to be contaminant free by performing a measurement of water-air surface tension using the pendant drop method at ambient conditions. The surface tension of water at ambient conditions lies between 72-73 mN/m (Vargaftik et al., 1983). This value is always verified prior to each measurement series. It is practically impossible to make a general quantitative statement on the impact of contamination on the overall uncertainty.

The combined standard uncertainty $U_c(\gamma)$ is calculated using the law of propagation of uncertainty as reported in (Taylor and Kuyatt, 1994):

$$U_c{}^2(\gamma) = \left(\frac{1}{\gamma}\left(\frac{\partial \gamma}{\partial T}\right)_{P,m_s} u(T)\right)^2 + \left(\frac{1}{\gamma}\left(\frac{\partial \gamma}{\partial P}\right)_{T,m_s} u(P)\right)^2 + \left(\frac{1}{\gamma}\left(\frac{\partial \gamma}{\partial m_s}\right)_{P,T} u(m_s)\right)^2 + \left(\frac{u(\Delta\rho)}{\Delta\rho}\right)^2 + \left(\frac{\sigma(\gamma)}{\gamma}\right)^2 \quad (3.34)$$

where $u(T)$, $u(P)$, $u(m_s)$ and $u(\Delta\rho)$ are the corresponding relative uncertainties in temperature, pressure, molality of the salt and density, respectively. $\sigma(\gamma)$ is the standard deviation at the measured point, calculated based on a minimum of 3 repeated measurements. In CO_2- oil systems, the relative uncertainty of molality was eliminated from the above equation as no aqueous phase is involved. All in all, accounting for all the previous error sources, in binary CO_2-brine systems, the combined uncertainty amounts to 1.1%. In binary CO_2-oil systems, the combined uncertainty at the low-pressure range amounts to 1.4%, and at the high-pressure range it increases to ±5 %. For ternary systems, the maximum combined uncertainty in IFT measurement is calculated to be around ±3%. For 95% level of confidence (k=2), the expanded relative uncertainties are 2.2, 2.8, 10 and 6% respectively.

3.2.11.3 Wettability and Volumetric Expansion

Errors associated with the wettability assessment mainly stem from the use of non-ideal surfaces with varying surface roughness. In this work, wettability assessment was performed on natural, untreated, unmodified (neither chemically nor mechanically) shale samples. Since shale is fissile and laminated, it readily splits into thin flat pieces of a thickness ranging between 0.5-1 cm upon pounding with a hammer and a broad-bladed steel chisel. The maximum uncertainty in contact angle associated with the surface roughness in the case of shale is in the range of ± 3°. The uncertainty in determining the baseline (tangent line) may have a significant impact on the measured values of contact angles. This uncertainty depends on the resolution of the camera, the magnification applied as well as the

tilt. While these were held constant throughout the related measurements, the maximum uncertainty associated with the baseline placement amounts to ± 2°.

Additionally, error may stem from the size of the liquid drop deposited on the surface of the solid. The Bond number is a unitless quantity that relates the gravitational forces to the surfaces forces and is calculated using equation 3.7 in section 3.2.4.

High bond numbers indicate that gravitational forces dominate and the drops sag, which may result in over or under estimating the contact angle depending on the configuration in use (sessile versus captive). On the other hand, low bond numbers are indicative of the domination of surface forces where spherical drops are formed in the absence of gravity, which is not representative of a realistic scenario. Experimental measurements were performed at 10 MPa (CO_2 pressure) and 60 °C in deionized water to infer the change in contact angle upon varying the drop size. Using equation 3.21, the optimal drop size was designated in the range of 15-25 µl, where the contact angle exhibits a reduced dependency on the drop volume. This, however, is out of the scope of the current study but further details can be found in (Samara and Jaeger, 2022). The maximum uncertainty in contact angle due to the drop volume is in the range of ± 5°. The uncertainty in volumetric expansion is less than ±1%, and mainly results from the imprecision in placing the baseline correctly.

3.2.11.4 Density

Errors in density measurement can result from the erroneous calibration of the instrument, a procedure where two fluids of known densities are used to set the calibration constants of the densitometer. The uncertainty in calibration was investigated by running a validation experiment where the density of pure water was measured at 60 °C as a function of pressure and the values were compared to the densities calculated with NIST (Wagner and Pruß, 2002). The deviation from

NIST values over the entire range of interest was calculated to be less than 1%. The results of the validation experiment are presented in figure 3.32 below.

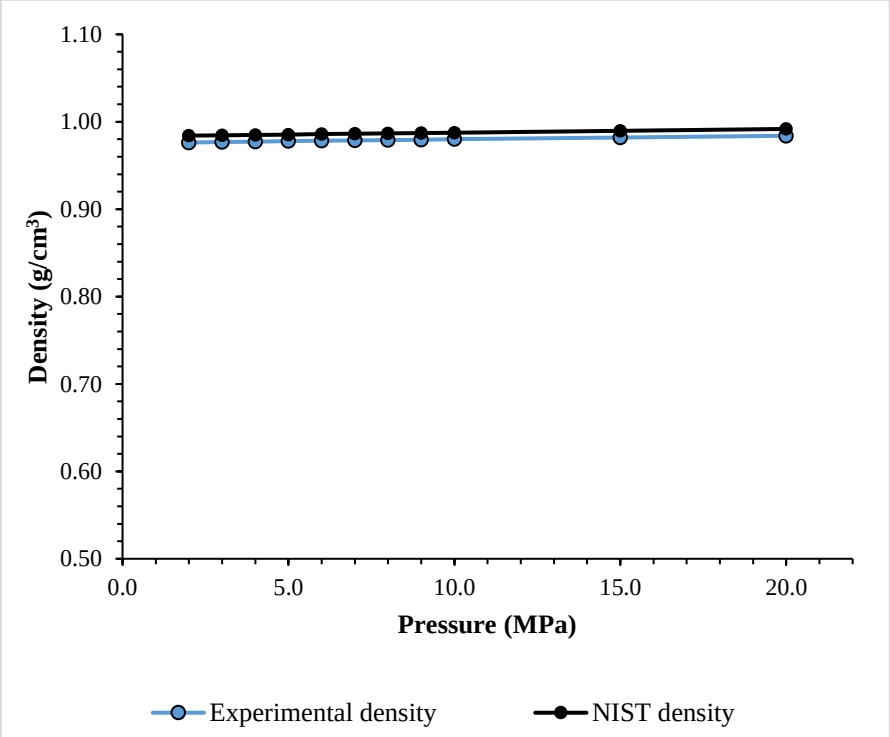

Figure 3.32 - Experimental and NIST densities of pure water as a function of pressure at 60 °C.

Additionally, errors may stem from corresponding standard uncertainties in pressure and the standard deviation of density of the measured point as shown in equation 3.35:

$$U_c{}^2(\rho) = \left(\frac{1}{\rho}\left(\frac{\partial\,\rho}{\partial\,P}\right)_{m_s} u(P)\right)^2 + \left(\frac{1}{\rho}\left(\frac{\partial\,\rho}{\partial\,m_s}\right)_{P} u(m_s)\right)^2 + \left(\frac{\sigma(\rho)}{\rho}\right)^2 \qquad (3.35)$$

For non-aqueous solutions the second term of the above equation is eliminated. For 95% level of confidence (k=2), the expanded relative uncertainty is less than ±1%. A further source of error that has to be considered for the density measurements of two-phase systems in thermodynamic equilibrium is the uncertainty of the time required to establish mutual saturation of the phases within the saturation vessel. Accordingly, a saturation test was performed to estimate the time period required for a liquid to be fully saturated with CO_2. An oil sample was saturated for 28 hours. After this period, density measurements were conducted

every two hours and the saturation period was extended until the measured density values became stable as depicted in figure 3.33. Further uncertainty maybe introduced due to phase separation during charging of the oscillating tube with the mixture due to a sudden pressure drop. Therefore, a buffer vessel was added to maintain the pressure at the outlet of the oscillating tube to prevent pressure drop and the consequent phase separation.

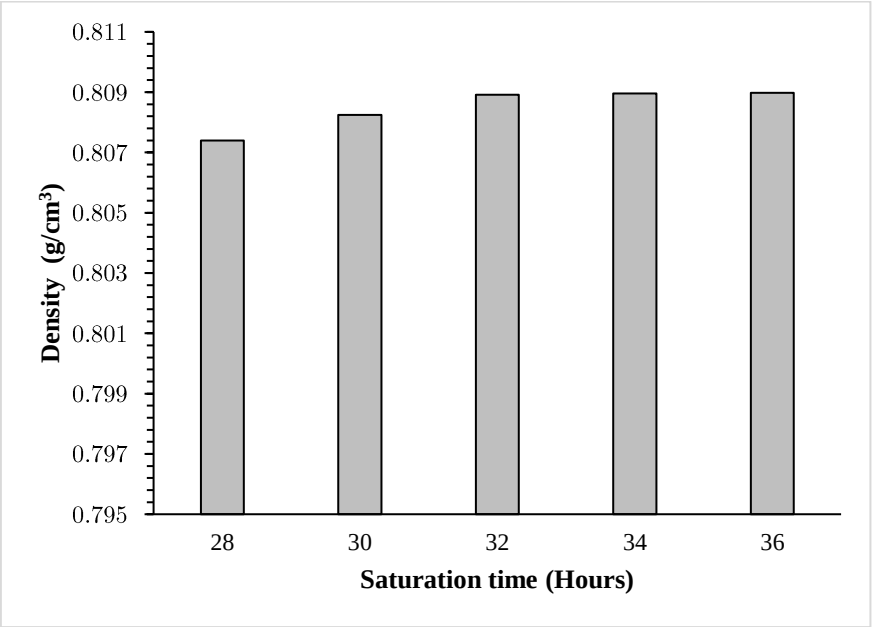

Figure 3.33 - Density of model oil saturated with CO_2 at 20 MPa as a function of saturation time.

3.2.11.5 Adsorption and Diffusion

The errors associated with measurement of CO_2 adsorption and the diffusion coefficient are attributed to the uncertainty in pressure and temperature readings, uncertainty of the starting weight signal, buoyancy effects, the extraction of soluble matter by $scCO_2$ and humidity. The pressure is determined by calibrated pressure sensors at an accuracy of ±0.02 MPa. The temperature is determined by thermocouples with an accuracy of ±0.5 °C. Therefore, the uncertainty associated with pressure and temperature amounts to less than ±1%. Directly after pressurizing the autoclave, the mass measurements are subject to an error which stems from the time needed for pressure and temperature equilibration. The error associated with this phenomenon is considered the most important, where a

deviation of -5% is possible, i.e. the real adsorbed CO_2 mass- in other words, the difference between the initial mass reading and final mass reading- could be up to 5% higher. The error resulting from buoyancy was not corrected. In this work, the reported results are those of the excess and not the absolute adsorption isotherms (see section 5.2). Last but not least, as the sample is placed in an atmosphere of pressurized CO_2, the extraction of fluids present in the sample pores by means of sc-CO_2 may lead to a lower apparent adsorption. To eliminate the error associated with this process, the tests are conducted on samples that have already undergone extraction prior to sorption measurements. Altogether, the uncertainty in the sorption and diffusivity data is in the range of –1 to +6 %.

4. Supercritical Fluid Extraction

Sultani shale underwent extraction with supercritical CO_2 at different conditions. The extraction kinetics are depicted in figure 4.1. The kinetics are expressed in terms of the yield- defined as the ratio of the cumulative mass of extract over time to the mass of the shale batch before extraction (wet basis) – and calculated using equation 4.1:

$$Y(t) = \frac{\sum_{t=1}^{n}(mass\ of\ collected\ oil)_t}{Mass\ of\ batch\ before\ extraction} x100 \qquad (4.1)$$

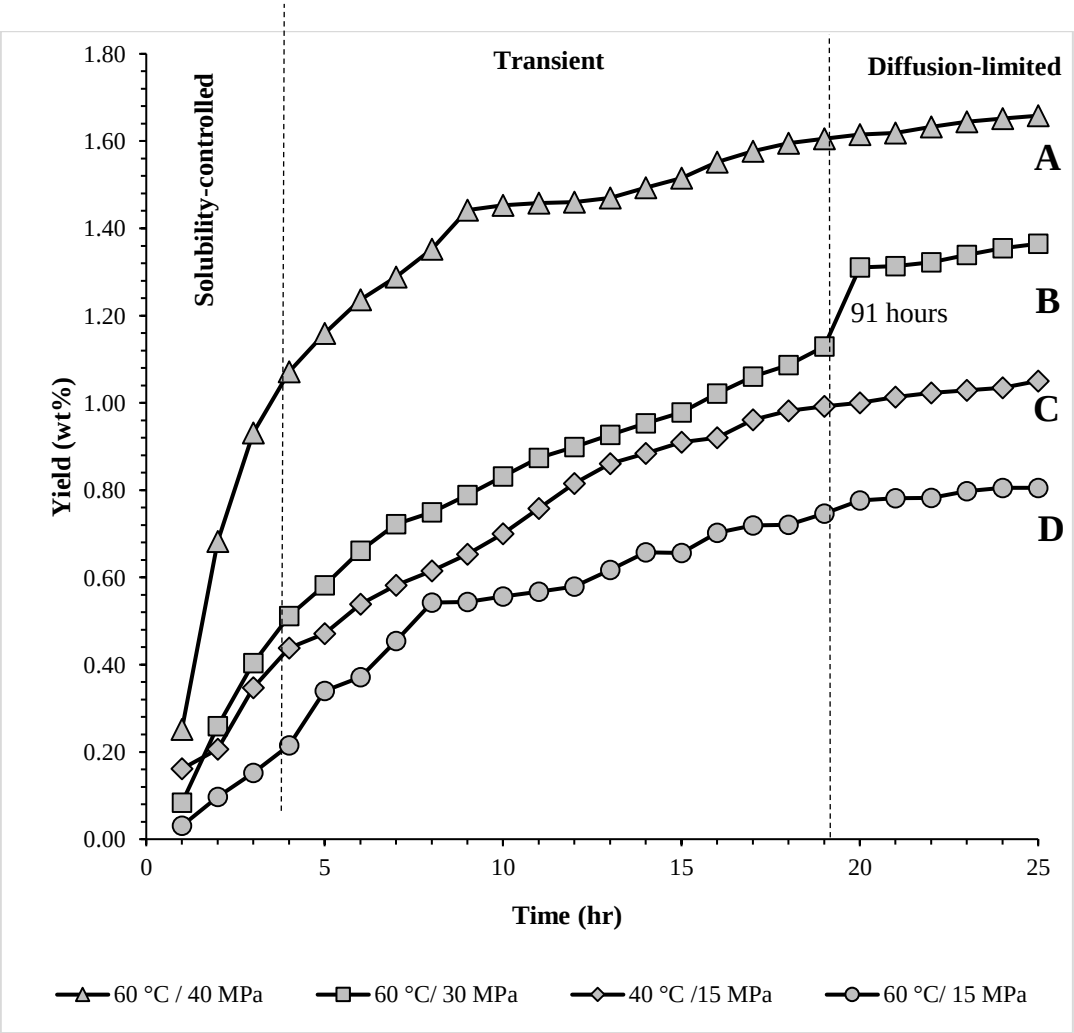

Figure 4.1 - Extraction kinetics of varying extraction conditions.

The mode of extraction for batches A, C and D was dynamic, i.e. sc-CO_2 is continuously circulated into the extraction vessel, then through the backpressure valve, proceeding to the separator where the CO_2 is regenerated, after which it enters the compressor and the cycle starts again. On a reservoir scale, this process

resembles continuous CO_2 flooding. The extraction of batch B started in a dynamic mode, followed by a static mode with a soaking period of 91 hours and was concluded with the dynamic mode. The soaking period resembles a CO_2 Huff and Puff process on a field scale.

Shales contain moisture, oil in inorganic pores, and oil in organic pores (kerogen) (Gu et al., 2022). Kerogen in particular stores a significant amount of hydrocarbons which are classified into 3 types: a free phase, an adsorbed phase on the surface and a phase absorbed within the kerogen matrix (Zhao et al., 2021). Here, the terms "extract" and "solute" will be used interchangeably to account for the inseparable extracted moisture and extracted hydrocarbons as they both constitute the yield. The extraction process happens such that $scCO_2$ initially enters the shale pores. The solute is simultaneously extracted by/dissolved into $scCO_2$ and is transported through the pore to the shale surface. Once the dissolved solute reaches the surface, it is transported into the bulk $scCO_2$ (Brunner, 1994). For each batch, it is observed that the kinetics curve is divided into 3 regions; in the first region, the extraction of the solute is fastest. This region depends mainly on the solubility of the solute readily available at the surface or residing in pores with the shortest diffusion path. Here, the mass transport resistance between the solute and $scCO_2$ dominates. The second region is characterized by a slower extraction rate where the process is transient, meaning that both solubility and diffusion govern the extraction. In this region, the readily available solute is further depleted, and the mass transport is also governed by longer diffusion paths. In the third region, the process becomes completely diffusion limited, and the readily available solute is completely depleted from regions where CO_2 diffusion is not the limiting mass transport mechanism.

The final yield versus particle size of each batch is demonstrated in figure 4.2 below. This is followed by a discussion on the influencing parameters of the extraction process and an interpretation of the results. Since the distribution of organic matter in shale is anisotropic, these interpretations are made under the

assumption that the initial concentration of moisture, free hydrocarbon, bitumen and kerogen is identical among the 4 batches. The values can be found in Appendix B-Table B1.

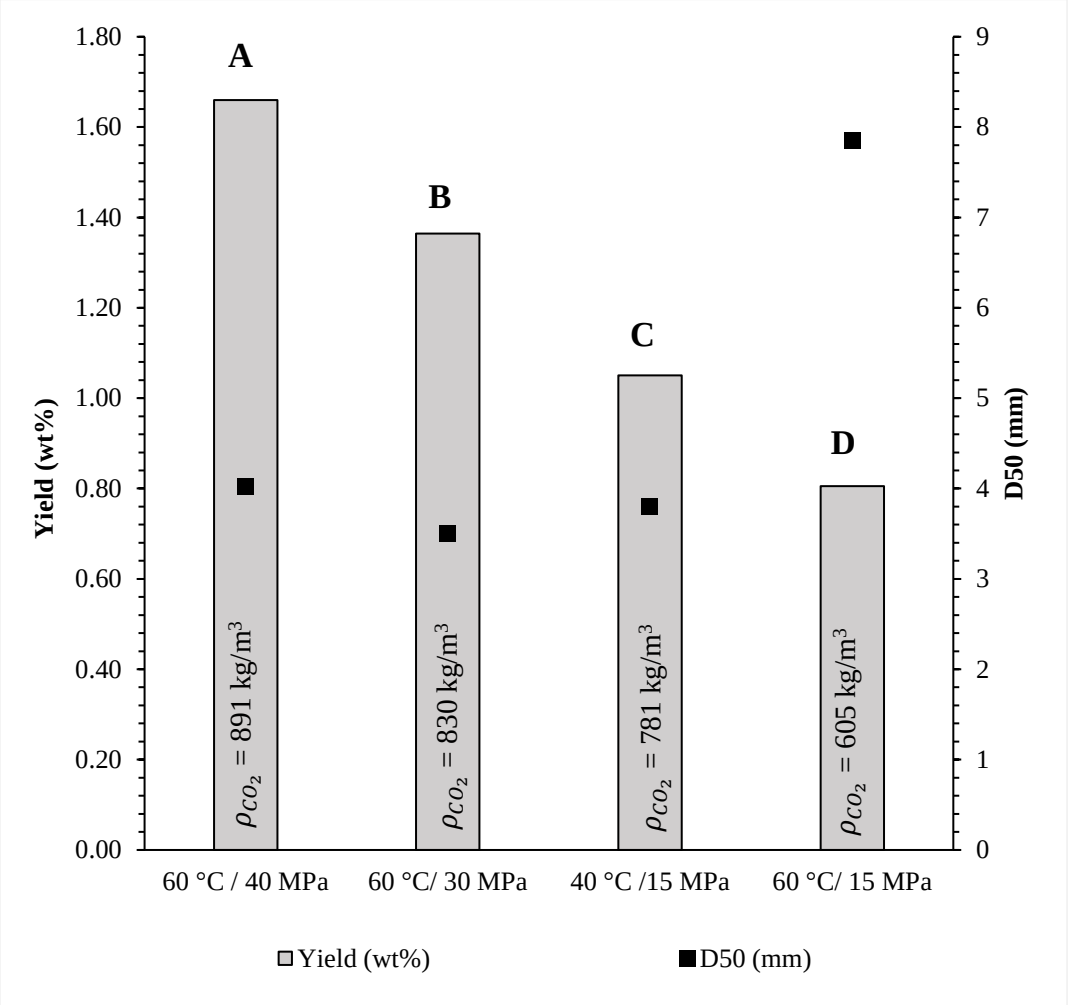

Figure 4.2 - Yield versus median particle size.

Comparing batches A, B and C where the particle size is similar, it is observed that the yield is mainly a function of pressure. The highest yield is observed for batch A, followed by batches B and C, which confirms that an increased solvent density increases its solvation power and therefore the yield, when the particle size is relatively similar. Comparing batches A and B, it is seen that increasing the pressure from 30 to 40 MPa increases the yield from 1.36 to 1.66%, signifying an increase of about 22% due to a corresponding increase in solvent density of about 7% (Case 1). The final cumulative yield is higher for batch B compared to C (1.36% versus 1.05%), where the percent increase in yield is around 29.5 % and

the density increase is 6% (Case 2). The percent increase in yield in case 1 is lower than in case 2 in spite of the density increase being higher for the former. This is attributed to the fact that increasing the pressure from 15 to 30 MPa in case 2 is accompanied by increasing the temperature from 40 to 60 ^{o}C. The higher temperature increases the vapor pressure of the solute, resulting in a further increase in oil yield as explained in section 2.1. Additionally, during the soaking period experienced by batch B, the extent of penetration of gas molecules into the porous medium and the transport of oil molecules to the surface are enhanced. On the other hand, the lowest yield is observed for batch D, this is ascribed to two reasons; the diffusion resistance due to the larger particle size in comparison with the other batches and the weaker solvation power of scCO_2 (lowest solvent density).

Figure 4.3 shows an example of a mixture of oil and water extracted at 15 MPa and 60 ^{o}C. Formation water was observed to be extracted first in batch C and D (i.e at 15 MPa). As extraction progressed, the percentage of oil in the extract started to increase over the amount of extracted water. The initial displacement of water is attributed to alteration in rock surface wettability as discussed in depth in section 5.4. At lower pressure the removal of water may be accomplished by means of wettability alteration since the solubilities of both water and oil in the CO_2 are low. On the other hand, the extraction of oil and formation water is simultaneous in batches A and B, owing to the high solubility of both, oil and water in CO_2 at higher pressures.

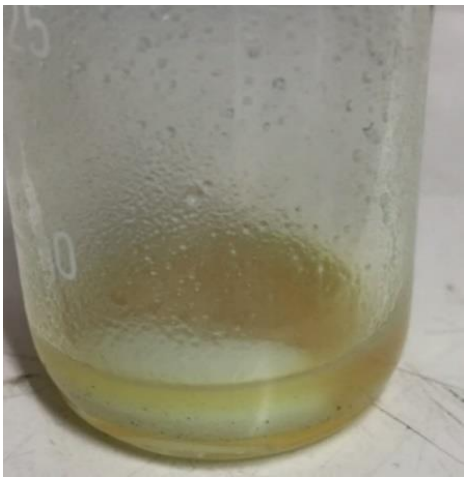

Figure 4.3 - Formation water in the extracted mixture.

A theoretical fit is applied to the extraction kinetics at 15 MPa and 60 °C using the analytical solution to Fick's diffusion as proposed by (Crank, 1975) (See section 3.2.8). This was done to estimate the apparent diffusion coefficient representative of the overall mass transport of oil as seen in figure 4.4. The apparent diffusivity of oil takes a value of $2x10^{-11}$ m^2/s. (Bueno et al., 1993; Lin and Tavlarides, 2010) measured the diffusivity of Benzene in CO_2 to be around 15 $x10^{-9}$ m^2/s at similar conditions. (Umezawa and Nagashima, 1992) measured the diffusivity of alkanes (C_5H_{12}-$C_{14}H_{30}$) in $scCO_2$ at 10.5 MPa and 35 ^oC. They reported values with a similar order of magnitude ranging between 14.1-17.6 x 10^{-9} m^2/s and showed a negative correlation between the molecular weight of the alkane and its diffusivity. In comparison to these studies, the value reported here is lower due to the higher molecular weight of Sultani oil constituents and due to the hindrance effect induced by the rock matrix (Wang and Hou, 2021) (Lou et al., 2021), where the porosity, permeability and tortuosity of the pore network play a significant role in the mass transport process (Javadpour et al., 2007) (See section 2.10 for further details). Further on, oil-pore wall interactions inside kerogen nanopores also contributes to diffusivity reduction (Bi et al., 2021; Elwinger et al., 2017).

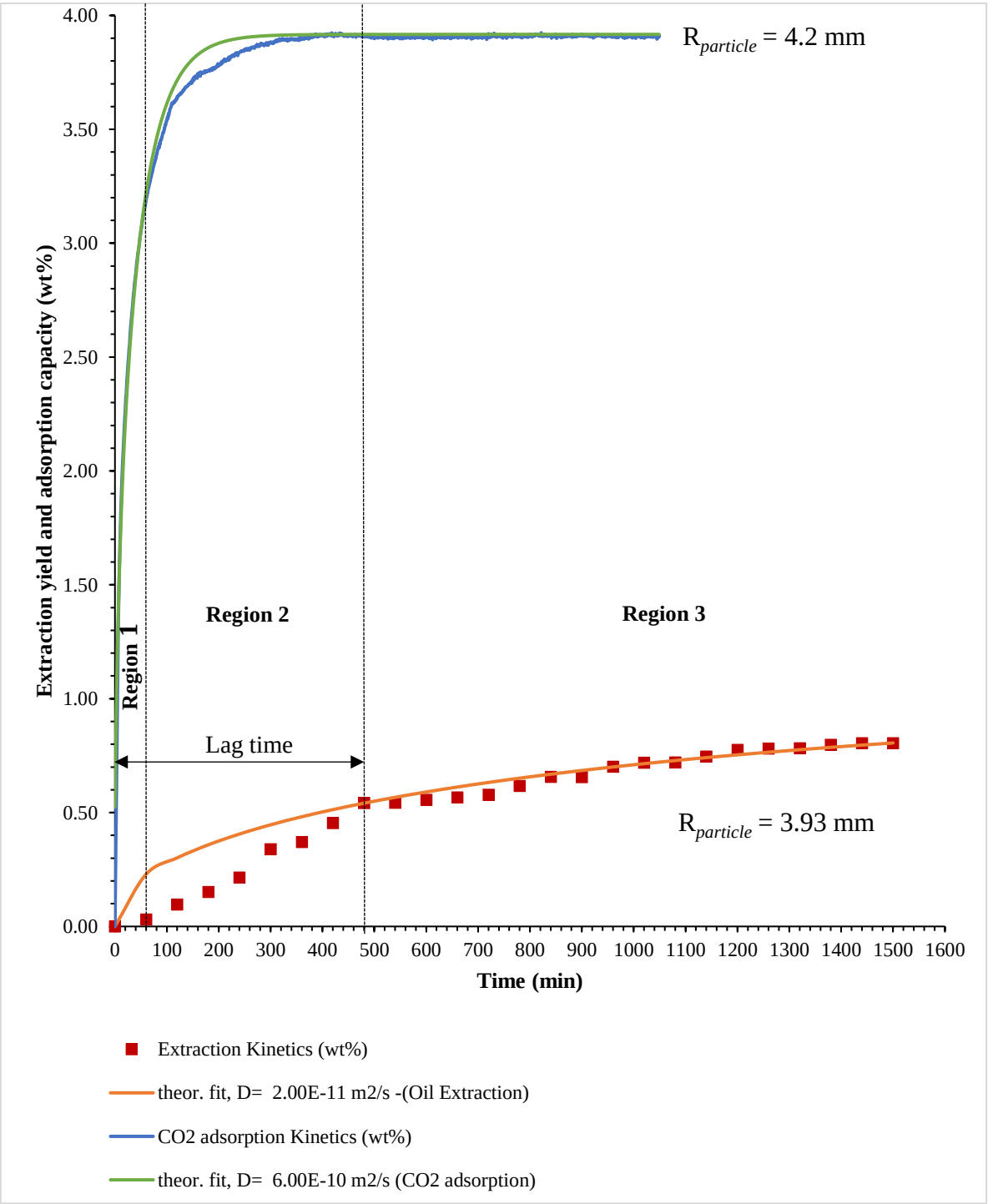

Figure 4.4 - Theoretical fitting of experimental oil extraction and CO_2 adsorption kinetics using apparent diffusion coefficients.

For comparison, the diffusion of CO_2 into the solid matrix is also demonstrated in figure 4.4, calculated based on CO_2 adsorption kinetics using the same approach and applying the CO_2 apparent diffusion coefficient determined in section 5.3 on a rock sample of a similar size. The diffusivity of CO_2 takes a value of $6x10^{-10}$

m^2/s, which is one order of magnitude higher than the diffusivity of oil within the rock matrix. While hindrance effects imposed by the rock matrix are present in both cases, the weight of a molecule is inversely proportional to its diffusivity (Jobic et al., 2004; Umezawa and Nagashima, 1992). Further on, according to the well-known Stokes-Einstein approach (Vardag et al., 1991) the diffusivity of a molecule is inversely proportional to its radius, which explains the lower diffusivity of oil molecules, owing to their higher molecular weight and larger radii compared to CO_2. Moreover, the presence of a counter current diffusion during extraction will highly influence the oil diffusivity.

The comparison between CO_2 adsorption kinetics and the oil extraction kinetics may assist in constructing a general understanding on processes simultaneously occurring within the pore during extraction. From figure 4.4 it is observed that the CO_2 adsorption reaches equilibrium at around 380 minutes. On the other hand, the extraction kinetics demonstrate a time lag up until minute 480, after which the curves of the experimental yield and the theoretical diffusion-based fit agree. This time lag indicates that the extraction depends on the availability of CO_2 inside the pores so that the oil is enabled to diffuse towards the surface. The situation is presented in figure 4.5 and explained as below:

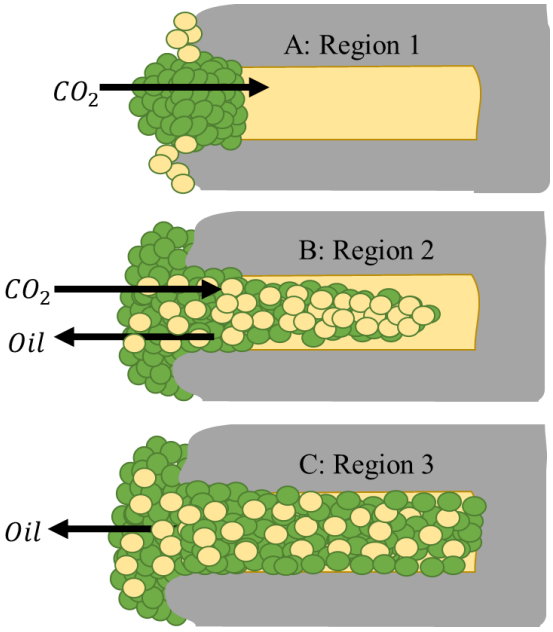

Figure 4.5 - Representation of extraction steps. CO_2; green, Oil; yellow.

Region 1: Drastic increase of CO_2 concentration at the surface of the particle (increase in adsorption capacity of around 3.3%). CO_2 pressure gradient within the pore is highest, this step is governed by a unidirectional diffusion of CO_2 into the oil residing within the pore. See figure 4.5-A.

Region 2: Reduced yet continued adsorption of CO_2 (increase in adsorption capacity of around 0.6% over end of region 1). Reduced CO_2 pressure gradient within the pore (CO_2 concentration inside the pore is higher in this region than region 1). This is accompanied by the desorption of oil and its diffusion into CO_2. This region is characterized by a bidirectional diffusion of both CO_2 and oil. (Notice that the mass transport of CO_2 into the pore constitutes resistance to the transport of oil out of the pore by means of countercurrent diffusion). See figure 4.5-B.

Region 3: Adsorption is complete and the maximum concentration of CO_2 inside the pore is reached (maximum density and therefore solvation power of CO_2). This is accompanied by a vanishing CO_2 pressure gradient and the process is governed by a unidirectional diffusion of oil within CO_2 and its consequent migration towards the particle surface. This is also accompanied by a reduced flux of oil due to a reduced concentration gradient of oil within the pore. See figure 4.5-C.

To determine the maximum possible yield from Sultani shale using another non-polar solvent, Soxhlet extraction was performed using Hexane at 80, 100 and 120 ^{o}C. These conditions were chosen as the operating temperature in Soxhlet extraction must exceed that of the boiling point of the solvent (69 ^{o}C for Hexane). The yield is shown in figure 4.6. and is not observed to vary with increasing temperature. On the other hand, it is observed that the yield of SFE is comparable to that of Soxhlet extraction using hexane. The values are listed in Appendix B-Table B.2.

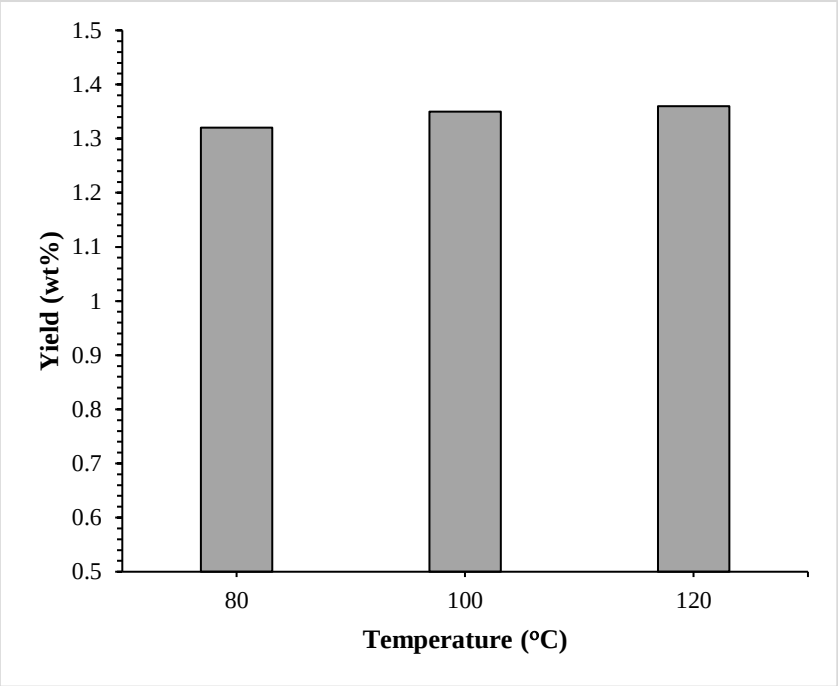

Figure 4.6 - Oil yield of Hexane Soxhlet extraction

5. Interfacial Properties and Mass Transport

5.1 Interfacial Tension

5.1.1 Interfacial Tension in Binary Systems

5.1.1.1 Interfacial Tension of CO_2-Brine Systems

The interfacial tension of systems comprising CO_2 and aqueous solutions containing 3 and 10 wt% NaCl have been investigated at 60° C and pressures up to 30 MPa. The equilibrium values thereof are depicted in figure 5.1 and tabulated in Appendix C – Table C.1.

Impact of pressure: Taking a closer look at one salt concentration at a time, it is observed that the IFT behavior is divided into two regions. In the first region, the IFT drops almost linearly with pressure. This is referred to as the Henry regime by (Chiquet et al., 2007), according to which the solubility of the CO_2 in the aqueous phase increases and this is reflected by the interfacial behavior. The reduction in IFT is further related to the change in bulk CO_2 density upon increasing pressure. At the critical pressure (7.4 MPa) and up to 15 MPa, the bulk density of CO_2 increases dramatically, this behavior also holds for the density of CO_2 in the vicinity of the interface. An increasing CO_2 density at the interface reflects an increasing positive surface excess concentration of CO_2, which in turn causes a reduction in IFT according to Gibb's adsorption isotherm expressed in equation 2.28 in section 2.3.

Within the second region, a pseudo plateau in the IFT is reached and is observed at 15-20 MPa and beyond. This is similar to the findings of several researchers including (Bachu and Bennion, 2009; Chalbaud et al., 2010; Chiquet et al., 2007) and many others. In this region, CO_2 becomes increasingly incompressible and the increase in density - due to an increasing pressure (i.e. $\Delta\rho/\Delta P$) – reduces. This also means that the increase in CO_2 accumulation at the interface in response to pressure and the consequent increase in the surface excess concentration (Γ_{CO2})

is reduced, hence the plateauing of the IFT values. The aforementioned is discussed in detail in the following paragraph.

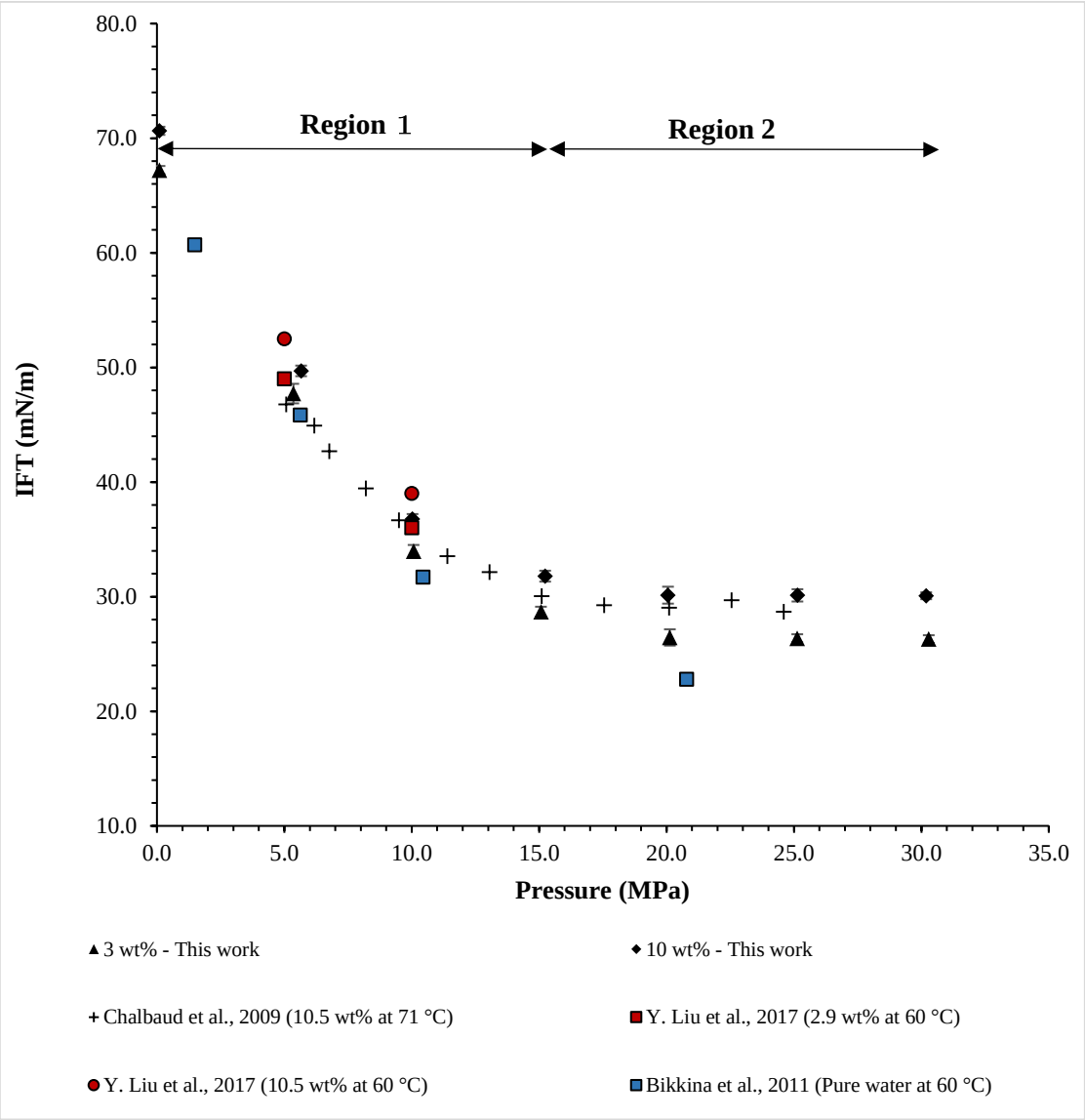

Figure 5.1 - Interfacial tension of CO_2-NaCl brines systems at 60 °C.

In figure 5.2, an illustration of density profiles of both water and CO_2 across the interface is presented at different pressure conditions. The density profiles of the participating phases is adapted from the molecular dynamic simulations (MDS) performed by (X. Li et al., 2013) and (Li and Jin, 2019). The behavior demonstrated in figure 5.2 in response to an increasing pressure qualitatively exhibits the situation at both the interface and bulk phase; increased CO_2 density at increased pressure, and an accompanying higher enrichment of CO_2 molecules at the interface (indicated by the density of CO_2 at the interface). To further

elucidate the interfacial behavior, a comparison is made between 5 and 15 MPa. Firstly, the interfacial thickness which is negatively correlated with IFT is found to increase (become broader) with an increasing CO_2 concentration in the bulk phases (by means of an increasing pressure). On the other hand, while both the bulk and interfacial densities of CO_2 at 15 MPa are higher, the ratio between these densities is lower at 15 MPa compared to 5 MPa, owing to the reduced compressibility of CO_2 at elevated pressures. This also results in a decreasing positive surface excess in the high-pressure region, and therefore a lower reduction in IFT is observed there (Nielsen et al., 2012). In accordance with the trend observed in figure 5.1, neither a significant enrichment of CO_2 at the interface nor a significant further broadening of the interfacial thickness take place when pressure rises above 20 MPa.

It is important to note that the density is not the only decisive parameter in the IFT behavior, rather, the IFT depends on the nature of the gas molecules adsorbing at the interface, which would ultimately determine the strength of intermolecular interaction between the participating phases (Naeiji et al., 2020), which in its turn is also reflected by the solubility.

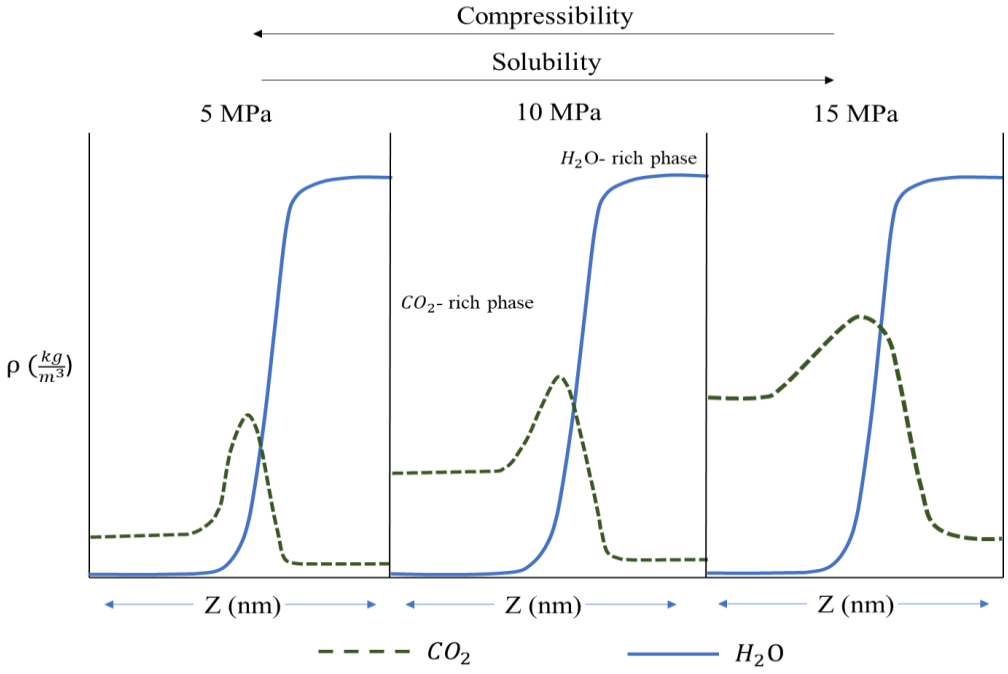

Figure 5.2 - Qualitative density profile of the participating phases across the interfacial region.

Impact of ion concentration: Investigating the impact of ion concentration on the surface tension and IFT, it is seen that higher salt concentrations result in higher IFT values. Comparing the results to those reported by (Bikkina et al., 2011) who investigated CO_2-pure water IFT at similar conditions further confirms the trend. The higher IFT at higher salinity is due to the spatial distribution of Na^+ and Cl^- in the aqueous phase and how it impacts the arrangement of molecules at the vicinity of the interface (Aggelopoulos et al., 2011). In the bulk phase, both Na^+ and Cl^- are solvated by water molecules such that a hydration cage of water molecules is created around the solvated ions (Mirchi et al., 2014). At the interface, a distinction in the literature is made regarding the behavior of cations and anions. Cations are said to be structure makers. Since they have higher ability to organize the water dipoles in the bulk phase than at the interface, their presence at the interface is not favorable, and the total energy of the system is minimized once they are repelled towards the bulk phase. On the other hand, anions are considered structure breakers, owing to the fact that water molecules can better organize their hydrogen bonding networks in the absence of these ions. As a result, the total energy of the system is minimized once these ions are pushed towards the interface. According to Gibb's adsorption equation (2.17), the IFT increases when a negative adsorption (i.e. desorption) occurs at the interface. Since both adsorption and desorption are occurring, an increasing IFT implies that the negative excess surface concentration of Na^+ at the interface exceeds the positive surface excess concentration of Cl^- ions (Manciu and Ruckenstein, 2003). The aforementioned hypothesis, however, has been refuted in the works of (Li and Jin, 2019; X. Li et al., 2013; Yang et al., 2019) who performed MDS and used the Density Gradient Theory to show a depleting concentration of both cations and anions in the vicinity of the interface. Nevertheless, there is wide consensus among researchers that the increase in IFT at higher salinity is mainly governed by the desorption of cations from the interface (Aggelopoulos et al., 2010, 2011; Chalbaud et al., 2010; Y. Liu et al., 2016; Mutailipu et al., 2019a). The higher the

amount of Na^+ in the bulk, the higher the desorption from the interface (increased negative excess surface concentration) and therefore the higher the IFT. It can be further observed from figure 5.1 that the impact of salinity on the IFT is more pronounced at elevated pressures; in line with the observations reported by (Aggelopoulos et al., 2011, 2010).

Despite the similar concentrations and conditions, the values reported in this work are slightly lower than those reported by (Liu et al., 2017). This could possibly be due to differences in the selected drop age at which the IFT values were taken or due to discrepancies in the densities utilized for IFT evaluation. (Chalbaud et al., 2009) investigated a similar concentration of 10.5 wt% NaCl brine at 71 °C. At 5 MPa, their reported values are lower than the ones reported in this work (47 versus 50 mN/m), which is an expected behavior at low to moderate pressures. However, as the pressure increases, their reported values exhibit similarity to those measured in this work, although higher IFT values at the high-pressure range would be expected. The reason for this discrepancy is not clear.

5.1.1.2 Interfacial Tension of CO_2-Oil Systems

Figure 5.3 shows the IFT of systems comprising CO_2 and oil. The values are tabulated in Appendix C – Table C.2 to C.4.

Impact of pressure: In all investigated systems and similar to the CO_2-brine systems, it is observed that at low to moderate pressures, the IFT reduces almost linearly in response to increasing the pressure (region 1). This behavior is seen until a certain pressure is reached, beyond which a significant reduction in IFT is no longer observable (second region). The second region is characterized by a reduced steepness of the IFT curve. The steep linear reduction in the first region of the IFT curve can be attributed to the increasing mutual miscibility between CO_2 and the light fractions of the oil as pressure increases. With a further increase in pressure, i.e. in the second region and already at very low absolute values of the IFT, the lower mutual miscibility between CO_2 and the heavier oil fractions dominates the course of the IFT as a measure of the overall interactions of both

phases. Once the critical point of the binary CO_2-oil mixture is reached, the interfacial thickness tends to infinity and the IFT vanishes (Niño Amézquita et al., 2010). Further on and as explained earlier in section 5.1.1.1, thermodynamically, a decreasing IFT signifies an accumulation (adsorption) of CO_2 at the interface. This accumulation is related to an increasing bulk CO_2 density with pressure. In region 1, the density of the CO_2 bulk phase increases drastically in response to an increasing pressure, while in the second region which covers higher pressures, the compressibility of CO_2 decreases and therefore the increase in bulk phase density with pressure is reduced. Accordingly, a further enrichment of the interface with CO_2 is suppressed (reduced positive surface excess concentration), reflecting a lower reduction in IFT as indicated by the flattening of the slope in the second region. It may be presumed, that the highest reduction in IFT occurs when the difference between the bulk and interfacial density of CO_2 is highest. The results are in line with the findings of (Yang et al., 2005b) who measured the IFT of CO_2-Ontario crude oil at 58 °C.

The impact of temperature on the IFT of the SFEM crude can be deduced by comparing the values at 40 °C and 60 °C in figure 5.3-A. At low to moderate pressure, the IFT at 60 °C is lower compared to that at 40 °C. However, at pressures higher than 5 MPa, an inversion occurs and the IFT at 40 °C is lower than that of the 60 °C (see crossover point in figure 5.3 A). This is attributed to the reduced mutual solubility of CO_2 and the oil at higher temperatures.

Impact of oil composition: It is well known that the interfacial behavior not only depends on pressure and temperature, rather the nature of the gaseous phase and the composition of the oleic phase as well, where higher molecular weight hydrocarbons at similar P/T conditions possess higher IFTs. Indeed, the latter statement applies to binary CO_2-pure alkanes systems as demonstrated by (Mutailipu et al., 2019a) and (Jaeger, 2014)**.** Below an extension on this phenomenon is provided to encompass multicomponent systems.

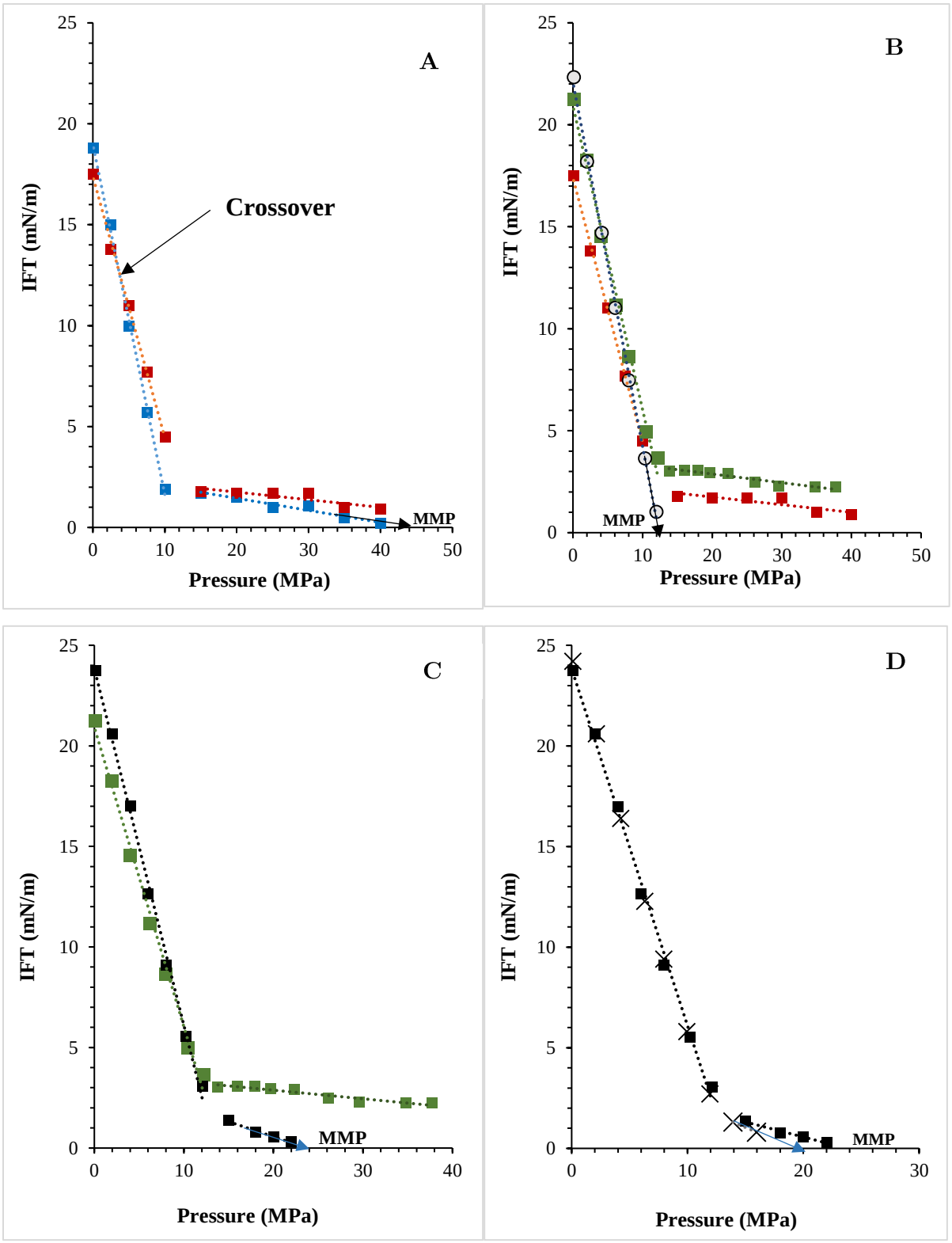

Figure 5.3 - Interfacial tension of binary CO_2-oil systems.

(SFEM – 40 °C: ■, SFEM – 60 °C: ■, SFE40 – 60 °C: ■, Model oil – 60 °C: ■, Dodecane - 60 °C: ○, and Hexadecane – 60 °C:×).

First region of the IFT curve: A question may arise regarding the behavior of the SFE40 crude in comparison to the model oil, especially in the first region (figure 5.3-C), where higher surface tension (SFT) and IFT values are found for the latter, despite the fact that the SFE40 crude contains hydrocarbons with higher molecular weight. The SFE40 crude constitutes a wide variety of light and heavy components (see GC analysis in section 3.1.3.1). The lightest thereof is dodecane ($C_{12}H_{26}$). On the other hand, the lightest hydrocarbon constituting the model oil is hexadecane ($C_{16}H_{34}$). It appears that the interfacial behavior in the first region is governed by the SFT/IFT of the lightest hydrocarbon constituting the oil (as discussed above). This idea is supported by SFT values of pure substances. For instance, the measured SFT of the model oil is 23.7 mN/m which is in good agreement with the SFT of hexadecane (24.1 mN/m at 60 °C) as reported by (Lyklema, 2000b). Regarding the SFE40 crude, the SFT is measured to be around 21.2 mN/m which takes a similar value as that of the dodecane's at 60 °C; 21.8 mN/m (Lyklema, 2000b). To further confirm the behavior, the measurements of CO_2-Hexadecane and CO_2-Dodecane IFT at 60 °C were also performed. In the first region, the behavior of the model oil is similar to that of hexadecane's as shown in figure 5.3-D, while for the crude oil, the IFT exhibits agreement with dodecane in the region of interest as seen in figure 5.3-B. As the pressures increases, the density of CO_2 is high enough that it is able to extract the dodecane more efficiently from the SFE40 crude. This results in the partitioning of dodecane among the SFE40 crude and the CO_2 surrounding phase. Further on, the dodecane may act as a cosolvent which increases the miscibility of the higher molecular weight hydrocarbons in the CO_2.

Such comparison is not possible for the mixed crude as no GC analysis is performed due to the limited amount of extract. All in all, it is likely that such analysis can be used to infer the light components constituting the crudes by comparing the IFT behavior of real systems to model systems (alkanes) at similar T/P conditions.

Second region of the IFT curve: The difference in absolute IFT values among the crude and mixed crude oils is attributed to the grand variety of hydrocarbons constituting both (figure 5.3-B). This difference stems from the different extraction conditions which influence the solvation power of CO_2 and therefore its ability to extract certain components in certain amounts. Considering the overall higher IFT values of the crude in the second region, these indicate the presence of heavier hydrocarbons in comparison to the mixed crude, which confirms the higher solvation power of CO_2 at 40 MPa (Guiliano et al., 2000). This is further confirmed by comparing the IFT values of the crude oil to the model oil (figure 5.3-C).

As a measure of mutual miscibility, the minimum miscibility pressure (MMP) is defined as the minimum pressure at which complete miscibility is achieved and the IFT value between the oil and the gas reduces to zero (i.e. a vanishing interface) (Ghorbani et al., 2014). Figure 5.4 shows an image of oil being injected into CO_2 at 25 MPa, where the interface vanishes and no drop can be formed. The MMP correlates with the oil composition and the temperature in the following way: The higher the molecular weight of the alkane or the higher the temperature, the higher the MMP. The MMPs of the investigated systems are estimated by extrapolating their respective IFT curves until they intersect with the x-axis. This is done in the first (and only) region for dodecane and the second region for hexadecane, model oil and SFEM crude at 40 °C in combination with CO_2 as indicated in figure 5.3. The MMP of dodecane is calculated to be 12 MPa. The MMP of hexadecane is around 20 MPa at 60° C which lies between what has been reported by (Hölscher et al., 1989) who found a mixture critical pressure of 18.2 MPa and (Charoensombut-amon et al., 1986) who found a critical pressure of 21.8 MPa. The MMP of the model oil takes a value of 24 MPa according to this procedure. An extrapolation of the slopes of the crude oils would give values of above 40 MPa which is not considered to be reliable since the uncertainties in the slopes would yield deviations that are too high. However, comparing the SFEM

crude IFT values at 40 and 60 °C (figure 5.3-A), it can be seen that qualitatively, the MMP tends to increase (decreased negative slope of IFT) as the temperature is increased, which is a well-known phenomenon and is caused by the reduced mutual miscibility at higher temperatures (Hemmati-Sarapardeh et al., 2014).

Figure 5.4 - Pendant drop of model oil in a CO_2 atmosphere at 25 MPa.

5.1.2 Interfacial Tension in Ternary Systems

The IFT is measured in binary water/brine-oil systems and ternary CO_2-water/brine-oil systems. The former constitutes a reference case for investigating the role of CO_2 in modifying the interfacial behavior at the water/brine-oil interface. The time dependent IFT values are exemplarily depicted for systems constituting DW-oil and CO_2-DW-oil as a function of pressure in figure 5.5. Equilibrium values for different pressures and aqueous phase compositions are shown in figure 5.6. The corresponding values are reported in Appendix C – Table C.5.

As demonstrated in figure 5.6, at atmospheric pressure, interfacial tension values of the oil-water/brine system are in the following order: $IFT_{10\%\ NaCl} > IFT_{3\%\ NaCl} > IFT_{DW}$. As reported by (Moeini et al., 2014) upon salt introduction into the aqueous phase and its dissociation into ions, water molecules orient themselves in a cage-like hydrogen bonded structure around these ions. This hydrogen bonding is disrupted at the interface where the water and oil are in contact and where a higher energy medium exists. Consequently, ion concentration at the interface is reduced. Accordingly, the surface excess concentration becomes negative ($\Gamma_{salt} < 0$) as per Gibbs adsorption theory (see equation 2.17), and the IFT increases. These results are in line with the findings of (Kakati and Sangwai, 2017) who reported a similar order of IFT between alkanes and 0, 3 and 10 wt% NaCl brines and the findings of (Ikeda et al., 1992) who reported increasing IFT with increasing salt concentration, which they also attribute to the negative adsorption of Na^+ at the water/hexane interface.

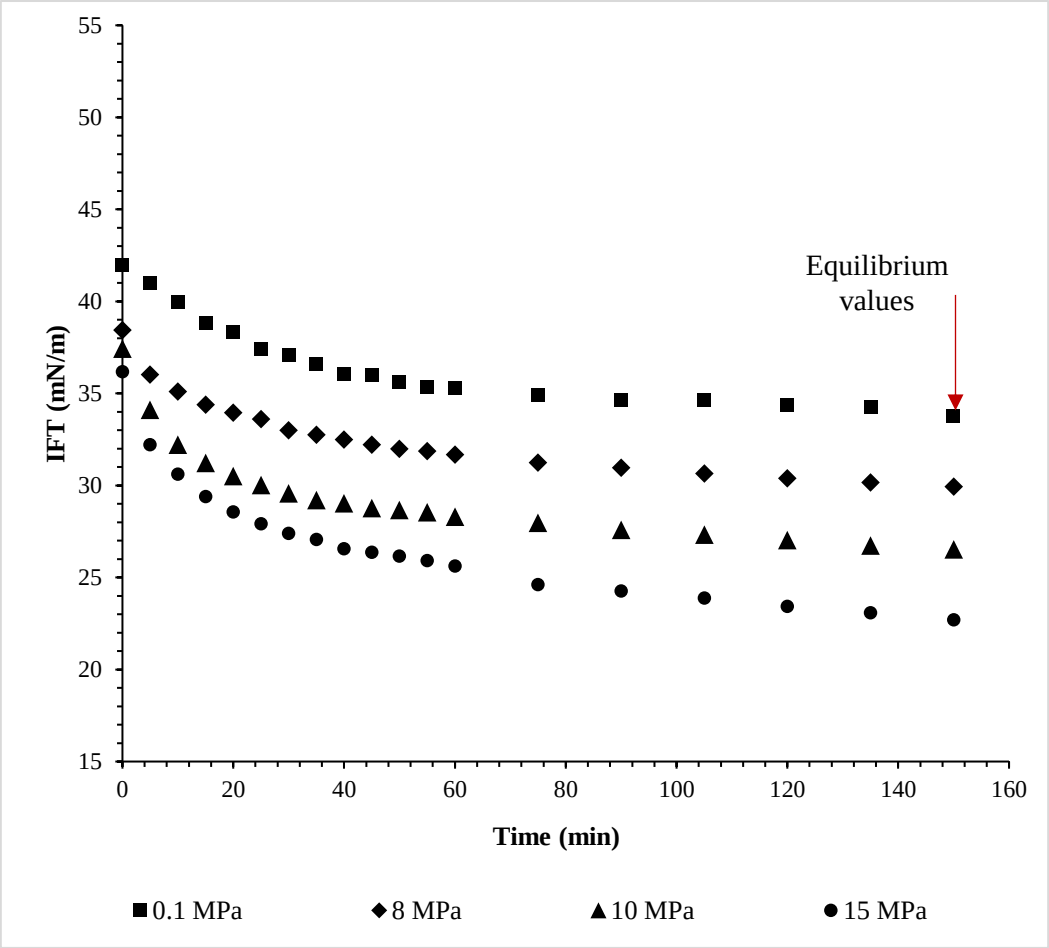

Figure 5.5 - Time dependent IFT of a DW-oil system versus CO_2 pressure at 60 °C.

Investigating the impact of CO_2 addition to the system, it is observed that CO_2 plays a significant role in reducing the oil-water IFT. In DW, the IFT reduction at 8 MPa is observed to be 11.3%. Further IFT reductions of 21.4 % and 32.7 % are observed at 10 and 15 MPa, respectively. This can be explained as follows: water and oil are immiscible fluids, therefore the interaction between these two phases happens only at the interface and is governed by repulsive forces. On the other hand, CO_2 is partially miscible in both phases. Upon CO_2 dissolution in the system (both aqueous and oleic phases), a film of CO_2 is formed in the interfacial region which displaces the oil away from the interface (B. Liu et al., 2016). This displacement weakens the intermolecular interaction between the water and oil on the one hand, and increases the water-CO_2 and oil-CO_2 interactions on the other, signifying an amphiphilic nature of CO_2, where it behaves similarly to a surfactant at the oil-water interface. At higher pressures, the solubility of CO_2 increases in

the aqueous phase (Mosavat et al., 2014), leading to higher CO_2 accumulation at the interface and the broadening of the interfacial thickness, which is inversely related to IFT, hence lower IFT values are found at higher pressures (Mohammed and Mansoori, 2018).

Regarding the impact of salt concentration on IFT, the values of DW and 3% NaCl brine fall within the experimental error, and therefore the results are inconclusive. On the other hand, for the 10% NaCl brine, an obvious trend is observed. As salt concentration is further increased in the solution, the effect imposed by CO_2 is significantly reduced. The solubility of CO_2 in the aqueous phase at 10 MPa and 60 °C – as calculated using the model of (Duan et al., 2006)– is 1.03, 0.92 and 0.73 mol CO_2/ kg H_2O in DW, 3% and 10% NaCl brine, respectively. Hence, the absolute amount of CO_2 in the bulk phase is significantly lower when the salinity is high. Consequently, CO_2 accumulation at the interface is also lower. In summary, the concentration of amphiphilic compounds at the interface that reduce IFT appear to result from the concentration in the bulk phases.

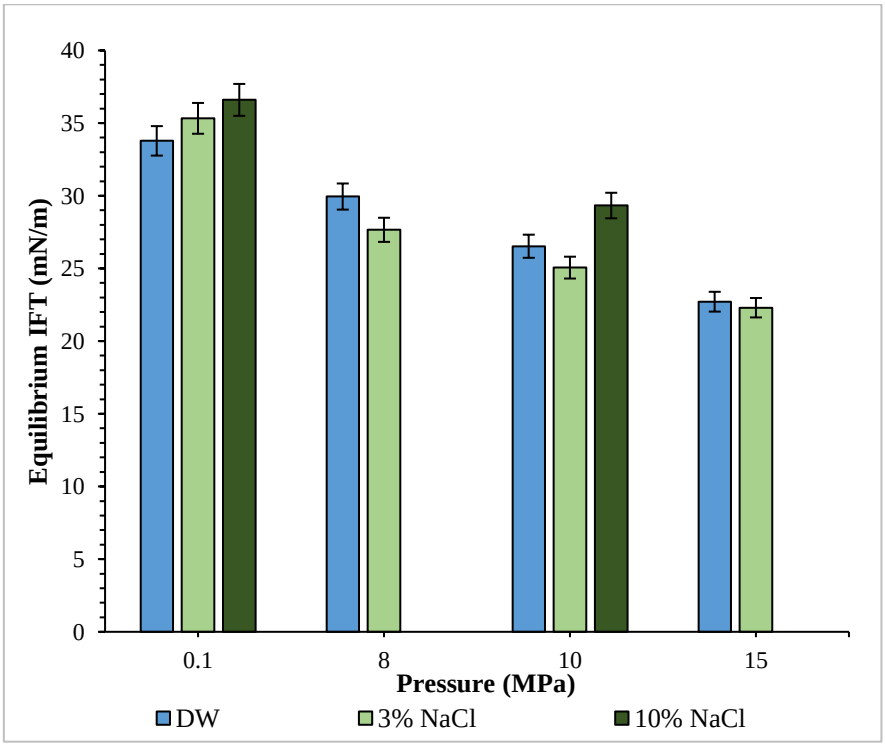

Figure 5.6 - Equilibrium IFT in CO_2-water/brine-oil systems versus pressure at 60 °C.

5.2 Adsorption

The adsorption of CO_2 on an extracted shale sample was investigated at 40 °C and 60 °C and pressures ranging between 5-30 MPa. The results of the adsorption measurements are demonstrated in figure 5.7. The adsorption capacities are reported as excess adsorption isotherms and are tabulated in Appendix C – Table C.6.

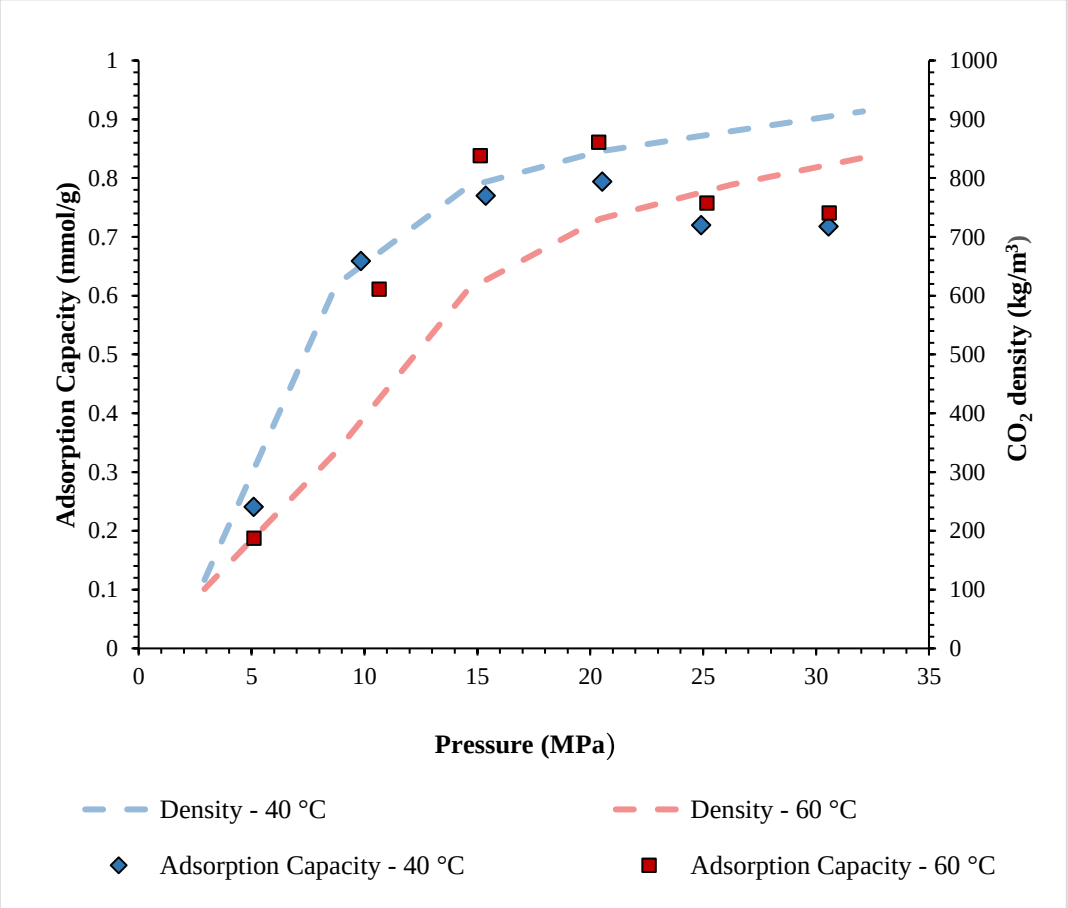

Figure 5.7 - Excess adsorption isotherms of CO_2 on shale as a function of pressure.

The adsorption capacities of Sultani as reported in this work cannot be precisely compared to those of other shales due to the varying experimental conditions and the methods utilized (see table 2.12 - section 2.9). However, a general comparison can be made as follows. (Hui et al., 2019) investigated the adsorption of CO_2 on Yanchang shale using the gravimetric method. They reported an excess adsorption capacity of 0.85 mmol/g at 10 MPa and 45 °C. At similar conditions, (Weniger et al., 2010) reported an excess adsorption capacity of 0.54 mmol/g on Brazilian

shale, measured using the volumetric method. The adsorption capacity of Sultani shale at 10 MPa and 40 °C is 0.66 mmol/g, and therefore falls within the same order of magnitude.

Impact of pressure: At a constant temperature, the adsorption isotherms show a strong increase in adsorption capacity close to the critical pressure of CO_2. This increase is related to the sharp increase in CO_2 density as it changes from the gaseous state to the supercritical state (Klewiah et al., 2020). Additionally, as the pressure increases, the gas is allowed to access pores and surfaces that are inaccessible at lower pressures (Ho et al., 2018). However, in figure 5.7 this increase is only observed until a certain pressure is reached. For both investigated temperatures, the adsorption capacity peaks at 20 MPa with no significant difference over values measured at 15 MPa.

In view of the conversion coefficient $(1 - \frac{\rho_{bulk}}{\rho_{ads}})$ relating the absolute adsorbed mass to the excess adsorbed mass (see equation 3.18 in section 3.2.7), at low to moderate pressures (5 and 10 MPa), the increase in the density of the adsorbed layer is more pronounced than the increase in the bulk phase density, therefore the effect of buoyancy is not manifested in the measured adsorption capacity and can be neglected ($m_{ads} \approx m_{ex}$). On the other hand, at elevated pressures the occupancy of sorption sites by the adsorbed molecules is already high, therefore it may be assumed that the density of the adsorbed phase does not significantly increase with pressure. The density of the bulk phase, however, does still significantly increase as demonstrated in figure 5.7. A maximum difference between the density of adsorbed layer and the density of the bulk phase will yield the highest excess adsorption isotherm (Wu et al., 2019). This is observed at 20 MPa. According to equation 3.18, and under the assumption that the increase in ρ_{ads} reduces at elevated pressures compared to the density of the bulk phase, a correction of the excess adsorption isotherm would yield higher adsorption capacities at higher pressures.

A similarly decreasing adsorption capacity at elevated pressures has also been reported by the following authors (Bakshi et al., 2020; Busch et al., 2008; Chareonsuppanimit et al., 2012; Hui et al., 2019; Lu et al., 2016; Merey and Sinayuc, 2016; Weniger et al., 2010; Wu et al., 2019) and (Fujii et al., 2010). Interestingly, what these authors have in common, is that they report a peak in adsorption capacity at or above the critical pressure and temperature of CO_2. This further confirms that the adsorption capacity only appears to be lower at elevated pressures due to the ongoing increase of bulk CO_2 density at supercritical conditions and is accordingly labelled the excess adsorption capacity.

Impact of temperature: It is well known that adsorption is an exothermic process during which heat evolves. When temperature increases, a reverse process is favored (desorption) in accordance with Le Chaterlier's principle. Moreover, as temperature increases, the kinetic energy of the adsorbate molecules increases and overcomes the electrostatic forces of attraction forming with the adsorbent and results in less adsorption (Bolis, 2013). Therefore, increasing the temperature is expected to reduce the adsorption capacity (Klewiah et al., 2020). In figure 5.7 at low pressures of 5 and 10 MPa the adsorption capacities at 40 °C are higher than 60 °C. As the pressure is further increased, the adsorption capacity at 60 °C appears to be higher. This can also be elucidated by the buoyancy effect previously mentioned. According to equation 3.12, the density of bulk CO_2 and the volume of adsorbed layer influence the buoyancy force that are the reason behind underestimated adsorption capacities at elevated pressures. Additionally, the density of the adsorbed layer plays a significant role in converting the excess adsorption isotherm into an absolute one (equation 3.18). However, one of the challenges experienced in gas adsorption measurements is the accurate evaluation of the adsorbed gas phase density (Memon et al., 2021). The density of the adsorbed layer depends on the pressure, temperature, pore size and pore geometry (Bakhshian and Hosseini, 2019) and similar to bulk phase density, the adsorbed layer density increases with decreasing temperature (Wu et al., 2021) and the

conversion coefficient in equation 3.18 is reported to be lower at lower temperatures (Qi et al., 2019), implying that the corrected absolute adsorption is higher.

Given the above, the buoyancy-induced error on the 40 °C adsorption isotherm is larger compared to the 60 °C isotherm. Thus, excess isotherm correction would yield higher absolute adsorption isotherms for 40 °C. These findings are in line with what was reported by (Fujii et al., 2010) who found a higher buoyancy effect at 50 °C compared to 100 °C. This phenomenon has also been reported in the work of (J. Li et al., 2019), (Ju et al., 2019) and (C. Wang et al., 2020) who found higher excess adsorption isotherms at higher temperatures in the high-pressure range. Through molecular dynamic simulation, and simplified local density theory, (Ju et al., 2019) and (C. Wang et al., 2020) corrected excess adsorption isotherms which resulted in higher absolute adsorption at lower temperatures.

The conversion of the excess isotherm (m_{ex}) to an absolute isotherm (m_{ads}) using equation 3.17 or 3.18, however, is not performed in the current study as neither the exact volume of adsorbed CO_2 layer (V_{ads}) nor the density of the adsorbed CO_2 layer (ρ_{ads}) can be quantified using the employed experimental setup. It is worth noting that the adsorbed layer density profile varies spatially along the distance Z which is perpendicular to the solid surface and that the extent of the interfacial region cannot be known (Myers and Monson, 2014). The situation is exemplarily illustrated in figure 5.8 for 40 and 60 °C.

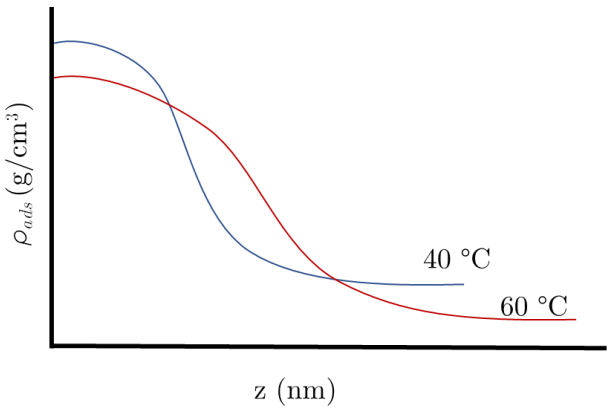

Figure 5.8 - Profile of the adsorbed layer density at the gas-solid interface.

Impact of surface chemistry and nature of the adsorbing gas: adsorption capacity depends on the strength of gas-gas and gas-solid interactions (Gonciaruk et al., 2021) which are dictated by the nature of adsorbate and the surface chemistry of the adsorbent (Mohammed and Gadikota, 2020). The shale sample under investigation is composed of a mineral matrix where calcite is the dominating mineral, and an insoluble organic fraction represented by kerogen. For Calcite, the affinity towards CO_2 and hence the tendency for CO_2 to adsorb is high (Gonciaruk et al., 2021; Mohammed and Gadikota, 2020). Calcite is made up of positively charged calcium (Ca^{2+}) ionically bonded to negatively charged carbonate (CO_3^{2-}). The partially positive Ca attracts species with negative or partially negative charges, while the partially negative oxygen atom of the carbonate attracts positively charged or partially positively charged species (Ataman et al., 2016). According to (Ralser et al., 2016), CO_2 is a roughly cylindrical molecule with a permanent quadrupole moment. This quadrupole moment corresponds to a slightly negative oxygen atom attracted to positively charged surfaces, and a slightly positive carbon atom attracted to negatively charged surfaces. Therefore, both CO_3^{2-} and Ca^{2+} constitute adsorption sites for CO_2 (Zhang et al., 2020), where CO_2 preferentially adsorbs on the latter due to higher electronegativity difference between O in CO_2 and Ca atoms compared to O of the CO_3 and C of the CO_2 (Carchini et al., 2020). On the other hand, the adsorption of CO_2 on calcite has been solely attributed to the interaction between CO_2 and the calcium ions in the works of (Mohammed and Gadikota, 2020; Santos et al., 2018; Tabrizy et al., 2013; Van Cuong et al., 2012).

Moreover, kerogen contributes significantly to the gas adsorption capacity of shale. In analogy to coal, the partially negatively charged groups of kerogen, such as carbonyl and carboxyl, constitute gas adsorption sites (Keshavarz et al., 2022). In addition to adsorption, CO_2 is absorbed by dissolution into the kerogen matrix (Gonciaruk et al., 2021), which further contributes to the amount of CO_2 retained in the shale. The electrostatic and dispersive molecular CO_2-shale interactions

appear to be strengthened by the strong quadrupole moment of the CO_2 molecule. Both electrostatic (columbic) and dispersive (Van der Waals) interactions were found to be significant in the case of CO_2 adsorption on kerogen (Sui and Yao, 2016), while electrostatic interactions between CO_2 and calcite were found to be dominating according to (Santos et al., 2018) and (Van Cuong et al., 2012).

Impact of structural properties: adsorption capacity further depends on the availability of adsorption sites which is directly related to the surface area (Liu, 2008; Mohammed and Gadikota, 2020). The surface area on its turn depends on the interrelation between pore volume and pore size. At a given pore volume, small pores generate high surface areas, implying higher availability of adsorption sites on the adsorbent to accommodate the adsorbate. Conversely, an increase in pore size at the same pore volume causes a decrease in surface area (Masika and Mokaya, 2012). Additionally, smaller pores, especially micropores, give rise to the overlapping of the attraction forces between the pore walls, which results in a stronger interaction with the adsorbing gas molecule (Broom and Thomas, 2013; Lowell et al., 2004). Organic-rich shales are characterized by a complex and heterogeneous pore structure, varying between micro, meso, macropores and fractures (Wei et al., 2016). In shales, the gas can either exist as a free phase in fractures, a free or an adsorbed phase in macropores (pore size>50 nm) which also provide flow paths for the gas into meso and micropores (Gasparik et al., 2015). The adsorption of gas in macropores starts with the formation of monolayer of gas molecules and progresses towards the formation of a multilayer of adsorbate (Memon et al., 2021). In mesopores (2-50 nm), and similar to macropores, the adsorption starts with a monolayer, followed by a multilayer of adsorbate forming as pressure is increased and eventually ends with the so-called capillary condensation (X. Wang et al., 2020). Capillary condensation is defined as the condensation of a gas below its saturation pressure and the formation of a meniscus within the pore. Lastly, in micropores, the adsorption mechanism is characterized by micropore filling. It is worth noting that these mechanisms apply

at conditions below the critical point (Choi et al., 2001). While the mesoporous Sultani shale has a surface area of around 2.25 m^2/g as measured by the BET method (see section 3.1.1.3), (Suekuni et al., 2022) report a surface area of 27 m^2/g in kerogen isolated from Jordanian shale, implying that the kerogen has a significant contribution in providing surface area for the gas to adsorb. A similar observation has been reported by (Zhao et al., 2017) who found higher surface area and pore volume in kerogen isolated from Neuquén shales compared to the original shale. Further insight into the contribution of Kerogen to gas storage in shale is presented in the following subsection.

Impact of Total Organic Carbon: In this section, the term sorption will be employed to incorporate both absorption and adsorption of CO_2. The sorption capacity has been found to positively correlate with the TOC content in the shale (Sui and Yao, 2016; Weniger et al., 2010; Wu et al., 2019; Zhao et al., 2017). This is because the oxygen, Sulphur and nitrogen-containing functional groups of the kerogen have a strong affinity to CO_2 (Wang et al., 2018). Further on, it is suggested that kerogen, due to its nanometer-sized pores (Pathak et al., 2017), provides large surface area for the intermolecular interaction with gas molecules (Pang et al., 2019). The impact of kerogen maturity on the sorption capacity has also been investigated. It was observed that high maturity shales possess higher sorption capacities per unit weight of TOC compared to immature shales. This is owing to the evolution of micropores in the organic matter upon its maturation, thereby increasing the surface area and the pore volume available for gas adsorption (Li et al., 2022; Ross and Marc Bustin, 2009). However, in immature shales such as Sultani, adsorption may not be the sole mechanism. For instance, (Ross and Marc Bustin, 2009) measured high gas sorption capacities in immature shales, however they found no correlation between the capacity and the pore volume, which implies that the CO_2 does not only adsorb but is also stored by means of absorption, i.e. dissolution into the organic matrix (Pang et al., 2019).

(Larsen et al., 2002) state that "Kerogens are cross-linked macromolecular systems. When contacted by a compatible fluid, the fluid dissolves in the solid polymer which expands to contain it". CO_2 absorption has been reported to cause kerogen swelling (Bakhshian and Hosseini, 2019; Tesson and Firoozabadi, 2019) which consequently results in changing the accessible pore volume and surface area. Kerogen swelling is positively correlated with the absolute amount of sorbed CO_2 (Pang et al., 2019; Yu et al., 2021).

(Pang et al., 2019) report a reduced pore volume upon kerogen swelling within confined slit pores. Therefore, kerogen swelling may reduce the amount of gas adsorbed in the pores by means of reduced pore volume, but its increase with increasing pressure, on the other hand, is an indication of higher amounts of gas absorbed/dissolved within the kerogen matrix. The two superposing effects are indistinguishable using the gravimetric method, however, by using the simplified local density model, Pang et al. found that the ratio of absorbed to adsorbed gas increases with increasing pressure and that adsorption dominates the overall sorption capacity of Barnett and Eagle Ford shale kerogens at pressures lower than 6 MPa, while at higher pressures absorption dominates.

The TOC content of Sultani shale is high (Li, 2022), which positively correlates with the adsorption capacity, and while the kerogen is immature, which may result in blocking the pores available for gas adsorption (Saidian et al., 2016), the contribution of absorption as an additional gas storage mechanism in Sultani shale cannot be ignored (Ho et al., 2018). It is generally stated that kerogen is responsible for the largest share of the sorption capacity in shales (Pang et al., 2019), nevertheless, the contribution of inorganic matter (minerals) should not be neglected (Wu et al., 2019) which is discussed in the following paragraph.

Impact of mineral composition: It has been reported that shales possessing a high content of calcite have higher adsorption capacities compared to shales where silicate minerals are predominant (Mohammed and Gadikota, 2020;

Tabrizy et al., 2013). This has also been confirmed by calculating the adsorption energies of CO_2 on both quartz and calcite where the latter is higher indicating higher affinity of CO_2 towards calcite (Budi et al., 2018). The calcite content of Sultani shale is high (see section 3.1.1.1), to which the high CO_2 adsorption capacity of Sultani shale can be attributed.

Additionally, the amount of clay minerals has also been positively correlated with the adsorption capacities of shale. This has been attributed to the layered crystal structure of Clay minerals which provides a significant share of mesopores (Ross and Marc Bustin, 2009) and large surface areas for gas adsorption (Klewiah et al., 2020; Rani et al., 2019b). In Sultani shale, the content of clay minerals varied and reached up to 17% in samples analyzed by (Sauerer et al., 2021), which further contributes to the CO_2 adsorption capacity of the shale.

Impact of moisture content: It has been frequently reported in the literature that moisture content negatively impacts the adsorption capacity of CO_2 (Klewiah et al., 2020; Rani et al., 2019b; Weniger et al., 2010). Through applying the density functional theory, (Carchini et al., 2020) were able to verify a stronger adsorption of water molecules to calcite surfaces compared to CO_2. This is attributed to the formation of strong hydrogen bonds between water molecules and oxygen atoms of the surface, which lowers site availability for CO_2 to adsorb. In a similar fashion, water adsorbed inside the kerogen matrix renders the moisture-filled organic pore volume ineffective for gas adsorption (Wang et al., 2018). The water, however, maybe displaced by CO_2 (W. Li et al., 2021; Wang et al., 2019), which is consistent with the findings of this work (See section 5.4.1). Additionally, it was found that the calcium atom of the calcite is attracted more strongly to the oxygen atom of the water molecule than the oxygen atom of CO_2 (C. Wang et al., 2020). Competitive adsorption between water molecules and CO_2 is not investigated in this study and is out of the current scope, however, to reduce the impact of moisture on adsorption, the investigated Sultani shale sample had undergone supercritical fluid extraction using CO_2 before the adsorption tests for

removing hydrocarbons and water. Further on, vacuum was applied to the sample prior to each test to eliminate the impact of any preabsorbed compounds on the adsorption capacity.

5.3 Diffusion

The apparent gas diffusion coefficient (representative of the overall diffusive mass transport mechanisms in the free and the sorbed phase within the porous media) at different pressures and temperatures was calculated based on the analytical solution proposed by (Crank, 1975) for Fick's diffusion and using the curve fitting method (see section 3.2.8). The results are shown in figure 5.9 and tabulated in Appendix C-Table C.7.

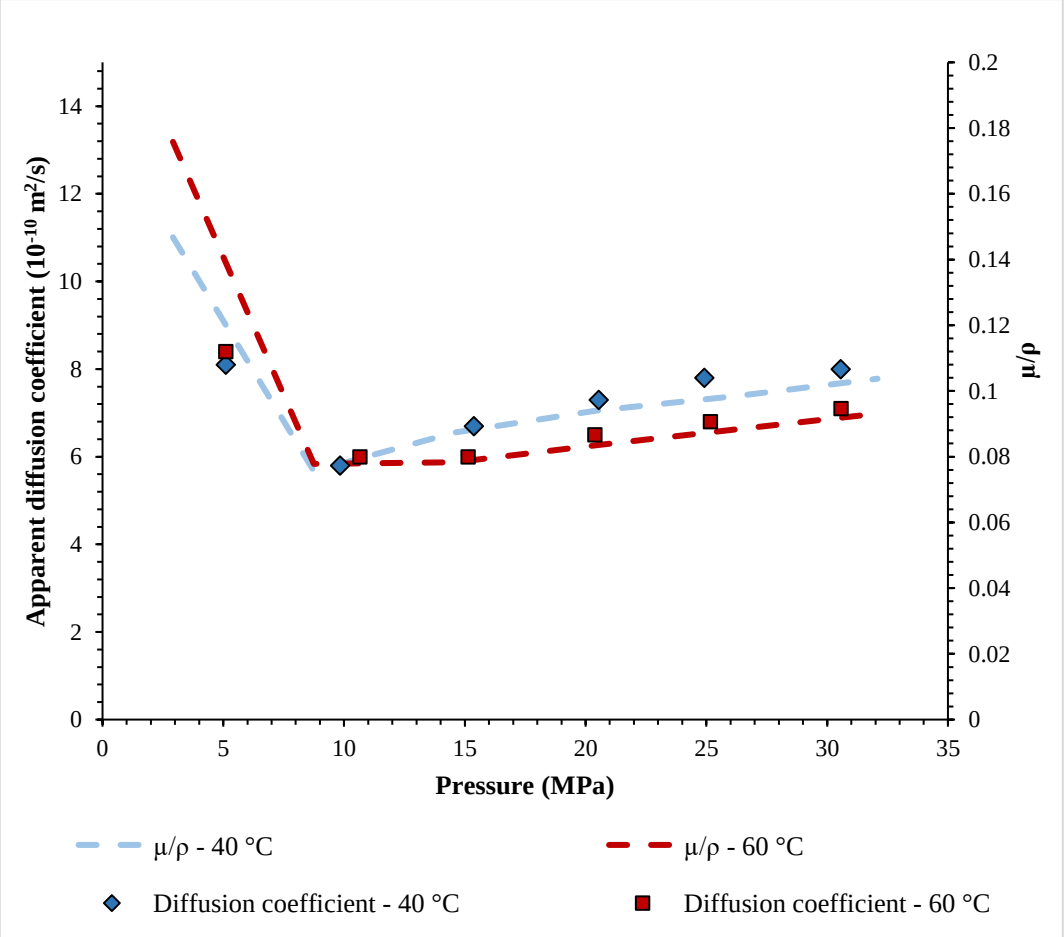

Figure 5.9 - CO_2 apparent diffusion coefficient as a function of pressure and temperature.

Impact of pressure: The diffusivities follow two distinct behaviors. the results show that as CO_2 transitions from the gaseous state into the supercritical state (5

to 10 MPa), the diffusion coefficient decreases. On the other hand, once the pressure exceeds 10 MPa, the CO_2 diffusivity tends to increase upon increasing the pressure. Molecular and/or Knudsen diffusivities decrease with increasing gas pressure due to the higher packing of molecules inside the pore. This is observed in the first segment of the diffusivity curve (5 to 10 MPa), implying that molecular and/or Knudsen diffusion dominate. However, the subsequent increase in diffusivity highlights another mass transport mechanism at elevated pressures, and that is surface diffusion. Surface diffusivity is reported to initially decrease with increasing surface concentration (adsorption)- a behavior observed as pressure is increased from 5 to 10 MPa- and then increase again with an increasing surface concentration (10 to 30 MPa) (Choi et al., 2001). The superposition at elevated pressures between molecular and/or Knudsen diffusivities and surface diffusivity results in the behavior observed at 10-30 MPa.

Impact of temperature: At 5 and 10 MPa, the diffusivity values at both temperatures are relatively similar (with a slightly higher diffusivity at the higher temperature). Conversely, at elevated pressures higher diffusivities are observed for the lower temperature (40 °C). Diffusion – regardless of the classification- is positively correlated with temperature. This would mean that the diffusivities are expected to be higher for the higher temperature across all experimental pressures. However, one more factor contributes to surface diffusivity specifically and that is the surface concentration. The lower apparent diffusivities at 60 °C and elevated pressures can be explained by the lower absolute adsorption capacities in comparison to those at 40 °C, i.e reduced surface concentration at the higher temperature, which is accompanied by a reduced surface diffusivity. The findings imply that surface diffusivity exhibits higher sensitivity towards surface coverage than temperature. The findings further confirm the significant contribution of surface diffusivity to the mass transport within shales at elevated pressures.

Kerogen swelling: Sorption-induced kerogen swelling influences the gas transport behavior in shale (Pang et al., 2019). The swelling is reported to reduce

the permeability of the porous media (Mazumder and Wolf, 2008; Wang et al., 2018) which will ultimately hinder the diffusivity of the gas. When kerogen is confined in a pore, its volume change upon gas dissolution will lead to pore shrinkage (Wu et al., 2019). Therefore, taking this phenomenon into account to justify the observed diffusivities is imperative. Kerogen swelling is reported to be a reversible structural change (Huang et al., 2020; Z. Li et al., 2021; Savest et al., 2007; Zhao et al., 2017). This is an important remark to establish that successive measurements conducted on the same sample will not influence one another. Second of all, kerogen swelling increases with increasing pressure in the low to moderate pressure range, reaches a maximum and then plateaus in the elevated pressure range due to the opposing effect of mechanical compression imposed by the bulk gas pressure (Bakhshian and Hosseini, 2019; Wang et al., 2018). Accordingly, the results seen in figure 5.9 maybe explained as follows: At 5 MPa and 60 °C, the sorption-induced swelling is relatively low and the diffusivity takes a value of 8.4 x 10^{-10} m^2/s, as the pressure is increased to 10 MPa, the diffusivity drops to 6 x 10^{-10} m^2/s due to pore volume reduction by means of higher kerogen swelling. As the pressure is further increased above 10 MPa, kerogen swelling plateaus and the impact of mechanical compression increases, to which the increasing diffusivity maybe attributed. The observed behavior is consistent in both isotherms.

In terms of temperature, no experimental studies have been reported in the literature regarding its' impact on kerogen swelling, while a positive effect on kerogen swelling is expected at lower temperatures (40 °C) due to higher absorption (solubility) of CO_2, the thermal expansion of the kerogen structure is higher at 60° C (Zhao et al., 2021). Hence, an unambiguous statement regarding the effect of temperature on kerogen swelling and subsequently on diffusivity cannot be made.

Gas self-diffusivity: Self-diffusion is a measure of the movement of molecules of the same species due to solely Brownian motion, where external driving forces

of mass transport such as pressure and concentration gradients are absent (Zmpitas and Gross, 2021). The experimental values qualitatively follow the first approximation of the rigid sphere model proposed by Chapman and Cowling in (Jost, 1952). This model estimates the coefficient of self-diffusion of the gas and is given by equation 5.1 below:

$$D_{11} = 1.2\frac{\mu}{\rho}, \qquad (5.1)$$

where μ and ρ are, respectively, the gas dynamic viscosity and density. Following equation 5.1 and in accordance with the experimental findings, the dynamic viscosity at lower temperature is the dominating effect at higher pressures. In the subcritical region, the viscosity at 40 °C is lower than that at 60 °C and will contribute to a lower diffusivity. Conversely, at supercritical conditions the viscosity at 40 °C is higher and will therefore result in a higher diffusivity. From this, it may be inferred that higher friction between molecules of the same specie enhances diffusion whereas it is well known that in binary diffusion (gas-liquid systems) the opposite occurs (Behzadfar and Hatzikiriakos, 2014; Unatrakarn et al., 2011), i.e. at lower temperatures, the viscosity of the liquid into which the gas diffuses increases and consequently limits gas diffusion (Renner, 1988). In studies conducted on the self-diffusion of CO_2 (Groß et al., 1998; Higashi et al., 2000; Takahashi and Iwasaki, 1966; Timmerhaus and Drickamer, 1951), it was reported that the diffusivity decreases upon increasing the pressure. The behavior reported here lies somewhere in between what has been reported regarding self-diffusivities of CO_2 and diffusivity of CO_2 through porous media. Therefore, there exists a superposition of several factors that render the mass transport phenomenon in shale an intricate subject. In order to infer an even clearer understanding of this phenomenon, the factors of influence need to be isolated and individually investigated, which is beyond the scope of the presented work.

5.4 Wettability

5.4.1 Ternary CO_2-Brine-Shale Systems

The contact angle of 3 wt% and 10 wt% NaCl brine on Sultani shale in a CO_2 atmosphere is presented in figure 5.10 below and the results are tabulated in Appendix C - Table C.8.

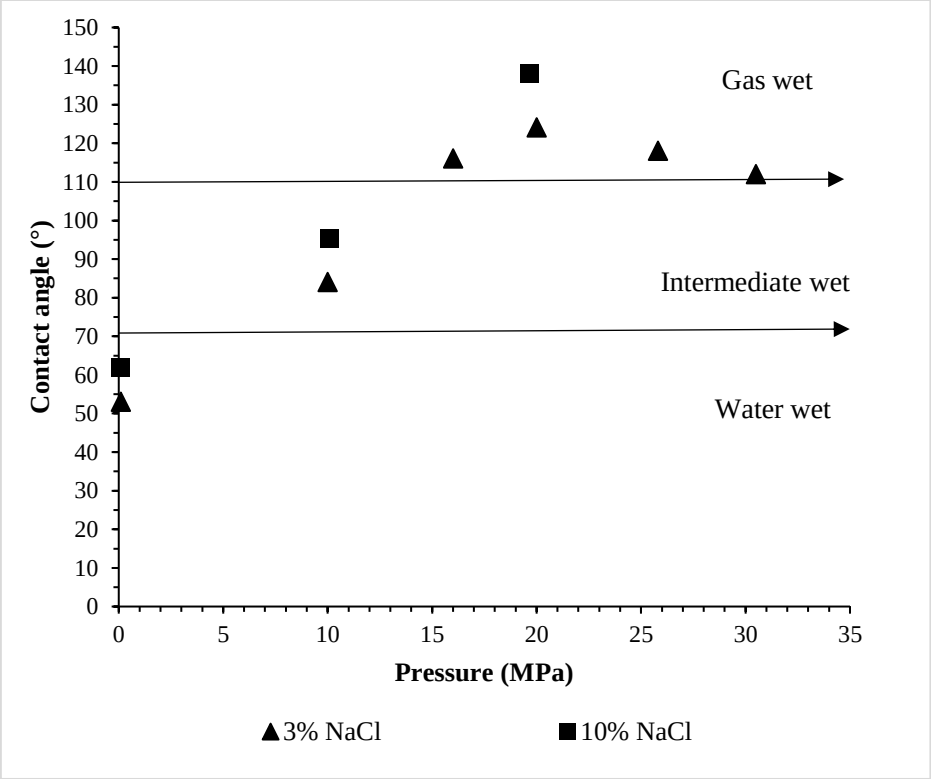

Figure 5.10 - Brine contact angle on Sultani shale as a function of CO_2 pressure at 60 °C.

Impact of pressure: It is observed that the brine contact angle increases with increasing pressure. Considering the 3% NaCl brine, this trend is seen for pressures ranging between 0.1 and 20 MPa where a maximum of 124° is found. At higher pressures, the contact angle drops. This can be attributed to the following: the contact angle is the result of the interrelation of the IFTs between CO_2-brine (γ_{lf}), CO_2-rock (γ_{sf}) and brine-rock (γ_{sl}) as indicated by young's equation (see equation 2.37 in section 2.4). By examining figure 5.7 (see section 5.2)**,** it can be seen that the adsorption capacity of CO_2 on the rock surface increases until a pressure of 20 MPa is reached, beyond which the adsorption capacity declines. The adsorption of CO_2 molecules on the rock surface reduces

the IFT between CO_2 and the rock surface (γ_{sf}) by means of higher CO_2- rock intermolecular interactions and results in a higher contact angle according to equation 2.37. On the other hand, figure 5.1 (see section 5.1.1.1) shows that the IFT between the CO_2 and the brine (γ_{lf}) reaches a minimum at 20 MPa. According to equation 2.37, γ_{lf} has a reducing effect on the contact angle at pressures below 20 MPa, but apparently the effect of γ_{sf} is more pronounced than that of γ_{lf} in determining the contact angle. All of this explains the transition of rock wettability from being water wet at atmospheric conditions to being intermediate or CO_2 wet at elevated pressures. This behavior is in line with the findings reported by (Arif et al., 2017a; Pan et al., 2020, 2018) who measured brine contact angles on shale in the presence of CO_2 and reported increasing contact angles at elevated pressures. The situation is illustrated in figure 5.11 for both a water wet and a gas wet system.

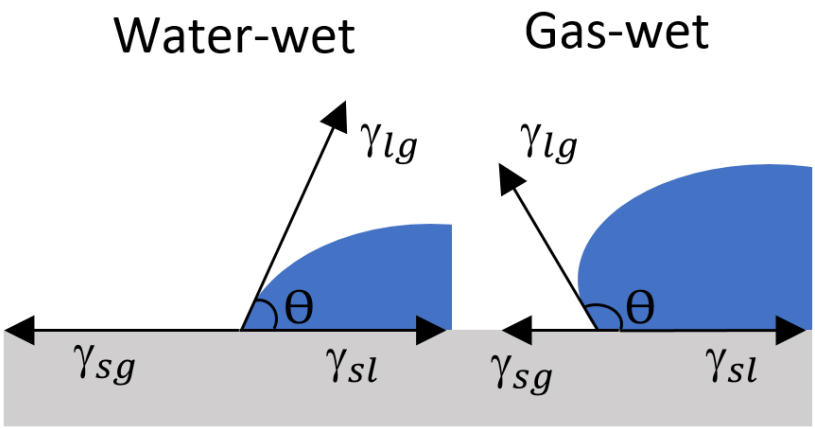

Figure 5.11 - Interfacial forces for a water-wet a gas-wet system.

Impact of salinity: From a general point of view, brine salinity does not seem to impact the wettability as the rock is classified as intermediate wet at 10 MPa and CO_2 wet at 20 MPa with both brines. However, the difference in contact angles in both brines can be attributed to the following: From equation 2.37, it can be seen that a higher γ_{lf} increases the contact angle. From figure 5.1, it is observed that $\gamma_{lf,10\%} > \gamma_{lf,3\%}$, which explains why the higher salinity brine exhibits higher

contact angles at similar pressures. This is in line with the findings of (Arif et al., 2017b) who showed higher contact angles for higher salinity brines on calcite, which is a major constituent of Sultani shale.

5.4.2 Ternary Oil-Brine-Shale Systems

In order to investigate the impact of formation water composition on the oil-water-shale wettability, the contact angle in a ternary oil-water/brine-shale system is investigated at atmospheric pressure and 60 °C. The aqueous phases investigated are: deionized water, 3 wt% NaCl brine (representing monovalent ions) and 3 wt% $CaCl_2$ brine (representing divalent ions). The results are shown in figure 5.12 below and tabulated in Table C.9 of Appendix C.

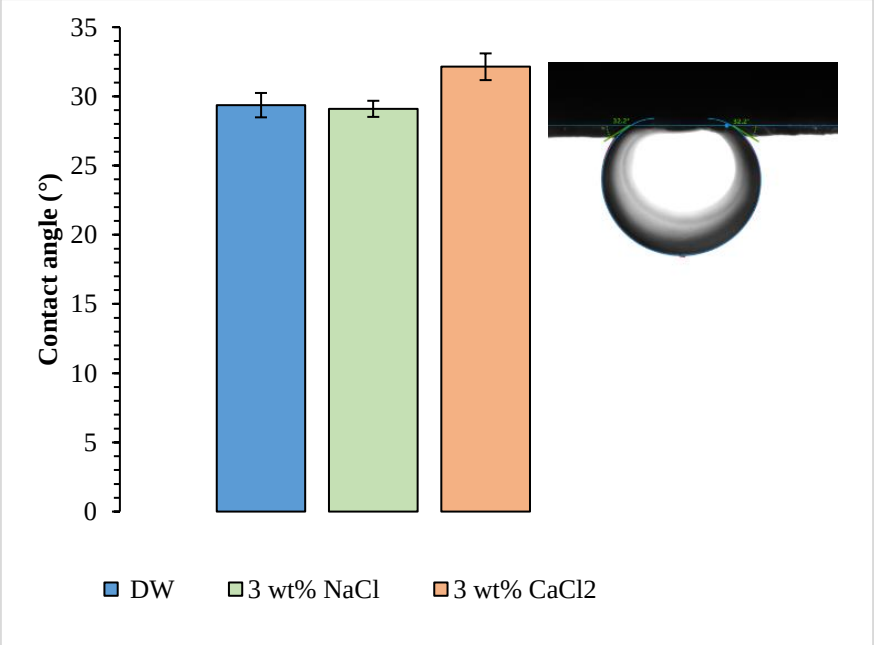

Figure 5.12 - Aqueous phase contact angles as a function of aqueous phase composition at 0.1 MPa and 60 °C.

It is observed that shale is strongly water wet in all aqueous phases. The aqueous phase contact angle in DW is measured to be around 29°. In NaCl brine, the average contact angle also takes a value of 29°. The presence of Na^+ ions in the water apparently has no impact on wetting, which is in line with the findings of (Roshan et al., 2016). (Pierre et al., 1990) state that NaCl behaves as an indifferent electrolyte. On the other hand, the contact angle of the $CaCl_2$ brine takes an

average value of 32°, exhibiting a slight tendency of lower water wetting although the behavior is not conclusive. This is also in line with what has been reported by (Roshan et al., 2016). Many attempts exist to understand the wetting behavior in terms of surface charges as being responsible for attractive or repulsive interactions developing at the electrolyte-solid interface. In order to understand the influence of the brine salinity and ion type on the evolution of the surface charge of the shale, zeta potential measurements of suspensions containing shale and aqueous phases with and without salts have been performed as demonstrated in figure 5.13. The results are tabulated in Table C.9 of Appendix C.

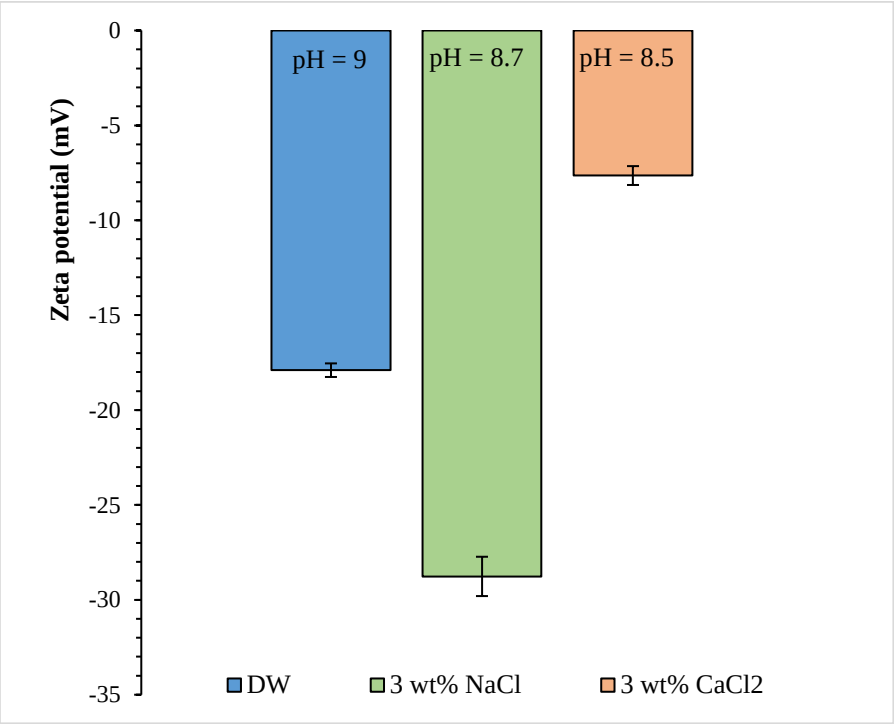

Figure 5.13 - Zeta potential of Shale-brine suspensions.

5.4.3 Interpretation of Shale Wettability based on Zeta Potential Measurements

Figure 5.13 indicates that the shale-brine interface is negatively charged under all the conditions investigated. This is reflected by the negative zeta potential values across all suspensions. Investigating the zeta potential in DW, it is seen that it takes a value of -18 mV at a pH of 9. Although the shale under investigation is majorly composed of calcite, the surface charge of shale under the examined

conditions does not follow that of pure Calcite. The isoelectric point (IEP) is defined as the pH at which the particles have no net flow in the presence of an electric field and therefore the zeta potential is zero (Almeida da Costa et al., 2020). The IEP of pure calcite suspended in DW is reported to be 9.5. Below a pH of 9.5, pure calcite is positively charged (El-Mofty et al., 2021; Vdović, 2001). In natural calcite, a negative zeta potential is observed below a similar pH (9.5) and is attributed to the presence of impurities such as clays, quartz and organic matter (Al Mahrouqi et al., 2017; Vdović, 2001), which is consistent with the mineral composition of shale and the TOC analysis listed in section 3.1.1.1. Therefore, at similar pH and electrolyte concentrations, the natural calcite exhibits a more negative surface charge than the pure calcite. In fact, natural calcite is reported to be negatively charged in the pH range of 5.5-11 (Al Mahrouqi et al., 2017).

With the addition of 3 wt% NaCl salt, the zeta potential becomes more negative, this is accompanied by a slight drop in the pH of the solution. Normally when the pH is constant, the addition of salt reduces the negative value of the zeta potential, i.e. the brine-calcite interface becomes more positive (Chen et al., 2014). A lower pH will also promote a more positive zeta potential (Al Mahrouqi et al., 2017). The superposition of the aforementioned should yield a more positive surface charge in the NaCl brine. The opposite, however, is observed and the exact reason thereof cannot be articulated as this can be the result of several overlapping effects including the dissolution of calcite in the aqueous phase, the amount of atmospheric CO_2 dissolved in the sample, and the presence of a highly complex organic matter. With the addition of $CaCl_2$ brine, the zeta potential becomes significantly less negative (or more positive) at a relatively similar pH, consistent with the earlier findings of (Jackson et al., 2016) and many others as reviewed and reported in the work of (Al Mahrouqi et al., 2017). This is attributed to the adsorption of Ca^{2+} ions on the shale, reducing its negative charge by means of

electrostatic screening with a much higher efficiency than Na^+ ions, owing to the divalence of the Ca^{2+} cation (Chen et al., 2014).

The measurement of zeta potential at the oil-brine interface was not performed in the current work due to the lack of the experimental means. Although scarce, available literature data were used instead. Model non-polar oils have been reported to have a negative charge by (Creux et al., 2009; Gray-Weale and Beattie, 2009; Maskari et al., 2019). For instance, the zeta potential of hexadecane-water emulsions at a pH of 9 was reported to take a value of around -90 mV according to (Stachurski and MichaŁek, 1996) and its magnitude reduces (becomes more positive) as the pH decreases. (Stachurski and MichaŁek, 1996) also report a positive correlation between the magnitude of the zeta potential and the alkane chain length. i.e. long chain alkanes have more negative zeta potential than short chain alkanes at similar pH. Therefore, and in accordance with what was reported by (Stachurski and MichaŁek, 1996), it is expected that at a pH of 8-9, the charge of the model oil- DW interface takes at least a value of -90 mV (disregarding the impact of temperature). No literature data exist on the impact of salinity on the zeta potential of model non-polar oils, however, crude oil-NaCl brine interfaces were investigated by (Collini and Jackson, 2021). They report that the zeta potential becomes more positive as the salt concentration increases. It is important to point out that the zeta potential is sensitive to the chemistry of the oil and that crude oils may exhibit a different behavior than pure alkanes due to the presence of surface-active species in the former.

Based on the previous discussion, and under the assumption that the pH of the aqueous phase during contact angle measurements takes a value above 5.5 (where natural calcite is negatively charged), the water wetness of the shale can be explained. As both the DW/brine-shale and the model oil-DW/brine interfaces are negatively charged, repulsion occurs and the electric double layer expands, promoting the water wetness observed in figure 5.12 (see section 2.5). On the other hand, the invariability of contact angles in different aqueous phases cannot

be solely justified by the zeta potential at the rock-brine interface and the zeta potential at the oil-brine interface has to also be considered.

In principle, an increased absolute sum of the zeta potentials of both interfaces, i.e. brine-rock and oil-brine, would reflect greater repulsive interaction (Tetteh et al., 2022), and a reduced absolute sum thereof would yield a lower water wetting by means of reduced repulsion (or increased attraction) of the interfaces. The absolute sum depends on the individual response of each interface when either the salt concentration, the ion type or the pH change. The contact angle measurements in figure 5.12 indicate that the change in the charge of each of the interfaces occurs such that the overall sum of the zeta potential does not change, i.e. no change in the interaction between these interfaces occurs.

On the other hand, skepticism is expressed regarding the relationship between the zeta potential of shale and wettability measurements. The grinding process of the shale during sample preparation for surface charge evaluation causes the redistribution of organic matter. This redistribution cannot reflect neither the arrangement nor the amount of organic matter in samples on which wetting tests are conducted, and where the organic matter distribution is inherently heterogeneous. This would ultimately result in an inconsistency between wetting and zeta potential measurements. Moreover, (Lu et al., 2017) claim that that zeta potential measurements do not reflect the electrical potential at the EDL, rather a region that is located far beyond it, consequently the properties of the EDL and its role in modifying the wettability may not be correctly accounted for. In general, and as a conclusion of the current research, it may be critically stated that the zeta potential as commonly measured has only a limited significance in explaining the wetting behavior and that there is still a lack in understanding.

5.4.4 Quaternary CO_2-Oil-Brine-Rock Systems

Figure 5.14 shows contact angle values as a function of CO_2 pressure and aqueous phase composition. The atmospheric values reported in figure 5.12 in the previous section have been included for facilitating the comparison. The results can be found in Table C.10 of Appendix C.

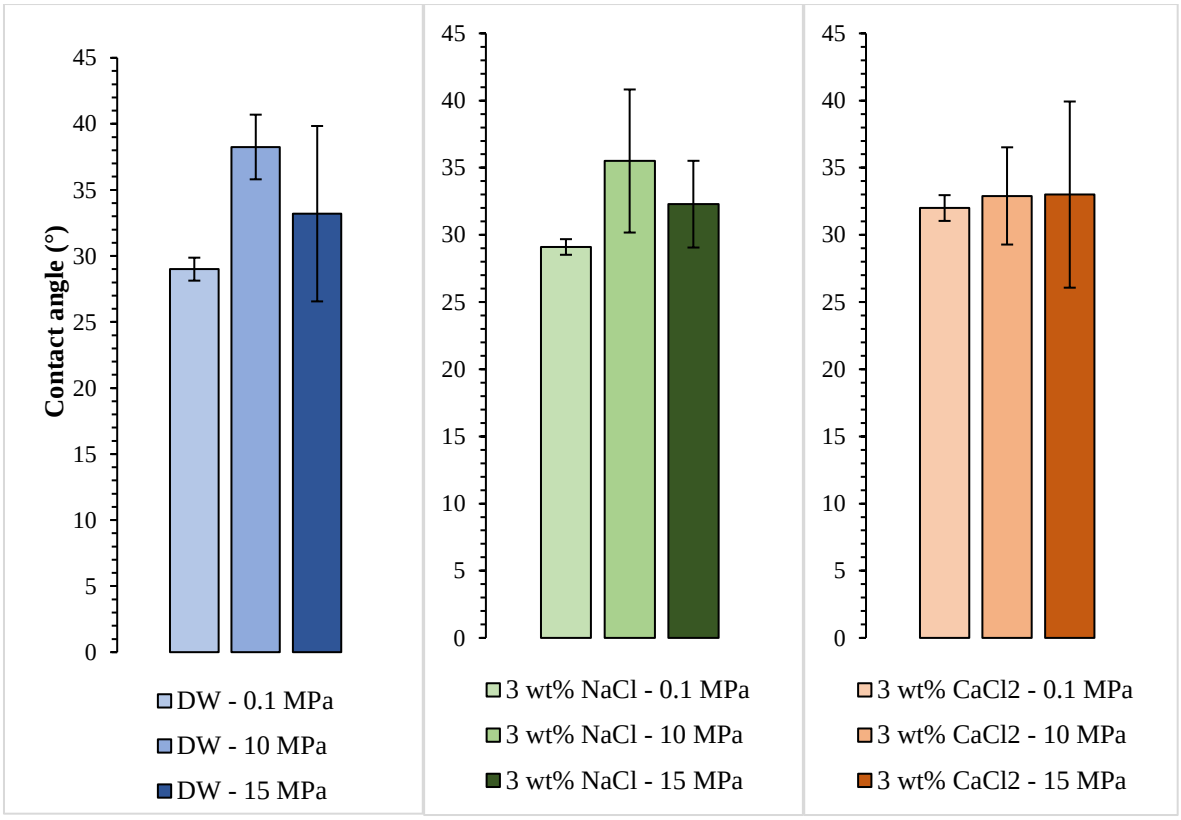

Figure 5.14 - Aqueous phase contact angles on shale as a function of aqueous phase and CO_2 pressure at 60 °C.

It is observed that there exists no clear trend regarding the wettability alteration of the shale upon introducing CO_2 into the system. In some samples, increasing the CO_2 pressure altered the sample to more water wet, while in others the contact angle increased, rendering the surface less water wet. In some cases, no change was observed at all. This variability of the measurements is shown by the error bars in figure 5.14. It would be expected for a surface where calcite is a dominating mineral that increasing the CO_2 pressure would always increase the hydrophilicity of the surface (higher water wetting). Therefore, additional measurements were conducted on a calcite crystal in DW using a simple alkane

(Hexadecane) at 60 °C to confirm the trend and rule out any measurement artifacts. The results are demonstrated in figure 5.15 and tabulated in Table C.11 of Appendix C.

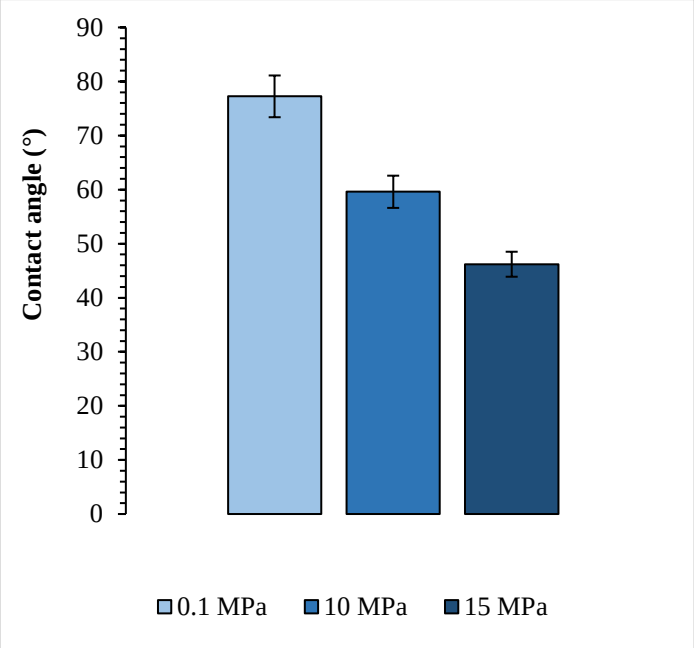

Figure 5.15 – Deionized water contact angles on Calcite as a function of CO_2 pressure at 60 °C. (Oleic phase: Hexadecane).

The calcite substrate indeed becomes more water wet upon CO_2 introduction into the system, in line with the findings of (Chen et al., 2018; Seyyedi et al., 2015) who also investigated the wettability alteration of pure calcite due to CO_2 dissolution. Note that the contact angles on pure calcite are higher than those measured on shale. This is justified by the more positive charge of the calcite-water interface in comparison to the shale-water interface as discussed in the previous sections.

When CO_2 dissolves into the aqueous phase, part of it forms carbonic acid (reaction 1) which consequently dissociates as per reactions 2 and 3 (Steel et al., 2016):

$$CO_2 + H_2O \longleftrightarrow H_2CO_3 \quad (1)$$

$$H_2CO_3 \longleftrightarrow HCO_3^- + H^+ \quad (2)$$

$HCO_3^- \longleftrightarrow H^+ + CO_3^{2-}$ (3)

The dissociations of the carbonic acid causes a reduction in pH (Haghi et al., 2017; X. Li et al., 2018), which ultimately influences the charge of the brine-rock and oil-brine interfaces. At 15 MPa and 60 °C, the pH of pure water due to CO_2 dissolution is found to be around 3 (Peng et al., 2013).

The reduction in pH is accompanied by the domination of positive species ($>Ca^{2+}$, $>CaOH^+$ and $>CaHCO_3^+$) on the calcite surface (Somasundaran and Agar, 1967; Thompson and Pownall, 1989; Vdović, 2001), rendering the surface of the calcite crystal more positive. As stated earlier, pure calcite is positively charged below a pH of 9.5 (Somasundaran and Agar, 1967). Simultaneously, the charge at the oil-brine interface becomes increasingly positive at low pH. For hexadecane, the pH at which the surface charge becomes zero is reported to be at pH of 2 – 4, below which the interface becomes positive (Beattie and Djerdjev, 2004; Stachurski and MichaŁek, 1996). Therefore, when both interfaces become more positive, and in accordance with the theory of EDL, the absolute sum of the zeta potential increases and repulsion occurs. Consequently, the electric double layer expands giving rise to the observed higher water wetting. (Xie et al., 2017) attribute the increased water wetness of calcite to the simultaneous adsorption of H^+ ions on both the oil-brine and brine-rock interface, rendering each of them more positive.

Several other mechanisms have been proposed to justify the wettability alteration of calcite due to CO_2 injection. (Al-Mutairi et al., 2014) justify the higher water wetting to the replacement of adsorbed oil molecules by CO_2. Alternatively, the oil-brine IFT decreases in the presence of CO_2 (see section 5.1.2). According to Young's equation (see equation 2.37), $\gamma_{ob} Cos\theta = \gamma_{so} - \gamma_{sb}$, a reduction in γ_{ob} will result in a lower contact angle (Jaeger et al., 2010; Yang et al., 2008). Additionally, calcite dissolution was observed as the surface of the calcite sample changed from a smooth to a rough surface after exposure to carbonated water. This may also explain the increased water wetting as follows: below a pH of 6,

the rate of calcite dissolution significantly increases (Dolgaleva et al., 2005; Mahani et al., 2017b; Pokrovsky et al., 2005). This dissolution causes the oil adsorbing to the surface of the calcite to break free and this results in higher water wetting. The situation is presented in figure 5.16.

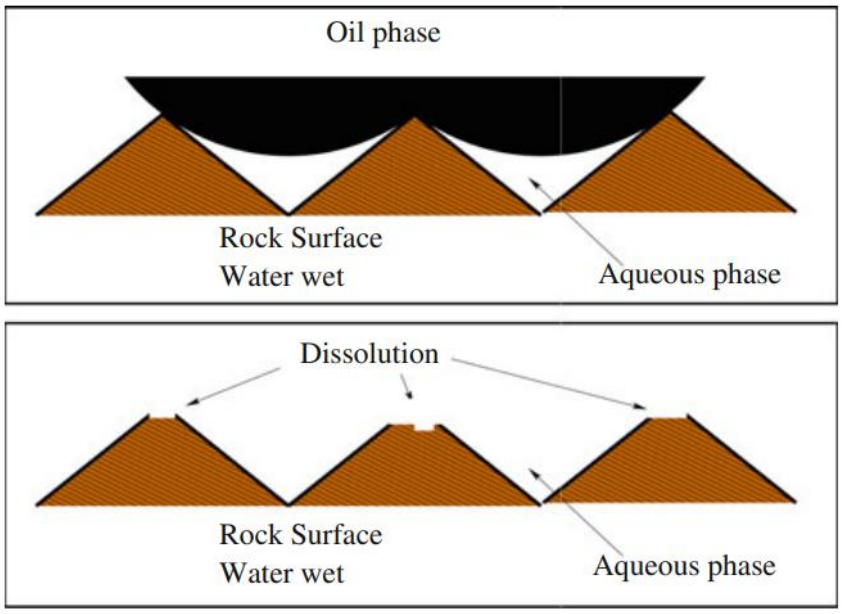

Figure 5.16 - Increased water wetting due to calcite dissolution, adapted from (Hiorth et al., 2010), reused with permission.

Returning to shale, it is imperative to make a statement on the heterogeneity of the shale in terms TOC. This heterogeneity is confirmed by the analysis performed by (K. Li et al., 2019) who measured a varying TOC content of samples collected from the same location. The TOC in the samples investigated by Li ranged between 10% to 21%. Since each wettability measurement was conducted on a fresh sample, the TOC variability among the tested samples also exists and cannot be controlled. In any case, there are superposing effects taking place in systems with TOC-rich shales that result in a nearly invariable wettability at increasing CO_2-pressure. Based on the mass transport mechanisms and phase behavior investigated throughout this work, the particular wetting behavior can be explained as follows: The hydrocarbons inherently present in shale are swollen (see section 6.2) and possibly expelled by means of $scCO_2$ entering the shale by diffusion. In this way they are brought into contact with the surface. This process

is aided by mineral dissolution from the surface. Figure 5.17 shows contact angle evolution due to CO_2 diffusion and the subsequent swelling/expulsion of oil.

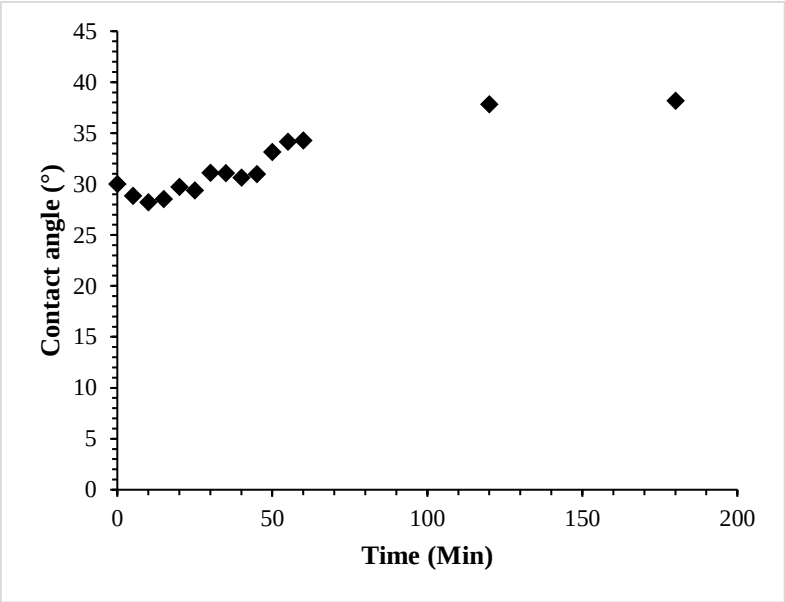

Figure 5.17 - Contact angle evolution in DW at 10 MPa and 60 °C.

The diffusion of CO_2 into the pores, the swelling of organic matter, the loss of hydrocarbons from the surface (indicated by a lighter surface color), and the dissolution of surface minerals (calcite) are confirmed by the observations demonstrated in figure 5.18. Figure A shows formation of gas bubbles on the surface of the shale due to CO_2 desorption from the pores upon depressurization. Figures 5.18- B and C show the surface of the shale with a magnification factor of 100 times: B. before the captive bubble test and C. after a captive bubble test. The images were taken using a digital microscope (VHX0-970, Keyence GmbH, Germany).

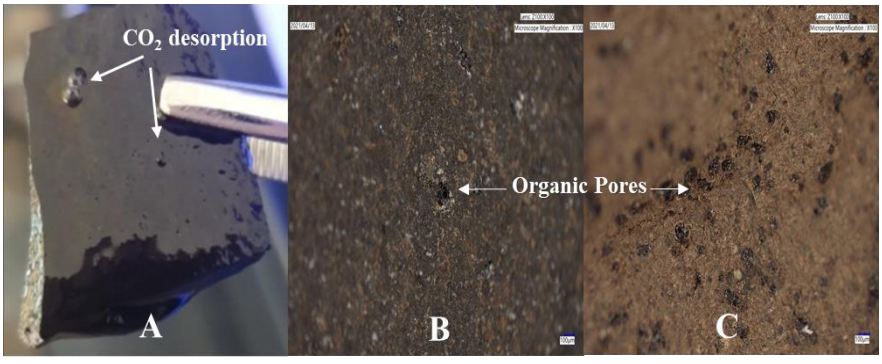

Figure 5.18 - A: CO_2 desorption, B: pre-exposure to CO_2 and C: post exposure to CO_2.

To further investigate this phenomenon and to isolate the impact of hydrocarbon swelling/expulsion during the measurement, tests were conducted on a sample that had been previously extracted with $scCO_2$ at 30 MPa and 60 °C for 48 hours. The results were compared with the wetting tests performed on a native sample. After the extraction, the surface of the sample was cleaned with acetone and the contact angle was reassessed via captive bubble tests at 0.1 MPa and 15 MPa in a 3 wt% NaCl brine. The contact angle values are shown in figure 5.19 and tabulated in Appendix C-Table C.12.

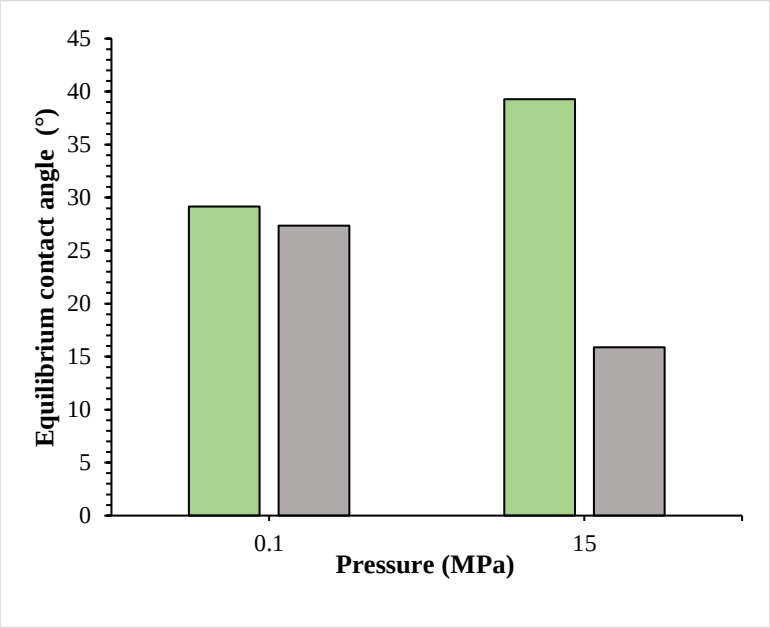

Figure 5.19 - NaCl brine contact angle on shale samples as a function of pressure at 60 °C (Green: original sample, grey: extracted sample).

The contact angle barely exhibits a change in comparison with the native sample at atmospheric pressure. Therefore, it is difficult to assess whether this is the result of the extraction as the contact angle falls within the experimental error of previous measurements. On the other hand, examining the contact angle evolution at 15 MPa on the extracted sample reveals a clear reduction compared to the value measured at 0.1 MPa (27° versus 15°). For the native sample, the contact angle at 15 MPa is higher than that measured at 0.1 MPa, exhibiting reduced water wetting. Further on, it takes a value of around 40°, a higher value than that measured on the extracted sample (15°) at 15 MPa. These observations confirm

the role of pore hydrocarbons on the evolution of the contact angle. No conclusive result is reached regarding the impact of salinity and ion type as the degree of wettability alteration in shale highly depends on the amount of TOC (Jia, 2019). The shale, however, exhibits strong water wetting under all investigated conditions.

6. Phase Behavior

6.1 Density

6.1.1 Density of Pure Substances

In this section, the densities of pure substances as measured using the experimental setup described in section 3.2.9 are presented and discussed.

6.1.1.1 Density of Brines

The density of NaCl brine is measured as a function of pressure and salt concentration at 60 °C and is demonstrated in figure 6.1 below. The experimental values are also presented in Appendix D - Table D.1.

At a given pressure, it can be seen that density is positively correlated with salinity. The increase in density upon increasing the salinity is attributed to a higher increase in solution mass in proportionality to the increase in solution volume when salt is added to the water. At 5 MPa, for example, the density of the 1% NaCl solution is measured to be 0.987 g/cm^3, while for the 10% NaCl brine, the density is 1.036 g/cm^3 at a similar pressure.

Investigating the impact of pressure for a given NaCl salt concentration, it is observed that increasing the pressure increases the density of the brine. This is due to the fact that the intermolecular spacing between the molecules is reduced when pressure is applied, i.e. the volume occupied by the solution reduces and therefore the density increases. Additionally, it is observed that the slope of the density curve is highest up to pressures of 2 MPa. At pressures above that, the slope of the density curve reduces. This is attributed to the following; as the pressure increases, the brine becomes less and less compressible. The results are further compared to densities of pure water obtained from NIST(Wagner and Pruß, 2002), with which there is good agreement. A similar method was employed by (Li et al., 2004) to measure the density of deionized water and Weyburn brine (9.295 wt%) at 59 °C. Their reported values as seen in figure 6.1 are higher for

both deionized water and Weyburn brine. The reason for this discrepancy is not clear.

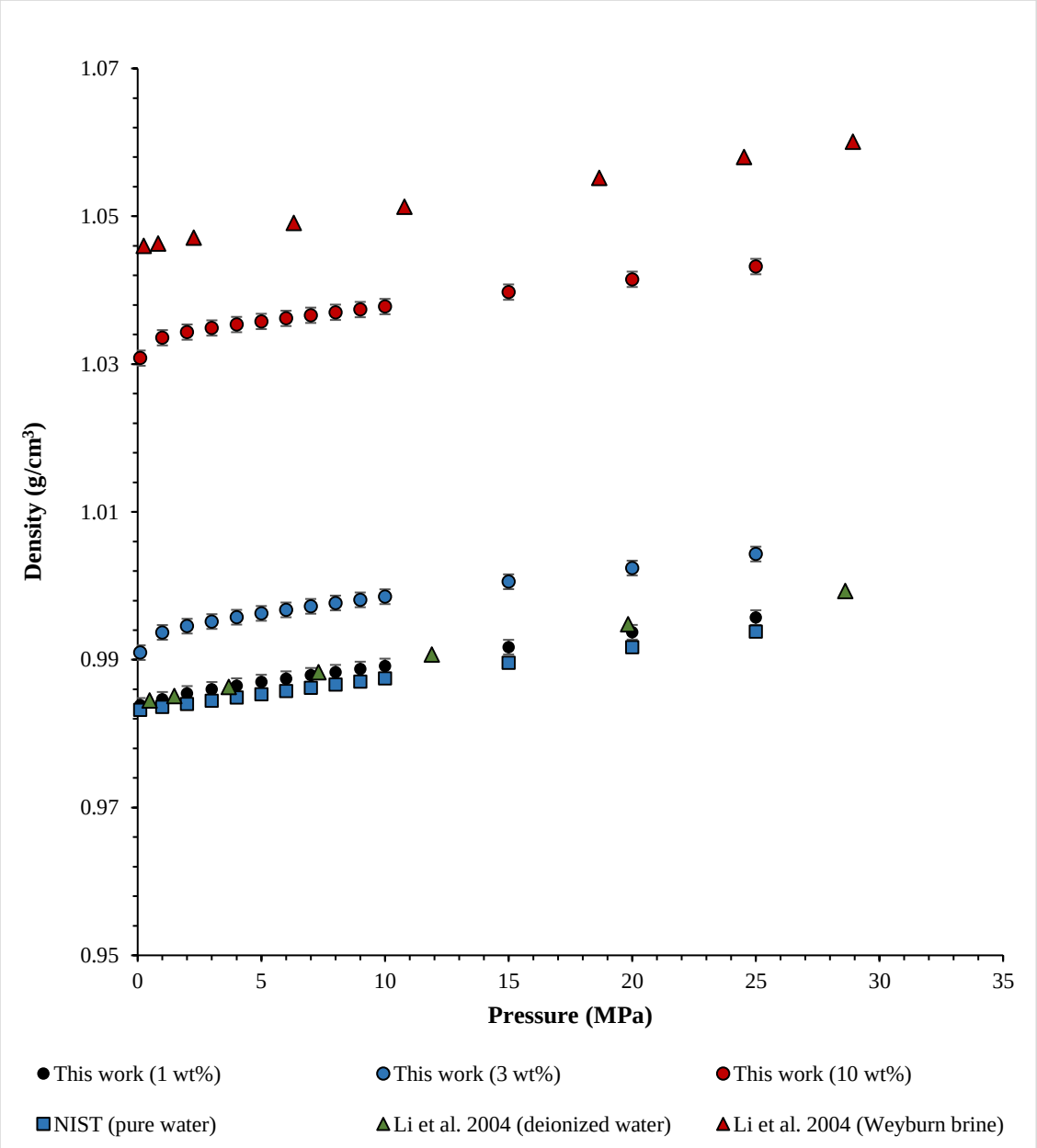

Figure 6.1 - Densities of NaCl brines as a function of pressure and salinity at 60 °C.

6.1.1.2 Density of Oils

The densities of both model oil and hexadecane as a function of pressure at 60 °C are shown in figure 6.2 and the corresponding values are reported in Appendix D - Table D.2. Similar to brines, increasing the pressure increases the density of the oil due to the reduction of the intermolecular spacing between the alkane molecules. Furthermore, the slope of the density curve is highest in the range

between 0.1 and 2 MPa. As the pressure is increased further, the steepness of the slope reduces due to the reduced compressibility of the oil.

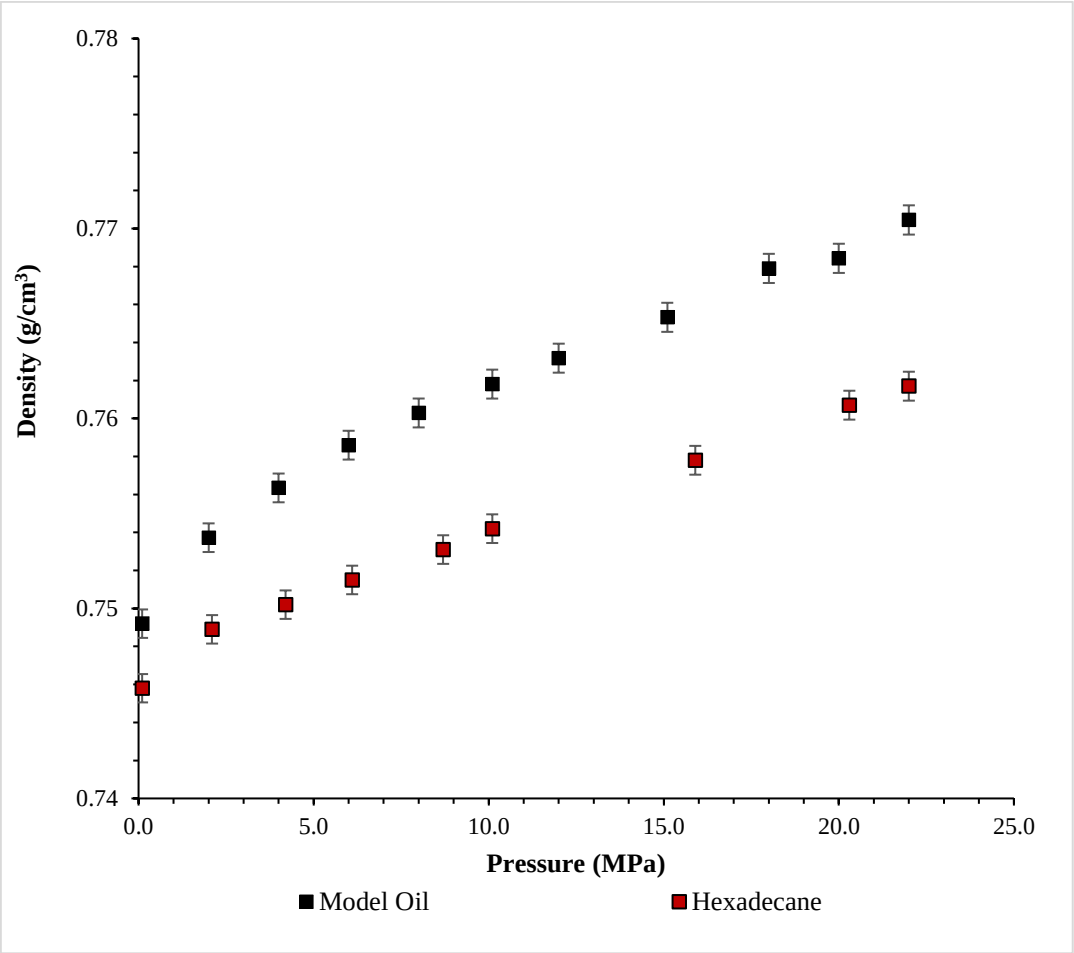

Figure 6.2 - Density of the model oil and Hexadecane as a function of pressure at 60 °C.

6.1.2 Density of Binary Systems

In this section, the densities of binary CO_2-brine and CO_2-oil systems are presented and discussed.

6.1.2.1 Densities of CO_2-saturated Aqueous Solutions

The densities of aqueous solutions saturated with CO_2 were measured experimentally using the method presented in section 3.2.9 and were also modeled using the correlation proposed by (Li et al., 2011) using equation 6.1 below:

$$\rho = [1000 + 58.4428\, m_{NaCl} + 44.0098\, m_{CO2}] / \left[\frac{1000+58.4428\, m_{NaCl}}{\rho_B} + \frac{18.0153.(1+k) m_{CO2}}{\rho_w}\right] \quad (6.1)$$

k is a coefficient that is pressure and temperature dependent and can be calculated using equation 6.2.

$$k = a_1 T^2 + a_2 T + a_3 + a_4 T^{-1} + a_5 T^{-2} + [a_6 T^2 + a_7 T + a_8 + a_9 T^{-1} + a_{10} T^{-2}]\, P \quad (6.2)$$

where T and P are temperature and pressure in Kelvin and bar, respectively. Parameters a_1 through a_{10} are listed in Appendix A - Table A.3.

Further, ρ_B is the pure phase density of the NaCl brines which are experimentally determined as reported in section 6.1.1.1. ρ_w is the density of pure water and is taken directly from NIST (Wagner and Pruß, 2002) at the corresponding P and T conditions.

m_{NaCl} and m_{CO2} are the molalities of NaCl and CO_2 in the solution in mol/kg, respectively. The molality of NaCl in the brine is calculated through equation 6.3 below:

$$m_{NaCl} = \frac{mass\ of\ suspended\ NaCl\ salt\ in\ 1\ kg\ of\ water}{molar\ mass\ of\ NaCl} \quad (6.3)$$

The molality of CO_2 (m_{CO2}) in the aqueous solutions is calculated using the model proposed by (Duan et al., 2006) as reported in section 3.2.10.1**.** The modeling results are presented in the section 6.3.1. Figure 6.3 shows the experimental and modeled densities of CO_2 saturated aqueous solutions as a function of pressure and aqueous phase composition. The values are reported in Appendix D - Table D.3.

The experimental densities are further compared to CO_2-saturated pure water densities at similar conditions as reported by (Hebach et al., 2004). It is observed that higher CO_2 pressures result in higher brine densities due to higher CO_2 solubility (see section 6.3.1), which is in line with the findings of (Chiquet et al.,

2007) and (Zhang et al., 2016). According to (Sato et al., 2000) a hydrogen bond is formed between the Oxygen atom in the CO_2 and the hydrogen atoms of water. An interaction between the carbon atom of CO_2 and the oxygen atom of water also exists. These interactions are strengthened with pressure resulting in the observed higher densities.

Compared to measured and literature values, those reported by (Li et al., 2004) appear to be slightly high for both binary mixtures. Their CO_2- saturated deionized water densities are higher than those reported by (Hebach et al., 2004) and their CO_2-saturated Weyburn brine densities -where the salt concentration is 9.295 wt%- are also higher than the values reported in this work. The values of (Hebach et al., 2004), however, show good agreement with the findings of the work at hand. Moreover, the model proposed by (Li et al., 2011) seems to be appropriate for very low salt concentrations (1 wt% NaCl), however, as the salt concentration increases, the density of the CO_2-saturated brine is underestimated. It is not quite clear whether this underestimation stems from Duan's model which is predictive of CO_2 solubility in aqueous solutions or Li's model itself, therefore, the experimental solubility data reported by (Bando et al., 2003) is used to investigate the validity of Li's model.

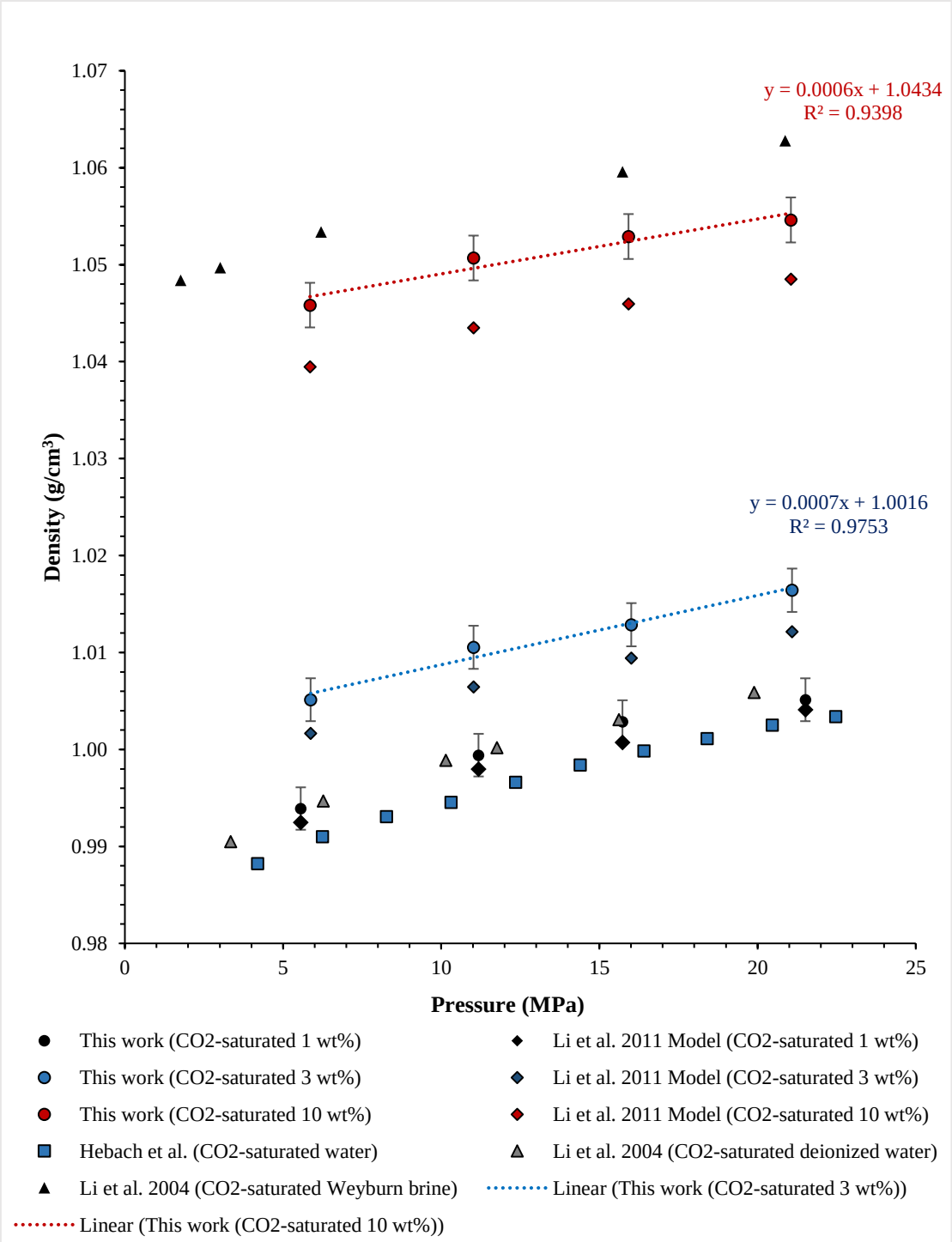

Figure 6.3 - Experimental and modeled densities of CO_2-saturated NaCl brines as a function of pressure at 60 °C.

Figure 6.4 shows the difference between the experimental brine densities reported in this work, the calculated densities using Li's model based on both the solubilities of Duan (modelled) and Bando (experimental). The calculation of density based on experimental solubility data for the 1% NaCl brine at 5 MPa

(subcritical) yielded excellent agreement with the experimental density values. At a similar pressure and higher salinity and at a similar salinity and higher pressure this agreement diminishes. On the other hand, no pronounced difference can be seen between densities calculated using either Duan's model or Bando's experimental solubility data, as both exhibit close agreement, especially above the critical pressure of CO_2 (See Table D.6 in Appendix D). These observations show that Li's model slightly underestimates the density of CO_2-saturated brines at high salinities.

As a general conclusion, it can be stated that higher pressures not only lead to higher CO_2 solubilities but also to higher densities. For example, at 21 MPa, the density of the gas-saturated 10 wt% NaCl brine takes a value of 1.055 g/cm^3, whereas the density of the respective pure phase (without gas) is in the range of 1.042-1.043 g/cm^3.

A regression model is presented in figure 6.3. In this way, interpolated data may be used for scenarios that do not match the experimental conditions investigated in this work, or for the evaluation of IFT in binary and ternary systems (see section 5.1.1.1 and section 5.1.2), which was conducted at slightly different pressures.

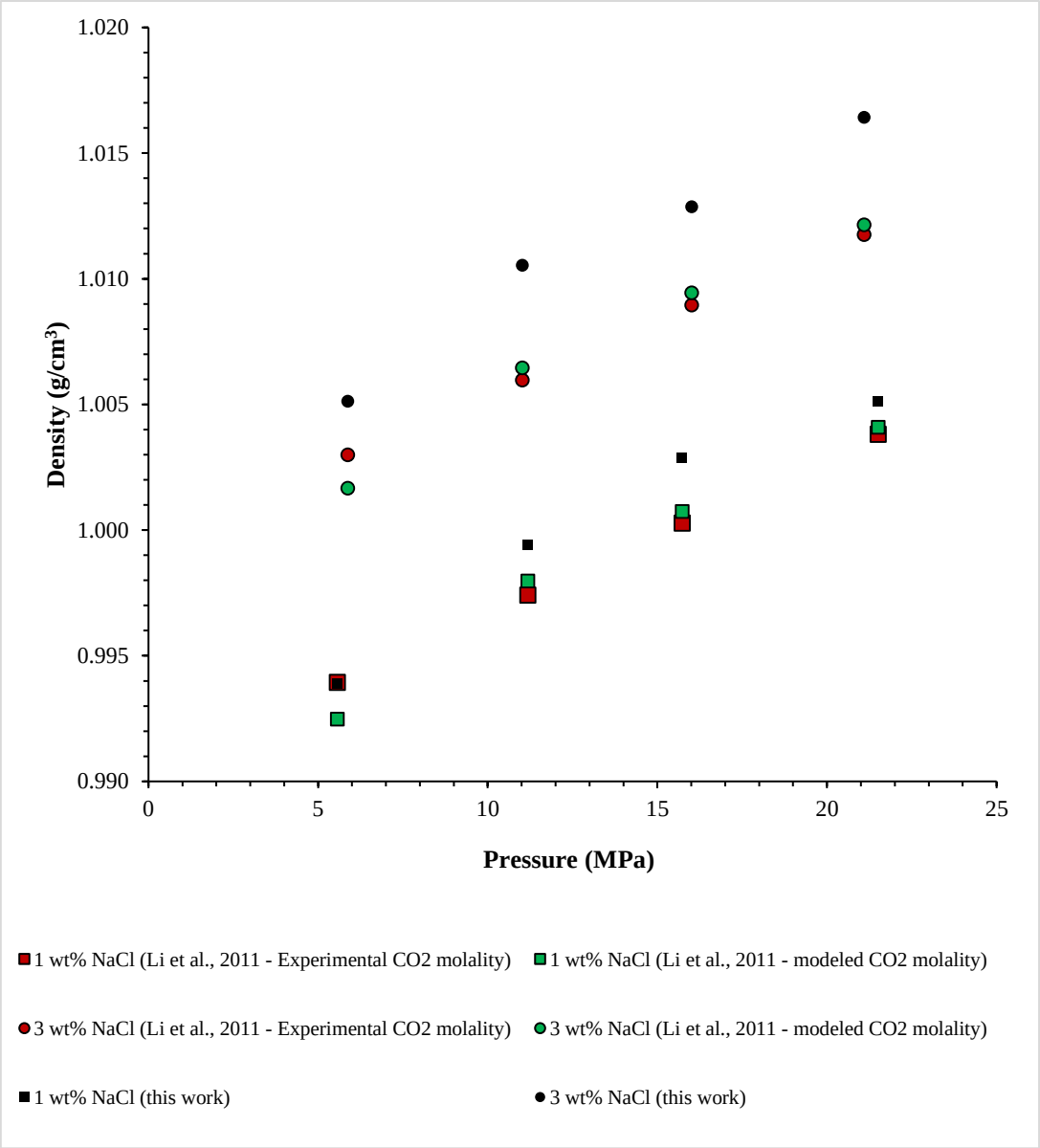

Figure 6.4 - Comparison of density values calculated using experimental and modeled CO_2 solubilities at 60 °C.

6.1.2.2 Densities of CO_2-saturated Oils

The densities of CO_2-saturated model oil and CO_2-saturated Hexadecane were measured as a function of pressure at 60 °C. The results are demonstrated in figure 6.5 and reported in Appendix D - Table D.4. It is observed that as the pressure increases, the densities of both systems increase to a higher extent in the presence of CO_2 compared to systems where only pressure is applied (See section 6.1.1.2). For instance, at 10 MPa, the density of the pure model oil is measured to be 0.7618 g/cm^3, while for the CO_2-saturated model oil it is 0.7798 g/cm^3. At 10 MPa the pure hexadecane density is 0.7542 g/cm^3 and the CO_2-saturated hexadecane has a density of 0.7714 g/cm^3 (Pure phase densities of hexadecane are reported again in figure 6.5 to facilitate comparison). This is in line with the findings of (Habibi et al., 2017) who measured the density of CO_2-Montney light crude mixtures and (H. Li et al., 2013) who measured the density of CO_2-Lloydminster heavy oil mixtures. (Lansangan and Smith, 1993) attribute the density increase in the binary system to the compact reorientation of hydrocarbon molecules upon CO_2 introduction into the liquid. The linear CO_2 molecule possesses a strong permanent quadrupole moment. This strong quadrupole moment significantly affects the thermodynamic properties of CO_2 molecules in comparison to other non-polar molecules having similar size and molecular weight. Alkanes, on the other hand, are symmetric non-polar molecules with no permanent dipole. Owing to the fact that the electron clouds of non-polar molecules can move from their original location, they create instantaneous dipoles that result from the oscillation of negative charges about the positive charges of a molecule (Donaldson and Alam, 2008). This causes the molecule to experience a temporary separation of charges, resulting in an instantaneous dipole moment accompanied by an instantaneous electrical field capable of polarizing neighboring atoms and molecules (Israelachvili, 2011; London, 1937; Maitland et al., 1981). The electron clouds of adjacent molecules synchronize momentarily, and the instantaneous dipoles orient themselves in an attractive configuration that lowers the total

energy of the engaged molecules (Donaldson and Alam, 2008). As a result, an instantaneous attractive force exists between the molecules. This intermolecular attractive force is termed the London dispersion force (also referred to as instantaneous dipole-induced dipole force) and it exists between alkane molecules. Molecular dynamic simulations have been performed based on this molecular interaction to describe the volumetric expansion and density in CO_2-alkane systems (C. Li et al., 2019; Liu et al., 2015; Yang et al., 2012). With its strong permanent quadrupole moment, CO_2 molecules stimulate this instantaneous polarity of hydrocarbon molecules by means of quadrupole-induced dipole interaction. As a result, the superposition of attractive coulombic forces and London dispersion forces occurs. Consequently, denser packing of molecules in a quasi-lattice structure is manifested macroscopically, giving rise to the observed increase in density (Lansangan and Smith, 1993).

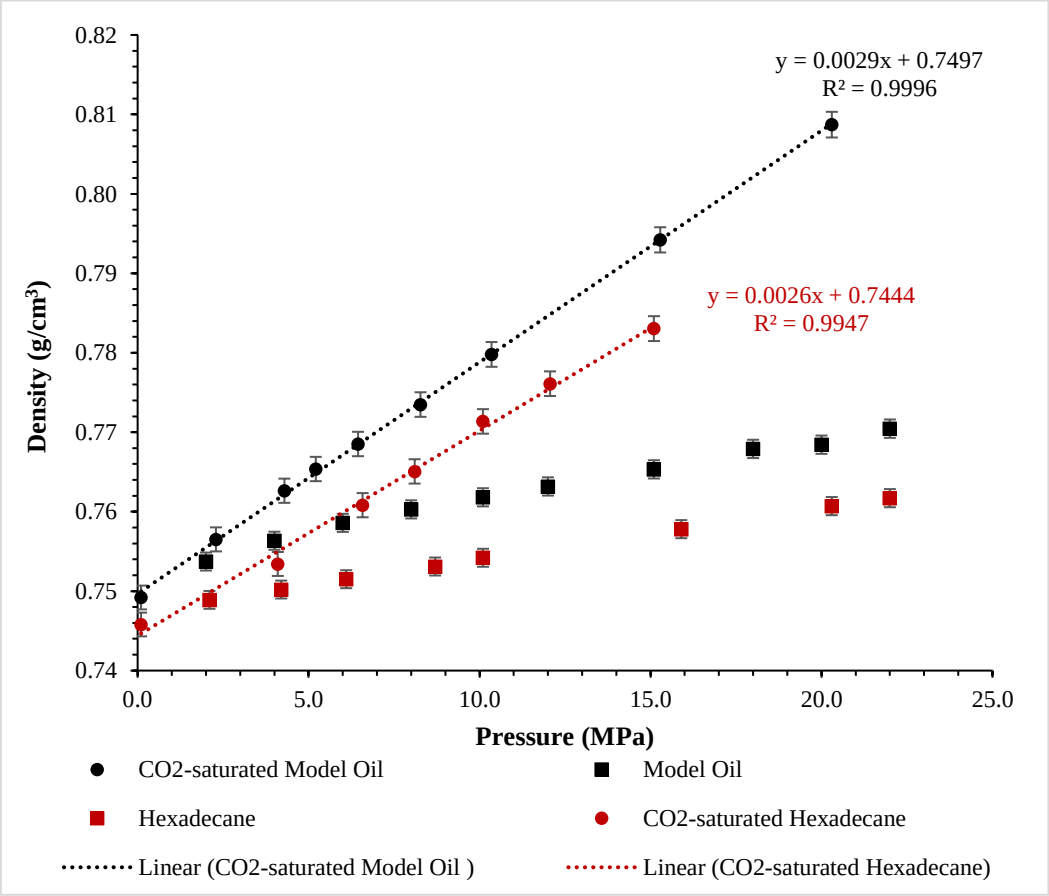

Figure 6.5 - Experimental densities of CO_2-saturated model oil and CO_2-saturated Hexadecane as a function of pressure at 60 °C.

6.2 Volumetric Expansion

Volumetric expansion of oil drops due to CO_2 dissolution has been measured using the experimental setup described in section 3.2.5 in a quaternary system containing calcite-oil-water/brine and CO_2. The results thereof are demonstrated in figure 6.6 and tabulated in Table D.5-A in Appendix D.

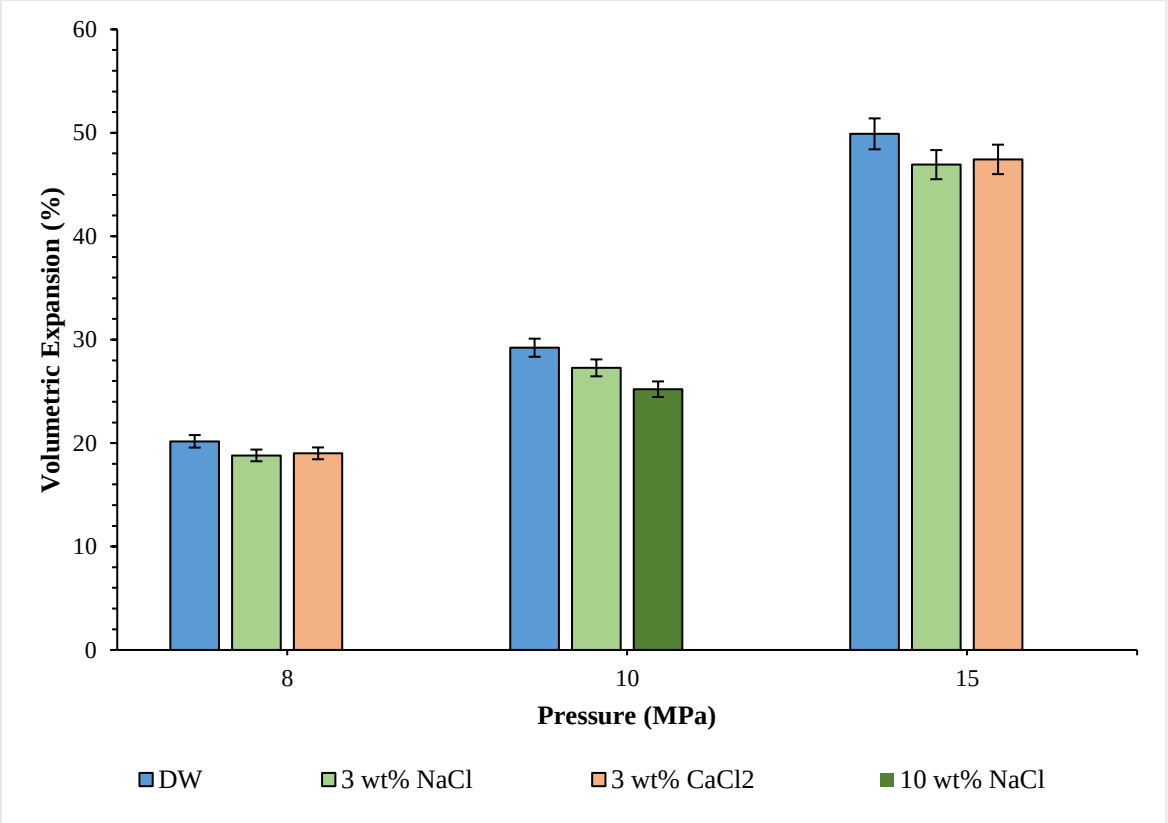

Figure 6.6 - Volumetric expansion of model oil as a function of pressure and aqueous phase composition at 60 °C and equilibrium.

It is observed that volumetric expansion is directly proportional to pressure regardless of the composition of the aqueous phase. At higher pressure the solubility of CO_2 in the aqueous phase increases (See section 6.3.1). At equilibrium, CO_2 is distributed between both phases according to the specific partitioning coefficient at the respective conditions. In general, a higher concentration of CO_2 in the aqueous phase implies a higher concentration of CO_2 in the oleic phase. On the other hand, phase equilibria can be described by postulating a constant fugacity of component I, in this case CO_2, in all participating phases. According to the theory of chemical thermodynamics,

fugacity of CO_2 in all participating phases at equilibrium is given by equation 6.4 (Gmehling and Kolbe, 1992):

$$f_{CO_2}^{v} = f_{CO_2}^{w} = f_{CO_2}^{o} \quad (6.4)$$

where v is the CO_2 phase, w is the aqueous phase and o is the oleic phase. The fugacity of CO_2 in each phase is expressed in equations 6.5 through 6.7 below:

$$f_{CO_2}^{v} = y_{CO_2}\varphi_{CO_2}^{v}P_T \quad (6.5)$$

$$f_{CO_2}^{w} = x_{CO_2}^{w}\varphi_{CO_2}^{w}P_T \quad (6.6)$$

$$f_{CO_2}^{o} = x_{CO_2}^{o}\varphi_{CO_2}^{o}P_T \quad (6.7)$$

where y_{CO_2} , $x_{CO_2}^{w}$ and $x_{CO_2}^{o}$ are the concentrations of CO_2 in the CO_2-rich phase, water phase and oil phase, respectively, and $\varphi_{CO_2}^{v}$, $\varphi_{CO_2}^{w}$, and $\varphi_{CO_2}^{o}$ are the fugacity coefficients of CO_2 in each of the phases.

Substituting equations 6.5-6.7 in equation 6.4 yields:

$$y_{CO_2}\varphi_{CO_2}^{v} = x_{CO_2}^{w}\varphi_{CO_2}^{w} = x_{CO_2}^{o}\varphi_{CO_2}^{o} \quad (6.8)$$

This implies that the concentration of CO_2 in each of the phases results from the fugacity coefficient of CO_2 in the respective phase, i.e. at equilibrium, the same fugacity results in different CO_2 concentrations in each phase. Assuming 100% CO_2 in the CO_2-rich phase, the fugacity of CO_2 at 10 MPa and 60 °C is 6.78 MPa as calculated by (Kunz and Wagner, 2012). This, however, also implies that the concentration of CO_2 in the aqueous phase should not take influence on the concentration in the oil phase, as long as there is excess CO_2 and the CO_2 rich phase is composed of 100 % CO_2. Nevertheless, at a given pressure it is seen that volumetric expansion of the oil is highest where DW is the surrounding aqueous phase, followed by the 3% $CaCl_2$ brine where volumetric expansion is slightly higher than that in the 3% NaCl brine. (Liu et al., 2011) report that CO_2 solubility in aqueous solutions are in the following order: pure water > $CaCl_2$ brine > NaCl brine at similar T/P conditions and similar brine concentration in wt%, which is

reflected in the swelling behavior of the oil drop, and the trend can be verified according to the measurements performed in the current study. (Note that the conversion of salt concentrations of 3 wt% yields concentrations of 0.51 mol/kg NaCl and 0.27 mol/kg $CaCl_2$ and justifies the higher solubility in the $CaCl_2$ brine. The reader is referred to section 6.3.1). On the other hand, the lowest volumetric expansion is observed to be in the 10% NaCl brine where the solubility of CO_2 in the aqueous phase is lowest. At 10 MPa and 60 °C, the solubility of CO_2 in aqueous solutions comprising different NaCl salt concentrations as calculated using Duan's model are: 1.03, 0.93 and 0.74 mol CO_2/ kg H_2O in DW, 3 wt% and 10 wt% NaCl brine, respectively, signifying that the volumetric expansion of the oleic phase is affected by the solubility of CO_2 in the aqueous phase. The deviation from the fugacity theory discussed earlier can be explained as follows: as CO_2 dissolves into the aqueous phase, part of it forms carbonic acid (H_2CO_3) which can also dissociate into bicarbonate anions (HCO^{3-}) upon first disassociation and carbonate anions (CO_3^{2-}) upon second disassociation (Knoche, 1980). The presence of salt in the solution influences carbonic acid formation and its disassociation and may lead to a deviation of the fugacity in the aqueous phase. This, however, is out of the scope of the current work.

In figure 6.7, volumetric expansion kinetics are depicted as a function of pressure and aqueous phase composition. Regardless of the pressure, it is seen that each curve is divided into two regions. In the first region, the fast increase in drop volume is represented by the sharp and nearly linear positive slope, while in the second region the volume increase slows down, indicated by a milder slope. The volumetric expansion process is governed by the difference in CO_2 concentrations in the aqueous and oleic phases (Hamouda and Bagalkot, 2019).

Initially, the concentration difference is high and will therefore result in a fast mass transfer of CO_2 from the aqueous phase into the oil, i.e. high diffusion. However, as CO_2 dissolution progresses with time, and the phases are approaching saturation (which ultimately depends on CO_2 solubility in each

phase), the mass transfer slows down due to a smaller concentration gradient, and results in the observed slope of the second region. It is further perceived that the higher the pressure, the steeper the initial slope, i.e. the faster the mass transfer. On the other hand, the kinetics are observed to be slower as the salinity increases, as indicated by a reduced initial slope, especially for the 10% NaCl brine. As the salinity of the brine increases, so does its viscosity, which will ultimately result in a lower CO_2 diffusivity and therefore a lower CO_2 diffusion rate into the aqueous phase (Zarghami et al., 2017). Additionally, the time required to establish equilibrium increases as the pressure is increased, this is attributed to the higher solubility of CO_2 in both phases at higher pressures.

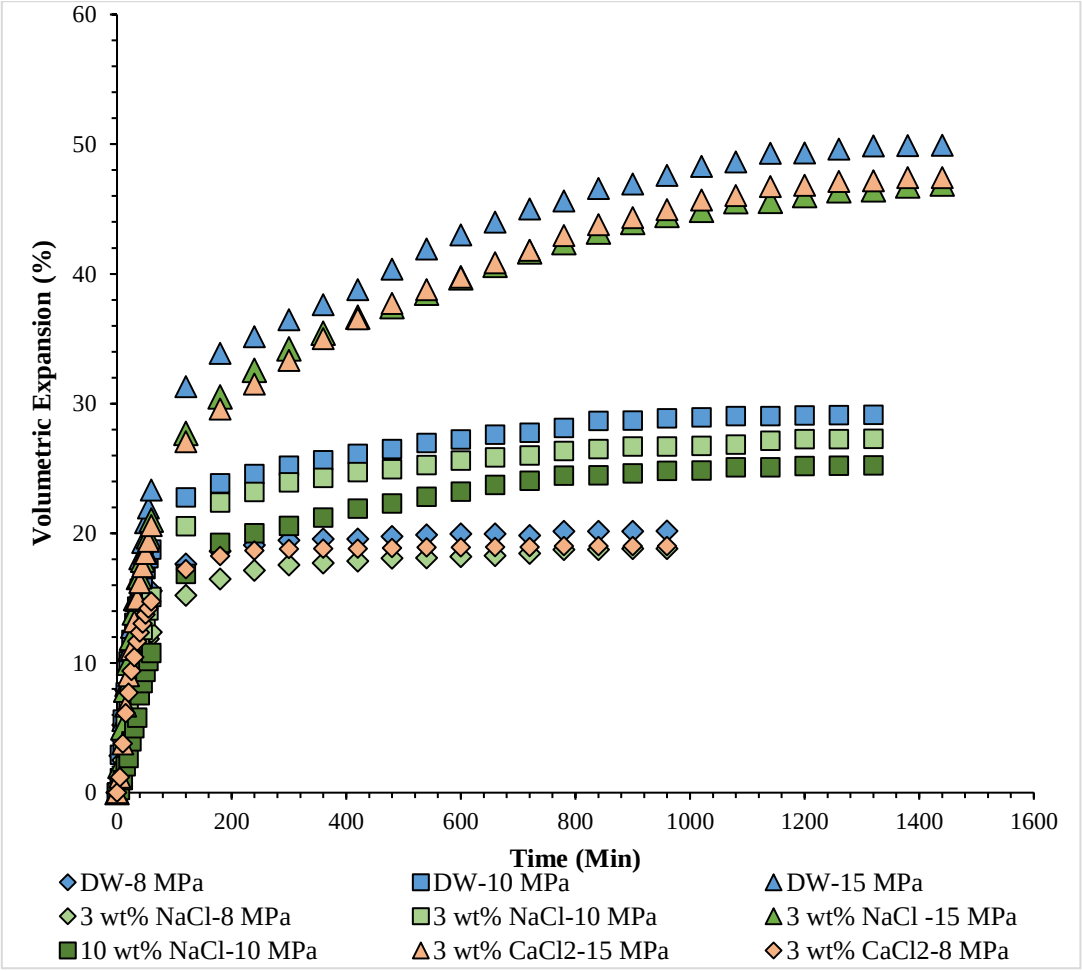

Figure 6.7 - Volumetric expansion kinetics as a function of pressure and aqueous phase composition at 60 °C.

The impact of hydrocarbon chain length on volumetric expansion is investigated by conducting the measurements at similar conditions using hexadecane where the surrounding phase is deionized water. The results are demonstrated in figure 6.8 below and the values are reported in Appendix D – Table D.5-B.

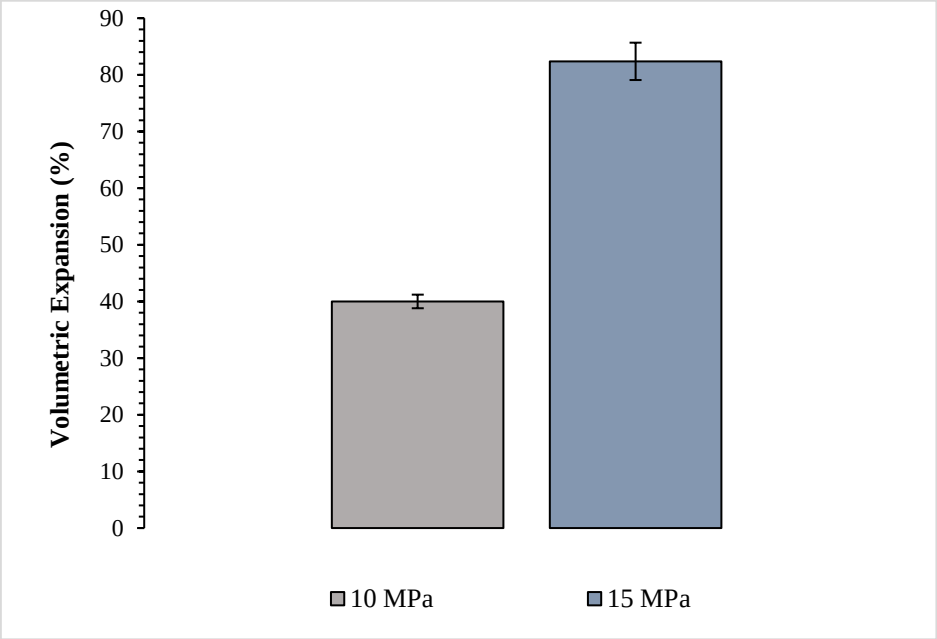

Figure 6.8 - Volumetric expansion of Hexadecane as a function of pressure at 60 °C and equilibrium.

It can be seen that the volumetric expansion of $C_{16}H_{34}$ exceeds that of the model oil. For example, at 10 MPa, volumetric expansion of hexadecane takes a value of 40%, while for the model oil it takes a value of 29%. Similarly, at 15 MPa the volumetric expansion is measured to be around 82% and 50% in hexadecane and the model oil, respectively. This is in line with the findings of (Simon and Graue, 1965) who found higher volumetric expansion in lighter oils. This phenomenon can be attributed to the higher solubility of CO_2 in oils with lower molecular size, which will be proven and discussed further in section 6.3.2.

6.3 Solubility

6.3.1 Solubility of Carbon Dioxide in the Aqueous Phase

Since experimental CO_2 solubility data that cover the entire range of conditions investigated in this work are lacking in the literature, the solubility of CO_2 in aqueous solutions containing salts is modeled using the method reported in section 3.2.10.1. The results thereof are demonstrated in figure 6.9 and reported in Appendix D - Table D.6.

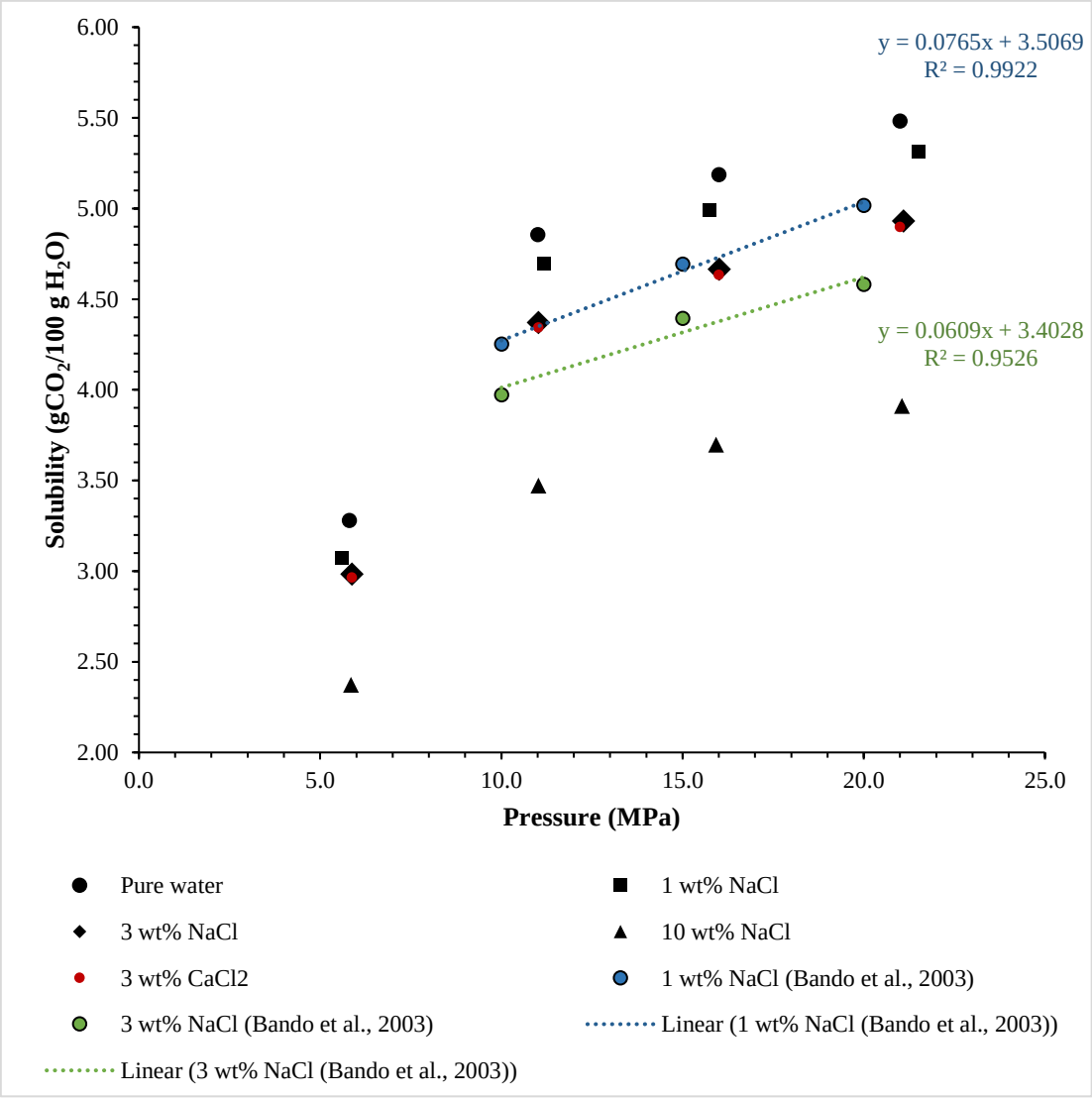

Figure 6.9 - CO_2 solubility in aqueous phases as modeled using (Duan et al., 2006).

As can be seen from the modeling results, the increasing pressure increases the solubility of CO_2 in the aqueous phase regardless of the composition. For instance, for the DW the solubility of CO_2 increases from 3.28 wt% (3.28 g CO_2 in 100 g

DW) at 5.8 MPa to 5.48 wt% at 21.0 MPa, both being at 60 °C. Alternatively, at the same pressure and temperature conditions, the solubility of CO_2 decreases when salt is added to the system. At a nominal pressure of 11.0 MPa, the solubility of CO_2 in the aqueous phase follows the following order DW>1 wt% NaCl> 3 wt% NaCl>10 wt% NaCl. This is also confirmed by the findings of (Bando et al., 2003) who experimentally determined the mole fraction of CO_2 in aqueous solutions containing 1 wt% and 3 wt% NaCl at 60 °C (See Appendix D - Table D.6.). This can be justified as follows; in the presence of an electrolyte species, a neutral species such as CO_2 is susceptible to the salting out phenomenon, whereby the solubility of a solute (CO_2) in a liquid solvent (water) decreases in the presence of a high concentration of salt (salt in- CO_2 out). An explanation to this phenomenon is that the presence of ions electrostricts the water molecules. Accordingly, the availability of water molecules to dissolve non-electrolytes (CO_2) is reduced. This electrostriction and the consequent salting out are governed by ion concentration, ion size and ion charge. Higher salt concentrations signify increased electrostiction and consequently reduced CO_2 solubility.

On the other hand, small ions are able to electrostrict hydration water molecules to a higher degree compared to large ions due to their higher charge density (a measure of the electric charge per unit area), i.e. the higher the charge density, the stronger the electrostriction (Gilbert et al., 2016). Based on the former statement, Ca^{2+} and Na^{+} have comparable ionic radii of 0.099 and 0.095 nm, however the charge of the Ca^{2+} is double that of Na^{+}. The hydration number -defined as the average number of water molecules that bind strongly to the ion – is estimated to be around 12 molecules for Ca^{2+} (Zavitsas, 2005) and 4 molecules for Na^{+} (Zavitsas, 2001). Therefore, at a similar molal concentration, a higher salting out effect is encountered in aqueous solutions containing the Ca^{2+} cations, where CO_2 experiences reduced solubility. For example, in a 3 wt% NaCl brine, the molal concentration is 0.51 mol/kg and the solubility of CO_2 at 16.0 MPa and 60 °C according to Duan's model is 4.7 wt% (or 1.06 mol CO_2/kg H_2O). For a $CaCl_2$

salt solution with a similar molal concentration of 0.51 mol/kg, the calculated CO_2 solubility is 4.3 wt% (0.95 mol CO_2/kg H_2O).

A regression model is created using the solubility values reported in (Bando et al., 2003). This regression model serves to infer the solubility of CO_2 at the experimental conditions investigated in this work, which are then used for the calculation of CO_2-saturated NaCl brine densities using the model by (Li et al., 2011) (See section 6.1.2.1).

6.3.2 Solubility of Carbon Dioxide in Oil

In this section, the impact of pressure and aqueous phase composition on the solubility of CO_2 in the oleic phase at 60 °C is investigated. As laid out in detail in section 3.2.10.2, the calculation of CO_2 solubility in the model oil relies on experimental oil densities (pure and CO_2-saturated phase) in conjunction with volumetric expansion values as reported in sections 6.1 and 6.2, respectively. The results are demonstrated in figure 6.10 and tabulated in Appendix D - Table D.7-A.

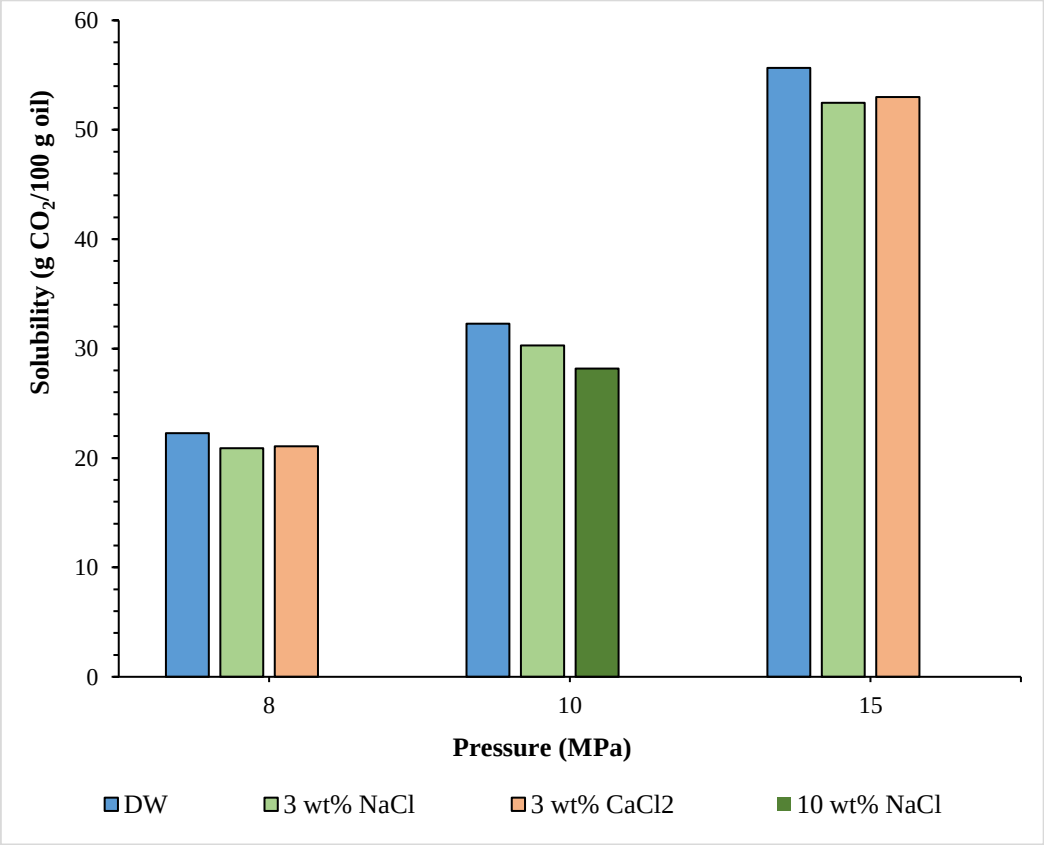

Figure 6.10 - CO_2 solubility in model oil as a function of pressure and aqueous phase composition.

The calculation of CO_2 solubility in the oleic phase are made based on the assumption that the aqueous phase composition has no impact on the density of the CO_2-saturated oil. As seen in figure 6.10, the solubility of CO_2 in the oleic phase increases with increasing pressure. Considering a given aqueous phase composition, for instance DW, the solubility increases from 22 % at 8 MPa to

55% at 15 MPa. The positive correlation between pressure and CO_2 solubility can also be seen for other aqueous phase compositions. The impact of ion concentration and type on the solubility of CO_2 in the aqueous phase and thereby the oleic phase is discussed in detail in section 6.2.

Experimental solubility data of CO_2 in a similar composite oil do not exist in the literature and neither do CO_2 solubilities in Eicosane and Tetracosane at similar P/T conditions. Therefore, a thorough comparison to the model oil is not possible. However, the solubilities of CO_2 in hexadecane at similar pressure and temperature conditions were reported by (Charoensombut-amon et al., 1986) , (Hölscher et al., 1989), (D'souza et al., 1988) and (He et al., 2021). Their findings are reported in table 6.1.

The reported values in the literature are in mole fraction of CO_2 (X_{CO_2}), therefore the following equations were used to convert the mole fraction to g CO_2/ 100 g oil for proper comparison:

The total composition of the hexadecane-rich phase is given by the following equations:

$$x_{co_2} + x_{c_{16}H_{34}} = 1 \tag{6.9}$$

$$Mass\% = \frac{Mass\ of\ solute}{mass\ of\ the\ solution} * 100\% \tag{6.10}$$

$$Mass\% = \frac{g_{CO_2}}{g_{oil}+g_{CO_2}} * 100 = \frac{x_{CO_2} * Molar\ mass\ of\ CO_2}{(x_{CO_2} * Molar\ mass\ of\ CO_2)+((1-x_{CO_2}) * Molar\ mass\ of\ C_{16}H_{34})} * 100 \tag{6.11}$$

To convert the mass% to g CO_2/100 g oil, the below equation is used:

$$\frac{g_{CO_2}}{g\ c_{16}H_{34}} = \frac{g_{CO_2}}{100\ \text{g} - g_{CO_2}} \tag{6.12}$$

Table 6.1 - CO_2 solubility in Hexadecane at 60 °C.

Reference	Pressure (MPa)	Solubility (gCO_2/100 $gC_{16}H_{34}$)
(Charoensombut-amon et al., 1986)	10.3	42.3
	15.1	98.9
(Hölscher et al., 1989)	10.0	35.1
	15.0	81.8
(D'souza et al., 1988)	9.7	35.6
	14.9	90.4
(He et al., 2021)	8.4	21.3
	10.8	37.4
	15.1	69.9

Despite the discrepancies among the findings of the authors, it can be seen that the CO_2 solubilities reported in table 6.1 are higher than those measured in the model oil. For instance, at 10 MPa, the measured solubility is 32.3 g CO_2/100 g oil (for the case of DW), while the authors report values ranging between 35.1 up to 42.3 g CO_2/ 100 g oil. This is due to the fact that the model oil is composed only of 45 wt% hexadecane, the remaining fraction is composed of eicosane and tetracosane.

To verify the validity of the method, the solubility calculations have been also applied to hexadecane based on volumetric expansion measurements performed at 60 °C in deionized water (see section 6.2). The results thereof are reported in figure 6.11 and tabulated in Table D.7-B in Appendix D.

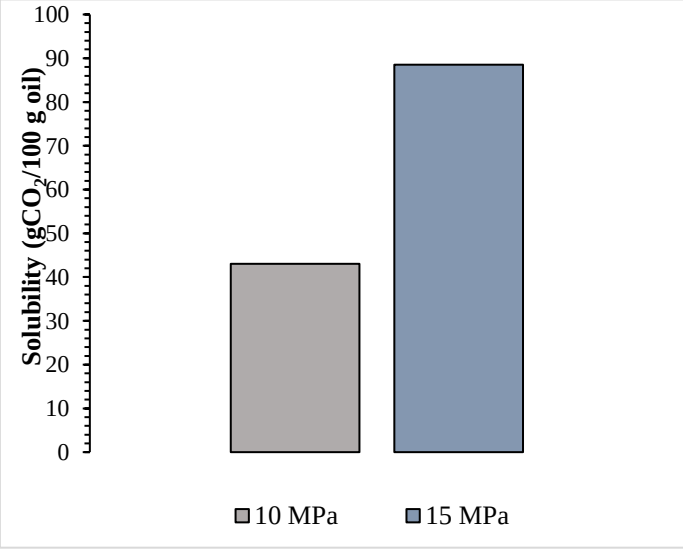

Figure 6.11 - CO_2 solubility in Hexadecane as a function of pressure at 60 °C.

At 10 MPa, the solubility of CO_2 is 43%, in line with what was reported by (Charoensombut-amon et al., 1986). At 15 MPa, however, the solubility of CO_2 in hexadecane is calculated to be around 88% and falls between the values reported by (Charoensombut-amon et al., 1986) and (Hölscher et al., 1989) but takes a value similar to what was reported by (D'souza et al., 1988). It is well known that the solubility of CO_2 is a function of the molecular size of the oil (Emera and Sarma, 2007; Simon and Graue, 1965). This is further confirmed by the results demonstrated in figures 6.10 and 6.11 where it is seen that the solubility of CO_2 in hexadecane exceeds that of the model oil, as the latter contains heavier and longer-chain hydrocarbons. This is in line with the findings of (He et al., 2021) which demonstrate a reduced solubility of CO_2 (reduced mol fraction of CO_2) in longer-chain alkanes at similar P/T conditions. Therefore, the validity of the method for estimating the solubility of CO_2 in oils can be confirmed.

The reduced solubility of CO_2 in longer change alkanes is attributed to the following; as the chain length of an alkane increases, the surface area of contact between the alkane molecules also increases, and the polarizability of the molecules increases. This implies that London dispersion forces (Van der Waals: induced dipole-induced dipole) between the molecules are stronger. As result, the penetration of CO_2 molecules between the alkane molecules becomes more difficult and results in a lower CO_2 solubility therein (Y. Wang et al., 2021; Yang et al., 2012).

7. Thermo-economic Analysis

7.1 Thermodynamic Considerations of the SFE Cycle

The supercritical extraction cycle employed in this work constitutes the following sub-processes as demonstrated in figure 7.1 and reported in table 7.1. The cycle is illustrated in a Temperature-Entropy diagram, where isobars and isenthalps are also shown, in order to facilitate the energetic analysis of the process. The extraction conditions represented are 40 MPa and 60 °C. The calculation of the energetic requirements of the process are listed in Tables E1 in Appendix E for operating conditions of 15 and 40 MPa at 60 °C, respectively.

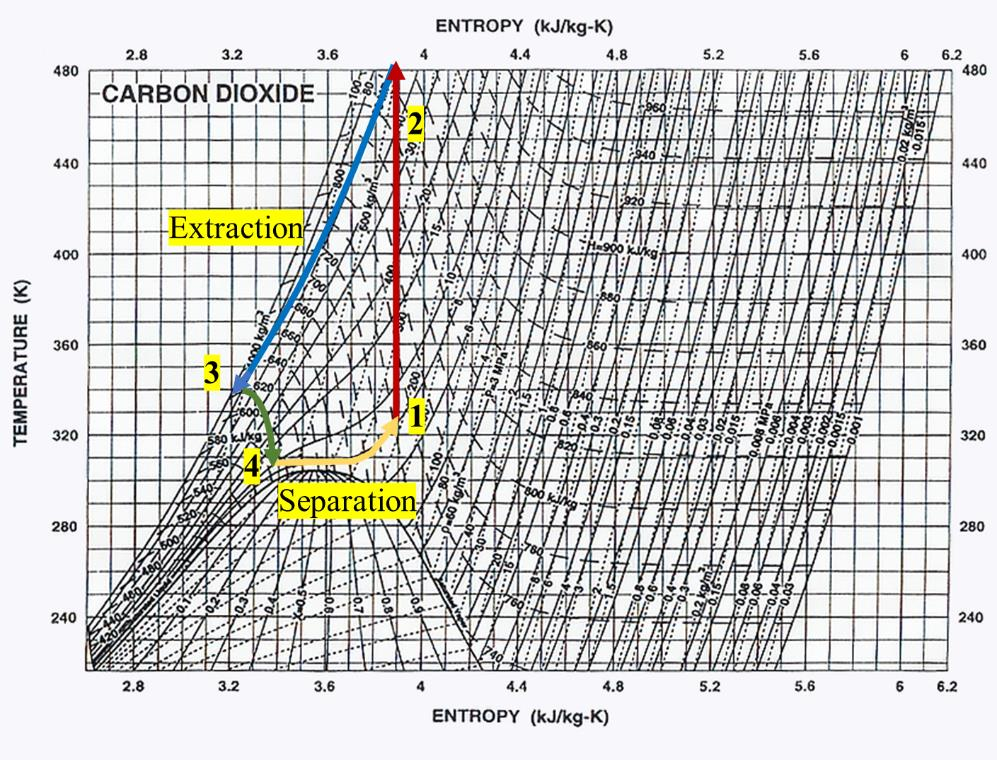

Figure 7.1 - T-S diagram of supercritical CO_2 extraction cycle.

Table 7.1 - Thermodynamic processes within the supercritical CO_2 extraction cycle.

Step	Component	Assumption
1-2	Compressor	Isentropic compression
2-3	Heat exchanger	Isobaric cooling
3-4	Back pressure valve	Isenthalpic expansion
4-1	Heat exchanger	Isobaric heating

7.2 Cost of Oil

The cost of electricity according to the National Electric Power Company of Jordan (NEPCO, 2023) is around 0.07 JOD/kWh (0.02 JOD/MJ) as of June 2022 (calculated based on averaged day and night tariffs. Assuming the shale oil has a similar calorific value of 39 MJ/kg as that of the Heavy Fuel Oil (HFO) (Amer et al., 2019; Senčić et al., 2019), for Sultani oil to be economically attractive, it has to be sold at a similar price as that of the imported HFO or lower. As of June 2022, HFO is sold for 348 JOD/ton according to the ministry of Energy and Mineral Resources of Jordan (MEMR, 2023), which corresponds to 0.008 JOD/MJ. To begin with, the cost of 1 MJ of electrical energy is already an order of magnitude higher than the cost of 1 MJ generated by HFO combustion. This incentivizes energy-intensive industries to replace the electrical energy with thermal energy through the use of generators and boilers. The question remains whether the production of Jordanian oil using SFE will be an attractive alternative to imports. Several scenarios are analyzed and compared as follows: a baseline scenario, a heat exchanger scenario and a third scenario where the inclusion of carbon tax to the second scenario is proposed. The cost analysis can be found in Appendix E-Table E.2.

The baseline scenario is simply an upscaling of the lab-scale CO_2 extraction processes conducted in this work. Extraction conditions of 15 and 40 MPa and 60 °C are considered for the analysis, which is conducted under the following assumptions:

- The process is operated in a quasi-continuous mode.
- The duration of the extraction of each batch is 5 hours.
- Three batches are extracted per day.
- Each batch contains 200 kg of shale (semi industrial scale).
- Capacity factor of the facility is 55%.

- Amount of extracted oil is the yield corresponding to each condition at the end of a 5-hour extraction duration.
- Flow rate of CO_2 is 2000 kg/hr.
- The extract is composed 100% of oil (no formation water).
- Complete governmental subsidy of the cost of CO_2.
- The costs considered in the current analysis are limited to the energetic requirement of the process, and no other costs such investment costs, surface mining, shale crushing and oil refining are considered. Clearly, such costs will levy more economical challenges to the process.

Based on the above, the cost of shale oil (JOD/kg) is shown in figure 7.2 for 15 MPa and 40 MPa extraction conditions. The prices demonstrated are unrealistically high in comparison to the price of HFO.

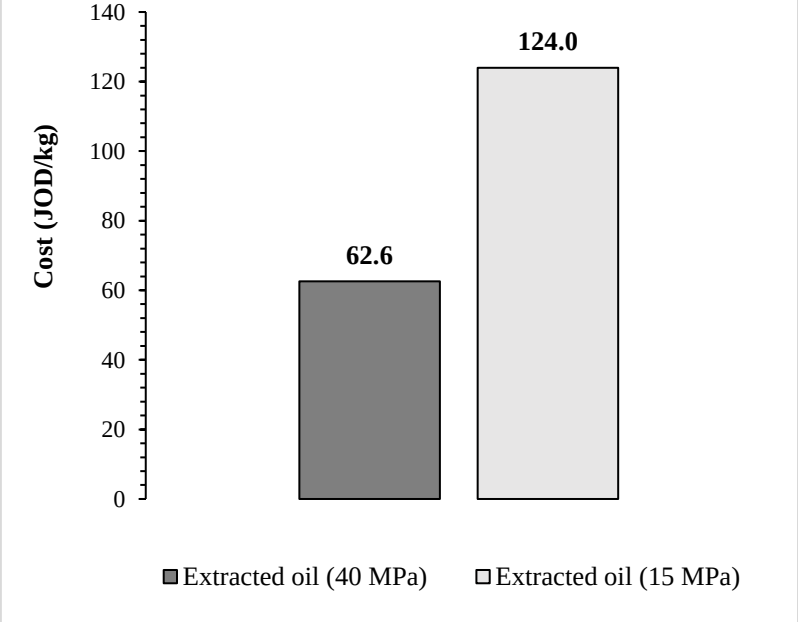

Figure 7.2 - Cost of oil according to the baseline scenario.

These costs stem from the high energetic requirements of gas compression, cooling of the extractor and heating of the separator. The heating requirement of the separator can completely be recovered from heat generated alongside compression through the use of a recuperative heat exchanger within the

extraction cycle. The suggested modification is illustrated in scenario HX in figure 7.3, and the costs of oil associated with this scenario are reported in figure 7.4. Further, the heat of compression associated with a single-stage compressor can be minimized through the use of multistage compressors with intermediate cooling, which will not be considered in the current analysis.

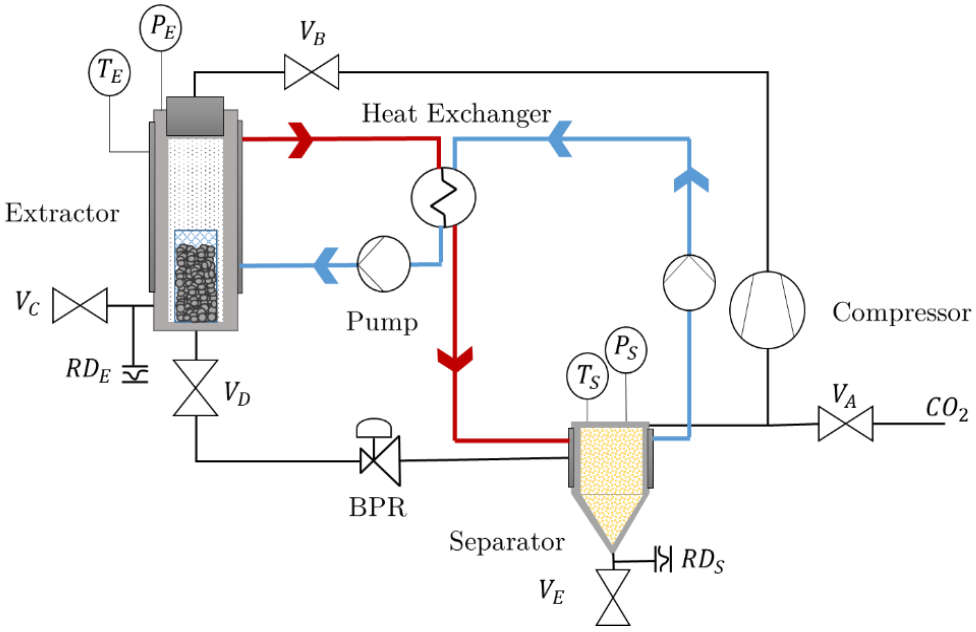

Figure 7.3 - Suggested modifications to the $scCO_2$ extraction cycle, scenario HX.

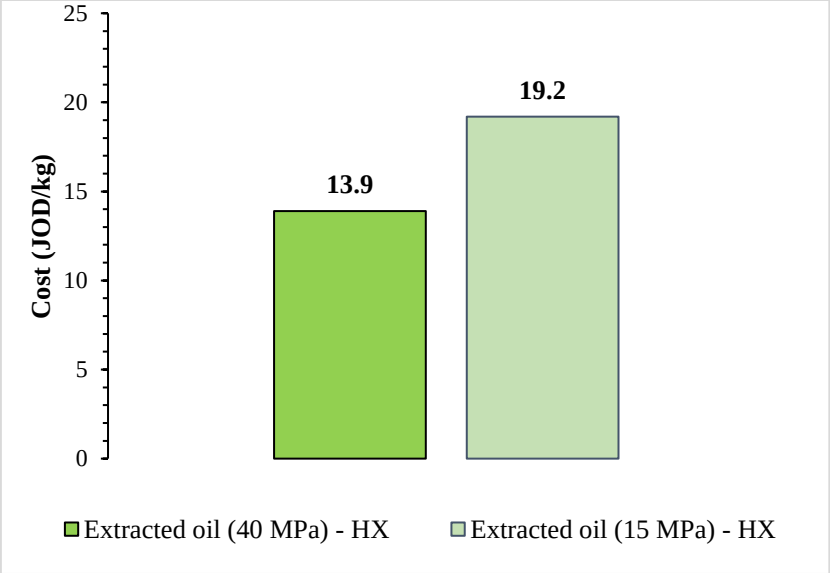

Figure 7.4 - Cost of oil according to scenario HX.

Despite the drastic reduction in the cost of oil using scenario HX, the cost of oil is almost 40 and 55 times the price of imported HFO, for 40 and 15 MPa extraction

conditions, respectively. Therefore, the extraction process in this scenario is still economically unattractive and can only be justified when the extracted oil is used as a high value chemical product or when the imported oil prices increase significantly.

The economic attractiveness of oil recovery from Jordanian shale may be enhanced by incentivizing emitters to store carbon, which is also an expensive process. This is achieved through the design and execution of a climate change policy in conjunction with carbon pricing to account for the environmental costs (pollution) of economic activities. The enactment of carbon pricing can either be achieved by "emission cap and trade" mechanism or by imposing a carbon tax, or a hybrid of both (Goulder and Schein, 2013). In the first mechanism, the allowable emission is capped and carbon credits are traded for a monetary value for every ton of CO_2 emitted above the allowable limit, while applying the carbon tax mechanism levies a direct price on emissions. A further stimulus for CCS and CCUS is the carbon tax credit, by which emitters are offered tax incentives for every ton of CO_2 captured and stored. It is important to note that tax credits and other financial incentives may also apply for CO_2-EOR projects, which were the main driver behind the use of CO_2 in enhanced oil recovery in the United States since 1979.

Should the above scenario be implemented and revenue is generated to support CCS-EOR projects, a suggested scenario is the concomitant injection and fracturing using CO_2 to increase the permeability of Sultani, followed by a static period of soaking (Huff and Puff), which on the one hand will increase the yield, and reduce the overall energy consumption on the other. The above is followed by the separation of CO_2 from the produced oil and its reinjection into the formation along with fresh supply of captured CO_2 to make up for the gas retained in the formation. After production is complete, CO_2 is stored permanently in the shale.

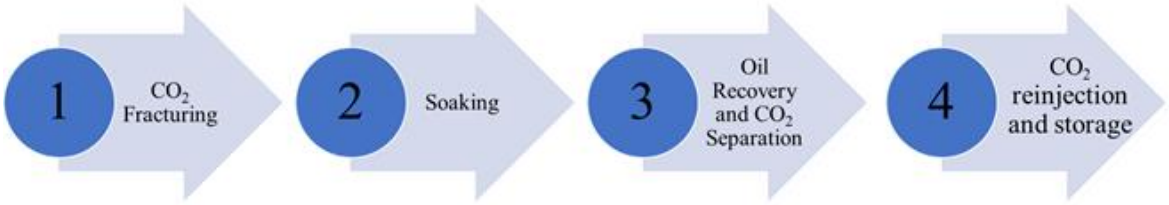

Figure 7.5 - Coupling of GCS and OR.

In one way or the other, both, recovery of oil and gas from unconventionals as well as CO_2 injection will have to be dealt with in future. A combination of both as already applied for conventional reservoirs will most probably be implemented. In any of the possible scenarios, the driving mechanisms, properties and critical factors investigated in this work are required in order to understand, design and optimize the respective process.

8. Conclusions and Future Outlook

8.1 Oil Recovery

Supercritical extraction of oil from Sultani shale was conducted as a starting point of the presented work for various reasons:

- Estimate the amount of oil recoverable by $scCO_2$ under varying conditions.
- Obtain an oil sample for further investigation.
- Study the governing transport mechanisms.
- Determine the optimum conditions for an oil recovery process using compressed CO_2.

Conclusions can be drawn regarding all the previously mentioned objectives that are relevant for designing processes of combined CO_2 injection and hydrocarbon recovery from unconventional reservoirs. In the first place, CO_2 was applied successfully to extract oil from Sultani shale. As expected, the highest recoverability is found at the highest applied pressure and the smallest particle size, as the process is diffusion controlled. Leaving some time for diffusion of CO_2 to take place during a soaking period further improves the yield. The extracted oil was subject to further investigations of relevant system properties such as the interfacial tension which is found to decrease with increasing pressure. At low to moderate pressures, IFT exhibits higher values at the lower temperature. Beyond an inversion pressure, the IFT increases following an isobaric increase in temperature. The IFT reduction is associated with a higher mutual miscibility and a concomitant reduction of capillary pressure which helps mobilize the oil within the shale matrix.

Further on, the IFT measurements conducted on extracted oil indicate that the selectivity of sCO_2 towards the solute is pressure-dependent. Oil extracted at lower pressures exhibits a lower SFT/IFT in comparison to oil extracted at 40 MPa, signifying a diminishing selectivity of CO_2 at elevated pressure and its

increased ability of extracting longer chain hydrocarbons. The mutual miscibility between CO_2 and hydrocarbon mixtures is reflected by the course of the IFT as a function of pressure: the heavier the hydrocarbon phase, the higher the minimum pressure of complete miscibility at which the IFT vanishes. The findings also show that the interfacial behavior of oil at low to moderate pressures is dictated by that of the lightest component in the mixture whereas the longer chain hydrocarbons dominate the interfacial behavior at higher pressures, i.e. the IFT decreases dramatically up to pressures of around 10 MPa beyond which the IFT curve exhibits a reduced negative slope in the presence of heavier components. As a result of increasing CO_2 solubility in the oil phase at increasing pressure, not only does the IFT significantly drop, but the oil phase expands and the density increases simultaneously. In the presence of connate water, the IFT of a CO_2-oil-water/brine system exhibits higher values than in a binary CO_2-oil system at similar conditions, yet a negative correlation between IFT and CO_2 injection pressure still holds. The salinity is found to negatively influence the IFT and its reduction due to CO_2 injection, i.e. higher IFT values and decreased IFT reduction are observed as the brine salinity increases. Sultani shale is highly water wet at all the tested experimental conditions, however, due to the above-mentioned volumetric expansion, oil inherently present in the samples is expelled towards the brine-rock interface, potentially decreasing the water wetting. As an overall conclusion it may be stated that the strong interactions of supercritical CO_2 with all coexisting phases alter the system properties significantly, and mainly in an advantageous way regarding the displacement of oil from the shale. Accounting for the high diffusion resistance in shale, the above findings imply that an injection scheme of CO_2 huff and puff at elevated pressures is most suitable for the Sultani shale.

8.2 Carbon Storage

The interfacial tension and wettability of systems comprising CO_2-formation water-rock are decisive properties that control the magnitude and direction of the capillary pressure in the porous media once the oil has been extracted. The implications of both properties on carbon storage will differ depending on how the shale is viewed, either as a caprock or as a reservoir.

The integrity of the structural trap (caprock) is reduced at elevated pressures. In terms of CO_2-brine IFT, a significant reduction is observed up to pressures of 20 MPa, beyond which no further reduction in IFT is observed. Accordingly, the impact of IFT on the capillary pressure at pressures exceeding 20 MPa is negligible. On the other hand, the caprock wettability is altered from water wet to intermediate wet and further to CO_2 wet as the pressure is increased, which reduces the maximum allowable column height of stored CO_2 beneath the caprock and lowers the breakthrough pressure. In the reservoir, a lower IFT implies a higher solubility of the CO_2 in the brine, a favorable storage condition, however, the lower water wetting reduces the efficiency of the capillary trapping mechanism by decreasing the portion of immobilized gas from the mobile CO_2 plume, and higher buoyant forces acting on the caprock should be expected. The higher adsorption capacity at elevated pressures increases the CO_2 storage capacity of the reservoir on the one hand, yet has implications on caprock integrity as it contributes to its wettability alteration. The maximum CO_2 adsorption capacity is measured at 20 MPa, where the highest gas wetting was also observed. The measured CO_2 diffusion indicates that, in the absence of fracture networks and open fault systems, the loss of CO_2 through the caprock by diffusion is a slow process, however, at elevated pressures, the increased CO_2 adsorption capacity and the higher diffusivities may contribute to increased CO_2 permeation. For the shale reservoir, the low diffusivity may result in injectivity issues, i.e. a pressure buildup near the injector as CO_2 injection continues, that may result in caprock failure. The low diffusion rates also result in low CO_2 sweep efficiencies, which

hinder attaining the full storage capacity of the reservoir in a practical and realistic time scale. Lower temperature zones of the reservoir and high injection pressures are favored, owing to the higher adsorption capacity and the higher diffusion rates of CO_2.

The solubility of CO_2 in the brine is found to increase with increasing pressure, thereby increasing the amount of trapped gas and consequently reducing the amount of CO_2 in the buoyant CO_2 plume. The density of CO_2-saturated brines is found to increase with increasing saturation pressure. The aforementioned has a positive impact on the storage capacity by enhancing the dissolution of CO_2 through convective mixing. The findings in terms of IFT, wettability, solubility and density also indicate that lower-salinity brine reservoirs are better-suited for CO_2 storage.

8.3 Future Outlook

The above conclusions of the work at hand provide an extensive range of innovative experimental methods and deliver a large number of mixture properties required for forthcoming investigations. Regarding gas storage, the planned future work includes the measurement of capillary displacement and breakthrough pressure using the step by step method. Further on, gas diffusivity and effective CO_2 permeability in Sultani shale will be measured using the pressure decay method. These measurements will also be applied to systems comprising Hydrogen (H_2) - a future energy carrier - and H_2/CO_2 mixtures, where the investigation of interfacial phenomena (interfacial tension, wettability and adsorption) and their impact on storage integrity and capacity will be intensified. Additionally, the impact of repetitive shale exposure to CO_2 on the adsorption capacity, surface area, pore volume and mass transport will be examined.

Concerning oil recovery, the fundamental work on the impact of supercritical CO_2 presented here will be extended to a systematic and thermodynamically based investigation of what petroleum engineers call multiple contact miscibility in multicomponent systems containing supercritical CO_2. Further on, the alteration in the phase behavior of confined mixtures, the so-called nanoconfinement effect, and its impact on the multiphase behavior will be subject of investigation.

Last but not least, the hydrogenation of Jordanian shale and its impact on organic matter conversion will be investigated using thermal gravimetry, nuclear magnetic resonance and gas chromatography – mass spectroscopy.

Bibliography

[1] Abdi, A., Bahmani, Z., Ranjbar, B., Riazi, M., 2022. Chapter 7 - Smart water injection, in: Hemmati-Sarapardeh, A., Schaffie, M., Ranjbar, M., Dong, M., Li, Z. (Eds.), Chemical Methods, Enhanced Oil Recovery Series. Gulf Professional Publishing, pp. 313–356. https://doi.org/10.1016/B978-0-12-821931-7.00008-0

[2] Abed, A.M., 2013. The eastern Mediterranean phosphorite giants: An interplay between tectonics and upwelling. GeoArabia 18, 67–94.

[3] Abed, A.M., Arouri, K., Amiereh, B.S., Al-Hawari, Z., 2010. Characterization and Genesis of Some Jordanian Oil Shales. Dirasat Pure Sci. 36.

[4] Abed, A.M., Arouri, K.R., Boreham, C.J., 2005. Source rock potential of the phosphorite–bituminous chalk–marl sequence in Jordan. Mar. Pet. Geol. 22, 413–425. https://doi.org/10.1016/j.marpetgeo.2004.12.004

[5] Abedini, A., Mosavat, N., Torabi, F., 2014. Determination of Minimum Miscibility Pressure of Crude Oil-CO_2 System by Oil Swelling/Extraction Test. Energy Technol. 2, 431–439. https://doi.org/10.1002/ente.201400005

[6] Abedini, A., Torabi, F., 2014a. Oil Recovery Performance of Immiscible and Miscible CO2 Huff-and-Puff Processes. Energy Fuels 28, 774–784. https://doi.org/10.1021/ef401363b

[7] Abedini, A., Torabi, F., 2014b. On the CO2 storage potential of cyclic CO2 injection process for enhanced oil recovery. Fuel 124, 14–27. https://doi.org/10.1016/j.fuel.2014.01.084

[8] Abedini, A., Torabi, F., 2013. Parametric Study of the Cyclic CO_2 Injection Process in Light Oil Systems. Ind. Eng. Chem. Res. 52, 15211–15223. https://doi.org/10.1021/ie402363h

[9] Aggelopoulos, C.A., Robin, M., Perfetti, E., Vizika, O., 2010. CO2/CaCl2 solution interfacial tensions under CO2 geological storage conditions: Influence of cation valence on interfacial tension. Adv. Water Resour. 33, 691–697. https://doi.org/10.1016/j.advwatres.2010.04.006

[10] Aggelopoulos, C.A., Robin, M., Vizika, O., 2011. Interfacial tension between CO2 and brine (NaCl+CaCl2) at elevated pressures and temperatures: The additive effect of different salts. Adv. Water Resour. 34, 505–511. https://doi.org/10.1016/j.advwatres.2011.01.007

[11] Al Ghafri, S.Z., Maitland, G.C., Trusler, J.P.M., 2014. Experimental and modeling study of the phase behavior of synthetic crude oil+CO2. Fluid Phase Equilibria 365, 20–40. https://doi.org/10.1016/j.fluid.2013.12.018

[12] Al Mahrouqi, D., Vinogradov, J., Jackson, M.D., 2017. Zeta potential of artificial and natural calcite in aqueous solution. Adv. Colloid Interface Sci. 240, 60–76. https://doi.org/10.1016/j.cis.2016.12.006

[13] Al Mahrouqi, D., Vinogradov, J., Jackson, M.D., 2016. Temperature dependence of the zeta potential in intact natural carbonates. Geophys. Res. Lett. 43. https://doi.org/10.1002/2016GL071151

[14] Alali, J., Abu Salah, A., Yasin, S., Alomari, W., 2014. Oil Shale - Mineral Status and Future Opportunity. Ministry of Energy and Mineral Resources.

[15] Ala-Nissila, T., Ferrando, R., Ying, S.C., 2002. Collective and single particle diffusion on surfaces. Adv. Phys. 51, 949–1078. https://doi.org/10.1080/00018730110107902

[16] Allawzi, M., Al-Otoom, A., Allaboun, H., Ajlouni, A., Al Nseirat, F., 2011. CO2 supercritical fluid extraction of Jordanian oil shale utilizing different co-solvents. Fuel Process. Technol. 92, 2016–2023. https://doi.org/10.1016/j.fuproc.2011.06.001

[17] Al-Marzouqi, A.H., Zekri, A.Y., Jobe, B., Dowaidar, A., 2007. Supercritical fluid extraction for the determination of optimum oil recovery conditions. J. Pet. Sci. Eng. 55, 37–47. https://doi.org/10.1016/j.petrol.2006.04.011

[18] Almeida da Costa, A., Trivedi, J., Soares, J., Rocha, P., Costa, G., Embiruçu, M., 2020. An experimental evaluation of low salinity water mechanisms in a typical Brazilian sandstone and light crude oil with low acid/basic number. Fuel 273, 117694. https://doi.org/10.1016/j.fuel.2020.117694

[19] Al-Mutairi, S.M., Abu-Khamsin, S.A., Okasha, T.M., Aramco, S., Hossain, M.E., 2014. An experimental investigation of wettability alteration during CO2 immiscible flooding. J. Pet. Sci. Eng. 120, 73–77. https://doi.org/10.1016/j.petrol.2014.05.008

[20] Amer, M.W., Aljariri Alhesan, J.S., Marshall, M., Awwad, A.M., Al-Ayed, O.S., 2019. Characterization of Jordanian oil shale and variation in oil properties with pyrolysis temperature. J. Anal. Appl. Pyrolysis 140, 219–226. https://doi.org/10.1016/j.jaap.2019.03.019

[21] Attarat Power Company (APCO),2020. [WWW Document]. URL https://attaratpower.com.jo/ (accessed 2.4.23).

[22] Arif, M., Lebedev, M., Barifcani, A., Iglauer, S., 2017a. Influence of shale-total organic content on CO2 geo-storage potential. Geophys. Res. Lett. 44, 8769–8775. https://doi.org/10.1002/2017GL073532

[23] Arif, M., Lebedev, M., Barifcani, A., Iglauer, S., 2017b. CO2 storage in carbonates: Wettability of calcite. Int. J. Greenh. Gas Control 62, 113–121. https://doi.org/10.1016/j.ijggc.2017.04.014

[24] Ataman, E., Andersson, M.P., Ceccato, M., Bovet, N., Stipp, S.L.S., 2016. Functional Group Adsorption on Calcite: I. Oxygen Containing and Nonpolar Organic Molecules. J. Phys. Chem. C 120, 16586–16596. https://doi.org/10.1021/acs.jpcc.6b01349

[25] Bachu, S., Bennion, D.B., 2009. Interfacial Tension between CO2, Freshwater, and Brine in the Range of Pressure from (2 to 27) MPa, Temperature from (20 to 125)°C, and Water Salinity from (0 to 334 000) mg·L−1. J. Chem. Eng. Data 54, 765–775. https://doi.org/10.1021/je800529x

[26] Bagalkot, N., Hamouda, A.A., 2018. Diffusion coefficient of CO_2 into light hydrocarbons and interfacial tension of carbonated water–hydrocarbon system. J. Geophys. Eng. 15, 2516–2529. https://doi.org/10.1088/1742-2140/aad432

[27] Bakhshian, S., Hosseini, S.A., 2019. Prediction of CO2 adsorption-induced deformation in shale nanopores. Fuel 241, 767–776. https://doi.org/10.1016/j.fuel.2018.12.095

[28] Bakshi, T., Vishal, V., Prusty, B.K., Pathak, K., 2020. Carbon dioxide and methane sorption characteristics of Damodar Valley and Upper Assam shale, India. Energy Clim. Change 1, 100002. https://doi.org/10.1016/j.egycc.2020.100002

[29] Bando, S., Takemura, F., Nishio, M., Hihara, E., Akai, M., 2003. Solubility of CO_2 in Aqueous Solutions of NaCl at (30 to 60) °C and (10 to 20) MPa. J. Chem. Eng. Data 48, 576–579. https://doi.org/10.1021/je0255832

[30] Beattie, J.K., Djerdjev, A.M., 2004. The Pristine Oil/Water Interface: Surfactant-Free Hydroxide-Charged Emulsions. Angew. Chem. Int. Ed. 43, 3568–3571. https://doi.org/10.1002/anie.200453916

[31] Behzadfar, E., Hatzikiriakos, S.G., 2014. Diffusivity of CO_2 in Bitumen: Pressure–Decay Measurements Coupled with Rheometry. Energy Fuels 28, 1304–1311. https://doi.org/10.1021/ef402392r

[32] Berry, J.D., Neeson, M.J., Dagastine, R.R., Chan, D.Y.C., Tabor, R.F., 2015. Measurement of surface and interfacial tension using pendant drop tensiometry. J. Colloid Interface Sci. 454, 226–237. https://doi.org/10.1016/j.jcis.2015.05.012

[33] Bi, J., Li, J., Chen, Z., Wu, K., Gao, Y., Tian, W., Zhang, S., 2021. Model for the Diffusion of N-alkane Confined in Nanopores: Effect of the Fluid/Pore-Wall Interaction. Presented at the IOR 2021, European Association of Geoscientists & Engineers, pp. 1–14. https://doi.org/10.3997/2214-4609.202133131

[34] Bikkina, P.K., Shoham, O., Uppaluri, R., 2011. Equilibrated Interfacial Tension Data of the CO_2 –Water System at High Pressures and Moderate Temperatures. J. Chem. Eng. Data 56, 3725–3733. https://doi.org/10.1021/je200302h

[35] Bolis, V., 2013. Fundamentals in Adsorption at the Solid-Gas Interface. Concepts and Thermodynamics, in: Auroux, A. (Ed.), Calorimetry and Thermal Methods in Catalysis, Springer Series in Materials Science. Springer Berlin Heidelberg, Berlin, Heidelberg, pp. 3–50. https://doi.org/10.1007/978-3-642-11954-5_1

[36] Bonto, M., Eftekhari, A.A., Nick, H.M., 2019. An overview of the oil-brine interfacial behavior and a new surface complexation model. Sci. Rep. 9, 6072. https://doi.org/10.1038/s41598-019-42505-2

[37] Broom, D.P., Thomas, K.M., 2013. Gas adsorption by nanoporous materials: Future applications and experimental challenges. MRS Bull. 38, 412–421. https://doi.org/10.1557/mrs.2013.105

[38] Brunner, G., 1994. Gas Extraction, Topics in Physical Chemistry. Steinkopff, Heidelberg. https://doi.org/10.1007/978-3-662-07380-3

[39] Buckley, J.S., Takamura, K., Morrow, N.R., 1989. Influence of Electrical Surface Charges on the Wetting Properties of Crude Oils. SPE Reserv. Eng. 4, 332–340. https://doi.org/10.2118/16964-PA

[40] Budi, A., Stipp, S.L.S., Andersson, M.P., 2018. Calculation of Entropy of Adsorption for Small Molecules on Mineral Surfaces. J. Phys. Chem. C 122, 8236–8243. https://doi.org/10.1021/acs.jpcc.7b11860

[41] Bueno, J.L., Suarez, J.J., Dizy, J., Medina, I., 1993. Infinite dilution diffusion coefficients: benzene derivatives as solutes in supercritical carbon dioxide. J. Chem. Eng. Data 38, 344–349. https://doi.org/10.1021/je00011a002

[42] Busch, A., Alles, S., Gensterblum, Y., Prinz, D., Dewhurst, D.N., Raven, M.D., Stanjek, H., Krooss, B.M., 2008. Carbon dioxide storage potential of shales. Int. J. Greenh. Gas Control 2, 297–308. https://doi.org/10.1016/j.ijggc.2008.03.003

[43] Cao, X., Peng, B., Ma, S., Ni, H., Zhang, L., Zhang, W., Li, M., Hsu, C.S., Shi, Q., 2017. Molecular Selectivity in Supercritical CO_2 Extraction of a Crude Oil. Energy Fuels 31, 4996–5002. https://doi.org/10.1021/acs.energyfuels.7b00415

[44] Carchini, G., Hussein, I., Al-Marri, M.J., Shawabkeh, R., Mahmoud, M., Aparicio, S., 2020. A theoretical study of gas adsorption on calcite for CO2 enhanced natural gas recovery. Appl. Surf. Sci. 504, 144575. https://doi.org/10.1016/j.apsusc.2019.144575

[45] Chacon Valero, A.M., Feitosa, F.X., Batista de Sant'Ana, H., 2020. Density and Volumetric Behavior of Binary CO_2 + *n* -Decane and Ternary CO_2 + *n* -Decane + Naphthalene Systems at High Pressure and High Temperature. J. Chem. Eng. Data 65, 3499–3509. https://doi.org/10.1021/acs.jced.0c00090

[46] Chalbaud, C., Robin, M., Lombard, J.-M., Bertin, H., Egermann, P., 2010. Brine/CO_2 Interfacial Properties and Effects on CO_2 Storage in Deep Saline Aquifers. Oil Gas Sci. Technol. – Rev. L'Institut Fr. Pétrole 65, 541–555. https://doi.org/10.2516/ogst/2009061

[47] Chalbaud, C., Robin, M., Lombard, J.-M., Martin, F., Egermann, P., Bertin, H., 2009. Interfacial tension measurements and wettability evaluation for geological CO2 storage. Adv. Water Resour. 32, 98–109. https://doi.org/10.1016/j.advwatres.2008.10.012

[48] Charcosset, C., 2016. Electrophoretic Mobility, in: Drioli, E., Giorno, L. (Eds.), Encyclopedia of Membranes. Springer Berlin Heidelberg, Berlin, Heidelberg, pp. 658–659. https://doi.org/10.1007/978-3-662-44324-8_208

[49] Chareonsuppanimit, P., Mohammad, S.A., Robinson, R.L., Gasem, K.A.M., 2012. High-pressure adsorption of gases on shales: Measurements and modeling. Int. J. Coal Geol. 95, 34–46. https://doi.org/10.1016/j.coal.2012.02.005

[50] Charoensombut-amon, T., Martin, R.J., Kobayashi, R., 1986. Application of a generalized multiproperty apparatus to measure phase equilibrium and vapor phase densities of supercritical carbon dioxide in n-hexadecane systems up to 26 MPa. Fluid Phase Equilibria 31, 89–104. https://doi.org/10.1016/S0378-3812(86)87033-9

[51] Charoensuppanimit, P., Mohammad, S.A., Gasem, K.A.M., 2016. Measurements and Modeling of Gas Adsorption on Shales. Energy Fuels 30, 2309–2319. https://doi.org/10.1021/acs.energyfuels.5b02751

[52] Chen, H., Yang, M., Huang, C., Wang, Y., Zhang, Y., Zuo, M., 2022. A dynamic model of CO2 diffusion coefficient in shale based on the whole process fitting. Chem. Eng. J. 428, 131151. https://doi.org/10.1016/j.cej.2021.131151

[53] Chen, L., Zhang, G., Wang, L., Wu, W., Ge, J., 2014. Zeta potential of limestone in a large range of salinity. Colloids Surf. Physicochem. Eng. Asp. 450, 1–8. https://doi.org/10.1016/j.colsurfa.2014.03.006

[54] Chen, Y., Sari, A., Xie, Q., Brady, P.V., Hossain, M.M., Saeedi, A., 2018. Electrostatic Origins of CO2-Increased Hydrophilicity in Carbonate Reservoirs. Sci. Rep. 8, 17691. https://doi.org/10.1038/s41598-018-35878-3

[55] Chi, Y., Liu, S., Jian, W., Zhao, C., Lv, J., Zhang, Y., 2020. The density characteristics of CO2 and alkane mixtures using PC-SAFT EoS. Greenh. Gases Sci. Technol. 10, 1063–1076. https://doi.org/10.1002/ghg.2026

[56] Chiquet, P., Daridon, J.-L., Broseta, D., Thibeau, S., 2007. CO2/water interfacial tensions under pressure and temperature conditions of CO2 geological storage. Energy Convers. Manag. 48, 736–744. https://doi.org/10.1016/j.enconman.2006.09.011

[57] Choi, J.-G., Do, D.D., Do, H.D., 2001. Surface Diffusion of Adsorbed Molecules in Porous Media: Monolayer, Multilayer, and Capillary Condensation Regimes. Ind. Eng. Chem. Res. 40, 4005–4031. https://doi.org/10.1021/ie010195z

[58] Collini, H., Jackson, M., 2021. Zeta Potential of the Crude Oil-Brine Interface and Implications for Controlled Salinity Waterflooding. Presented at the IOR 2021, European Association of Geoscientists & Engineers, pp. 1–12. https://doi.org/10.3997/2214-4609.202133090

[59] Cooper, A., 2000. Polymer synthesis and processing using supercritical carbon dioxide. J. Mater. Chem. 10, 207–234. https://doi.org/10.1039/A906486I

[60] Craddock, P.R., Le Doan, T.V., Bake, K., Polyakov, M., Charsky, A.M., Pomerantz, A.E., 2015. Evolution of Kerogen and Bitumen during Thermal Maturation via Semi-Open Pyrolysis Investigated by Infrared Spectroscopy. Energy Fuels 29, 2197–2210. https://doi.org/10.1021/ef5027532

[61] Crank, J., 1975. The mathematics of diffusion, 2d ed. ed. Clarendon Press, Oxford, [Eng].

[62] Creux, P., Lachaise, J., Graciaa, A., Beattie, J.K., Djerdjev, A.M., 2009. Strong Specific Hydroxide Ion Binding at the Pristine Oil/Water and Air/Water Interfaces. J. Phys. Chem. B 113, 14146–14150. https://doi.org/10.1021/jp906978v

[63] Cunningham, R.E., Williams, R.J.J., 1980. Diffusion in Gases and Porous Media. Springer US, Boston, MA. https://doi.org/10.1007/978-1-4757-4983-0

[64] Delgado, A.V., González-Caballero, F., Hunter, R.J., Koopal, L.K., Lyklema, J., 2007. Measurement and interpretation of electrokinetic phenomena. J. Colloid Interface Sci. 309, 194–224. https://doi.org/10.1016/j.jcis.2006.12.075

[65] Do, D.D., Wang, K., 1998. A new model for the description of adsorption kinetics in heterogeneous activated carbon. Carbon 36, 1539–1554. https://doi.org/10.1016/S0008-6223(98)00145-6

[66] Do, H.D., Do, D.D., Prasetyo, I., 2001. On the surface di usion of hydrocarbons in microporous activated carbon. Chem. Eng. Sci.

[67] Dolgaleva, I.V., Gorichev, I.G., Izotov, A.D., Stepanov, V.M., 2005. Modeling of the Effect of pH on the Calcite Dissolution Kinetics. Theor. Found. Chem. Eng. 39, 614–621. https://doi.org/10.1007/s11236-005-0125-1

[68] Donaldson, E.C., Alam, W., 2008. Surface Forces, in: Wettability. Elsevier, pp. 57–119. https://doi.org/10.1016/B978-1-933762-29-6.50008-9

[69] Dongari, N., Sharma, A., Durst, F., 2009. Pressure-driven diffusive gas flows in micro-channels: from the Knudsen to the continuum regimes. Microfluid. Nanofluidics 6, 679–692. https://doi.org/10.1007/s10404-008-0344-y

[70] D'souza, R., Patrick, J.R., Teja, A.S., 1988. High pressure phase equilibria in the carbon dioxide - *n* -Hexadecane and carbon dioxide - water systems. Can. J. Chem. Eng. 66, 319–323. https://doi.org/10.1002/cjce.5450660221

[71] Du, F., Nojabaei, B., 2020. Estimating diffusion coefficients of shale oil, gas, and condensate with nano-confinement effect. J. Pet. Sci. Eng. 193, 107362. https://doi.org/10.1016/j.petrol.2020.107362

[72] Du, X., Gu, M., Hou, Z., Liu, Z., Wu, T., 2019. Experimental Study on the Kinetics of Adsorption of CO_2 and CH_4 in Gas-Bearing Shale Reservoirs. Energy Fuels 33, 12587–12600. https://doi.org/10.1021/acs.energyfuels.9b03176

[73] Duan, S., Gu, M., Du, X., Xian, X., 2016. Adsorption Equilibrium of CO_2 and CH_4 and Their Mixture on Sichuan Basin Shale. Energy Fuels 30, 2248–2256. https://doi.org/10.1021/acs.energyfuels.5b02088

[74] Duan, Z., Sun, R., 2003. An improved model calculating CO2 solubility in pure water and aqueous NaCl solutions from 273 to 533 K and from 0 to 2000 bar. Chem. Geol. 193, 257–271. https://doi.org/10.1016/S0009-2541(02)00263-2

[75] Duan, Z., Sun, R., Zhu, C., Chou, I.-M., 2006. An improved model for the calculation of CO2 solubility in aqueous solutions containing Na+, K+, Ca2+, Mg2+, Cl−, and SO42−. Mar. Chem. 98, 131–139. https://doi.org/10.1016/j.marchem.2005.09.001

[76] Eggers, R., 2008. Innovative Verfahrensansätze in der Speiseölprozesstechnik. Chem. Ing. Tech. 80, 1059–1068. https://doi.org/10.1002/cite.200800063

[77] Elenius, M.T., Gasda, S.E., 2021. Convective Mixing Driven by Non-monotonic Density. Transp. Porous Media 138, 133–155. https://doi.org/10.1007/s11242-021-01593-3

[78] El-Mofty, S.E., Patra, P., El-Midany, A.A., Somasundaran, P., 2021. Dissolved Ca2+ ions adsorption and speciation at calcite-water interfaces: Dissolution and zeta potential studies. Sep. Purif. Technol. 257, 117924. https://doi.org/10.1016/j.seppur.2020.117924

[79] Elwinger, F., Pourmand, P., Furó, I., 2017. Diffusive Transport in Pores. Tortuosity and Molecular Interaction with the Pore Wall. J. Phys. Chem. C 121, 13757–13764. https://doi.org/10.1021/acs.jpcc.7b03885

[80] Emera, M.K., Sarma, H.K., 2007. Prediction of CO_2 Solubility in Oil and the Effects on the Oil Physical Properties. Energy Sources Part Recovery Util. Environ. Eff. 29, 1233–1242. https://doi.org/10.1080/00908310500434481

[81] Extrand, C.W., 2016. Origins of Wetting. Langmuir 32, 7697–7706. https://doi.org/10.1021/acs.langmuir.6b01935

[82] Fakher, S., Imqam, A., 2020. High pressure-high temperature carbon dioxide adsorption to shale rocks using a volumetric method. Int. J. Greenh. Gas Control 95, 102998. https://doi.org/10.1016/j.ijggc.2020.102998

[83] Farahabadi, Z.T., Lashkarbolooki, M., 2022. Effect of CO2 on the interfacial tension and swelling of crude oil during carbonated water flooding. J. Pet. Explor. Prod. Technol. https://doi.org/10.1007/s13202-022-01554-6

[84] Fleury, M., Pironon, J., Le Nindre, Y.M., Bildstein, O., Berne, P., Lagneau, V., Broseta, D., Pichery, T., Fillacier, S., Lescanne, M., Vidal, O., 2010. Evaluating Sealing Efficiency of Caprocks for CO_2 Storage: an Overview of the Geocarbone-Integrity

Program and Results. Oil Gas Sci. Technol. – Rev. L'Institut Fr. Pétrole 65, 435–444. https://doi.org/10.2516/ogst/2010007

[85] Fujii, T., Nakagawa, S., Sato, Y., Inomata, H., Hashida, T., 2010. Sorption Characteristics of CO2 on Rocks and Minerals in Storing CO2 Processes. Nat. Resour. 01, 1–10. https://doi.org/10.4236/nr.2010.11001

[86] Gao, H., Zhang, B., Fan, L., Zhang, H., Chen, G., Tontiwachwuthikul, P., Liang, Z., 2019. Study on Diffusivity of CO2 in Oil-Saturated Porous Media under High Pressure and Temperature. Energy Fuels. https://doi.org/10.1021/acs.energyfuels.9b01947

[87] Gasem, K.A.M., Robinson, R.L.Jr., 1985. Solubilities of carbon dioxide in heavy normal paraffins (C20-C44) at pressures to 9.6 MPa and temperatures from 323 to 423 K. J. Chem. Eng. Data 30, 53–56. https://doi.org/10.1021/je00039a018

[88] Gasparik, M.., Gensterblum, Y.., Ghanizadeh, A.., Weniger, P.., Krooss, B.M., 2015. High-Pressure/High-Temperature Methane-Sorption Measurements on Carbonaceous Shales by the Manometric Method: Experimental and Data-Evaluation Considerations for Improved Accuracy. SPE J. 20, 790–809. https://doi.org/10.2118/174543-PA

[89] Gasparik, M., Rexer, T.F.T., Aplin, A.C., Billemont, P., De Weireld, G., Gensterblum, Y., Henry, M., Krooss, B.M., Liu, S., Ma, X., Sakurovs, R., Song, Z., Staib, G., Thomas, K.M., Wang, S., Zhang, T., 2014. First International Inter-laboratory Comparison of High-pressure CH4, CO2 and C2H6 Sorption Isotherms on Carbonaceous Shales. Int. J. Coal Geol. 132, 131–146. https://doi.org/10.1016/j.coal.2014.07.010

[90] Georgiadis, A., Llovell, F., Bismarck, A., Blas, F.J., Galindo, A., Maitland, G.C., Trusler, J.P.M., Jackson, G., 2010. Interfacial tension measurements and modelling of (carbon dioxide+n-alkane) and (carbon dioxide+water) binary mixtures at elevated pressures and temperatures. J. Supercrit. Fluids 55, 743–754. https://doi.org/10.1016/j.supflu.2010.09.028

[91] Georgiadis, A., Maitland, G., Trusler, J.P.M., Bismarck, A., 2011. Interfacial Tension Measurements of the (H_2O + *n*-Decane + CO_2) Ternary System at Elevated Pressures and Temperatures. J. Chem. Eng. Data 56, 4900–4908. https://doi.org/10.1021/je200825j

[92] Ghorbani, M., Momeni, A., Safavi, S., Gandomkar, A., 2014. Modified vanishing interfacial tension (VIT) test for CO2–oil minimum miscibility pressure (MMP) measurement. J. Nat. Gas Sci. Eng. 20, 92–98. https://doi.org/10.1016/j.jngse.2014.06.006

[93] Gilbert, K., Bennett, P.C., Wolfe, W., Zhang, T., Romanak, K.D., 2016. CO2 solubility in aqueous solutions containing Na+, Ca2+, Cl−, SO42− and HCO3-: The effects of electrostricted water and ion hydration thermodynamics. Appl. Geochem. 67, 59–67. https://doi.org/10.1016/j.apgeochem.2016.02.002

[94] Gmehling, J., Kolbe, B., 1992. Thermodynamik. Wiley.

[95] Gonciaruk, A., Hall, M.R., Fay, M.W., Parmenter, C.D.J., Vane, C.H., Khlobystov, A.N., Ripepi, N., 2021. Kerogen nanoscale structure and CO2 adsorption in shale micropores. Sci. Rep. 11, 3920. https://doi.org/10.1038/s41598-021-83179-z

[96] Goulder, L.H., Schein, A.R., 2013. Carbon Taxes versus Cap and Trade: A Critical Review. Clim. Change Econ. 04, 1350010. https://doi.org/10.1142/S2010007813500103

[97] Graciaa, A., Creux, P., Dicharry, C., Lachaise, J., 2002. Measurement of the Zeta Potential of Oil Drops with the Spinning Tube Zetameter. J. Dispers. Sci. Technol. 23, 301–307. https://doi.org/10.1080/01932690208984206

[98] Gray-Weale, A., Beattie, J.K., 2009. An explanation for the charge on water's surface. Phys. Chem. Chem. Phys. 11, 10994. https://doi.org/10.1039/b901806a

[99] Groß, T., Buchhauser, J., Lüdemann, H.-D., 1998. Self-diffusion in fluid carbon dioxide at high pressures. J. Chem. Phys. 109, 4518–4522. https://doi.org/10.1063/1.477055

[100] Grunau, H.R., 1987. A Worldwide Look at the Cap-rock Problem. J. Pet. Geol. 10, 245–265. https://doi.org/10.1111/j.1747-5457.1987.tb00945.x

[101] Gu, M., Xian, X., Duan, S., Du, X., 2017. Influences of the composition and pore structure of a shale on its selective adsorption of CO2 over CH4. J. Nat. Gas Sci. Eng. 46, 296–306. https://doi.org/10.1016/j.jngse.2017.07.011

[102] Gu, M., Xie, R., Jin, G., 2022. A new quantitative evaluation method for fluid constituents with NMR T1-T2 spectra in shale reservoirs. J. Nat. Gas Sci. Eng. 99, 104412. https://doi.org/10.1016/j.jngse.2022.104412

[103] Guiliano, M., Boukir, A., Doumenq, P., Mille, G., Crampon, C., Badens, E., Charbit, G., 2000. Supercritical Fluid Extraction of Bal 150 Crude Oil Asphaltenes. Energy Fuels 14, 89–94. https://doi.org/10.1021/ef9900435

[104] Guo, B., Schechter, D.S., 1997. A simple and Accurate Method for Determining Low IFT from Pendant Drop Measurements. Int. Symp. Oilfield Chem. Soc. Pet. Eng.

[105] Habibi, A., Yassin, M.R., Dehghanpour, H., Bryan, D., 2017. Experimental investigation of CO2-oil interactions in tight rocks: A Montney case study. Fuel 203, 853–867. https://doi.org/10.1016/j.fuel.2017.04.077

[106] Haghi, R.K., Chapoy, A., Peirera, L.M.C., Yang, J., Tohidi, B., 2017. pH of CO 2 saturated water and CO 2 saturated brines: Experimental measurements and modelling. Int. J. Greenh. Gas Control 66, 190–203. https://doi.org/10.1016/j.ijggc.2017.10.001

[107] Hakimi, M.H., Abdullah, W.H., Alqudah, M., Makeen, Y.M., Mustapha, K.A., 2016. Organic geochemical and petrographic characteristics of the oil shales in the Lajjun area, Central Jordan: Origin of organic matter input and preservation conditions. Fuel 181, 34–45. https://doi.org/10.1016/j.fuel.2016.04.070

[108] Hakimi, M.H., Abdullah, W.H., Alqudah, M., Makeen, Y.M., Mustapha, K.A., Hatem, B.A., 2018. Pyrolysis analyses and bulk kinetic models of the Late Cretaceous oil shales in Jordan and their implications for early mature sulphur-rich oil generation potential. Mar. Pet. Geol. 91, 764–775. https://doi.org/10.1016/j.marpetgeo.2018.01.036

[109] Hamouda, A., Bagalkot, N., 2019. Effect of Salts on Interfacial Tension and CO2 Mass Transfer in Carbonated Water Injection. Energies 12, 748. https://doi.org/10.3390/en12040748

[110] Hamouda, A.A., Gomari, K. a. R., 2006. Influence of Temperature on Wettability Alteration of Carbonate Reservoirs. Presented at the SPE/DOE Symposium on Improved Oil Recovery, OnePetro. https://doi.org/10.2118/99848-MS

[111] Hangx, S.J.T., 2005. Behaviour of the CO2-H2O system and preliminary mineralisation model and experiments. Utrecht University.

[112] He, J., Xu, X., Gui, X., 2021. New Vapor–Liquid Phase Equilibrium Data of CO_2 in Several Heavy *n* -Alkanes at High Pressures. J. Chem. Eng. Data 66, 1600–1610. https://doi.org/10.1021/acs.jced.0c00834

[113] Hebach, A., Oberhof, A., Dahmen, N., 2004. Density of Water + Carbon Dioxide at Elevated Pressures: Measurements and Correlation. J. Chem. Eng. Data 49, 950–953. https://doi.org/10.1021/je034260i

[114] Hebach, A., Oberhof, A., Dahmen, N., Kögel, A., Ederer, H., Dinjus, E., 2002. Interfacial Tension at Elevated PressuresMeasurements and Correlations in the Water + Carbon Dioxide System. J. Chem. Eng. Data 47, 1540–1546. https://doi.org/10.1021/je025569p

[115] Heller, R., Zoback, M., 2014. Adsorption of methane and carbon dioxide on gas shale and pure mineral samples. J. Unconv. Oil Gas Resour. 8, 14–24. https://doi.org/10.1016/j.juogr.2014.06.001

[116] Hemmati-Sarapardeh, A., Ayatollahi, S., Ghazanfari, M.-H., Masihi, M., 2014. Experimental Determination of Interfacial Tension and Miscibility of the CO_2 –Crude Oil System; Temperature, Pressure, and Composition Effects. J. Chem. Eng. Data 59, 61–69. https://doi.org/10.1021/je400811h

[117] Higashi, H., Iwai, Y., Arai, Y., 2000. Calculation of Self-Diffusion and Tracer Diffusion Coefficients near the Critical Point of Carbon Dioxide Using Molecular Dynamics Simulation. Ind. Eng. Chem. Res. 39, 4567–4570. https://doi.org/10.1021/ie000173x

[118] Hiorth, A., Cathles, L.M., Madland, M.V., 2010. The Impact of Pore Water Chemistry on Carbonate Surface Charge and Oil Wettability. Transp. Porous Media 85, 1–21. https://doi.org/10.1007/s11242-010-9543-6

[119] Ho, T.A., Wang, Y., Criscenti, L.J., 2018. Chemo-mechanical coupling in kerogen gas adsorption/desorption. Phys. Chem. Chem. Phys. 20, 12390–12395. https://doi.org/10.1039/C8CP01068D

[120] Hölscher, I.F., Spee, M., Schneider, G.M., 1989. Fluid-phase equilibria of binary and ternary mixtures of CO2 with hexadecane, 1-dodecanol, 1-hexadecanol and 2-ethoxy-ethanol at 333.2 and 393.2 K and at pressures up to 33 MPa. Fluid Phase Equilibria 49, 103–113. https://doi.org/10.1016/0378-3812(89)80008-1

[121] Honarvar, B., Azdarpour, A., Karimi, M., Rahimi, A., Afkhami Karaei, M., Hamidi, H., Ing, J., Mohammadian, E., 2017. Experimental Investigation of Interfacial Tension Measurement and Oil Recovery by Carbonated Water Injection: A Case Study Using Core Samples from an Iranian Carbonate Oil Reservoir. Energy Fuels 31, 2740–2748. https://doi.org/10.1021/acs.energyfuels.6b03365

[122] Horikawa, T., Do, D.D., Nicholson, D., 2011. Capillary condensation of adsorbates in porous materials. Adv. Colloid Interface Sci. 169, 40–58. https://doi.org/10.1016/j.cis.2011.08.003

[123] Huang, L., Khoshnood, A., Firoozabadi, A., 2020. Swelling of Kimmeridge kerogen by normal-alkanes, naphthenes and aromatics. Fuel 267, 117155. https://doi.org/10.1016/j.fuel.2020.117155

[124] Huang, S.H., Lin, H.M., Chao, K.C., 1988. Solubility of carbon dioxide, methane, and ethane in n-eicosane. J. Chem. Eng. Data 33, 145–147. https://doi.org/10.1021/je00052a026

[125] Hui, D., Pan, Y., Luo, P., Zhang, Y., Sun, L., Lin, C., 2019. Effect of supercritical CO2 exposure on the high-pressure CO2 adsorption performance of shales. Fuel 247, 57–66. https://doi.org/10.1016/j.fuel.2019.03.013

[126] Huie, N.C., Luks, K.D., Kohn, J.P., 1973. Phase-equilibriums behavior of systems carbon dioxide-n-eicosane and carbon dioxide-n-decane-n-eicosane. J. Chem. Eng. Data 18, 311–313. https://doi.org/10.1021/je60058a008

[127] Hutton, A., Bharati, S., Robl, T., 1994. Chemical and Petrographic Classification of Kerogen/Macerals. Energy Fuels 8, 1478–1488.

[128] Ibrahim, A.F., Abdelgawad, K.Z., Al-Anazi, A., Al Hamad, J.S., 2022. Effect of Crude Oil Properties on the Interfacial Tension of Crude Oil/CO2 Under HPHT Conditions. Arab. J. Sci. Eng. https://doi.org/10.1007/s13369-022-07291-6

[129] International Energy Agency (IEA), 2023. Country Information - Jordan [WWW Document]. URL www.eia.gov

[130] Ikeda, N., Aratono, M., Motomura, K., 1992. Thermodynamic study on the adsorption of sodium chloride at the water/hexane interface. J. Colloid Interface Sci. 149, 208–215. https://doi.org/10.1016/0021-9797(92)90405-B

[131] IPCC, 2005: IPCC Special Report on Carbon Dioxide Capture and Storage. Prepared by Working Group III of the Intergovernmental Panel on Climate Change [Metz, B., O. Davidson, H. C. de Coninck, M. Loos, and L. A. Meyer (eds.)]. Cambridge University Press, Cambridge, United Kingdom and New York, NY, USA, 442 ppIsraelachvili, J.N., 2011. Van der Waals Forces, in: Intermolecular and Surface Forces. Elsevier, pp. 107–132. https://doi.org/10.1016/B978-0-12-375182-9.10006-5

[132] Jaber, J.O., 2000. Gasification potential of Ellujjun oil shale. Energy Convers. Manag. 41, 1615–1624. https://doi.org/10.1016/S0196-8904(00)00006-6

[133] Jaber, J.O., Amri, A., Ibrahim, K., 2011. Experimental investigation of effects of oil shale composition on its calorific value and oil yield. Int. J. Oil Gas Coal Technol. 4, 307. https://doi.org/10.1504/IJOGCT.2011.043714

[134] Jaber, J.O., Probert, S.D., 1997. Exploitation of Jordanian oil-shales. Appl. Energy 58, 161–175. https://doi.org/10.1016/S0306-2619(97)00041-X

[135] Jackson, M.D., Al-Mahrouqi, D., Vinogradov, J., 2016. Zeta potential in oil-water-carbonate systems and its impact on oil recovery during controlled salinity water-flooding. Sci. Rep. 6, 37363. https://doi.org/10.1038/srep37363

[136] Jaeger, P., 2014. Interfacial Phenomena in Enhanced Oil and Gas Recovery (Habilitation). Hamburg University of Technology, Hamburg.

[137] Jaeger, P.T., Alotaibi, M.B., Nasr-El-Din, H.A., 2010. Influence of Compressed Carbon Dioxide on the Capillarity of the Gas−Crude Oil−Reservoir Water System. J. Chem. Eng. Data 55, 5246–5251. https://doi.org/10.1021/je100825b

[138] Javadpour, F., Fisher, D., Unsworth, M., 2007. Nanoscale Gas Flow in Shale Gas Sediments. J. Can. Pet. Technol. 46. https://doi.org/10.2118/07-10-06

[139] Jia, B., 2019. Carbonated water injection (CWI) for improved oil recovery and carbon storage in high-salinity carbonate reservoir. J. Taiwan Inst. Chem. Eng. 104, 82–93. https://doi.org/10.1016/j.jtice.2019.08.014

[140] Jia, B., Chen, Z., Xian, C., 2022. Investigations of CO2 storage capacity and flow behavior in shale formation. J. Pet. Sci. Eng. 208, 109659. https://doi.org/10.1016/j.petrol.2021.109659

[141] Jia, B., Tsau, J.-S., Barati, R., 2019. A review of the current progress of CO2 injection EOR and carbon storage in shale oil reservoirs. Fuel 236, 404–427. https://doi.org/10.1016/j.fuel.2018.08.103

[142] Jian, X., Guan, P., Zhang, W., 2012. Carbon dioxide sorption and diffusion in coals: Experimental investigation and modeling. Sci. China Earth Sci. 55, 633–643. https://doi.org/10.1007/s11430-011-4272-4

[143] Jobic, H., Méthivier, A., Ehlers, G., Farago, B., Haeussler, W., 2004. Accelerated Diffusion of Long-Chain Alkanes between Nanosized Cavities. Angew. Chem. Int. Ed. 43, 364–366. https://doi.org/10.1002/anie.200352691

[144] Jost, W., 1952. Diffusion in Solids, Liquids, Gases. Academic Press, New York.

[145] Ju, Y., He, J., Chang, E., Zheng, L., 2019. Quantification of CH4 adsorption capacity in kerogen-rich reservoir shales: An experimental investigation and molecular dynamic simulation. Energy 170, 411–422. https://doi.org/10.1016/j.energy.2018.12.087

[146] Kakati, A., Sangwai, J.S., 2017. Effect of monovalent and divalent salts on the interfacial tension of pure hydrocarbon-brine systems relevant for low salinity water flooding. J. Pet. Sci. Eng. 157, 1106–1114. https://doi.org/10.1016/j.petrol.2017.08.017

[147] Kankala, R.K., Zhang, Y.S., Wang, S.-B., Lee, C.-H., Chen, A.-Z., 2017. Supercritical Fluid Technology: An Emphasis on Drug Delivery and Related Biomedical Applications. Adv. Healthc. Mater. 6, 1700433. https://doi.org/10.1002/adhm.201700433

[148] Kauffman, J.F., 2001. Quadrupolar Solvent Effects on Solvation and Reactivity of Solutes Dissolved in Supercritical CO $_2$. J. Phys. Chem. A 105, 3433–3442. https://doi.org/10.1021/jp004359l

[149] Keshavarz, A., Abid, H., Ali, M., Iglauer, S., 2022. Hydrogen diffusion in coal: Implications for hydrogen geo-storage. J. Colloid Interface Sci. 608, 1457–1462. https://doi.org/10.1016/j.jcis.2021.10.050

[150] Keyes, F.G., Kirkwood, J.G., 1930. The Dielectric Constant of Carbon Dioxide as a Function of Temperature and Density. Phys. Rev. 36, 754–761. https://doi.org/10.1103/PhysRev.36.754

[151] Khaksar Manshad, A., Olad, M., Taghipour, S.A., Nowrouzi, I., Mohammadi, A.H., 2016. Effects of water soluble ions on interfacial tension (IFT) between oil and brine in smart and carbonated smart water injection process in oil reservoirs. J. Mol. Liq. 223, 987–993. https://doi.org/10.1016/j.molliq.2016.08.089

[152] Khrewesh, A.M., Hamad, A.A., Abed, A.M., 2014. Late Cretaceous Muwaqqar Formation Ammonites in Southeastern Jordan 6, 7.

[153] Kim, C., Jang, H., Lee, J., 2015. Experimental investigation on the characteristics of gas diffusion in shale gas reservoir using porosity and permeability of nanopore scale. J. Pet. Sci. Eng. 133, 226–237. https://doi.org/10.1016/j.petrol.2015.06.008

[154] Kleiner, M., Sadowski, G., 2007. Modeling of Polar Systems Using PCP-SAFT: An Approach to Account for Induced-Association Interactions. J. Phys. Chem. C 111, 15544–15553. https://doi.org/10.1021/jp072640v

[155] Klewiah, I., Berawala, D.S., Alexander Walker, H.C., Andersen, P.Ø., Nadeau, P.H., 2020. Review of experimental sorption studies of CO2 and CH4 in shales. J. Nat. Gas Sci. Eng. 73, 103045. https://doi.org/10.1016/j.jngse.2019.103045

[156] Knoche, W., 1980. Chemical Reactions of CO2 in Water, in: Bauer, C., Gros, G., Bartels, H. (Eds.), Biophysics and Physiology of Carbon Dioxide, Proceedings in Life Sciences. Springer Berlin Heidelberg, Berlin, Heidelberg, pp. 3–11. https://doi.org/10.1007/978-3-642-67572-0_1

[157] Koleini, M.M., Badizad, M.H., Kargozarfard, Z., Ayatollahi, S., 2019. Interactions between Rock/Brine and Oil/Brine Interfaces within Thin Brine Film Wetting Carbonates: A Molecular Dynamics Simulation Study. Energy Fuels 33, 7983–7992. https://doi.org/10.1021/acs.energyfuels.9b00496

[158] Kordikowski, A., Schneider, G.M., 1993. Fluid phase equilibria of binary and ternary mixtures of supercritical carbon dioxide with low-volatility organic substances up to 100 MPa and 393 K: c. Fluid Phase Equilibria 90, 149–162. https://doi.org/10.1016/0378-3812(93)85010-J

[159] Koschel, D., Coxam, J.-Y., Rodier, L., Majer, V., 2006. Enthalpy and solubility data of CO2 in water and NaCl(aq) at conditions of interest for geological sequestration. Fluid Phase Equilibria 247, 107–120. https://doi.org/10.1016/j.fluid.2006.06.006

[160] Krevor, S., Blunt, M.J., Benson, S.M., Pentland, C.H., Reynolds, C., Al-Menhali, A., Niu, B., 2015. Capillary trapping for geologic carbon dioxide storage – From pore scale physics to field scale implications. Int. J. Greenh. Gas Control 40, 221–237. https://doi.org/10.1016/j.ijggc.2015.04.006

[161] Kuila, U., Prasad, M., 2013. Specific surface area and pore-size distribution in clays and shales. Geophys. Prospect. 61, 341–362. https://doi.org/10.1111/1365-2478.12028

[162] Kumar, N., Augusto Sampaio, M., Ojha, K., Hoteit, H., Mandal, A., 2022. Fundamental aspects, mechanisms and emerging possibilities of CO2 miscible flooding in enhanced oil recovery: A review. Fuel 330, 125633. https://doi.org/10.1016/j.fuel.2022.125633

[163] Kunz, O., Wagner, W., 2012. The GERG-2008 Wide-Range Equation of State for Natural Gases and Other Mixtures: An Expansion of GERG-2004. J. Chem. Eng. Data 57, 3032–3091. https://doi.org/10.1021/je300655b

[164] Lafortune, S., Adelise, F., Garrido, D.R.R., Pokryszka, Z., 2014. Assessing CO2 Adsorption Capacities onto Shales Through Gravimetric Experiments: A First Step in the Feasibility Study of Coupling "Fracking" with Carbon Storage. Energy Procedia 63, 5933–5937. https://doi.org/10.1016/j.egypro.2014.11.629

[165] Lansangan, R.M., Smith, J.L., 1993. Viscosity, Density, and Composition Measurements of CO2/West Texas Oil Systems. SPE Reserv. Eng. 8, 175–182. https://doi.org/10.2118/21017-PA

[166] Larsen, J.W., Parikh, H., Michels, R., 2002. Changes in the cross-link density of Paris Basin Toarcian kerogen during maturation. Org. Geochem. 33, 1143–1152. https://doi.org/10.1016/S0146-6380(02)00102-X

[167] Lashkarbolooki, M., Ayatollahi, S., 2018. Experimental investigation on CO2-light crude oil interfacial and swelling behavior. Chin. J. Chem. Eng. 26, 373–379. https://doi.org/10.1016/j.cjche.2017.07.010

[168] Lashkarbolooki, M., Hezave, A.Z., Ayatollahi, S., 2019. Swelling behavior of heavy crude oil during injection of carbonated brine containing chloride anion. J. Mol. Liq. 276, 7–14. https://doi.org/10.1016/j.molliq.2018.11.112

[169] Lashkarbolooki, M., Hezave, A.Z., Riazi, M., Ayatollahi, S., 2020. New insight on dynamic behavior of swelling and bond number of light and heavy crude oil during carbonated water flooding. Eur. Phys. J. Plus 135, 91. https://doi.org/10.1140/epjp/s13360-020-00104-5

[170] Lashkarbolooki, M., Riazi, M., Ayatollahi, S., 2018. Effect of CO2 and crude oil type on the dynamic interfacial tension of crude oil/carbonated water at different operational conditions. J. Pet. Sci. Eng. 170, 576–581. https://doi.org/10.1016/j.petrol.2018.07.002

[171] Lashkarbolooki, M., Riazi, M., Ayatollahi, S., 2017. Effect of CO2 and natural surfactant of crude oil on the dynamic interfacial tensions during carbonated water flooding: Experimental and modeling investigation. J. Pet. Sci. Eng. 159, 58–67. https://doi.org/10.1016/j.petrol.2017.09.023

[172] Lemmon, E.W., Huber, M.L., 2004. Thermodynamic Properties of n-Dodecane. Energy Fuels 18, 960–967. https://doi.org/10.1021/ef0341062

[173] Leonard, M.D., Michaelides, E.E., Michaelides, D.N., 2020. Energy storage needs for the substitution of fossil fuel power plants with renewables. Renew. Energy 145, 951–962. https://doi.org/10.1016/j.renene.2019.06.066

[174] Li, C., Pu, H., Zhao, J.X., 2019. Molecular Simulation Study on the Volume Swelling and the Viscosity Reduction of *n* -Alkane/CO_2 Systems. Ind. Eng. Chem. Res. 58, 8871–8877. https://doi.org/10.1021/acs.iecr.9b01268

[175] Li, D., Graupner, B.J., Bauer, S., 2011. A method for calculating the liquid density for the CO2–H2O–NaCl system under CO2 storage condition. Energy Procedia 4, 3817–3824. https://doi.org/10.1016/j.egypro.2011.02.317

[176] Li, H., Zheng, S., Yang, D., 2013. Enhanced Swelling Effect and Viscosity Reduction of Solvent(s)/CO2/Heavy-Oil Systems. SPE J. 13.

[177] Li, J., Wu, K., Chen, Z., Wang, W., Yang, B., Wang, K., Luo, J., Yu, R., 2019. Effects of energetic heterogeneity on gas adsorption and gas storage in geologic shale systems. Appl. Energy 251, 113368. https://doi.org/10.1016/j.apenergy.2019.113368

[178] Li, K., 2022. An assessment of oil shale resources in the sultani formation, central of Jordan. [Doctoral dissertation – TU Clausthal]

[179] Li, K., Samara, H., Wang, X., Jaeger, P., Ganzer, L., Wegner, J., Xie, L., 2019. Reservoir Characteristics and Resource Potential of Oil Shale in Sultani Area, Central of Jordan, in: Day 4 Thu, November 14, 2019. Presented at the Abu Dhabi International Petroleum Exhibition & Conference, SPE, Abu Dhabi, UAE, p. D041S110R003. https://doi.org/10.2118/197606-MS

[180] Li, N., Zhang, C.-W., Ma, Q.-L., Jiang, L.-Y., Xu, Y.-X., Chen, G.-J., Sun, C.-Y., Yang, L.-Y., 2017. Interfacial Tension Measurement and Calculation of (Carbon Dioxide + *n*

-Alkane) Binary Mixtures. J. Chem. Eng. Data 62, 2861–2871. https://doi.org/10.1021/acs.jced.7b00159

[181] Li, S., Li, Z., Dong, Q., 2016. Diffusion coefficients of supercritical CO 2 in oil-saturated cores under low permeability reservoir conditions. J. CO2 Util. 14, 47–60. https://doi.org/10.1016/j.jcou.2016.02.002

[182] Li, S., Qiao, C., Li, Z., Hui, Y., 2018a. The effect of permeability on supercritical CO2 diffusion coefficient and determination of diffusive tortuosity of porous media under reservoir conditions. J. CO2 Util. 28, 1–14. https://doi.org/10.1016/j.jcou.2018.09.007

[183] Li, S., Qiao, C., Zhang, C., Li, Z., 2018b. Determination of diffusion coefficients of supercritical CO2 under tight oil reservoir conditions with pressure-decay method. J. CO2 Util. 24, 430–443. https://doi.org/10.1016/j.jcou.2018.02.002

[184] Li, S., Wang, Y., Zhang, K., Qiao, C., 2019. Diffusion Behavior of Supercritical CO_2 in Micro- to Nanoconfined Pores. Ind. Eng. Chem. Res. 58, 21772–21784. https://doi.org/10.1021/acs.iecr.9b04750

[185] Li, W., Jin, Z., 2019. Effect of ion concentration and multivalence on methane-brine interfacial tension and phenomena from molecular perspectives. Fuel 254, 115657. https://doi.org/10.1016/j.fuel.2019.115657

[186] Li, W., Stevens, L.A., Zhang, B., Zheng, D., Snape, C.E., 2022. Combining molecular simulation and experiment to prove micropore distribution controls methane adsorption in kerogens. Int. J. Coal Geol. 261, 104092. https://doi.org/10.1016/j.coal.2022.104092

[187] Li, W., Zhang, M., Nan, Y., Pang, W., Jin, Z., 2021. Molecular Dynamics Study on CO_2 Storage in Water-Filled Kerogen Nanopores in Shale Reservoirs: Effects of Kerogen Maturity and Pore Size. Langmuir 37, 542–552. https://doi.org/10.1021/acs.langmuir.0c03232

[188] Li, X., Boek, E., Maitland, G.C., Trusler, J.P.M., 2012a. Interfacial Tension of (Brines + CO2): (0.864 NaCl + 0.136 KCl) at Temperatures between (298 and 448) K, Pressures between (2 and 50) MPa, and Total Molalities of (1 to 5) mol·kg–1. J. Chem. Eng. Data 57, 1078–1088. https://doi.org/10.1021/je201062r

[189] Li, X., Boek, E.S., Maitland, G.C., Trusler, J.P.M., 2012b. Interfacial Tension of (Brines + CO_2): $CaCl_2$ (aq), $MgCl_2$ (aq), and Na_2SO_4 (aq) at Temperatures between (343 and 423) K, Pressures between (2 and 50) MPa, and Molalities of (0.5 to 5) mol·kg $^{-1}$. J. Chem. Eng. Data 57, 1369–1375. https://doi.org/10.1021/je300304p

[190] Li, X., Peng, C., Crawshaw, J.P., Maitland, G.C., Trusler, J.P.M., 2018. The pH of CO2-saturated aqueous NaCl and NaHCO3 solutions at temperatures between 308 K and 373 K at pressures up to 15 MPa. Fluid Phase Equilibria 458, 253–263. https://doi.org/10.1016/j.fluid.2017.11.023

[191] Li, X., Ross, D.A., Trusler, J.P.M., Maitland, G.C., Boek, E.S., 2013. Molecular Dynamics Simulations of CO_2 and Brine Interfacial Tension at High Temperatures and Pressures. J. Phys. Chem. B 117, 5647–5652. https://doi.org/10.1021/jp309730m

[192] Li, Z., Dong, M., 2009. Experimental Study of Carbon Dioxide Diffusion in Oil-Saturated Porous Media under Reservoir Conditions. Ind. Eng. Chem. Res. 48, 9307–9317. https://doi.org/10.1021/ie900145c

[193] Li, Z., Dong, M., Li, S., Dai, L., 2006. A New Method for Gas Effective Diffusion Coefficient Measurement in Water-Saturated Porous Rocks under High Pressures. J. Porous Media 9. https://doi.org/10.1615/JPorMedia.v9.i5.50

[194] Li, Z., Dong, M., Li, S., Dai, L., 2004. Densities and Solubilities for Binary Systems of Carbon Dioxide + Water and Carbon Dioxide + Brine at 59 °C and Pressures to 29 MPa. J. Chem. Eng. Data 49, 1026–1031. https://doi.org/10.1021/je049945c

[195] Li, Z., Yao, J., Firoozabadi, A., 2021. Kerogen Swelling in Light Hydrocarbon Gases and Liquids and Validity of Schroeder's Paradox. J. Phys. Chem. C 125, 8137–8147. https://doi.org/10.1021/acs.jpcc.0c10362

[196] Lin, R., Tavlarides, L.L., 2010. Diffusion coefficients of diesel fuel and surrogate compounds in supercritical carbon dioxide. J. Supercrit. Fluids 52, 47–55. https://doi.org/10.1016/j.supflu.2009.12.002

[197] Liu, B., Shi, J., Sun, B., Shen, Y., Zhang, J., Chen, X., Wang, M., 2015. Molecular dynamics simulation on volume swelling of CO2–alkane system. Fuel 143, 194–201. https://doi.org/10.1016/j.fuel.2014.11.046

[198] Liu, B., Shi, J., Wang, M., Zhang, J., Sun, B., Shen, Y., Sun, X., 2016. Reduction in interfacial tension of water–oil interface by supercritical CO2 in enhanced oil recovery processes studied with molecular dynamics simulation. J. Supercrit. Fluids 111, 171–178. https://doi.org/10.1016/j.supflu.2015.11.001

[199] Liu, D., Guo, X., Xiao, B., 2019. What causes growth of global greenhouse gas emissions? Evidence from 40 countries. Sci. Total Environ. 661, 750–766. https://doi.org/10.1016/j.scitotenv.2019.01.197

[200] Liu, J., Xie, L., Elsworth, D., Gan, Q., 2019. CO_2 /CH_4 Competitive Adsorption in Shale: Implications for Enhancement in Gas Production and Reduction in Carbon Emissions. Environ. Sci. Technol. 53, 9328–9336. https://doi.org/10.1021/acs.est.9b02432

[201] Liu, K., Zakharova, N., Adeyilola, A., Zeng, L., 2021. Experimental Study on the Pore Shape Damage of Shale Samples during the Crushing Process. Energy Fuels 35, 2183–2191. https://doi.org/10.1021/acs.energyfuels.0c03297

[202] Liu, Y., 2008. New insights into pseudo-second-order kinetic equation for adsorption. Colloids Surf. Physicochem. Eng. Asp. 320, 275–278. https://doi.org/10.1016/j.colsurfa.2008.01.032

[203] Liu, Y., Hou, M., Yang, G., Han, B., 2011. Solubility of CO2 in aqueous solutions of NaCl, KCl, CaCl2 and their mixed salts at different temperatures and pressures. J. Supercrit. Fluids 56, 125–129. https://doi.org/10.1016/j.supflu.2010.12.003

[204] Liu, Y., Li, H.A., Okuno, R., 2016. Measurements and Modeling of Interfacial Tension for CO_2 /CH_4 /Brine Systems under Reservoir Conditions. Ind. Eng. Chem. Res. 55, 12358–12375. https://doi.org/10.1021/acs.iecr.6b02446

[205] Liu, Y., Tang, J., Wang, M., Wang, Q., Tong, J., Zhao, J., Song, Y., 2017. Measurement of Interfacial Tension of CO2 and NaCl Aqueous Solution over Wide Temperature, Pressure, and Salinity Ranges. J. Chem. Eng. Data 62, 1036–1046. https://doi.org/10.1021/acs.jced.6b00858

[206] Liu, Z., Emami-Meybodi, H., 2022. Apparent diffusion coefficient for adsorption-controlled gas transport in nanoporous media. Chem. Eng. J. 450, 138105. https://doi.org/10.1016/j.cej.2022.138105

[207] London, F., 1937. The general theory of molecular forces. Trans. Faraday Soc. 33, 8b. https://doi.org/10.1039/tf937330008b

[208] Long, H., Lin, H., Yan, M., Bai, Y., Tong, X., Kong, X., Li, S., 2021. Adsorption and diffusion characteristics of CH4, CO2, and N2 in micropores and mesopores of bituminous coal: Molecular dynamics. Fuel 292, 120268. https://doi.org/10.1016/j.fuel.2021.120268

[209] Lou, X., Chakraborty, N., Karpyn, Z.T., Ayala, L.F., Nagarajan, N., Wijaya, Z., 2021. Experimental Study of Gas/Liquid Diffusion in Porous Rocks and Bulk Fluids To Investigate the Effect of Rock-Matrix Hindrance. SPE J. 26, 1174–1188. https://doi.org/10.2118/195941-PA

[210] Lowell, S., Shields, J.E., Thomas, M.A., Thommes, M., 2004. Adsorption Isotherms, in: Lowell, S., Shields, J.E., Thomas, M.A., Thommes, M. (Eds.), Characterization of Porous Solids and Powders: Surface Area, Pore Size and Density. Springer Netherlands, Dordrecht, pp. 11–14. https://doi.org/10.1007/978-1-4020-2303-3_3

[211] Lu, C., Han, W.S., Lee, S.-Y., McPherson, B.J., Lichtner, P.C., 2009. Effects of density and mutual solubility of a –brine system on storage in geological formations: "Warm" vs. "cold" formations. Adv. Water Resour. 32, 1685–1702. https://doi.org/10.1016/j.advwatres.2009.07.008

[212] Lu, Y., Ao, X., Tang, J., Jia, Y., Zhang, X., Chen, Y., 2016. Swelling of shale in supercritical carbon dioxide. J. Nat. Gas Sci. Eng. 30, 268–275. https://doi.org/10.1016/j.jngse.2016.02.011

[213] Lu, Y., Najafabadi, N.F., Firoozabadi, A., 2017. Effect of Temperature on Wettability of Oil/Brine/Rock Systems. Energy Fuels 31, 4989–4995. https://doi.org/10.1021/acs.energyfuels.7b00370

[214] Lun, Z., Fan, H., Wang, H., Luo, M., Pan, W., Wang, R., 2012. Interfacial Tensions between Reservoir Brine and CO_2 at High Pressures for Different Salinity. Energy Fuels 26, 3958–3962. https://doi.org/10.1021/ef300440w

[215] Lutyński, M., Waszczuk, P., Słomski, P., Szczepański, J., 2017. CO 2 sorption of Pomeranian gas bearing shales – the effect of clay minerals. Energy Procedia 125, 457–466. https://doi.org/10.1016/j.egypro.2017.08.153

[216] Lv, J., Chi, Y., Zhao, C., Zhang, Y., Mu, H., 2019. Experimental study of the supercritical CO_2 diffusion coefficient in porous media under reservoir conditions. R. Soc. Open Sci. 6, 181902. https://doi.org/10.1098/rsos.181902

[217] Lyklema, J., 2000a. 2 - Interfacial Tension: Molecular Interpretation, in: Fundamentals of Interface and Colloid Science, Liquid-Fluid Interfaces. Academic Press, p. 2.1-2.78. https://doi.org/10.1016/S1874-5679(00)80005-7

[218] Lyklema, J., 2000b. Surface Tensions of Pure Liquids and Mixtures, in: Fundamentals of Interface and Colloid Science. Elsevier, p. A1.1-A1.48. https://doi.org/10.1016/S1874-5679(00)80009-4

[219] Lyklema, J., 1991. Fundamentals of Interface and Colloid Science: Fundamentals. Academic Press.

[220] Mahani, H., Keya, A.L., Berg, S., Nasralla, R., 2017a. Electrokinetics of Carbonate/Brine Interface in Low-Salinity Waterflooding: Effect of Brine Salinity, Composition, Rock Type, and pH on ζ-Potential and a Surface-Complexation Model. SPE J. 22, 53–68. https://doi.org/10.2118/181745-PA

[221] Mahani, H., Menezes, R., Berg, S., Fadili, A., Nasralla, R., Voskov, D., Joekar-Niasar, V., 2017b. Insights into the Impact of Temperature on the Wettability Alteration by Low Salinity in Carbonate Rocks. Energy Fuels 31, 7839–7853. https://doi.org/10.1021/acs.energyfuels.7b00776

[222] Mahmoud, M., Hamza, A., Hussein, I.A., Eliebid, M., Kamal, M.S., Abouelresh, M., Shawabkeh, R., Al-Marri, M.J., 2020. Carbon dioxide EGR and sequestration in mature and immature shale: Adsorption study. J. Pet. Sci. Eng. 188, 106923. https://doi.org/10.1016/j.petrol.2020.106923

[223] Mahzari, P., Tsolis, P., Sohrabi, M., Enezi, S., Yousef, A.A., Eidan, A.A., 2018. Carbonated water injection under reservoir conditions; in-situ WAG-type EOR. Fuel 217, 285–296. https://doi.org/10.1016/j.fuel.2017.12.096

[224] Maitland, G.C., Maitland, G.D., C, M.G., Rigby, M., Smith, E.B., Wakeham, P. of C.P.D. of C.E.W.A., Wakeham, W.A., Smith, F. of S.C.C. and L. in P.C.E.B., Rigby, L.D. of C.M., 1981. Intermolecular Forces: Their Origin and Determination. Clarendon Press.

[225] Manciu, M., Ruckenstein, E., 2003. Specific ion effects via ion hydration: I. Surface tension. Adv. Colloid Interface Sci. 105, 63–101. https://doi.org/10.1016/S0001-8686(03)00018-6

[226] Marinova, K.G., Alargova, R.G., Denkov, N.D., Velev, O.D., Petsev, D.N., Ivanov, I.B., Borwankar, R.P., 1996. Charging of Oil−Water Interfaces Due to Spontaneous Adsorption of Hydroxyl Ions. Langmuir 12, 2045–2051. https://doi.org/10.1021/la950928i

[227] Marra, R.K., Poettmann, F.H., Thompson, R.S., 1987. Density of Crude Oil Saturated With Carbon Dioxide, in: All Days. Presented at the SPE California Regional Meeting, SPE, Ventura, California, p. SPE-16350-MS. https://doi.org/10.2118/16350-MS

[228] Martinus Oversteegen, S., Barneveld, P.A., van Male, J., Leermakers, F.A.M., Lyklema, J., 1999. Thermodynamic derivation of mechanical expressions for interfacial parameters. Phys. Chem. Chem. Phys. 1, 4987–4994. https://doi.org/10.1039/a906437k

[229] Masika, E., Mokaya, R., 2012. Hydrogen Storage in High Surface Area Carbons with Identical Surface Areas but Different Pore Sizes: Direct Demonstration of the Effects of Pore Size. J. Phys. Chem. C 116, 25734–25740. https://doi.org/10.1021/jp3100365

[230] Maskari, N.S.A., Sari, A., Hossain, M.M., Saeedi, A., Xie, Q., 2019. Response of Non-Polar Oil Component on Low Salinity Effect in Carbonate Reservoirs: Adhesion Force Measurement Using Atomic Force Microscopy. Energies 13, 77. https://doi.org/10.3390/en13010077

[231] Mays, T.J., 2007. A new classification of pore sizes, in: Studies in Surface Science and Catalysis. Elsevier, pp. 57–62. https://doi.org/10.1016/S0167-2991(07)80009-7

[232] Mazumder, S., Wolf, K.H., 2008. Differential swelling and permeability change of coal in response to CO2 injection for ECBM. Int. J. Coal Geol. 74, 123–138. https://doi.org/10.1016/j.coal.2007.11.001

[233] McHugh, M.A., Krukonis, V.J., 1994. Supercritical fluid extraction: principles and practice, 2nd ed. ed, Butterworth-Heinemann series in chemical engineering. Butterworth-Heinemann, Boston.

[234] McWhorter, D., 2021. Flux Equations for Gas Diffusion in Porous Media. The Groundwater Project. https://doi.org/10.21083/978-1-77470-003-7

[235] Medveď, I., Černý, R., 2011. Surface diffusion in porous media: A critical review. Microporous Mesoporous Mater. 142, 405–422. https://doi.org/10.1016/j.micromeso.2011.01.015

[236] Meijssen, T., Emmen, J., Fowler, T., 2014. In-situ Oil Shale Development in Jordan through ICP Technology, in: Day 2 Tue, November 11, 2014. Presented at the Abu Dhabi International Petroleum Exhibition and Conference, SPE, Abu Dhabi, UAE, p. D021S023R002. https://doi.org/10.2118/172135-MS

[237] Memon, A., Li, A., Memon, B.S., Muther, T., Han, W., Kashif, M., Tahir, M.U., Akbar, I., 2021. Gas Adsorption and Controlling Factors of Shale: Review, Application, Comparison and Challenges. Nat. Resour. Res. 30, 827–848. https://doi.org/10.1007/s11053-020-09738-9

[238] Ministry of Energy and Mineral Resources (MEMR, 2023). Retail Prices of Petroleum Products [WWW Document]. URL http://memr.gov.jo (accessed 1.7.23).

[239] Merey, S., Sinayuc, C., 2016. Analysis of carbon dioxide sequestration in shale gas reservoirs by using experimental adsorption data and adsorption models. J. Nat. Gas Sci. Eng. 36, 1087–1105. https://doi.org/10.1016/j.jngse.2016.02.052

[240] Mirchi, V., Saraji, S., Goual, L., Piri, M., 2015. Dynamic interfacial tension and wettability of shale in the presence of surfactants at reservoir conditions. Fuel 148, 127–138. https://doi.org/10.1016/j.fuel.2015.01.077

[241] Mirchi, V., Saraji, S., Goual, L., Piri, M., 2014. Dynamic Interfacial Tensions and Contact Angles of Surfactant-in-Brine/Oil/Shale Systems: Implications to Enhanced Oil Recovery in Shale Oil Reservoirs, in: SPE Improved Oil Recovery Symposium. Presented at the SPE Improved Oil Recovery Symposium, Society of Petroleum Engineers, Tulsa, Oklahoma, USA. https://doi.org/10.2118/169171-MS

[242] Mißfeldt, F., Gurikov, P., Lölsberg, W., Weinrich, D., Lied, F., Fricke, M., Smirnova, I., 2020. Continuous Supercritical Drying of Aerogel Particles: Proof of Concept. Ind. Eng. Chem. Res. 59, 11284–11295. https://doi.org/10.1021/acs.iecr.0c01356

[243] Moeini, F., Hemmati-Sarapardeh, A., Ghazanfari, M.-H., Masihi, M., Ayatollahi, S., 2014. Toward mechanistic understanding of heavy crude oil/brine interfacial tension: The roles of salinity, temperature and pressure. Fluid Phase Equilibria 375, 191–200. https://doi.org/10.1016/j.fluid.2014.04.017

[244] Mohammed, S., Gadikota, G., 2020. Exploring the Role of Inorganic and Organic Interfaces on CO_2 and CH_4 Partitioning: Case Study of Silica, Illite, Calcite, and Kerogen Nanopores on Gas Adsorption and Nanoscale Transport Behaviors. Energy Fuels 34, 3578–3590. https://doi.org/10.1021/acs.energyfuels.0c00052

[245] Mohammed, S., Mansoori, G.A., 2018. The Role of Supercritical/Dense CO_2 Gas in Altering Aqueous/Oil Interfacial Properties: A Molecular Dynamics Study. Energy Fuels 32, 2095–2103. https://doi.org/10.1021/acs.energyfuels.7b03863

[246] Montero, G.A., Smith, C.B., Hendrix, W.A., Butcher, D.L., 2000. Supercritical Fluid Technology in Textile Processing: An Overview. Ind. Eng. Chem. Res. 39, 4806–4812. https://doi.org/10.1021/ie0002475

[247] Mosavat, N., 2014. Utilization of Carbonated Water Injection (CWI) as a means of improved oil recovery in light oil systems: Pore-scale mechanisms and recovery evaluation [Doctoral thesis].

[248] Mosavat, N., Abedini, A., Torabi, F., 2014. Phase Behaviour of CO2–Brine and CO2–Oil Systems for CO2 Storage and Enhanced Oil Recovery: Experimental Studies. Energy Procedia 63, 5631–5645. https://doi.org/10.1016/j.egypro.2014.11.596

[249] Mulliken, C.A., Sandler, S.I., 1980. The Prediction of CO2 Solubility and Swelling Factors for Enhanced Oil Recovery. Ind. Eng. Chem. Process Des. Dev. 19, 709–711. https://doi.org/10.1021/i260076a033

[250] Mutailipu, M., Jiang, L., Liu, X., Liu, Y., Zhao, J., 2019a. CO2 and alkane minimum miscible pressure estimation by the extrapolation of interfacial tension. Fluid Phase Equilibria 494, 103–114. https://doi.org/10.1016/j.fluid.2019.05.002

[251] Mutailipu, M., Liu, Y., Jiang, L., Zhang, Y., 2019b. Measurement and estimation of CO2–brine interfacial tension and rock wettability under CO2 sub- and super-critical conditions. J. Colloid Interface Sci. 534, 605–617. https://doi.org/10.1016/j.jcis.2018.09.031

[252] Myers, A.L., Monson, P.A., 2014. Physical adsorption of gases: the case for absolute adsorption as the basis for thermodynamic analysis. Adsorption 20, 591–622. https://doi.org/10.1007/s10450-014-9604-1

[253] Naeiji, P., Woo, T.K., Alavi, S., Ohmura, R., 2020. Molecular dynamics simulations of interfacial properties of the CO_2–water and CO_2–CH_4–water systems. J. Chem. Phys. 153, 044701. https://doi.org/10.1063/5.0008114

[254] Nasralla, R.A., Nasr-El-Din, H.A., 2012. Double-Layer Expansion: Is It A Primary Mechanism of Improved Oil Recovery by Low-Salinity Waterflooding? Presented at the SPE Improved Oil Recovery Symposium, OnePetro. https://doi.org/10.2118/154334-MS

[255] National Electric Power Company (NEPCO), 2023. Electricity Tariff in Jordan [WWW Document]. URL https://www.nepco.com.jo/en/electricity_tariff_en.aspx (accessed 1.7.23).

[256] Nielsen, L.C., Bourg, I.C., Sposito, G., 2012. Predicting CO2–water interfacial tension under pressure and temperature conditions of geologic CO2 storage. Geochim. Cosmochim. Acta 81, 28–38. https://doi.org/10.1016/j.gca.2011.12.018

[257] Nieuwoudt, I., du Rand, M., 2002. Measurement of phase equilibria of supercritical carbon dioxide and paraffins. J. Supercrit. Fluids 22, 185–199. https://doi.org/10.1016/S0896-8446(01)00122-X

[258] Niño Amézquita, O.G., Enders, S., Jaeger, P.T., Eggers, R., 2010. Interfacial properties of mixtures containing supercritical gases. J. Supercrit. Fluids 55, 724–734. https://doi.org/10.1016/j.supflu.2010.09.040

[259] Nourozieh, H., Bayestehparvin, B., Kariznovi, M., Abedi, J., 2013a. Equilibrium Properties of (Carbon Dioxide + *n* -Decane + *n* -Octadecane) Systems: Experiments and Thermodynamic Modeling. J. Chem. Eng. Data 58, 1236–1243. https://doi.org/10.1021/je4000394

[260] Nourozieh, H., Kariznovi, M., Abedi, J., 2013b. Measurement and correlation of saturated liquid properties and gas solubility for decane, tetradecane and their binary mixtures saturated with carbon dioxide. Fluid Phase Equilibria 337, 246–254. https://doi.org/10.1016/j.fluid.2012.09.037

[261] Nowrouzi, I., Manshad, A.K., Mohammadi, A.H., 2019. Effects of dissolved carbon dioxide and ions in water on the dynamic interfacial tension of water and oil in the process of carbonated smart water injection into oil reservoirs. Fuel 243, 569–578. https://doi.org/10.1016/j.fuel.2019.01.069

[262] Orr, F.M., Taber, J.J., 1984. Use of Carbon Dioxide in Enhanced Oil Recovery. Science 224, 563–569. https://doi.org/10.1126/science.224.4649.563

[263] Pan, B., Li, Y., Wang, H., Jones, F., Iglauer, S., 2018. CO_2 and CH_4 Wettabilities of Organic-Rich Shale. Energy Fuels 32, 1914–1922. https://doi.org/10.1021/acs.energyfuels.7b01147

[264] Pan, B., Li, Y., Zhang, M., Wang, X., Iglauer, S., 2020. Effect of total organic carbon (TOC) content on shale wettability at high pressure and high temperature conditions. J. Pet. Sci. Eng. 193, 107374. https://doi.org/10.1016/j.petrol.2020.107374

[265] Pang, Y., He, Y., Chen, S., 2019. An innovative method to characterize sorption-induced kerogen swelling in organic-rich shales. Fuel 254, 115629. https://doi.org/10.1016/j.fuel.2019.115629

[266] Parker, M.E., Meyer, J.P., Meadows, S.R., 2009. Carbon Dioxide Enhanced Oil Recovery Injection Operations Technologies (Poster Presentation). Energy Procedia 1, 3141–3148. https://doi.org/10.1016/j.egypro.2009.02.096

[267] Pathak, M., Kweon, H., Deo, M., Huang, H., 2017. Kerogen Swelling and Confinement: Its implication on Fluid Thermodynamic Properties in Shales. Sci. Rep. 7, 12530. https://doi.org/10.1038/s41598-017-12982-4

[268] P.d., S.H., Prabha, S.K., Sathian, S.P., 2015. The effect of characteristic length on mean free path for confined gases. Phys. Stat. Mech. Its Appl. 437, 68–74. https://doi.org/10.1016/j.physa.2015.05.022

[269] Peng, C., Crawshaw, J.P., Maitland, G.C., Martin Trusler, J.P., Vega-Maza, D., 2013. The pH of CO2-saturated water at temperatures between 308K and 423K at pressures up to 15MPa. J. Supercrit. Fluids 82, 129–137. https://doi.org/10.1016/j.supflu.2013.07.001

[270] Peng, Z., Sheng, J., 2023. Diffusion Effect on Shale Oil Recovery by CO_2 Huff-n-Puff. Energy Fuels acs.energyfuels.2c03871. https://doi.org/10.1021/acs.energyfuels.2c03871

[271] Phelps, C.L., Smart, N.G., Wai, C.M., 1996. Past, Present, and Possible Future Applications of Supercritical Fluid Extraction Technology. J. Chem. Educ. 73, 1163. https://doi.org/10.1021/ed073p1163

[272] Pierre, A., Lamarche, J.M., Mercier, R., Foissy, A., Persello, J., 1990. Calcium as Potential Determining Ion in Aqueous Calcite Suspensions. J. Dispers. Sci. Technol. 11, 611–635. https://doi.org/10.1080/01932699008943286

[273] Pokrovsky, O.S., Golubev, S.V., Schott, J., 2005. Dissolution kinetics of calcite, dolomite and magnesite at 25 °C and 0 to 50 atm pCO2. Chem. Geol. 217, 239–255. https://doi.org/10.1016/j.chemgeo.2004.12.012

[274] Qamar, S., Torres, Y.J.M., Parekh, H.S., Robert Falconer, J., 2021. Extraction of medicinal cannabinoids through supercritical carbon dioxide technologies: A review. J. Chromatogr. B 1167, 122581. https://doi.org/10.1016/j.jchromb.2021.122581

[275] Qi, R., Ning, Z., Wang, Q., Huang, L., Wu, X., Cheng, Z., Zhang, W., 2019. Measurements and modeling of high-pressure adsorption of CH4 and CO2 on shales. Fuel 242, 728–743. https://doi.org/10.1016/j.fuel.2018.12.086

[276] Qin, C., Jiang, Y., Luo, Y., Xian, X., Liu, H., Li, Y., 2017. Effect of Supercritical Carbon Dioxide Treatment Time, Pressure, and Temperature on Shale Water Wettability. Energy Fuels 31, 493–503. https://doi.org/10.1021/acs.energyfuels.6b03257

[277] Qin, C., Jiang, Y., Zuo, S., Chen, S., Xiao, S., Liu, Z., 2021. Investigation of adsorption kinetics of CH4 and CO2 on shale exposure to supercritical CO2. Energy 236, 121410. https://doi.org/10.1016/j.energy.2021.121410

[278] Rahimi, A., Safari, M., Honarvar, B., Chabook, H., Gholami, R., 2020. On time dependency of interfacial tension through low salinity carbonated water injection. Fuel 280, 118492. https://doi.org/10.1016/j.fuel.2020.118492

[279] Ralser, S., Kaiser, A., Probst, M., Postler, J., Renzler, M., Bohme, D.K., Scheier, P., 2016. Experimental evidence for the influence of charge on the adsorption capacity of carbon dioxide on charged fullerenes. Phys. Chem. Chem. Phys. 18, 3048–3055. https://doi.org/10.1039/C5CP06587A

[280] Rani, S., Padmanabhan, E., Bakshi, T., Prusty, B.K., Pal, S.K., 2019a. CO2 sorption and rate characteristics in micropores of shales. J. Nat. Gas Sci. Eng. 68, 102903. https://doi.org/10.1016/j.jngse.2019.102903

[281] Rani, S., Padmanabhan, E., Prusty, B.K., 2019b. Review of gas adsorption in shales for enhanced methane recovery and CO2 storage. J. Pet. Sci. Eng. 175, 634–643. https://doi.org/10.1016/j.petrol.2018.12.081

[282] Rani, S., Prusty, B.K., Pal, S.K., 2018. Adsorption kinetics and diffusion modeling of CH4 and CO2 in Indian shales. Fuel 216, 61–70. https://doi.org/10.1016/j.fuel.2017.11.124

[283] Raveendran, P., Ikushima, Y., Wallen, S.L., 2005. Polar Attributes of Supercritical Carbon Dioxide. Acc. Chem. Res. 38, 478–485. https://doi.org/10.1021/ar040082m

[284] Rechberger, A., Amsüss, R., Rossegger, S., Breidler, R., Steiner, G., 2019. High Precision Vibration-Type Densitometers Based on Pulsed Excitation Measurements. Sensors 19, 1627. https://doi.org/10.3390/s19071627

[285] Regueira, T., Pantelide, G., Yan, W., Stenby, E.H., 2016. Density and phase equilibrium of the binary system methane + n-decane under high temperatures and pressures. Fluid Phase Equilibria 428, 48–61. https://doi.org/10.1016/j.fluid.2016.08.004

[286] Ren, W., Scurto, A.M., 2007. High-pressure phase equilibria with compressed gases. Rev. Sci. Instrum. 78, 125104. https://doi.org/10.1063/1.2814025

[287] Renner, T.A., 1988. Measurement and Correlation of Diffusion Coefficients for CO2 and Rich-Gas Applications. SPE Reserv. Eng. 3, 517–523. https://doi.org/10.2118/15391-PA

[288] Rezk, M.G., Foroozesh, J., 2019. Phase behavior and fluid interactions of a CO2-Light oil system at high pressures and temperatures. Heliyon 5, e02057. https://doi.org/10.1016/j.heliyon.2019.e02057

[289] Roshan, H., Al-Yaseri, A.Z., Sarmadivaleh, M., Iglauer, S., 2016. On wettability of shale rocks. J. Colloid Interface Sci. 475, 104–111. https://doi.org/10.1016/j.jcis.2016.04.041

[290] Ross, D.J.K., Marc Bustin, R., 2009. The importance of shale composition and pore structure upon gas storage potential of shale gas reservoirs. Mar. Pet. Geol. 26, 916–927. https://doi.org/10.1016/j.marpetgeo.2008.06.004

[291] Rudyk, S., Spirov, P., Sogaard, E., 2013. Application of GC–MS chromatography for the analysis of the oil fractions extracted by supercritical CO2 at high pressure. Fuel 106, 139–146. https://doi.org/10.1016/j.fuel.2012.12.004

[292] Safari, M., Rahimi, A., Gholami, R., Permana, A., Siaw Khur, W., 2022. Underlying mechanisms of shale wettability alteration by low salinity water injection (LSWI). J. Dispers. Sci. Technol. 43, 33–41. https://doi.org/10.1080/01932691.2020.1813156

[293] Saidian, M., Godinez, L.J., Prasad, M., 2016. Effect of clay and organic matter on nitrogen adsorption specific surface area and cation exchange capacity in shales (mudrocks). J. Nat. Gas Sci. Eng. 33, 1095–1106. https://doi.org/10.1016/j.jngse.2016.05.064

[294] Salah Alaloul, W., Al Salaheen, M., Malkawi, A.B., Alzubi, K., Al-Sabaeei, A.M., Ali Musarat, M., 2021. Utilizing of oil shale ash as a construction material: A systematic review. Constr. Build. Mater. 299, 123844. https://doi.org/10.1016/j.conbuildmat.2021.123844

[295] Samara, H., Al-Eryani, M., Jaeger, P., 2022a. The role of supercritical carbon dioxide in modifying the phase and interfacial properties of multiphase systems relevant to combined EOR-CCS. Fuel 323, 124271. https://doi.org/10.1016/j.fuel.2022.124271

[296] Samara, H., Jaeger, P., 2022. Experimental determination of wetting behavior under non-atmospheric conditions relevant to reservoirs: a practical guide. SN Appl. Sci. 4, 85. https://doi.org/10.1007/s42452-022-04963-8

[297] Samara, H., Ke, L., Ostrowski, T. v., Ganzer, L., Jaeger, P., 2019. Unconventional oil recovery from Al Sultani tight rock formations using supercritical CO2. J. Supercrit. Fluids 152, 104562. https://doi.org/10.1016/j.supflu.2019.104562

[298] Samara, H., Ostrowski, T.V., Abdulkareem, F.A., Padmanabhan, E., Jaeger, P., 2021. Carbon dioxide adsorption and interaction with formation fluids of Jordanian

unconventional reservoirs. J. Pet. Explor. Prod. Technol. https://doi.org/10.1007/s13202-021-01333-9

[299] Samara, H., Von Ostrowski, T., Jaeger, P., 2022b. Geological Storage of Carbon Dioxide and Hydrogen in Jordanian Shale Formations, in: Day 2 Tue, October 04, 2022. Presented at the SPE Annual Technical Conference and Exhibition, SPE, Houston, Texas, USA, p. D021S029R002. https://doi.org/10.2118/210202-MS

[300] Santos, D.C., Lamim, M.N., Costa, D.S., Mehl, A., Couto, P., Paredes, M.L.L., 2021. Experimental and modeling studies of density and viscosity behavior of a live fluid due to CO_2 injection at reservoir condition. Oil Gas Sci. Technol. – Rev. D'IFP Energ. Nouv. 76, 45. https://doi.org/10.2516/ogst/2021026

[301] Santos, M.S., Franco, L.F.M., Castier, M., Economou, I.G., 2018. Molecular Dynamics Simulation of *n* -Alkanes and CO_2 Confined by Calcite Nanopores. Energy Fuels 32, 1934–1941. https://doi.org/10.1021/acs.energyfuels.7b02451

[302] Sato, H., Matubayasi, N., Nakahara, M., Hirata, F., 2000. Which carbon oxide is more soluble? Ab initio study on carbon monoxide and dioxide in aqueous solution. Chem. Phys. Lett. 323, 257–262. https://doi.org/10.1016/S0009-2614(00)00508-X

[303] Sato, Y., Tagashira, Y., Maruyama, D., Takishima, S., Masuoka, H., 1998. Solubility of carbon dioxide in eicosane, docosane, tetracosane, and octacosane at temperatures from 323 to 473 K and pressures up to 40 MPa. Fluid Phase Equilibria 147, 181–193. https://doi.org/10.1016/S0378-3812(98)00250-7

[304] Sauerer, B., Furmann, A., Fernandes, A., Samara, H., Jaeger, P., Al-Ayed, O., Abdallah, W., 2021. Assessing extreme maturities – Challenging examples from immature Jordanian to overmature Far Eastern unconventional formations. Mar. Pet. Geol. 129, 105103. https://doi.org/10.1016/j.marpetgeo.2021.105103

[305] Savest, N., Oja, V., Kaevand, T., Lille, Ü., 2007. Interaction of Estonian kukersite with organic solvents: A volumetric swelling and molecular simulation study. Fuel 86, 17–21. https://doi.org/10.1016/j.fuel.2006.06.016

[306] Schön, J.H., 2011. Pore Space Properties, in: Handbook of Petroleum Exploration and Production. Elsevier, pp. 17–73. https://doi.org/10.1016/S1567-8032(11)08002-5

[307] Senčić, Mrzljak, Blecich, Bonefačić, 2019. 2D CFD Simulation of Water Injection Strategies in a Large Marine Engine. J. Mar. Sci. Eng. 7, 296. https://doi.org/10.3390/jmse7090296

[308] Seyer, Wm.F., Patterson, R.F., Keays, J.L., 1944. The Density and Transition Points of the n-Paraffin Hydrocarbons. J. Am. Chem. Soc. 66, 179–182. https://doi.org/10.1021/ja01230a004

[309] Seyyedi, M., Sohrabi, M., Farzaneh, A., 2015. Investigation of Rock Wettability Alteration by Carbonated Water through Contact Angle Measurements. Energy Fuels 29, 5544–5553. https://doi.org/10.1021/acs.energyfuels.5b01069

[310] Shaver, R.D., Robinson, R.L., Gasem, K.A.M., 2001. An automated apparatus for equilibrium phase compositions, densities, and interfacial tensions: data for carbon dioxide + decane. Fluid Phase Equilibria 179, 43–66. https://doi.org/10.1016/S0378-3812(00)00475-1

[311] Sheng, J.J., 2017. Critical review of field EOR projects in shale and tight reservoirs. J. Pet. Sci. Eng. 159, 654–665. https://doi.org/10.1016/j.petrol.2017.09.022

[312] Shojai Kaveh, N., Barnhoorn, A., Wolf, K.-H., 2016. Wettability evaluation of silty shale caprocks for CO 2 storage. Int. J. Greenh. Gas Control 49, 425–435. https://doi.org/10.1016/j.ijggc.2016.04.003

[313] Simon, R., Graue, D.J., 1965. Generalized Correlations for Predicting Solubility, Swelling and Viscosity Behavior of CO2 -Crude Oil Systems. J. Pet. Technol. 17, 102–106. https://doi.org/10.2118/917-PA

[314] Somasundaran, P., Agar, G.E., 1967. The zero point of charge of calcite. J. Colloid Interface Sci. 24, 433–440. https://doi.org/10.1016/0021-9797(67)90241-X

[315] Song, B., Springer, J., 1996a. Determination of Interfacial Tension from the Profile of a Pendant Drop Using Computer-Aided Image Processing: 1. Theoretical. J. Colloid Interface Sci. 184, 64–76. https://doi.org/10.1006/jcis.1996.0597

[316] Song, B., Springer, J., 1996b. Determination of Interfacial Tension from the Profile of a Pendant Drop Using Computer-Aided Image Processing: 2. Experimental. J. Colloid Interface Sci. 184, 77–91. https://doi.org/10.1006/jcis.1996.0598

[317] Song, Y., Jian, W., Zhang, Y., Shen, Y., Zhan, Y., Zhao, J., Liu, Y., Wang, D., 2012. Densities and Volumetric Characteristics of Binary System of CO_2 + Decane from (303.15 to 353.15) K and Pressures up to 19 MPa. J. Chem. Eng. Data 57, 3399–3407. https://doi.org/10.1021/je300388b

[318] Song, Y., Zhan, Y., Zhang, Y., Liu, S., Jian, W., Liu, Y., Wang, D., 2013. Measurements of CO_2–H_2O–NaCl Solution Densities over a Wide Range of Temperatures, Pressures, and NaCl Concentrations. J. Chem. Eng. Data 58, 3342–3350. https://doi.org/10.1021/je400459y

[319] Sovová, H., 2012. Steps of supercritical fluid extraction of natural products and their characteristic times. J. Supercrit. Fluids 66, 73–79. https://doi.org/10.1016/j.supflu.2011.11.004

[320] Spanakos, D., Rigby, S.P., 2020. Predicting Surface Diffusivities of Gas Molecules in Shale. Energy Fuels 34, 12417–12428. https://doi.org/10.1021/acs.energyfuels.0c02441

[321] Stachurski, J., MichaŁek, M., 1996. The Effect of the ζ Potential on the Stability of a Non-Polar Oil-in-Water Emulsion. J. Colloid Interface Sci. 184, 433–436. https://doi.org/10.1006/jcis.1996.0637

[322] Steel, L., Liu, Q., Mackay, E., Maroto-Valer, M.M., 2016. CO_2 solubility measurements in brine under reservoir conditions: A comparison of experimental and geochemical modeling methods: CO_2 solubility measurements in brine under reservoir conditions. Greenh. Gases Sci. Technol. 6, 197–217. https://doi.org/10.1002/ghg.1590

[323] Strangfeld, C., 2021. Quantification of the Knudsen Effect on the Effective Gas Diffusion Coefficient in Partially Saturated Pore Distributions. Adv. Eng. Mater. 23, 2100106. https://doi.org/10.1002/adem.202100106

[324] Suekuni, M.T., Craddock, P.R., Douglas, J.T., Pomerantz, A.E., Allgeier, A.M., 2022. Critical Practices for the Preparation and Analysis of Kerogen. Energy Fuels 36, 8828–8843. https://doi.org/10.1021/acs.energyfuels.2c01063

[325] Sui, H., Yao, J., 2016. Effect of surface chemistry for CH4/CO2 adsorption in kerogen: A molecular simulation study. J. Nat. Gas Sci. Eng. 31, 738–746. https://doi.org/10.1016/j.jngse.2016.03.097

[326] Sunarso, J., Ismadji, S., 2009. Decontamination of hazardous substances from solid matrices and liquids using supercritical fluids extraction: A review. J. Hazard. Mater. 161, 1–20. https://doi.org/10.1016/j.jhazmat.2008.03.069

[327] Tabrizy, V.A., Hamouda, A.A., Soubeyrand-Lenoir, E., Denoyel, R., 2013. CO_2 Adsorption Isotherm on Modified Calcite, Quartz, and Kaolinite Surfaces: Surface Energy Analysis. Pet. Sci. Technol. 31, 1532–1543. https://doi.org/10.1080/10916466.2011.586962

[328] Takahashi, S., Iwasaki, H., 1966. The Diffusion of Gases at High Pressures. I. The Self-diffusion Coefficient of Carbon Dioxide. Bull. Chem. Soc. Jpn. 39, 2105–2109. https://doi.org/10.1246/bcsj.39.2105

[329] Tanaka, H., Yamaki, Y., Kato, M., 1993. Solubility of carbon dioxide in pentadecane, hexadecane, and pentadecane + hexadecane. J. Chem. Eng. Data 38, 386–388. https://doi.org/10.1021/je00011a013

[330] Tang, Y., Li, Z., Wang, R., Cui, M., Wang, X., Lun, Z., Lu, Y., 2019. Experimental Study on the Density-Driven Carbon Dioxide Convective Diffusion in Formation Water at Reservoir Conditions. ACS Omega 4, 11082–11092. https://doi.org/10.1021/acsomega.9b00627

[331] Taylor, B.N., Kuyatt, C.E., 1994. Guidlines for Evauating and Expressing the Uncertainty of NIST Measurement Results. Natl. Inst. Stand. Technol.

[332] Tegetmeier, A., Dittmar, D., Fredenhagen, A., Eggers, R., 2000. Density and volume of water and triglyceride mixtures in contact with carbon dioxide. Chem. Eng. Process. Process Intensif. 39, 399–405. https://doi.org/10.1016/S0255-2701(99)00102-6

[333] Tesson, S., Firoozabadi, A., 2019. Deformation and Swelling of Kerogen Matrix in Light Hydrocarbons and Carbon Dioxide. J. Phys. Chem. C 123, 29173–29183. https://doi.org/10.1021/acs.jpcc.9b04592

[334] Tetteh, J.T., Barimah, R., Korsah, P.K., 2022. Ionic Interactions at the Crude Oil–Brine–Rock Interfaces Using Different Surface Complexation Models and DLVO Theory: Application to Carbonate Wettability. ACS Omega 7, 7199–7212. https://doi.org/10.1021/acsomega.1c06954

[335] Thommes, M., Kaneko, K., Neimark, A.V., Olivier, J.P., Rodriguez-Reinoso, F., Rouquerol, J., Sing, K.S.W., 2015. Physisorption of gases, with special reference to the evaluation of surface area and pore size distribution (IUPAC Technical Report). Pure Appl. Chem. 87, 1051–1069. https://doi.org/10.1515/pac-2014-1117

[336] Thompson, D.W., Pownall, P.G., 1989. Surface electrical properties of calcite. J. Colloid Interface Sci. 131, 74–82. https://doi.org/10.1016/0021-9797(89)90147-1

[337] Timmerhaus, K.D., Drickamer, H.G., 1951. Self-Diffusion in CO_2 at Moderate Pressures. J. Chem. Phys. 19, 1242–1243. https://doi.org/10.1063/1.1748003

[338] Tong, D., Trusler, J.P.M., Vega-Maza, D., 2013. Solubility of CO_2 in Aqueous Solutions of $CaCl_2$ or $MgCl_2$ and in a Synthetic Formation Brine at Temperatures up

to 423 K and Pressures up to 40 MPa. J. Chem. Eng. Data 58, 2116–2124. https://doi.org/10.1021/je400396s

[339] Umezawa, S., Nagashima, A., 1992. Measurement of the diffusion coefficients of acetone, benzene, and alkane in supercritical CO2 by the Taylor dispersion method. J. Supercrit. Fluids 5, 242–250. https://doi.org/10.1016/0896-8446(92)90014-B

[340] Unatrakarn, D., Asghari, K., Condor, J., 2011. Experimental studies of CO2 and CH4 diffusion coefficient in bulk oil and porous media. Energy Procedia 4, 2170–2177. https://doi.org/10.1016/j.egypro.2011.02.103

[341] United Nations Development Program (UNDP), 2023. Jordan [WWW Document]. URL https://climatepromise.undp.org/what-we-do/where-we-work/jordan (accessed 2.16.23).

[342] Van Cuong, P., Kvamme, B., Kuznetsova, T., Jensen, B., 2012. Molecular dynamics study of calcite, hydrate and the temperature effect on CO_2 transport and adsorption stability in geological formations. Mol. Phys. 110, 1097–1106. https://doi.org/10.1080/00268976.2012.679629

[343] Vardag, T., Karger, N., Lüdemann, H.-D., 1991. Temperature and Pressure Dependence of Self Diffusion in Long Liquid n-Alkanes. Berichte Bunsenges. Für Phys. Chem. 95, 859–865. https://doi.org/10.1002/bbpc.19910950803

[344] Vargaftik, N.B., Volkov, B.N., Voljak, L.D., 1983. International Tables of the Surface Tension of Water. J. Phys. Chem. Ref. Data 12, 817–820. https://doi.org/10.1063/1.555688

[345] Vdović, N., 2001. Electrokinetic behaviour of calcite—the relationship with other calcite properties. Chem. Geol. 177, 241–248. https://doi.org/10.1016/S0009-2541(00)00397-1

[346] Viganó, J., Coutinho, J.P., Souza, D.S., Baroni, N.A.F., Godoy, H.T., Macedo, J.A., Martínez, J., 2016. Exploring the selectivity of supercritical CO2 to obtain nonpolar fractions of passion fruit bagasse extracts. J. Supercrit. Fluids 110, 1–10. https://doi.org/10.1016/j.supflu.2015.12.001

[347] Vincenti, W.G., Kruger, C.H., 1965. Introduction to physical gas dynamics, Introduction to physical gas dynamics.

[348] Wagner, W., Pruß, A., 2002. The IAPWS Formulation 1995 for the Thermodynamic Properties of Ordinary Water Substance for General and Scientific Use. J. Phys. Chem. Ref. Data 31, 387–535. https://doi.org/10.1063/1.1461829

[349] Wang, C., Liu, Y., Gao, Y., 2020. Comparison of the Absolute Adsorption of CH_4, *n*-C_4H_{10}, and CO_2 on Shale. Energy Fuels 34, 4466–4473. https://doi.org/10.1021/acs.energyfuels.0c00278

[350] Wang, J., Ryan, D., Szabries, M., Jaeger, P., 2019. A Study for Using CO_2 To Enhance Natural Gas Recovery from Tight Reservoirs. Energy Fuels 33, 3821–3827. https://doi.org/10.1021/acs.energyfuels.8b04464

[351] Wang, J., Samara, H., Jaeger, P., Ko, V., Rodgers, D., Ryan, D., 2022. Investigation for CO_2 Adsorption and Wettability of Reservoir Rocks. Energy Fuels 36, 1626–1634. https://doi.org/10.1021/acs.energyfuels.1c03366

[352] Wang, T., Tian, S., Li, G., Sheng, M., Ren, W., Liu, Q., Zhang, S., 2018. Molecular Simulation of CO_2 /CH_4 Competitive Adsorption on Shale Kerogen for CO_2 Sequestration and Enhanced Gas Recovery. J. Phys. Chem. C 122, 17009–17018. https://doi.org/10.1021/acs.jpcc.8b02061

[353] Wang, W., Rao, L., Wu, X., Wang, Y., Zhao, L., Liao, X., 2021. Supercritical Carbon Dioxide Applications in Food Processing. Food Eng. Rev. 13, 570–591. https://doi.org/10.1007/s12393-020-09270-9

[354] Wang, X., Cheng, H., Chai, P., Bian, J., Wang, Xiaoming, Liu, Y., Yin, X., Pan, S., Pan, Z., 2020. Pore Characterization of Different Clay Minerals and Its Impact on Methane Adsorption Capacity. Energy Fuels 34, 12204–12214. https://doi.org/10.1021/acs.energyfuels.0c01922

[355] Wang, Y., Chen, Y., Wang, J., Pan, Z., Liu, J., 2021. Molecular Simulation Study on the Density Behavior of *n* -Alkane/CO_2 Systems. ACS Omega 6, 29618–29628. https://doi.org/10.1021/acsomega.1c03889

[356] Wang, Y., Wei, D., Dave, R., Pfeffer, R., Sauceau, M., Letourneau, J.-J., Fages, J., 2002. Extraction and precipitation particle coating using supercritical CO2. Powder Technol. 127, 32–44. https://doi.org/10.1016/S0032-5910(02)00102-X

[357] Wang, Z., Hou, J., 2021. Measurement of CO_2 diffusion coefficients in both bulk liquids and carven filling porous media of fractured-vuggy carbonate reservoirs at 50 MPa and 393 K. RSC Adv. 11, 19712–19722. https://doi.org/10.1039/D1RA02549J

[358] Weck, P.F., Kim, E., Wang, Y., Kruichak, J.N., Mills, M.M., Matteo, E.N., Pellenq, R.J.-M., 2017. Model representations of kerogen structures: An insight from density functional theory calculations and spectroscopic measurements. Sci. Rep. 7, 7068. https://doi.org/10.1038/s41598-017-07310-9

[359] Wei, M., Zhang, L., Xiong, Y., Li, J., Peng, P., 2016. Nanopore structure characterization for organic-rich shale using the non-local-density functional theory by a combination of N2 and CO2 adsorption. Microporous Mesoporous Mater. 227, 88–94. https://doi.org/10.1016/j.micromeso.2016.02.050

[360] Weireld, G.D., Frère, M., Jadot, R., 1999. Automated determination of high-temperature and high-pressure gas adsorption isotherms using a magnetic suspension balance. Meas. Sci. Technol. 10, 117–126. https://doi.org/10.1088/0957-0233/10/2/010

[361] Weniger, P., Kalkreuth, W., Busch, A., Krooss, B.M., 2010. High-pressure methane and carbon dioxide sorption on coal and shale samples from the Paraná Basin, Brazil. Int. J. Coal Geol. 84, 190–205. https://doi.org/10.1016/j.coal.2010.08.003

[362] Whyman, G., Bormashenko, E., Stein, T., 2008. The rigorous derivation of Young, Cassie–Baxter and Wenzel equations and the analysis of the contact angle hysteresis phenomenon. Chem. Phys. Lett. 450, 355–359. https://doi.org/10.1016/j.cplett.2007.11.033

[363] Wiebe, R., Gaddy, V.L., 1940. The Solubility of Carbon Dioxide in Water at Various Temperatures from 12 to 40° and at Pressures to 500 Atmospheres. Critical Phenomena. J. Am. Chem. Soc. 62, 815–817. https://doi.org/10.1021/ja01861a033

[364] Wu, D., Miao, F., Liu, X., Xiao, X., Zhai, W., 2021. Prediction of high-pressure adsorption of CH4 and CO2 in shale. Int. J. Greenh. Gas Control 110, 103440. https://doi.org/10.1016/j.ijggc.2021.103440

[365] Wu, K., Li, X., Wang, C., Yu, W., Chen, Z., 2015. Model for Surface Diffusion of Adsorbed Gas in Nanopores of Shale Gas Reservoirs. Ind. Eng. Chem. Res. 54, 3225–3236. https://doi.org/10.1021/ie504030v

[366] Wu, T., Zhao, H., Tesson, S., Firoozabadi, A., 2019. Absolute adsorption of light hydrocarbons and carbon dioxide in shale rock and isolated kerogen. Fuel 235, 855–867. https://doi.org/10.1016/j.fuel.2018.08.023

[367] Xie, Q., Chen, Y., Sari, A., Pu, W., Saeedi, A., Liao, X., 2017. A pH-Resolved Wettability Alteration: Implications for CO_2 -Assisted EOR in Carbonate Reservoirs. Energy Fuels 31, 13593–13599. https://doi.org/10.1021/acs.energyfuels.7b03071

[368] Yan, W., Huang, S., Stenby, E.H., 2011. Measurement and modeling of CO2 solubility in NaCl brine and CO2–saturated NaCl brine density. Int. J. Greenh. Gas Control 5, 1460–1477. https://doi.org/10.1016/j.ijggc.2011.08.004

[369] Yang, C., Gu, Y., 2006. Accelerated Mass Transfer of CO_2 in Reservoir Brine Due to Density-Driven Natural Convection at High Pressures and Elevated Temperatures. Ind. Eng. Chem. Res. 45, 2430–2436. https://doi.org/10.1021/ie050497r

[370] Yang, D., Gu, Y., Tontiwachwuthikul, P., 2008. Wettability Determination of the Crude Oil−Reservoir Brine−Reservoir Rock System with Dissolution of CO_2 at High Pressures and Elevated Temperatures. Energy Fuels 22, 2362–2371. https://doi.org/10.1021/ef800012w

[371] Yang, D., Tontiwachwuthikul, P., Gu, Y., 2005a. Interfacial Interactions between Reservoir Brine and CO_2 at High Pressures and Elevated Temperatures. Energy Fuels 19, 216–223. https://doi.org/10.1021/ef049792z

[372] Yang, D., Tontiwachwuthikul, P., Gu, Y., 2005b. Interfacial Tensions of the Crude Oil + Reservoir Brine + CO_2 Systems at Pressures up to 31 MPa and Temperatures of 27 °C and 58 °C. J. Chem. Eng. Data 50, 1242–1249. https://doi.org/10.1021/je0500227

[373] Yang, K., Zhou, J., Xian, X., Zhang, C., Tian, S., Dong, Z., Fan, M., Cai, J., 2021. Adsorption Characteristics and Thermodynamic Analysis of CH4 and CO2 on Continental and Marine Shale. Transp. Porous Media 140, 763–788. https://doi.org/10.1007/s11242-021-01599-x

[374] Yang, T., Sun, Y., Meng, X., Wu, J., Ilja Siepmann, J., 2021. Simultaneous measurement of the density and viscosity for n-Decane + CO2 binary mixtures at temperature between (303.15 to 373.15) K and pressures up to 80 MPa. J. Mol. Liq. 338, 116646. https://doi.org/10.1016/j.molliq.2021.116646

[375] Yang, Y., Che Ruslan, M.F.A., Narayanan Nair, A.K., Sun, S., 2019. Effect of Ion Valency on the Properties of the Carbon Dioxide–Methane–Brine System. J. Phys. Chem. B 123, 2719–2727. https://doi.org/10.1021/acs.jpcb.8b12033

[376] Yang, Z., Dong, Z., Wang, L., Yin, T., Fan, X., Lin, M., Zhang, J., 2018. Experimental Study on Selective Adsorption/Desorption of CO_2 and CH_4 Behaviors on Shale under a High-Pressure Condition. Energy Fuels 32, 9255–9262. https://doi.org/10.1021/acs.energyfuels.8b02068

[377] Yang, Z., Li, M., Peng, B., Lin, M., Dong, Z., 2012. Dispersion Property of CO_2 in Oil. 1. Volume Expansion of CO_2 + Alkane at near Critical and Supercritical Condition of CO_2. J. Chem. Eng. Data 57, 882–889. https://doi.org/10.1021/je201114g

[378] Yang, Z., Liu, X., Hua, Z., Ling, Y., Li, M., Lin, M., Dong, Z., 2015. Interfacial tension of CO2 and crude oils under high pressure and temperature. Colloids Surf. Physicochem. Eng. Asp. 482, 611–616. https://doi.org/10.1016/j.colsurfa.2015.05.058

[379] Yekeen, N., Padmanabhan, E., Abdulelah, H., Irfan, S.A., Okunade, O.A., Khan, J.A., Negash, B.M., 2021. CO2/brine interfacial tension and rock wettability at reservoir conditions: A critical review of previous studies and case study of black shale from Malaysian formation. J. Pet. Sci. Eng. 196, 107673. https://doi.org/10.1016/j.petrol.2020.107673

[380] Yekeen, N., Padmanabhan, E., Sevoo, T.A., Kanesen, K.A., Okunade, O.A., 2020. Wettability of rock/CO2/brine systems: A critical review of influencing parameters and recent advances. J. Ind. Eng. Chem. 88, 1–28. https://doi.org/10.1016/j.jiec.2020.03.021

[381] York, R., 2012. Do alternative energy sources displace fossil fuels? Nat. Clim. Change 2, 441–443. https://doi.org/10.1038/nclimate1451

[382] Young, T., 1805. III. An essay on the cohesion of fluids. Philos. Trans. R. Soc. Lond. 95, 65–87. https://doi.org/10.1098/rstl.1805.0005

[383] Yu, J., Wang, S., Tian, Y., 2006. Experimental determination and calculation of thermodynamic properties of CO2+octane to high temperatures and high pressures. Fluid Phase Equilibria 246, 6–14. https://doi.org/10.1016/j.fluid.2006.05.014

[384] Yu, X., Li, J., Chen, Z., Wu, K., Zhang, L., Yang, S., Hui, G., Yang, M., 2021. Determination of CH4, C2H6 and CO2 adsorption in shale kerogens coupling sorption-induced swelling. Chem. Eng. J. 410, 127690. https://doi.org/10.1016/j.cej.2020.127690

[385] Yuan, W., Pan, Z., Li, X., Yang, Y., Zhao, C., Connell, L.D., Li, S., He, J., 2014. Experimental study and modelling of methane adsorption and diffusion in shale. Fuel 117, 509–519. https://doi.org/10.1016/j.fuel.2013.09.046

[386] Zabot, G.L., 2020. Chapter 11 - Decaffeination using supercritical carbon dioxide, in: Inamuddin, Asiri, A.M., Isloor, A.M. (Eds.), Green Sustainable Process for Chemical and Environmental Engineering and Science. Elsevier, pp. 255–278. https://doi.org/10.1016/B978-0-12-817388-6.00011-8

[387] Zaker, S., Parvizi, R., Ghaseminejad, E., Moradi, A., 2021. Effect of brine type and pH on the interfacial tension behavior of carbonated brine/crude oil. J. Dispers. Sci. Technol. 42, 1184–1195. https://doi.org/10.1080/01932691.2020.1735409

[388] Zaker, S., Parvizi, R., Hosseini, S., Ghaseminejad, E., 2020a. Crude oil behavior during injection of solutions containing $MgSO_4$ in the presence and absence of CO_2. Energy Sources Part Recovery Util. Environ. Eff. 1–18. https://doi.org/10.1080/15567036.2020.1783397

[389] Zaker, S., Sharafi, A., Parvizi, R., Esmaeili-Faraj, S.H., Ghaseminejad, E., 2020b. Swelling behavior of heavy crude oil in carbonated water at the presence of Na2SO4 and Mg2SO4. J. Pet. Explor. Prod. Technol. 10, 2759–2769. https://doi.org/10.1007/s13202-020-00927-z

[390] Zarghami, S., Boukadi, F., Al-Wahaibi, Y., 2017. Diffusion of carbon dioxide in formation water as a result of CO2 enhanced oil recovery and CO2 sequestration. J. Pet. Explor. Prod. Technol. 7, 161–168. https://doi.org/10.1007/s13202-016-0261-7

[391] Zavitsas, A.A., 2005. Aqueous Solutions of Calcium Ions: Hydration Numbers and the Effect of Temperature. J. Phys. Chem. B 109, 20636–20640. https://doi.org/10.1021/jp053909i

[392] Zavitsas, A.A., 2001. Properties of Water Solutions of Electrolytes and Nonelectrolytes. J. Phys. Chem. B 105, 7805–7817. https://doi.org/10.1021/jp011053l

[393] Zhang, D., 2005. Surfactant-enhanced oil recovery process for a fractured, oil-wet carbonate reservoir (Thesis). Rice University.

[394] Zhang, D., Song, J., 2014. Mechanisms for Geological Carbon Sequestration. Procedia IUTAM 10, 319–327. https://doi.org/10.1016/j.piutam.2014.01.027

[395] Zhang, K., Gu, Y., 2016. Two new quantitative technical criteria for determining the minimum miscibility pressures (MMPs) from the vanishing interfacial tension (VIT) technique. Fuel 184, 136–144. https://doi.org/10.1016/j.fuel.2016.06.128

[396] Zhang, M., Li, J., Zhao, J., Cui, Y., Luo, X., 2020. Comparison of CH_4 and CO_2 Adsorptions onto Calcite(10.4), Aragonite(011)Ca, and Vaterite(010)CO_3 Surfaces: An MD and DFT Investigation. ACS Omega 5, 11369–11377. https://doi.org/10.1021/acsomega.0c00345

[397] Zhang, T., Sun, S., 2021. Thermodynamics-Informed Neural Network (TINN) for Phase Equilibrium Calculations Considering Capillary Pressure. Energies 14, 7724. https://doi.org/10.3390/en14227724

[398] Zhang, W., Li, Y., Omambia, A.N., 2011. Reactive transport modeling of effects of convective mixing on long-term CO2 geological storage in deep saline formations. Int. J. Greenh. Gas Control 5, 241–256. https://doi.org/10.1016/j.ijggc.2010.10.007

[399] Zhang, Y., Chang, F., Song, Y., Zhao, J., Zhan, Y., Jian, W., 2011. Density of Carbon Dioxide + Brine Solution from Tianjin Reservoir under Sequestration Conditions. J. Chem. Eng. Data 56, 565–573. https://doi.org/10.1021/je101214e

[400] Zhang, Y., Li, T., Chen, B., Nishio, M., Song, Y., 2016. Density Measurement and Modeling of CO_2 −Brine System at Temperature and Pressure Corresponding to Storage Conditions. J. Chem. Eng. Data 61, 873–880. https://doi.org/10.1021/acs.jced.5b00719

[401] Zhao, H., Lai, Z., Firoozabadi, A., 2017. Sorption Hysteresis of Light Hydrocarbons and Carbon Dioxide in Shale and Kerogen. Sci. Rep. 7, 16209. https://doi.org/10.1038/s41598-017-13123-7

[402] Zhao, X., Sang, Q., Li, Y., Liu, H., Dong, M., 2021. CO2-kerogen interaction dominated CO2-oil counter-current diffusion and its effect on ad-/absorbed oil recovery and CO2 sequestration in shale. Fuel 294, 120500. https://doi.org/10.1016/j.fuel.2021.120500

[403] Zhao, Y., Feng, Y., Zhang, X., 2016. Molecular simulation of CO 2 /CH 4 self- and transport diffusion coefficients in coal. Fuel 165, 19–27. https://doi.org/10.1016/j.fuel.2015.10.035

[404] Zhou, J., Xie, S., Jiang, Y., Xian, X., Liu, Q., Lu, Z., Lyu, Q., 2018. Influence of Supercritical CO_2 Exposure on CH_4 and CO_2 Adsorption Behaviors of Shale: Implications for CO_2 Sequestration. Energy Fuels 32, 6073–6089. https://doi.org/10.1021/acs.energyfuels.8b00551

[405] Zhu, C., Li, Y., Zhao, Q., Gong, H., Sang, Q., Zou, H., Dong, M., 2018. Experimental study and simulation of CO2 transfer processes in shale oil reservoir. Int. J. Coal Geol. 191, 24–36. https://doi.org/10.1016/j.coal.2018.03.002

[406] Zmpitas, J., Gross, J., 2021. Modified Stokes–Einstein Equation for Molecular Self-Diffusion Based on Entropy Scaling. Ind. Eng. Chem. Res. 60, 4453–4459. https://doi.org/10.1021/acs.iecr.0c060

Appendices

Appendix A: Modelling Parameters of CO_2 Solubility in Aqueous Solutions

Table A.1 – Duan's parameters for calculating CO_2 fugacity coefficient in regions 1 and 2.

Parameter	Region	
	1	2
b_1	1.0	-7.1734882x10^{-1}
b_2	4.7586835x10^{-3}	1.5985379x10^{-4}
b_3	-3.3569963x10^{-6}	-4.9286471x10^{-7}
b_4	0.0	0.0
b_5	-1.3179396	0.0
b_6	-3.8389101x10^{-6}	-2.7855285x10^{-7}
b_7	0.0	1.1877015x10^{-9}
b_8	2.2815104x10^{-3}	0.0
b_9	0.0	0.0
b_{10}	0.0	0.0
b_{11}	0.0	0.0
b_{12}	0.0	-96.539512
b_{13}	0.0	4.4774938x10^{-1}
b_{14}	0.0	101.81078
b_{15}	0.0	5.3783879x10^{-6}

Table A.2 – Duan's parameters for calculating CO_2 and ions interaction parameters and chemical potential of CO_2.

Parameter	$\mu_{CO2}^{1(0)}/RT$	λ_{CO2-Na}	$\xi_{CO2-Na-Cl}$
C_1	28.9447706	-0.411370585	3.36389723x10^{-4}
C_2	-0.0354581768	6.07632013x10^{-4}	- 1.98298980x10^{-5}
C_3	-4770.67077	97.5347708	
C_4	1.02782768x10^{-5}		
C_5	33.8126098		
C_6	9.04037140x10^{-3}		
C_7	-0.00114934031		
C_8	-0.307405726000	-0.0237622469	2.12220830x10^{-3}
C_9	-0.0907301486	0.0170656236	-5.24873303x10^{-3}
C_{10}	9.32713393x10^{-4}		
C_{11}		1.41335834x10^{-5}	

Table A.3 – Li's parameters for the calculation of k coefficient.

Parameter	Value
a_1	0.00038384
a_2	-0.5595385
a_3	304.29268
a_4	-72044.305
a_5	6300338.8
a_6	-5.77093×10^{-7}
a_7	0.000827647
a_8	-0.43813556
a_9	101.44907
a_{10}	-8677.7045

Appendix B: Supercritical Extraction

Table B.1 – Yield, median particle size and applied $scCO_2$ extraction parameters.

Extraction Parameters	60 °C/40 MPa	60 °C/30 MPa	40 °C/15 MPa	60 °C/15 MPa
Yield (wt%)	1.7	1.4	1.1	0.8
D50 (mm)	4.0	3.5	3.8	7.9

Table B.2 – Yield of Soxhlet extraction using Hexadecane.

Temperature (°C)	Yield (wt%)
80	1.3
100	1.4
120	1.4

Appendix C: Interfacial Properties

Table C.1 - Interfacial tension of CO_2-NaCl brines systems versus pressure at 60 °C.

3 wt% NaCl Brine		10 wt% NaCl Brine	
Pressure (MPa)	**IFT (mN/m)**	**Pressure (MPa)**	**IFT (mN/m)**
0.1	67.2	0.1	70.6
5.4	47.7	5.7	49.7
10.1	34.0	10.0	36.8
15.1	28.7	15.2	31.8
20.1	26.4	20.1	30.1
25.1	26.4	25.1	30.1
30.3	26.3	30.2	30.0

Table C.2 – Interfacial tension of CO_2-SFEM crude oil systems versus pressure.

Temperature (°C)	**40**	**60**
Pressure (MPa)	**IFT (mN/m)**	
0.1	18.8	17.5
2.5	15.0	13.8
5.0	12.2	11.0
7.5	5.7	7.7
10.0	1.9	4.5
15.0	1.8	1.8
20.0	1.5	1.7
25.1	1.0	1.7
30.0	1.1	1.7
35.0	0.5	1.0
40.0	0.2	0.9

Table C.3 – Interfacial tension of CO_2-SFE40 Crude oil versus pressure at 60 °C.

Pressure (MPa)	**IFT (mN/m)**
0.1	21.2
2.0	18.3
4.0	14.5
6.2	11.2
8.0	8.6
10.5	5.0
12.2	3.7
13.8	3.0
15.7	3.1
17.9	3.1
19.7	3.0
22.3	2.9
26.1	2.5
29.6	2.3
34.8	2.2
37.7	2.2

Table C.4 – IFT of CO_2-Model oil, CO_2-Hexadecane and CO_2-Dodecane at 60 °C.

Model Oil		Hexadecane		Dodecane	
Pressure (MPa)	**IFT (mN/m)**	**Pressure (MPa)**	**IFT (mN/m)**	**Pressure (MPa)**	**IFT (mN/m)**
0.1	23.7	0.1	24.2	0.1	22.3
2.0	20.6	2.1	20.6	2.0	18.2
4.0	17.0	4.2	16.4	4.1	14.7
6.0	12.6	6.3	12.3	6.1	11.0
8.0	9.1	8.0	9.4	8.0	7.5
10.2	5.5	9.9	5.8	10.3	3.6
12.1	3.1	11.9	2.7	12.0	1.0
15.0	1.4	13.9	1.3		
18.0	0.8	16.0	0.8		
20.0	0.6				
22.0	0.3				

Table C.5 – Equilibrium IFT in CO_2-water/brine-oil systems at 60 °C.

Aqueous phase composition	**Deionized water**	**3 wt% NaCl**	**10 wt% NaCl**
Pressure (MPa)	**IFT (mN/m)**		
0.1	33.8	35.3	36.6
8	30.0	27.7	
10	26.5	25.1	29.3
15	22.7	22.3	

Table C.6 – CO_2 adsorption capacity of Sultani shale as a function of pressure and temperature.

40 °C		60 °C	
Pressure (MPa)	**Adsorption capacity (mmol/g)**	**Pressure (MPa)**	**Adsorption capacity (mmol/g)**
5.1	0.24	5.1	0.19
9.8	0.66	10.7	0.61
15.4	0.77	15.1	0.84
20.5	0.79	20.4	0.86
24.9	0.72	25.2	0.76
30.6	0.72	30.6	0.74

Table C.7 – CO_2 diffusion coefficient as a function of pressure and temperature.

40 °C		60 °C	
Pressure (MPa)	**Diffusion coefficient x10^{-10} m^2/s**	**Pressure (MPa)**	**Diffusion coefficient x10^{-10} m^2/s**
5.1	8.1	5.1	8.4
9.8	5.8	10.7	6
15.4	6.7	15.1	6
20.5	7.3	20.4	6.5
24.9	7.8	25.2	6.8
30.6	8	30.6	7.1

Table C.8 – Brine contact angle in a ternary CO_2-brine-shale system as a function of pressure at 60 °C.

3 wt% NaCl		10 wt% NaCl	
Pressure (MPa)	**Contact angle (°)**	**Pressure (MPa)**	**Contact angle (°)**
0.1	53	0.1	62
10	84	10.1	95
16	116	20.2	138
20	124		
26	118		
31	112		

Table C.9 - Zeta potential of shale-water/brine suspensions and contact angles in ternary oil-water/brine-shale system at 60 °C.

Aqueous Phase composition	Contact angle (°)	Zeta Potential (mV)	pH
DW	29	-17.9	9
3 wt% NaCl	29	-28.8	8.6
3 wt% $CaCl_2$	32	-7.6	8.5

Table C.10 - Aqueous phase contact angles in quaternary CO_2-model oil-water/brine-shale system at 60 °C.

Aqueous Phase composition	Pressure (MPa)	Contact angle (°)
DW	10	38
	15	33
3 wt% NaCl	10	36
	15	32
3 wt% $CaCl_2$	10	33
	15	33

Table C.11 - Deionized water contact angles in ternary Hexadecane-DW-calcite and quaternary CO_2-Hexadecane-DW-calcite system at 60 °C.

Pressure (MPa)	Contact angle (°)
0.1	78
10	60
15	46

Table C.12 - Brine contact angles on original and extracted shale samples as a function of pressure at 60 °C.

Sample	Pressure (MPa)	Contact angle (°)
Original	0.1	29
	15	39
Extracted	0.1	27
	15	16

Appendix D: Phase Behavior

Table D.1 -Densities of NaCl brines as a function of pressure and salinity at 60 °C.

NaCl Salt Concentration (wt%)	1	3	10
Pressure (MPa)	Density (g/cm^3)		
0.1	0.9839	0.9910	1.0308
1.0	0.9846	0.9937	1.0336
2.0	0.9854	0.9945	1.0343
3.0	0.9860	0.9952	1.0349
4.0	0.9865	0.9958	1.0354
5.0	0.9870	0.9963	1.0358
6.0	0.9874	0.9967	1.0362
7.0	0.9879	0.9972	1.0366
8.0	0.9883	0.9977	1.0370
9.0	0.9887	0.9981	1.0374
10.0	0.9892	0.9985	1.0378
15.0	0.9917	1.0006	1.0397
20.0	0.9937	1.0024	1.0415
25.0	0.9957	1.0043	1.0432

Table D.2 - Density of the model oil and Hexadecane as a function of pressure at 60 °C.

Model Oil		Hexadecane	
Pressure (MPa)	Density (g/cm^3)	Pressure (MPa)	Density (g/cm^3)
0.1	0.7492	0.1	0.7458
2.0	0.7537	2.1	0.7489
4.0	0.7563	4.2	0.7502
6.0	0.7586	6.1	0.7515
8.0	0.7603	8.7	0.7531
10.1	0.7618	10.1	0.7542
12.0	0.7632	15.9	0.7578
15.1	0.7653	20.3	0.7607
18.0	0.7679	22.0	0.7617
20.0	0.7684		
22.0	0.7705		

Table D.3 - Experimental and modelled densities of CO_2-saturated NaCl brines at 60 °C.

NaCl Salt Concentration (wt%) -Experimental Data					
1		**3**		**10**	
Pressure (MPa)	**Density (g/cm^3)**	**Pressure (MPa)**	**Density (g/cm^3)**	**Pressure (MPa)**	**Density (g/cm^3)**
5.6	0.9939	5.9	1.0051	5.9	1.0458
11.2	0.9994	11.0	1.0105	11.0	1.0507
15.7	1.0029	16.0	1.0129	15.9	1.0529
21.5	1.0051	21.1	1.0164	21.1	1.0546
NaCl Salt Concentration (wt%) -Modelling Data					
1		**3**		**10**	
Pressure (MPa)	**Density (g/cm^3)**	**Pressure (MPa)**	**Density (g/cm^3)**	**Pressure (MPa)**	**Density (g/cm^3)**
5.6	0.9925	5.9	1.0017	5.9	1.0395
11.2	0.9980	11.0	1.0065	11.0	1.0435
15.7	1.0007	16.0	1.0094	15.9	1.0460
21.5	1.0041	21.1	1.0122	21.1	1.0485

Table D.4 - Experimental densities of CO_2-saturated oleic phase versus pressure at 60 °C.

Model Oil		**Hexadecane**	
Pressure (MPa)	**Density (g/cm^3)**	**Pressure (MPa)**	**Density (g/cm^3)**
0.1	0.7492	0.1	0.7458
2.3	0.7565	4.1	0.7534
4.3	0.7626	6.6	0.7608
5.2	0.7654	8.1	0.7651
6.4	0.7685	10.1	0.7714
8.3	0.7735	12.1	0.7761
10.4	0.7798	15.1	0.7830
15.3	0.7942		
20.3	0.8087		

Table D.5-A - Volumetric expansion of model oil on Calcite as a function of pressure and aqueous phase composition at equilibrium and 60 °C.

Calcite				
Aqueous phase composition	**Deionized water**	**3 wt% NaCl**	**3 wt% $CaCl_2$**	**10 wt% NaCl**
Pressure (MPa)	**Volumetric expansion (%)**			
8.0	20.2	18.8	19.0	
10.0	29.2	27.2		25.2
15.0	49.9	46.9	47.4	

Table D.5-B - Volumetric expansion of $C_{16}H_{34}$ on Calcite as a function of pressure at equilibrium and 60 °C.

Pressure (MPa)	**Volumetric expansion (%)**
10.1	40.0
15.2	82.4

Table D.6 - The solubility of CO_2 in water/brine as a function of pressure at 60 °C.

Salt concentration (wt%)	Source	Pressure (MPa)	Solubility (mol/kg H_2O)	Solubility (g CO_2/100 g H_2O)
Pure water	Modeled after (Duan et al., 2006)	5.8	0.75	3.3
		11.0	1.075	4.9
		16.0	1.18	5.2
		21.0	1.25	5.5
1 wt% NaCl		5.6	0.70	3.1
		11.2	1.07	4.7
		15.7	1.137	5.0
		21.5	1.21	5.3
3 wt% NaCl		5.9	0.68	3.0
		11.0	0.99	4.4
		16.0	1.06	4.7
		21.1	1.12	4.9
10 wt% NaCl		5.9	0.54	2.4
		11.0	0.79	3.5
		15.9	0.84	3.7
		21.1	0.89	3.9
3 wt% $CaCl_2$		5.9	0.67	3.0
		11.0	0.99	4.3
		16.0	1.05	4.6
		21.0	1.11	4.9
1 wt% NaCl	Experimental data adapted from (Bando et al., 2003)	10.0	0.97	4.3
		15.0	1.07	4.7
		20.0	1.14	5.0
3 wt% NaCl		10.0	0.90	4.0
		15.0	1.00	4.4
		20.0	1.04	4.6

Table D.7-A - Solubility of CO_2 in model oil as a function of pressure and aqueous phase composition.

Aqueous phase composition	**Deionized water**	**3 wt% NaCl**	**3 wt% $CaCl_2$**	**10 wt% NaCl**
Pressure (MPa)	**Solubility (g CO_2/100 g oil)**			
8.0	22.3	20.9	21.1	
10.0	32.3	30.3		28.2
15.0	55.7	52.5	53.0	

Table D.7-B - Solubility of CO_2 in Hexadecane as a function of pressure.

Pressure (MPa)	**Solubility (g CO_2/100 g oil)**
10.1	43.0
15.2	88.5

Appendix E: Thermo-economic Analysis

Table E.1 – Energetic calculations of the supercritical CO_2 extraction cycle considering operating conditions of 15 MPa and 40 MPa at 60 °C.

Component	Assumption	P (MPa)		T (°C)		h (kJ/kg)		s (kJ/kg.k)		Delta h (kJ/kg)	CO2 Flow rate (kg/s)	Work required by the System (kW)	Efficiency of the respective component (%)	Power Consumption (kW)	Total Energy Consumption (kWh)
Compressor	Isentropic Compression	Initial	6	Initial	40	Initial	452	Initial	1.8462	41.7	0.5556	23.14	0.75	30.85	154.26
		Final	**15**	Final	116	Final	493	Final	1.8462						
Heat Exchanger	Isobaric cooling	Initial	**15**	Initial	116	Initial	493	Initial	1.8462	-146.8	0.5556	81.57	0.80	101.97	509.83
		Final	**15**	Final	60	Final	347	Final	1.4348						
Back pressure valve	Adiabatic Isenthalpic expansion	Initial	**15**	Initial	60	Initial	347	Initial	1.4348						
		Final	6	Final	22	Final	347	Final	1.4938						
Heat Exchanger	Isobaric heating	Initial	6	Initial	22	Initial	347	Initial	1.4938	105.2	0.5556	58.43	0.80	73.04	365.21
		Final	6	Final	40	Final	452	Final	1.8462						
Component	**Assumption**	**P (MPa)**		**T (°C)**		**h (kJ/kg)**		**s (kJ/kg.k)**		**Delta h (kJ/kg)**	**CO2 Flow rate (kg/s)**	**Work required by the System (kW)**	**Efficiency of the respective component (%)**	**Power Consumption (kW)**	**Total Energy Consumption (kWh)**
Compressor	Isentropic Compression	Initial	6	Initial	40	Initial	452	Initial	1.8462	105.0	0.5556	58.33	0.75	77.78	388.89
		Final	**40**	Final	203	Final	557	Final	1.8462						
Heat Exchanger	Isobaric cooling	Initial	**40**	Initial	203	Initial	557	Initial	1.8462	-251.8	0.5556	139.91	0.80	174.88	874.41
		Final	**40**	Final	60	Final	305	Final	1.2142						
Back pressure valve	Adiabatic Isenthalpic expansion	Initial	**40**	Initial	60	Initial	305	Initial	1.2142						
		Final	6	Final	22	Final	305	Final	1.3527						
Heat Excchanger	Isobaric heating	Initial	6	Initial	22	Initial	305	Initial	1.3527	146.8	0.5556	81.57	0.80	101.97	509.83
		Final	6	Final	40	Final	452	Final	1.8462						

Table E.2 – Costs associated with the extraction Process for different scenarios.

Baseline Scenario	**15 MPa**	**40 MPa**
Yield (kg/a)	408.0	1392.0
Energy consumption (kWh/a)	617576.4	1063875.0
Cost of energy (JD/a)	43230.3	74471.3
Peak demand charges (JD/a)	7361.5	12681.4
Total cost of energy (JD/a)	50591.9	87152.6
Cost of Oil (JD/kg)	**124.0**	**62.6**
Scenario HX	**15 MPa**	**40 MPa**
Yield (kg/a)	408.0	1392.0
Energy consumption (kWh/a)	95855.6	236633.3
Cost of energy (JD/a)	6709.9	16564.3
Peak demand charges (JD/a)	1142.6	2820.7
Total cost of energy (JD/a)	7852.5	19385.0
Cost of Oil (JD/kg)	**19.2**	**13.9**